Rheological Characterization of LDPE and PMMA with Optical Methods

by

David Shu Chung Lee

B.E. Chemical Engineering, The Cooper Union (1992)

M.S. Chemical Engineering Practice, Massachusetts Institute of Technology (1994)

Submitted to the Department of Chemical Engineering in partial fulfillment of the requirements for the degree of

DOCTOR OF PHILOSOPHY

at the

MASSACHUSETTS INSTITUTE OF TECHNOLOGY

June, 1998

Author .....
Chemical Engineering
May 22, 1998

Certified by .....
Robert C. Armstrong
Professor of Chemical Engineering
Thesis Supervisor

Accepted by .....
Robert E. Cohen
Professor of Chemical Engineering
Graduate Officer, Committee for Graduate Students

Rheological Characterization of LDPE and PMMA with Optical Methods

by

David Shu Chung Lee

Submitted to the Department of Chemical Engineering on May 22, 1998, in partial fulfillment of the requirements for the degree of Doctor of Philosophy in Chemical Engineering

Abstract

An optical method was developed to measure the viscosity and first normal stress coefficient of polymer melts containing volatile components. This method suppresses foaming of materials and provides results on-line. The shear-rate-dependent viscosity of a LDPE melt was measured in a channel die by combining the shear rates calculated from the velocity profile with shear stresses calculated from the pressure profile. The first normal stress coefficient was measured from the local shear rates and normal stress differences, which were in turn calculated using the stress-optic rule. The necessary birefringence and extinction angle profiles were measured by using a point-wise birefringence technique. The effects of the finite beam cross-sectional area and the end walls on the results were analyzed. The viscosity and first normal stress coefficient measured from LDPE using this method agreed with those obtained from parallel-plate rheometry and capillary viscometry to $\pm 25\%$ and $\pm 33\%$, respectively.

To demonstrate an application of this method to a material which foams at processing temperatures, the viscosity of two kinds of PMMA were measured with the optical method. PMMA depolymerizes at processing temperatures under atmospheric pressure to form methyl methacrylate, which foams the material. The viscosity of PMMA measured by using the optical method was compared to that obtained by using capillary viscometry. Measurement of the first normal stress coefficient was also demonstrated.

Thesis Supervisor: Robert C. Armstrong
Title: Professor, Chemical Engineering

Acknowledgments

I would like to express my gratitude to my advisor, Professor Robert Armstrong. Among his many outstanding qualities, he impressed me the most with his uncompromising quest for a logical explanation to all the discoveries. Throughout these years I learned not only a lot of interesting ideas from him, but I also learned from the way he handles demanding situations. I benefited immensely from being his student. Also, I would like to thank Professors Edward Merrill, Edwin Thomas, and Robert Brown for their valuable comments during progress report meetings, group seminars, and other times.

Very few people had been directly involved in this project besides my advisor and myself, but a lot of people should be credited here, most noticeably Dr. Ramon Albalak and Nina Shapley. Ramon acted as my informal advisor in the early stages of this project. I gained so much from his insight and skills at solving hands-on problems. My lab-mate Nina has never failed to be supportive and encouraging. Of course, the friendship of the Bob and Bob group has made the research experience so much more enjoyable.

At this final stage of my project I would like to thank all the people who have ever cared to asked about my research progress. In those days when problems kept coming and the solution seemed nowhere to be found, these people reminded me that there were a lot of people sharing the same kind of experience. Lastly, I would like to thank my family and my girlfriend Jenny for their patience and love. I was particularly impressed by their effort to understand my technical problems with no background and probably no interest in polymer processing.

Table of Contents

List of Figures

List of Tables

Chapter 1

Introduction

Rheology is the study of the relationship between stress and deformation of a fluid. Polymer rheology in particular captures the attention of many scientists and engineers because of both the interesting physics involved and the need of rheological information to understand and control a wide variety of commercial processes. Rheological information is usually expressed in terms of material functions. Common material functions include viscosity and the first and second normal stress coefficients. They describe the viscous and elastic properties a polymer, respectively, in steady simple shear flow. Although many methods have been developed to measure these functions for both polymer solutions and polymer melts, there are still a number of unsolved problems. This thesis is concerned with developing a method to measure these material functions for polymer melts. Specifically, this method aims at a class of materials whose rheology is difficult to study by conventional means because of their tendency to foam under ambient pressures.

Section 1.1 discusses the significance of rheology in polymer science and processing. Section 1.2 describes a problem associated with studying polymer melts. The method of approaching this problem is detailed in Section 1.3. The goals of this thesis are then stated in Section 1.4 along with an outline of its organization.

1.1 Rheology in Polymer Characterization and Processing

Rheology is important both in material characterization and determining process variables. In material characterization, the zero-shear-rate values of viscosity η and first normal stress coefficient Ψ_1 are useful because they are very sensitive to large-scale

structures in the fluid (Bird et al., 1987). Thus they can be used to give information about molecular weights. The longest relaxation time of the polymer can be approximated by the reciprocal of the shear rate at the which the material begins to shear-thin. An accurate characteristic relaxation time is necessary to define a meaningful Deborah number which determines the dynamics of molecular relaxation and the onset of elastic instabilities.

Rheological properties also play a crucial role in the area of materials processing. These properties are the parameters which relate the power input to macroscopic variables such as throughput per hour and other variables such as velocity and molecular orientation. Mechanical properties are functions of molecular orientation, and surface smoothness on the melt depends on the Deborah number which characterizes the onset of elastic instability. Key rheological properties like viscosity and first normal stress coefficient strongly depend on processing variables such as shear rate and temperature. Therefore, in order to optimize cost and material properties, it is necessary to have a good understanding of the material rheology. The following example, adapted from Dealy & Wissbrun (1990), illustrates how rheological information is used in a common polymer processing operation - extrusion.

As a first approximation to relate the output of the extruder conveying zone and the process variables, it is convenient to assume the polymer melt has a Newtonian viscosity η. The two driving forces for the flow of polymer inside the extruder barrel are the drag force exerted by the screw surface and the pressure gradient along the length of the channel. In Equation 1.1 the first term describes the contribution from the drag flow while the second terms describes the pressure-driven flow.

$$Q = \frac{\pi^2 N D_b^2 H \cos\theta \sin\theta}{2} - \frac{\pi D_b H^3}{12\eta}\frac{\partial P}{\partial l}\sin\theta \qquad (1.1)$$

where Q is the volumetric flow rate, N equals the screw speed in rpm, D_b is the screw base diameter, H equals the depth of the gap in which polymer flows, θ is the screw flight angle, $\frac{\partial P}{\partial l}$ equals the pressure drop and, η is the Newtonian viscosity. It is convenient to group several parameters together and simplify the equation in the form of Equation 1.2:

$$Q = Q_d - CP_e \tag{1.2}$$

where Q_d is the flow rate due to drag flow, C is the constant product which depends inversely on viscosity, and P_e is the exit pressure at the end of the extruder barrel.

Melt is supplied to the extruder die at the exit pressure of the barrel P_e. For a Newtonian viscosity approximation, the output is related to the exit pressure and the viscosity by:

$$Q = \frac{KP_e}{\eta} \tag{1.3}$$

where K is a constant that characterizes the resistance of the die to flow. For instance, if the die were a long pipe of radius R and length L, the K would be $\frac{\pi R^4}{8L}$.

It is common to use an operating diagram to determine the operating exit pressure and flow rate for a system with certain characteristics. Figure 1.1 is such an operating diagram with the output versus exit pressure. The intersecting point between the screw curve and the die curve is the operating point. For non-Newtonian viscosities, both the screw and the die characteristic curves are shifted and distorted. Figure 1.2 shows how the screw characteristic curve is altered for different power-law indices n on a plot of the dimensionless throughput against dimensionless pressure. Throughput is made dimensionless by the drag flow rate Q_d, and the pressure is non-dimensionalized by the maximum pressure generated by the screw given by $P_{max} = \frac{6\eta L v_{bz}}{H^2}$, where η is the viscosity at a shear rate equal

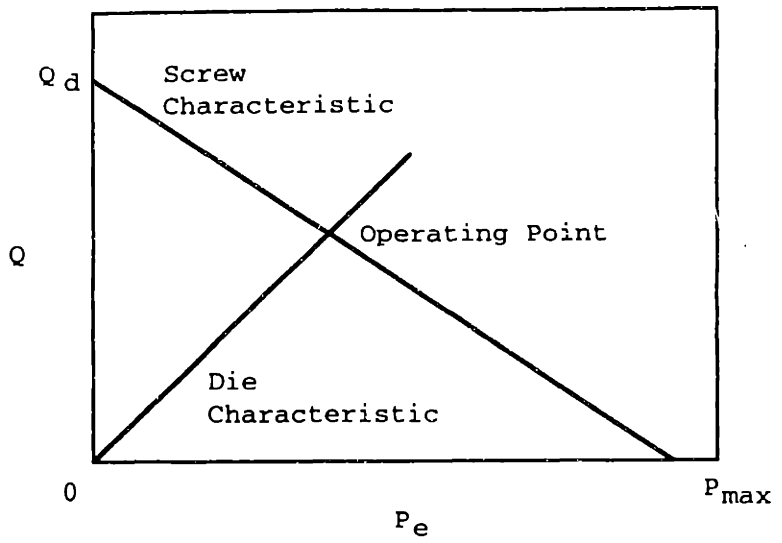

Figure 1.1: Operating diagram for extruder (Dealy and Wissbrun, 1994).

to the characteristic shear rate $\frac{\pi N D_b}{H}$ (linear velocity of the barrel divided by the channel depth). Increasing shear-thinning shifts the screw characteristic curve to the left, indicating a lower die pressure will be achieved with the same flow rate. How the die characteristic curve is repositioned strongly depends on the geometry of the die and the rheology of the melt. But it should be clear that the operating point is not the same as that in the Newtonian case. In general, numerical methods with detailed rheological information provide the most accurate estimation of the operating pressure and flow rate.

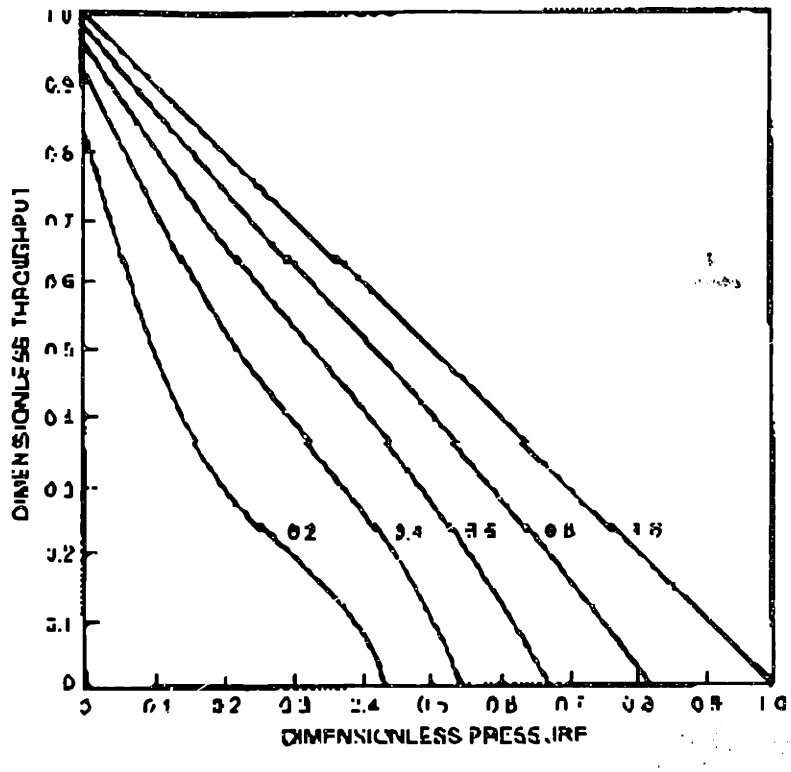

Figure 1.2: Screw characteristic curve for non-Newtonian fluid with power-law index n (Dealy and Wissbrun, 1990).

1.2 A Problem in Rheometry

Rheometry is a branch of rheology which concerns with developing and using experimental techniques to measure rheological properties. In particular, polymer melt rheometry represents quite a challenge because the melts have to be maintained at a sufficiently high and uniform temperature; furthermore the stresses they exert on the transducers cover a wide range, and the instrument transducers have to be sensitive at both the upper and lower limits.

1.2.1 Conventional Methods

The two material functions investigated in this study - viscosity and first normal stress coefficient - are strong functions of shear rate and temperature. The parallel-plate and capillary arrangements are common geometries used in measuring these functions. Figure 1.3 shows a schematic diagram of the parallel plate mode of a Rheometrics Mechanical Spectrometer (RMS-800). The sample is sandwiched between the two circular plates. When the bottom plate is rotated at a fixed angular velocity, the viscosity and first normal stress coefficient can be calculated from the measured torque and normal force exerted by the sample on the top plate.

A schematic diagram of a capillary viscometer is shown in Figure 1.4. Molten polymer, melted under pressure and high temperature, is extruded through a fine capillary with a plunger. By measuring the volumetric flow rate of the extrudate and the amount of force needed to extrude the material at that flow rate, the viscosity of the material at the capillary wall can be calculated.

In general the parallel-plate geometry is suitable for low shear rate measurements whereas the capillary is more appropriate for high shear rate measurements. This is because for parallel-plate rheometry, melt fracture and other free surface instabilities occur beyond certain critical Deborah numbers which generally correspond to moderate shear rates. In capillary viscometry, the frictional drag between the plunger and the barrel becomes significantly large compared to the net force required to extrude the sample at low shear rates. For common polymer melts such as low density polyethylene, the critical shear rate which determines which method to use turns out to be about 3 s^{-1}.

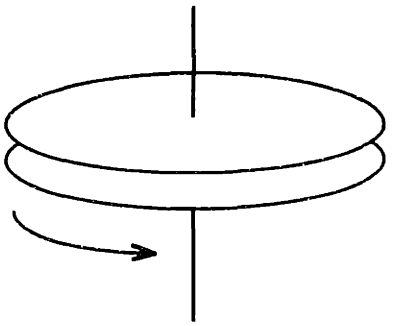

Figure 1.3: Parallel plate rheometry.

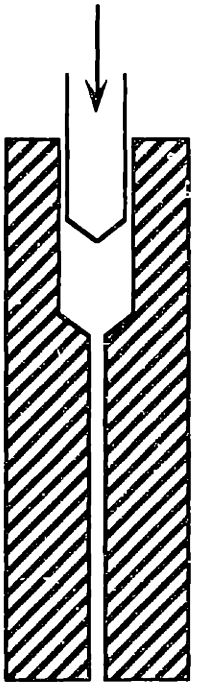

Figure 1.4: Capillary viscometry.

The first normal stress coefficient can be measured with the parallel-plate geometry but not with the standard capillary viscometer. Therefore, most first normal stress coefficient data exist in the literature were obtained at low shear rates. Besides the range of shear rate studied, a further distinction between the two geometries concerns with their readiness to be implemented for studying rheological functions in real time. The capillary

can be more readily incorporated into polymer processing equipment because most processes involve polymer melts flowing continuously through a channel. However, the parallel-plate measurement cannot be naturally fitted into common processes. As a result, low shear rate data are difficult to obtain on-line.

1.2.2 Measurement Difficulties with Foaming Materials

A number of polymeric materials tend to foam at processing temperatures and atmospheric pressure. The foaming renders the sample inhomogeneous and thus prevents any meaningful rheological measurement from being made at atmospheric pressure. Recall that low shear rate data are generally obtained with rotary devices operating at one atmosphere. Therefore, there is a lack of low shear rate viscosity and first normal stress coefficient data for such materials. Two common examples which fall into this category are poly(methyl methacrylate) and starch-containing polymers. Their chemical structures are shown in Figures 1.5 and 1.6, respectively. Poly(methyl methacrylate) or PMMA foams because of the depolymerization reaction which occurs at high enough temperatures. The kinetics of this reaction are detailed below. Starch normally contains a substantial amount of water. The water boils above 100°C and foams the sample during measurement (Weigand, 1992). Both of these polymers are investigated in this study, and the results are discussed in Chapter 4 and Appendix A of this thesis. The first paragraph in Appendix A details the compositions of the starch/EVOH blends studied in this project. The problem at hand is how to successfully measure the rheology of materials which tend to foam. Before explaining the method of approach to this problem, the following paragraphs explain why it is important to study the rheology of PMMA and starch-containing polymers.

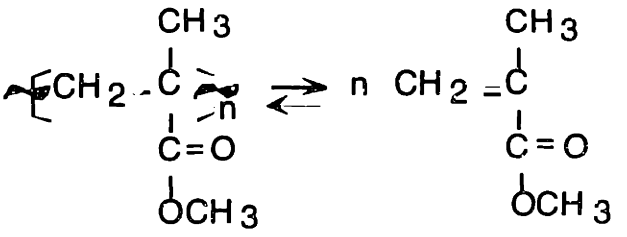

Figure 1.5: Poly(methyl methacrylate) in equilibrium with its monomer - methyl methacrylate.

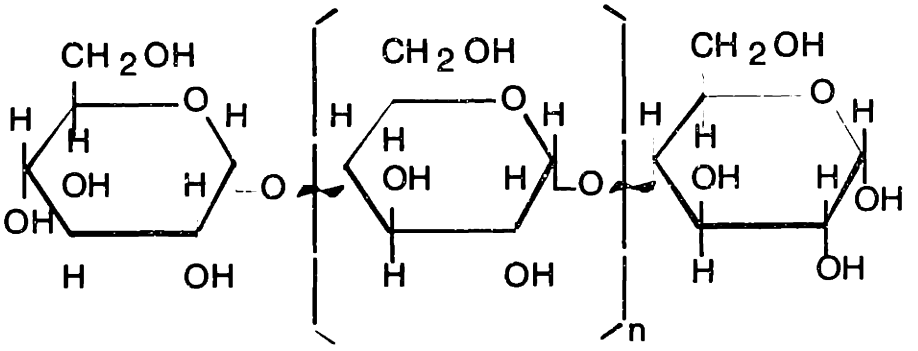

Figure 1.6: A glucose chain - the building block of starch.

PMMA is widely used in sheets and molds. It has high thermal stability, weatherability, and optical clarity. Common brand names of PMMA include Plexiglas^{TM}, Perspex^{TM}, and Lucite^{TM}. Rheology of PMMA is important in injection molding and extrusion, but not so in bulk casting. The importance of rheology to extrusion has been explained in Section 1.1 of this thesis. For bulk coasted objects such as lens and prisms, optical clarity is often the main concern. However, optical clarity will be compromised if either the monomer of PMMA, methyl methacrylate, vaporizes or the cast has non-uniform properties due to a different time-temperature history. The polymerization of methyl methacrylate is highly exothermic, producing about 140 cal of energy per gram. To avoid monomer evap-

oration, polymerization is usually carried out in a high-pressure autoclave. To avoid non-uniform properties induced by a different time-temperature history, the thermal gradients within the cast have to be kept to a minimum by maintaining a very low reaction rate (ICI Acrylics, Lucite Embedment description).

At atmospheric pressure, PMMA is observed to foam at processing temperatures in the range of 180°C to 260°C. The phenomenon of bubbling in PMMA is caused by unzipping (depropagation) of the polymer with monomer release (Rempp and Merrill, 1991). The following discussion outlines the kinetics of this reaction.

PMMA can be made in bulk, suspension, or emulsion by radical or anionic polymerization, although radical polymerization is the most common polymerization mechanism. Considering the propagation and depropagation for a chain of length i monomer units,

$$\underline{\quad i-1 \quad}M^* + M \underset{k_u}{\overset{k_p}{\rightleftharpoons}} \underline{\quad i \quad}M^*$$

where $\underline{\quad i \quad}M^*$ is a polymer chain of i monomer units with an active site M*. The active site in radical polymerization is a radial with an unpaired electron, and k_p and k_u are the rate constants of the forward and reverse reactions respectively. The equilibrium concentration of monomer in the solution $[M]_e$ is important since polymerization will not go forward once the monomer concentration drops to this equilibrium value. At equilibrium, both reactions proceed at the same rate, and the equilibrium monomer concentration can be calculated as:

$$-\frac{d[M]}{dt} \cong (k_p[M]_e - k_u)[M^*]_e = 0 \tag{1.4}$$

$$[M]_e \cong \frac{k_u}{k_p} \tag{1.5}$$

where [M*] represents the concentration of the polymers with active sites. Strictly speaking, [M*] should be a sum of concentrations of polymers with different lengths. The reaction rate constants k_u and k_p depend on temperature in an Arrhenius manner. $[M]_e$ is the equilibrium concentration of monomer in the solution. Alternatively, $[M]_e$ can be expressed in terms of the reaction enthalpy change ΔH and entropy change in the standard state ΔS^0,

$$\ln([M]_e/[M]_s) = \frac{\Delta H}{RT_c} - \frac{\Delta S^0}{R} \tag{1.6}$$

where $[M]_s$ is the monomer concentration in the standard state, T_c is the so-called "ceiling temperature." Each ceiling temperature has to refer to a stated monomer concentration $[M]_s$. Since the heat of reaction ΔH is negative, the equilibrium monomer concentration $[M]_e$ increases as the temperature increases (Rempp and Merrill, 1991).

A poly(methyl methacrylate) chain is subject to unzipping reaction upon cleavage of a C-C bond induced by, for example, UV irradiation. The methyl methacrylate monomer is commonly copolymerized with a small percent of ethyl acetate to inhibit the unzipping reaction along the polymer backbone. However, unzipping will still take place at high enough temperatures. From the results obtained in this study, it was found that a pressure of 8.5×10^5 Pa should enable the rheology of PMMA to be measured to a temperature of 215°C.

Within the past five years low-moisture starch/polymer blends have become a subject of great interest because of their potential to substitute for certain types of common plastics. Starch is considered for this purpose because it is both biodegradable and comes from renewable, sustainable, and inexpensive resources as compared to petroleum resources as explained below.

Increasing energy and environmental concern from the government and the general public prompts the development of biodegradable materials from sustainable resources. Since plastics come mainly from refinement of petroleum, plastic disposal represents a drain on petroleum resources. Although the idea of burning plastics to recover the energy value has been advocated, the infrastructures for residential and commercial heating still favor using oil or gas as the main sources of fuel. Because solid waste made out of plastics cannot be naturally decomposed, landfill and incineration become the main plastic disposal means. Landfill sites, however, are running out quickly. The toxicological effects of gases resulting from incineration of plastics is not clear yet (Doane et al., 1991). Recycling of plastics has been enforced for many kinds of plastics but there are still many plastic products such as dinnerware and bags that are not being recycled. Using renewable biodegradable material has advantages for both energy saving and environmental protection. On the one hand, plastics made from natural resources could ease pressure on oil supplies if their price soars. On the other hand, biodegradable plastics can be decomposed into benign components quickly and completely after use.

The main reason why conventional plastics are not biodegradable is that many of their monomers are not found in nature, and thus few organisms have adapted to feed on them (The New York Times, 1990). But when plastics are formed from material found in living plants, they become easily digestible food sources for microorganisms in the soil. Starch is one of the most abundant materials produced in nature, and it is easily recovered from plant organs holding it. That is why starch is a favorite material to be studied for its potential to be used as a common plastic substitute. It also has the advantage of being relatively low in cost and is readily converted chemically, physically, and biologically into useful low molecular weight compounds or high molecular polymers.

The main problems that prevent starch from being widely used as a plastic substitute include a lack of understanding in how to process low-moisture-content starch and the mechanical instability of starch-based plastic articles caused primarily by variations in their moisture content. Thus it is important to understand the rheology of these materials before they can be more widely used. The feasibility of processing starch using standard thermoplastic processing equipment is evident from patents in the literature (Tomka et al., 1987 European Patent Applications 88810130.0 and 88810548.3). However, understanding and controlling processing variables such as how much and when plasticizers should be added have not yet been mastered. Although blending non-volatile plasticizers improves the mechanical properties of the product by making it less sensitive to moisture content, lots of improvements in formulation and processing are needed to produce high quality blends with mechanical properties and stability competitive to those of existing thermoplastics. For instance, many utensils made from mostly starch are still too brittle to be considered functional. Moreover, the relatively short shelf life of existing products is also problem.

The potential benefit of exploring new uses for starch is huge. The degradability of starchy products makes them a probable candidate for replacing conventional packaging materials such as polystyrene foams. It was calculated that there is an over one billion pounds per year polystyrene market which is excellent candidate for biodegradable materials (Narayan, 1994). Other major target markets for biodegradable polymeric materials include food handling products such as cups, plates, cutlery, containers, etc. and certain disposable materials like diapers, personal care and feminine hygiene products, and certain medical plastics. To realize fully the potential of starch as a raw material, the first step is to gain a better understanding of its various properties. In particular, it is important to understand the relationship between starch type, molecular structure and molecular

weight, and composition of blends of starch with other polymers and additives on the mechanical and chemical properties of products. At the same time the relationship between these characteristics and the processibility of the starch and/or starch blends must be understood for these materials to be exploited commercially. Rheological information of starch and starch blends strongly depends on the molecular structure, and is crucial in determining process parameters. Therefore, there is a need to measure the rheological properties of these materials.

1.3 Method of Approach

The mechanical techniques described so far suffer from a lack of low shear rate viscosity and first normal stress coefficient data due to the problem of sample foaming. A suitable device should allow viscosity and first normal stress coefficient to be measured at a high pressure so that foaming is suppressed. A high-pressure environment can be realized inside a die. Consider the cross-sectional diagram of a polymer melt flowing down a rectangular channel (Figure 1.5). The velocity continuously changes from the centerline to the wall, and likewise does the shear rate. Viscosity, defined as the ratio of shear stress to shear rate, varies across the gap due to its strong dependence on shear rate. To measure the shear rate at each position, laser Doppler velocimetry (LDV) is used in this study. LDV is an

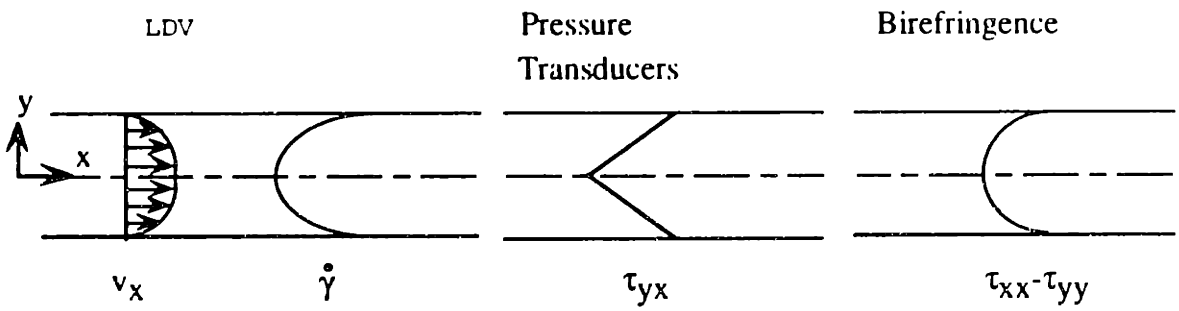

Figure 1.7: Optical method.

optical method that measures the velocity of fluid particles at a certain position in space. Its principle and implementation in this study are discussed in detail in Section 3.3 of this thesis. After the velocity profile v_x is recorded by scanning the laser beams along the gap, differentiating the velocity with respect to position in the gradient direction (y) yields the shear rate profile $\dot{\gamma}$. From a momentum balance, the shear stress τ_{yx} is well known to be proportional to the pressure gradient and to vary linearly across the gap:

$$\tau_{yx} = \left(-\frac{dp}{dx}\right)y \tag{1.7}$$

where $\frac{dp}{dx}$ is the pressure gradient along the flow direction and y is the distance along the velocity gradient direction. Monitoring the pressure drop gives the shear stress at any position across the gap. Taking the ratio of shear stress to the shear rate at a specific location yields the viscosity η at that location.

The first normal stress coefficient Ψ_1 is the ratio of negative of the first normal stress difference $-(\tau_{xx}-\tau_{yy})$ to the square of the shear rate $\dot{\gamma}^2$. The first normal stress difference profile is probed by using the birefringence technique coupled with the stress-optic law. This law states that the stress tensor of a polymer solution or a polymer melt is linearly related to and coaxial with its refractive index tensor:

$$\mathbf{n} = C\boldsymbol{\tau} + A\mathbf{I} \tag{1.8}$$

where $\mathbf{n}$ is the refractive index tensor, C is the stress-optical coefficient, τ is the stress tensor, A is a constant, and $\mathbf{I}$ is the identity tensor.

The principle and implementation of this technique will be detailed in Section 3.4 of this thesis. The first normal stress coefficient can be studied as a function of shear rate and by relating the first normal stress difference and the shear rate at different positions in the

flow field. Temperature dependence can be studied by extruding the polymer at different temperatures.

1.4 Thesis Goals

The goal of this thesis is to develop and demonstrate an optical technique for measuring the viscosity and first normal stress coefficient of polymer melts, especially for those which foam at ambient temperature and processing temperatures. First, the accuracy of the optical method is quantified by comparing the optical results from low density polyethylene to those obtained from the conventional methods. Next, the optical method is applied to study the rheology of poly(methyl methacrylate). To accomplish these goals, the organization of this thesis is outlined below.

Current development in the areas of PMMA and low-moisture starch rheology, LDV, and birefringence were reviewed in Chapter 2. A brief background of birefringence is provided in this chapter to help readers understand the relevant literature. Chapter 3 details the experimental system. It explains the principles and implementation of the two optical techniques used in this study - LDV and birefringence. It also discusses the specifics of the fluid transport system and how this system is coupled with the optical instruments. In order to verify the measured flow field, a commercial fluid mechanics package FIDAP^{TM} was used to simulate the experimental flow condition. The theory and implementation of this simulation exercise is explained in Appendix B. Chapter 4 summaries all the results. Section 4.1 focuses on rheological data obtained with LDPE by using conventional mechanical instruments. Section 4.2 focuses on the viscosity measurement of LDPE by the optical method. Prior to that all the supporting data, namely the velocity, shear rate, and shear stress profiles are presented. The first normal stress coefficient measurement of

LDPE by optical methods is discussed Section 4.3. This section also explains the data regression scheme which is essential for interpreting point-wise birefringence data. A case study of applying the optical method to PMMA is detailed in Section 4.4. Observations during application of the optical method to starch-polymer blends are described in Appendix A. Major conclusions and are summarized in Chapter 5.

Chapter 2

Literature Review

This chapter summarizes the important prior research related to this thesis. It is divided into three sections. The first section details the development of optical techniques for polymer flow studies. The second one highlights literature on the rheology of PMMA. The last one focuses on the rheology of low-moisture starch melt.

2.1 Optical Techniques

The two optical techniques, laser Doppler velocimetry and birefringence, have been widely used in studying fluid mechanics and polymer rheology. To provide the necessary background for understanding the various contributions on birefringence measurements, Section 2.1.1 is devoted to a discussion of the principles behind measuring flow induced birefringence, Section 2.1.2 is a review of the important works in using optical techniques to study polymer melts, and Section 2.1.3 discusses two issues associated with birefringence studies. They are the difficulty in calculating the orientation angle when the retardance is equal to a multiple of 2π, and the effects of the side walls of a flow cell which are normal to the beam propagation direction.

2.1.1 Principles of Birefringence Measurements

Birefringence techniques have been used to study the stress fields of polymer flow with the help of the stress-optical law. This law states that the refractive index tensor is linearly related to and coaxial with the stress tensor. This relationship and the relevant termi-

nology are briefly explained below. For a more detailed explanation, Quinzani (1991) provides an excellent discussion in her thesis.

The principal axis system of a tensor is an axis system in which the off-diagonal terms of the tensor are zero. The stress-optical law states that in the principal axis system, the stress tensor and the refractive index tensor are linearly related with a constant C, the stress-optical coefficient:

$$\begin{bmatrix} n_{11} & 0 & 0 \\ 0 & n_{22} & 0 \\ 0 & 0 & n_{33} \end{bmatrix} = C \cdot \begin{bmatrix} \tau_{11} & 0 & 0 \\ 0 & \tau_{22} & 0 \\ 0 & 0 & \tau_{33} \end{bmatrix} + A \cdot \begin{bmatrix} 1 & 0 & 0 \\ 0 & 1 & 0 \\ 0 & 0 & 1 \end{bmatrix} \tag{2.1}$$

where n_{11}, n_{22}, n_{33} are the principal values of the refractive index tensor, τ_{11}, τ_{22},τ_{33} are the principal values of the stress tensor, and C and A are constant scalars.

Generally, the principal axis system does not coincide with the laboratory axis system. For instance, when they are offset by an angle χ in the 1-2 plane around the 3 axis (Figure 2.1), then the components of the stress tensor in the laboratory coordinates are related to those in the principal axis system by the rotation matrix $\mathbf{R}(\chi)$.

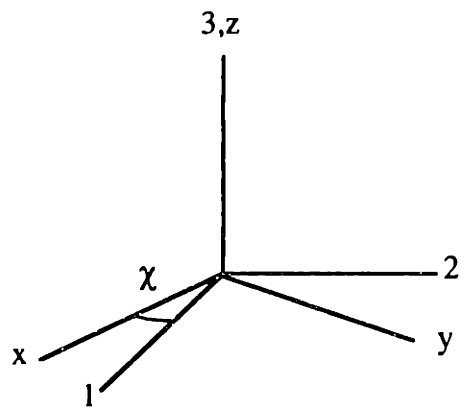

Figure 2.1: Principal axis systems (1-2-3) and laboratory axis system (x-y-z).

$$\begin{bmatrix} \tau_{xx} & \tau_{yx} & \tau_{zx} \\ \tau_{yx} & \tau_{yy} & \tau_{yz} \\ \tau_{zx} & \tau_{yz} & \tau_{zz} \end{bmatrix} = R(-\chi) \begin{bmatrix} \tau_{11} & 0 & 0 \\ 0 & \tau_{22} & 0 \\ 0 & 0 & \tau_{33} \end{bmatrix} R(\chi) \tag{2.2}$$

Combining Equations 2.1 & 2.2 leads to:

$$\tau_{yx} = \frac{n_{11} - n_{22}}{2C} \sin(2\chi) \tag{2.3}$$

$$\tau_{xx} - \tau_{yy} = \frac{n_{11} - n_{22}}{C} \cos(2\chi) \tag{2.4}$$

The terms birefringence, retardance, and extinction angle are frequently used in describing the results. First, birefringence is defined as the difference in refractive indices between the two orthogonal principal directions in an anisotropic medium:

$$\Delta n = n_{11} - n_{22} \tag{2.5}$$

Retardance is an angular measurement of the birefringence. Consider the change in polarization state for plane-polarized light traveling through a birefringent medium of thickness d as illustrated in Figure 2.2. Before entering the sample, both components of the light wave have the same wavelength λ. Inside the anisotropic sample, the wavelength of the horizontal component and that of the vertical component are retarded differently because of the two different refractive indices n_1 and n_2. After the wave comes out of the sample, the wavelength of each component returns to λ. However, there is now a phase shift between the two orthogonal components in the 1 and 2 directions. The polarization state of the wave has changed from linear to elliptical.

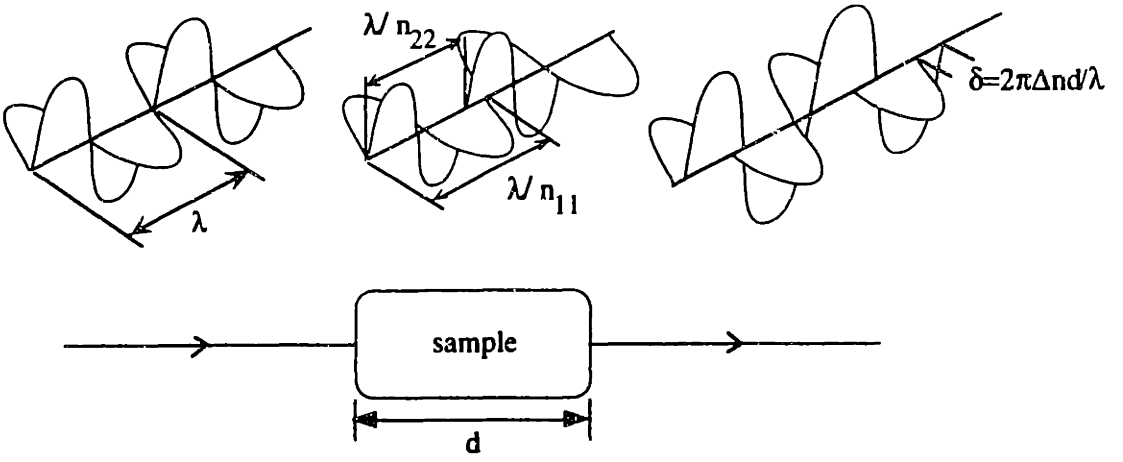

Figure 2.2: Retardance as a measurement of the phase difference.

The retardance, δ, is an angular measurement of this phase shift:

$$\delta = 2\pi\left(\frac{d}{\lambda/n_{11}} - \frac{d}{\lambda/n_{22}}\right) \tag{2.6}$$

The extinction angle χ is the angle made by the principal stress axis system with the laboratory axis system, which is usually defined by the direction of the flow. Polymer molecules orient themselves with the direction of the principal stress, so the extinction angle is also a measure of how the polymer molecules align themselves with the flow. Figure 2.3 shows two examples of a shear flow. On the left the fluid is sheared between a stationary plate and a moving plate. The shear stress is uniform across the gap, so that all the polymer molecules between the plates are oriented at one single angle with respect to the flow direction. On the right there is a pressure-driven flow with a changing shear stress across the channel. Thus, the extinction angle χ changes from the centerline to the walls.

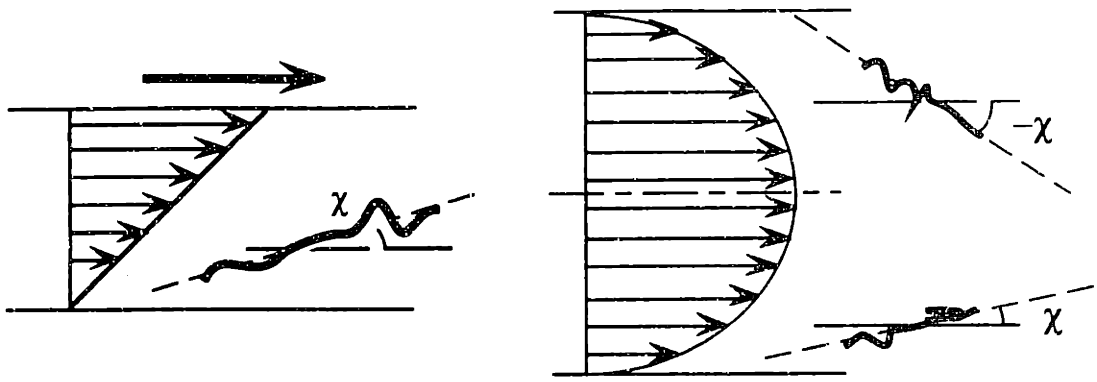

Figure 2.3: Extinction angles in planar shear flow and pressure-driven flow.

Two optical configurations are commonly used to study birefringence. One configuration involves illuminating the entire flow field which is located between two crossed polarizers. This method is called the full-field birefringence method in this thesis. If white light is used, then color fringes will be seen. In most cases experiments are performed with a monochromatic light source, so that bright and dark fringes of one color are seen instead. The birefringence pattern is studied and the stress field can be calculated with the stress-optical law. The method to study this pattern is explained in the next paragraphs. The another optical configuration is to use a fine light beam (usually a laser) to measure the birefringence at one well-defined position in the flow field. This method is called the point-wise birefringence method. With this method, the intensity of light at each position in the flow is related to the birefringence and extinction angle at that position. The birefringence field can be measured by scanning the light beam across the location of interest.

Two kinds of fringes, isochromatics and isoclinics, are seen from the illumination scheme used in the full-field birefringence method. From Equation 2.7, dark fringes of the isochromatics are observed when the intensity of light is nullified at places where the

retardance δ is equal to a multiple of 2π. The other kind of dark fringes, the isoclinics, appear when the extinction angle is aligned with the one of the crossed polarizers, i.e. $\chi = \theta$.

$$I = \frac{I_0}{4}\sin^2\left(\frac{\delta}{2}\right)\sin^2(2(\chi-\theta)) \tag{2.7}$$

where I is the intensity detected, I_0 is the original light intensity before the light hits the first polarizer, and θ is the angle made by the polarizer with respect to the flow (laboratory axis system). To distinguish between the isochromatics and the isoclinics, one needs to rotate the polarizer and the analyzer by the same amount at the same time. This way the isoclinics move as the angle θ is changed while the isochromatics should stay still. In practice, however, it is very difficult to discern the exact locations of the isoclinics since a moving thick dark band, instead of a fine line, was usually observed when the polarizer-analyzer pair are rotated (Mackay, 1985; Wales, 1976; McHugh et al., 1987).

The isoclinics can be eliminated from the illumination pattern through crossed polarizers by modifying the optical train as follows. One quarter-wave plate, oriented at 45° with respect to the first polarizer, is placed between the first polarizer and the sample. The second quarter-wave plate, oriented 90° with respect to the first one, is inserted between the sample and the second polarizer. The intensity detected becomes (Mackay and Boger, 1986):

$$I = \frac{I_0}{2}\sin^2\left(\frac{\delta}{2}\right) \tag{2.8}$$

2.1.2 Review of Birefringence Studies on Polymer Melts

The full-field birefringence method has been a very popular method for studying polymer melts. This subsection summaries the more important and innovative contributions in this field. Some of the pioneering work was done by Wales (1976). He extensively investigated the stress-optical relationship with a number of flow geometries, including truncated cone-and-plate, slit, and cylindrical capillary. The working principles of these apparatuses are briefly described below, followed by some important discoveries he obtained by using them. Detailed accounts of these experiments can be found in Wales (1976) and Janeschitz-Kriegl (1983).

The shear rate of a fluid is constant in the region confined by the cone-and-plate geometry for small cone angles. In Wales' cone-and-plate apparatus, light entered radially into the gap between the plate and the cone after passing through the incident polarizer. It then came out along the axis through a prism mounted at about the center of the structure before hitting the analyzer. Retardance was determined by the insertion of an appropriate compensator aligned 45° with respect to the polarizer and the analyzer. The compensator reversed the effect of the flow on the polarization state of the light, so a dark field was observed again after the light passed the analyzer. Extinction angles were measured from the position of the crossed polarizers when a dark field was observed as the two polarizers were rotated simultaneously.

The coordinate system used to describe the slit flow apparatus that Wales used is defined as follows: 1 denotes the flow direction; 2, the direction of the velocity gradient, and 3, the neutral direction. Wales reported difficulty in measuring the birefringence in the 1-2 plane. He attributed his problem to the absence of a clear and narrow fringe that should represent the isoclinic line. A broad shadow instead of a fine line was observed. He

also reported very large amount of scattering as polystyrene and polyethylene were extruded through the slit at high stresses. In view of those difficulties, he designed an algorithm to calculate the birefringence in the 1-3 plane (n_{11}-n_{33}) at the wall from the averaged birefringence he measured by sending the beam in the 2 direction. The birefringence (n_{11}-n_{33}) is known to be changing along the velocity gradient direction. A variable called the path difference P was defined, which was related to the retardance δ defined earlier in this chapter by:

$$P = \frac{\lambda}{2\pi} \cdot \delta \tag{2.9}$$

For an infinitesimal thickness dy, the birefringence (n_{11}-n_{33}) can be approximated as constant.

$$dP = (n_{11} - n_{33})dy \tag{2.10}$$

where P is the path difference, and y is the distance in the velocity gradient direction. Integrating along the velocity gradient direction from one end wall (y=0) to the other (y=a),the total path difference P_{total} between the two end walls is:

$$P_{total} = 2\int_0^{a/2} (n_{11} - n_{33})dy \tag{2.11}$$

Using the proportionality of shear stress $\tau(y)$ to distance y in the velocity gradient direction, P_{total} can be expressed by:

$$P_{total} = \frac{a}{\tau_w}\int_0^{\tau_w} (n_{11} - n_{33})d\tau \tag{2.12}$$

where τ_w is the wall shear stress. The measured averaged birefringence ϕ, is equal to P_{total}/a. Differentiating Equation 2.12 with respect to the wall shear stress τ_w, an equation relating the birefringence at the wall ϕ_w, the measured averaged birefringence, and wall shear stress can be established:

$$\phi_w = (n_{11} - n_{33})_w = \phi\left(1 + \frac{d\ln\phi}{d\ln\tau_w}\right) \tag{2.13}$$

The cylindrical capillary device was used to measure the birefringence between the velocity gradient (2) and the flow (3) directions (n_{22}-n_{33}). Light was directed along the flow axis of the capillary. By using a microscope, a Maltese cross was seen (Figure 2.4 left). During compensation, the compensator was placed at 45° to the crossed polarizers, the cross split into two fringes (Figure 2.4 right) which moved toward the edge formed by the wall of the capillary. Compensation was achieved when the apex of each fringe was judged to be at the wall of the die.

Maltese cross Two fringes

Figure 2.4: Fringe patterns observed by Wales (1976) with his cylindrical capillary device.

With these three pieces of equipment, Wales was able to study in detail the stress-optical law for melts. Some of the key results are summarized here. First, the validity of the stress optical law was investigated by measuring the ratio $\frac{\Delta n \cdot \sin 2\chi}{2\tau_{12}}$ as a function of shear stress. It was found that the ratio was constant up to a shear stress of 10^4 Pa, beyond

which "depolarization due to the parasitic gradients at the windows" prevented accurate measurements (Wales, 1976). As required by the theory (Lodge, 1955), the stress-optical coefficient was found to be independent of shear rate, molecular weight, and molecular weight distribution.

Next, Wales compared the extinction angle $\chi = \text{atan}\frac{1}{2}\frac{2\tau_{12}}{\tau_{11}-\tau_{22}}$ obtained from measurements using both the optical (truncated cone-and-plate) and mechanical (Weissenberg cone-and-plate). The ratios calculated from these two methods were in good agreement. This study was conducted for both polypropylene (PP) and polyethylene (PE). The maximum shear rates achieved by both methods for PP and PE were 2.3 s^{-1} and 0.2 s^{-1}, respectively; and the extinction angle at the highest shear rates was about 23° for both polymers.

The edge effect for a slit channel was also studied with his slit apparatus. Channels with different aspect ratio 30:1 to 10:1 were found to give the same (n_{11}-n_{33}) over a range of shear rates. Recall that no results were reported from measurements in the 1-2 plane, so there is no direct evidence to support the independence of (n_{11}-n_{22}) on the aspect ratio, when this ratio is larger than 10:1. However, most researchers have ignored the effects of the end walls on the measurement of n_{11}-n_{22} when the aspect ratio in their slit geometry is larger than 10:1. In this study, the effects of the end walls in a slit channel is examined, and the analysis is detailed in Section 4.3 of this thesis.

Wales' experimental results provided the only reliable proof, that the author is aware of, for the proportionality and coaxiality between the stress and refractive index tensor of polymer melts under shear flow up to a certain shear stress. The maximum shear stress achieved in his experiments, 10^4 Pa, has been quoted as the benchmark shear stress under which the stress-optical relation is expected to hold in a shear flow. However, Wales did not explicity give a measure of the accuracy of the data he obtained. Also, the scheme he

used to determine when complete compensation was achieved, though might be consistent, was subject to a certain level of arbitration.

Han and Drexler (1973) measured stress field of HDPE in slit dies with both sudden and tapered die entrances by the full-field method. With a white, diffused light source, the isoclinic fringes appeared as sharp dark bands over the colored isochromatics. It was not clear from their publications how they managed to quantify the positions of both the isochromatics and the isoclinics despite the broadening of the isoclinics. To convert the optical data (isochromatics and isoclinics) to stress data, the stress-optical coefficient was needed. It was measured by using Equation 2.3 by comparing the shear stress calculated from the pressure drop along the downstream slit to the quantity $0.5\ \Delta n \sin 2\chi$. In addition to measuring the stress fields of sudden and tapered contraction by using full-field birefringence, these researchers also estimated the velocity profiles by photographing the streak lines (Drexler and Han, 1973).

A plot between $0.5\ \Delta n \sin 2\chi$ and the shear stress for a polymer under shear flow in a slit channel should reveal whether the stress-optical relation holds at a known shear stress. However, as pointed out by Mackay (1985), most publications of full-field birefringence experiments in a slit channel did not include any plot of $0.5\ \Delta n \sin 2\chi$ over shear stress to show how the stress-optical coefficients were obtained. Also, usually no uncertainty estimate for this coefficient was given. Therefore, it is difficult to assess the reliability of these results.

The stress measurement by using birefringence was often coupled with flow kinematics measurements by using streak photography or laser Doppler velocimetry (LDV). Kramer and Meissner (1982) showed that laser Doppler velocimetry could measure velocity in polymer melt flowing at high temperature and pressure. In their planar contraction flow cell x was the flow direction, y was the velocity gradient direction, and z was the neu-

tral direction. The contraction ratio measured from the y dimensions upstream and downstream was 10 to 1. The velocity profiles across the gradient $v_x(y)$ and neutral $v_x(z)$ direction were measured at many positions along flow axis of a sudden contraction die. The volumetric flow rate was calculated by integration by combining profiles of $v_x(y)$ and $v_x(z)$. However, many of the velocity profiles $v_x(y)$ at $z \neq 0$ were not measurable because of the way the flow cell was designed. They were calculated by assuming that the profiles of $v_x(y)$ off the centerline had the same shape as $v_x(y)$ on the centerline (z=0) but scaled down by $v_x(z)$ at y=0. The flow rate calculated this way agreed with that measured by cutting and weighing the extrudate to within 3.4%. For the flow with a downstream wall shear rate $\dot{\gamma}_w$ of 13.7 s^{-1}, the fully developed velocity profile was achieved at 15 slit heights down the channel. For the case with $\dot{\gamma}_w = 65\ s^{-1}$, the fully developed velocity profile was not achieved at the end of the die, which was 20 slit height down the channel. The assumptions of a constant density and $\frac{\partial v_z}{\partial z} = 0$ were verified at the die entrance by calculating $\frac{\partial v_x}{\partial x}$ and $\frac{\partial v_y}{\partial y}$ from $v_x(x)$ and $v_y(y)$.

The smoothness of the polymer melt velocity profiles measured by Kramer and Meissner was not frequently seen in other results in the literature. These researchers showed that relatively smooth velocity profiles could be obtained by careful temperature and flow rate control, so that the shear rate profiles could be determinated by differentiating the velocity profiles. Unfortunately, no estimate of uncertainty was shown in the paper.

Mackley and Moore (1986) measured the velocity profile of HDPE in a sudden contraction die. They discovered the LDV instrument measured a non-zero velocity right at the wall. To find out the origin of this non-zero velocity, a numerical simulation was carried out to predict the velocity measured by the LDV instrument using the same auto-correlation algorithm used by the LDV spectrum analyzer and a power-law velocity profile. It was found that because part of the finite beam cross-sectional area was blocked, a non-

zero average velocity was expected when the velocity covered by the partially blocked beam was averaged with the beam center right at the interface. Moreover, it was suggested that the power-law model was adequate in general to describe the velocity profile. By measuring the centerline velocity $v_x(0)$ along the length of the flow direction (x), a characteristic shape of elongation rate profile $\frac{\partial v_x}{\partial x}(x)$, peaking right before the entrance, was found. The profiles obtained at different temperatures, flow rates, and for different molecular weights all showed the same characteristic features.

Stress field measurement using full-field birefringence were coupled to the flow kinematic measurements using LDV with the aforementioned experimental system (Mackley and Moore, 1986) by Aldhouse et al. (1986). The aim was to test whether the corotational Goddard-Miller type constitutive equation (Equations 2.14 and 2.15) was sufficient to describe the stress-strain behavior along the centerline.

$$\tau_{ij}(t) = -\int_{-\infty}^{t} G(t-t')\dot{\gamma}_{ij}(t')dt' \tag{2.14}$$

$$\tau_{11} - \tau_{22} = -4\int_{-\infty}^{t} G(t-t')\left(\frac{dv_x}{dx}\right)(t')dt' \tag{2.15}$$

where $\tau_{ij}(t)$ is the ij^{th} component of the stress tensor as a function with time, G(t-t') is the relaxation function, $\dot{\gamma}_{ij}$ is the ij^{th} component of the corotation rate-of-strain tensor as a function of time along the centerline.

The relaxation spectrum was estimated from the storage and loss moduli (G' and G'') measured with parallel plate rheometry (Rheometrics System Four Mechanical Spectrometer). The rate of strain $\frac{\partial v_x}{\partial x}$ was calculated from the velocity data obtained by laser Doppler velocimetry. The stress field was determined by full-field birefringence measurement. Only the isochromatics were recorded, and the first principle normal stress difference

$\tau_{11} - \tau_{22}$ along the centerline was calculated based on the stress-optical coefficients measured by Wales (1976). The principle stress difference calculated by the constitutive equation agreed reasonably well with the measured stress at lower temperatures (150°C - 170°C) for the material with lower molecular weight (HDPE $\overline{M_n}$=14,000 and $\overline{M_w}$=65,000), but not so well at higher temperatures and with the higher molecular weight sample (Temperature = 190°C - 210°C, $\overline{M_n}$=20,000 and $\overline{M_w}$=130,000). The researchers found that the calculated stress profiles were highly sensitive to the relaxation times used to fit the linear viscoelastic data G' and G''.

McHugh et al. (1987) tried to explain and use the broadened isoclinics observed when a polymer melt was flowing along a slit channel die. They found that the isoclinics became thick dark bands once a critical extinction angle was reached. Recall that Wales (1976) suggested the broadening of isoclinics might be due to the parasitic shear stress in the 1-3 direction (τ_{13}). However, the state of polarization of light traveling in the x_3 direction should not be directly affected by the stress in the 1-3 direction τ_{13} (Frocht, 1941). It was proposed that viscous heating might divert the beam (Wales, 1976). McHugh et al. did not give an estimate of the importance of viscous heating by calculating whether the change in refractive index along the beam propagation direction is significant to cause beam bending. Instead, they calculated that a shear rate exceeding 500 s^{-1} would be needed to raise the melt temperature by 10°C in order to affect significantly the velocity and shear rate profiles. At those shear rates, secondary flow would become important.

Using the computational fluid dynamics software package FIDAP, McHugh et al. were able to calculate the variation in shear stress τ_{12} along the direction of the beam (x_3). They pointed out that in deriving the equation which described the light intensity (Equation 2.16), a constant shear stress had been assumed.

$$T = \frac{1}{2}\left(\sin\frac{\pi L\Delta n}{\lambda}\right)^2[1-\cos(\chi-\alpha)] \tag{2.16}$$

where T is the transmittance, L is the depth of the optical path, Δn is the birefringence, λ is the wavelength, χ is the extinction angle, and α is the angle between the polarizer axis and the flow direction.

Using both a Newtonian and a power-law fluid model, the researchers showed that τ_{12} changed along x_3, the neutral direction. The strong functional dependence of τ_{12} on x_3 near the wall led to a range of x_2 values over which a given stress level and associated ellipsoid orientation would occur that satisfied the conditions for a dark isoclinic fringe (McHugh et al., 1987). From plots of shear stress versus distance in both the velocity gradient and beam propagation directions (x_2 and x_3 respectively), there was a smaller variation in shear stress at the position (a certain x_2) which corresponded to the inside edge of the isoclinic band (the edge closer to the centerline). Therefore, the inside edge of the dark band should be used to locate the extinction angle. Using this guideline, the McHugh et al. showed that the data which they used to calculated the stress-optical coefficient seemed to scatter less than the ones obtained by using the center position of the dark band. Also, from the simulation, they showed that changing the flow rate or the zero-shear-rate viscosity would not change the width of these bands.

Mackay (1985), who was one of the authors in the paper by McHugh et al., admitted that using the inside edge to locate the extinction angle did not always yield a constant ratio of $\frac{\Delta n \cdot \sin 2\chi}{2\tau_{12}}$ at different shear stresses across the gap for all the materials that he studied. Moreover, McHugh et al. did not show any extinction angle profile across the gap determined by using their scheme. Therefore, the results they reported cannot be taken as a proof for the validity of the stress-optical rule at the stress levels of their experiment.

Baaijens (1994) studied the flow of LDPE around a cylinder by using both LDV and full-field birefringence. Photos of birefringence fringes were compared to finite element simulation of the flow obtained for both the Phan-Thien Tanner and Giseskus models. Good qualitative agreement was obtained, but the measured isochromatic contours were closer to the cylinder than the calculated ones, and the measured downstream relaxation was slower than that in the simulation. The discrepancy points to the fact that their simulation did not accurately describe the stress field. Possible explanation include the incapability of these fluid models to describe the stress field in complex flows, and the lack of a proper account for the end wall effects on the birefringence pattern.

2.1.3 Two Problems with Using the Birefringence Technique

There are two main problems associated with interpreting the results from birefringence experiments. The first one is the difficulty in calculating the orientation angle when the retardance is equal to a multiple of 2π. The second one is the issue concerning the effect of the side walls of a flow cell which are normal to the beam propagation direction. These walls make the flow field three-dimensional in reality. Before discussing the approaches in tackling these problems, it is necessary to explain briefly how a point-wise birefringence experiment is conducted since most studies summarized below were carried out using this optical configuration instead of the full-field configuration.

A typical point-wise birefringence apparatus is shown in Figure 2.5. Plane-polarized light is obtained by passing a light source with a small beam diameter (usually a laser) through a plane polarizer. This light then goes through a modulation element to acquire a time dependence. Common examples of this modulation element include a rotating quarter wave-plate and a photoelastic modulator. The sample, with its unique retardance and

extinction angle, further alters the polarization state of the light. Finally, the light passes through an analyzer before its intensity is recorded by the detector. Because of the imposed modulation, the intensity of light detected contains some time-dependent components:

$$I(t) = I_{dc} + I_{\omega}(\delta, \chi)\sin(\omega t) + I_{2w}(\delta, \chi)\sin(2\omega t) + \ldots \tag{2.17}$$

where I(t) is the time-varying intensity detected, I_{dc} is the time-invariant component of the intensity, $I_{\omega}(\delta,\chi)$ is the first harmonic, and $I_{2\omega}(\delta,\chi)$ is the second harmonic.

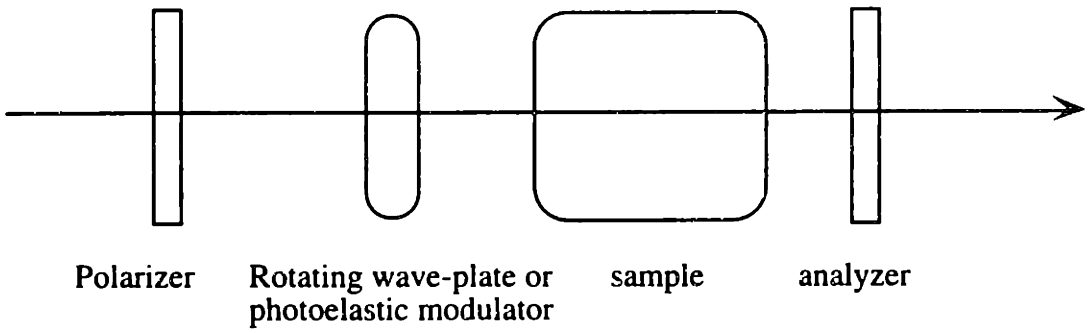

Figure 2.5: Typical pointwise birefringence apparatus configuration

By using locked-in amplifiers or other numerical FFT methods, the constant part I_{dc} and the coefficients of the time-dependent terms $I_{\omega}(\delta,\chi)$ and $I_{2\omega}(\delta,\chi)$ can be obtained. These coefficients are then used to calculate the unknown retardance δ and extinction angle χ. Some configurations include one or two extra quarter wave-plates. The unknown retardance and extinction angles will then be different functions of the measured coefficients.

The first problem, namely the ambiguity of the extinction angle when the retardance is a multiple of 2π, is a problem for both full-field and pointwise birefringence measure-

ments. Equations 2.18 and 2.19 show that when the retardance is close to a multiple of 2π, then the intensity for both full-field and point-wise birefringence measurement will be equal to zero, nullifying the terms containing the extinction angle. Thus the extinction angle χ cannot be determined from these equations. (Note: Equation 2.18 is true for a pointwise birefringence system with a photo-elastic modulator vibrating at a frequency ω as the modulation element).

$$I = I_0 \sin^2\left(\frac{\delta}{2}\right)\sin^2(2(\chi-\theta)) \tag{2.18}$$

$$I(t) = I_0/2 + J_1(A)I_0[\sin\delta\cos 2\chi]\sin\omega t + J_2(A)I_0[(1-\cos\delta)\sin 2\chi\cos 2\chi]\cos 2\omega t + \ldots \tag{2.19}$$

Larson et al. (1988) reported that it was difficult to obtain reliable orientation angle data at specific times during the stress relaxation experiment of a polystyrene solution using a Couette cell. He attributed the lack of reliable data to the high sensitivity of noise of the extinction angle at specific times when the retardance went through different orders. Abetz and Fuller (1990) tried to solve this problem by using two laser beams with different wavelengths simultaneously to study the sample. The experiment was conducted with a double Couette cell with two concentric cylinders. This two-color setup was different from the original two-color birefringence experiment (Chow et al., 1985) because both of the beams in this experiment were phase-modulated. When the retardance of one color is equal to 2π or its multiples (a change order), the other should not be close to an order change. However, in the paper where Abetz and Fuller showed the results for a shear inception experiment, it was not clear what the maximum retardance achievable was.

The idea of using multiple wavelength was further exploited by Hongladarom and Burghardt (1993). They studied the molecular alignment of polymer liquid crystals in a

shear flow between two parallel plates. After passing through the sample sandwiched between parallel or crossed polarizers, the white halogen light used was directed into a grating spectrograph before being measured by an array of photodiodes. Accounting for the dependence of birefringence and light intensity on wavelength, the researchers were able to measure the polymer orientations at a wide range of shear rates (0.02 s^{-1} to 100 s^{-1}). No modulation technique was used in this study. While the birefringence was determined through analyzing the intensity at different wavelengths, the orientation angie was calculated from the absolute incident and resultant intensities.

Instead of changing the wavelength, Zhang et al. (1994) used two different optical configurations to solve the problem of measuring the extinction angle at multiple order retardation. In one configuration a quarter wave-plate and an analyzer were used between the sample and the detector. In another only an analyzer was used in that position. These two configurations yielded different dependencies of retardance δ on the coefficients: one as a sine function and the other as a cosin function. Because sine and cosine have zeroes at even and odd multiples of $\pi/2$ respectively, the two measurements would not go to zero at the same time. Unfortunately, the researchers only showed retardance data that barely exceeded 2π.

The second problem in using the birefringence technique is primarily caused by the edge effects of the side walls of a flow cell. Although Wales (1976) has shown that the 1-3 birefringence (n_{11}-n_{33}) between the flow and neutral direction (z) does not change with aspect ratio when this ratio is bigger than 10, many researchers believe that the edge effect should not be ignored. Burghardt and Fuller (1990) used the three dimensional equivalence theorem to calculate the error induced by using the stress-optical law directly in a Couette flow by a numerical simulation. They showed that the continuous variation of birefringence and orientation in the beam propagation direction can be approximated by a

series of discrete retarders $G(\delta_i)$ at discrete orientations χ_i. With the composite sample retardance (U) represented as a product of Jones matrices,

$$U = \prod_{i=1}^{N} R(\chi_i)G(\delta_i)R(-\chi_i) \tag{2.20}$$

The product U can be expressed as the product of a pure retarder of retardance δ oriented at angle χ, followed by a rotation matrix $R(\theta)$ at angle θ,

$$U = R(\chi)G(\delta)R(-\chi)R(\theta) \tag{2.21}$$

The researchers defined a "symmetric" flow to be one whose composite sample retardance U can be represented by $U = R(\chi)G(\delta)R(-\chi)$, or θ=0; whereas an asymmetric is one whose composite sample retardance has to be expressed as $U = R(\chi)G(\delta)R(-\chi)R(\theta)$ with a non-zero θ. One example of such a symmetric flow is a generated by a Couette cell with both windows being stationary, whereas an asymmetric flow is produced by having one of the two windows moving with the moving cylindrical wall. Galante and Frattini (1991) pointed out that it was impossible to assign any physical meaning to χ, δ, and θ, since there was no single representative χ or δ for the sample. Using a finite difference method, Burghardt and Fuller nonetheless calculated the χ and δ variation along z for the whole flow field from the velocity field with an upper-convected Maxwell model. They then compared them with the χ and δ using the stress-optic law directly and calculated the discrepancy as functions of position along the velocity gradient direction and Weissenberg number (We), defined as N_1/τ_{yx}. It was found that the errors were largest near the intersections of moving and stationary boundaries, for example, in the vicinity of the moving cylinder wall and the stationary windows. They also

found that the error in retardance increased as We was increased, but the error in extinction angle was smallest at intermediate We. With the symmetric flows, measuring the first normal stress coefficient N_1 at a position midway between the moving and stationary cylinder walls showed no end effects for aspect ratios bigger than 3. For shear stress, increasing the aspect ratio from 10 to 20 reduced the error from 5% to 3%. Therefore, it was recommended that for Couette flows, the measurements should be made at midway across the gradient direction (y=0.5) for symmetric flows, and closer to the stationary cylinder wall (y=0.36) for asymmetric flows in order to minimize the edge effect. In their paper the researchers did not suggest any physical phenomenon that would have explained their observations.

Galante and Frattini (1991) used the differential propagation Mueller matrix formalism developed by Azzam (1973) to trace the polarization state of light along the neutral (3) axis in a slit geometry. Again, the flow axis is (1), the velocity gradient axis is (2), and the neutral axis is (3). Before going into their results obtained from a three-dimensional slit geometry, it should be pointed out that these researchers showed with an upper-convected Maxwell fluid model that assuming no variable changed along the neutral direction, the extinction angle profile (χ versus x_2) changed only by seven degrees toward the lateral walls as the Weissenberg number increased beyond 3. The Weissenberg number was defined as $We = \tau\left\{\frac{B}{\eta}\left(-\frac{dP}{dx_1}\right)\right\}$, where τ is the wall shear stress, B is the gap half width, η is the viscosity, and $-dp/dx_1$ is the pressure drop along the flow direction. Therefore, a broadening of isoclinic band was predicted even though there were no edge effects. Note that this Weissenberg number was not related to that defined by Burghardt and Fuller (1990).

To investigate edge effects, the main assumption the Galante and Frattini made was that only the shear stress τ_{12} could affect the polarization state of light. The fluid model

used was again the upper-convected Maxwell fluid model. For low retardance levels (δ_0 of order 1), and low Weissenburg number (of order 1), neither the retardance nor the extinction angle profiles were affected in the velocity gradient direction. The characteristic retardance δ_0 was defined as $\delta_0 = \frac{4\pi CW}{\lambda} \cdot \left\{ B\left(-\frac{dp}{dx_1}\right)\right\}$, where C is the stress-optical coefficient and W is the length of the optical path. For higher We (We of order 10), they found a uniform reduction in retardance across the channel, but the extinction angle was not affected. They proposed a sandwich model to describe the optical properties of the fluid along the 3 direction where there were two optically isotropic layers sandwiching the anisotropic core. Therefore, the "effective optical path" was shorter than the real optical path, as indicated by the uniform reduction in retardance. At high retardance level, the simulation showed dramatic spikes in the extinction angle profiles in the vicinity of $\delta=2n\pi$, where n is an integer. The error introduced by these spikes was not reduced by using a higher aspect ratio like 20:1, where the retardance profile had the same shape as the ideal 2-D profiles. The origin of these spikes in the extinction angle profiles was not explained in their paper (Galante and Frattini, 1991). For a non-elastic power-law fluid, it was found that as the power-law index n decreased, the shear stress changed less along the neutral direction. This is because as n decreased, the shear-thinning increased and the boundary layer thickness decreased, so that the resultant edge effect was also smaller.

Both the edge effect and the difficulty in determining the extinction angle when retardance passes through multiples of 2π were experienced during the study described in this thesis. The details of how the data were interpreted are explained in Chapter 4.

2.2 Rheology of PMMA Melts

The rheology of poly(methyl methacrylate) has been studied for decades. Berry and Fox (1968) used a capillary device to measure the apparent viscosity of PMMA. In such an experiment the melt was pressured to flow through a capillary at a very low speed. The flow rate was measured by the recording the time t required for the melt to go between two marks along the length of the capillary. If the fluid were Newtonian, then the viscosity η could be calculated by:

$$\eta = ktp \tag{2.22}$$

where p is the pressure difference between the two ends of the capillary, k is a constant determined by repeating the same experiment with a fluid with known viscosity. One limitation of this method is that Equation 2.22 is only valid for a constant-viscosity fluid. Since viscosity generally starts decreasing with shear rate beyond a certain shear rate, this capillary experiment has to be repeated many times to ensure that the fluid is still in the Newtonian region. Moreover, moving the fluid at such low shear rate demands a very small pressure difference as the driving force. It is difficult to measure such a small force accurately. For example, if a plunger is used to provide the driving force, the frictional drag becomes comparable in size to the net force required itself.

Capillary viscometry has been successful in measuring the viscosity of PMMA at high shear rate. Nagal et al. (1984) used a capillary viscometer to measure a brand of PMMA copolymerized with 2% methyl acrylate (polydispersity index = 1.7). They observed no Newtonian plateau at all temperatures between 182°C and 272°C. The viscosity was found to decrease with shear rate with a slope n of -0.63 at all temperatures. In the experiments the shear rate ranged from 6.7 s^{-1} to 1330 s^{-1} and length-to-diameter ratio of the capillary

ranged from 5 to 40. The Bagley correction was found unnecessary because no entrance pressure drop was observed.

Wippler (1991) estimated the zero-shear-rate viscosity of PMMA from a Cole-cole diagram of the data obtained from the oscillatory mode of parallel-plate geometry. A Cole-cole diagram is a plot of η'' versus η' at different oscillation frequencies. The zero-shear-rate viscosity η_0 is estimated by the η' value at the position the curve intersects the η' axis. This method is not as direct as a plot of $\eta'(\omega)$ and take the value at the limit of ω goes to zero.

Other researchers estimated η_0 using Cox-Merz rule. It states that the magnitude of the complex viscosity is equal to the viscosity at corresponding values of frequency and shear rate:

$$\eta(\dot{\gamma}) = \eta^*(\omega)\big|_{\omega=\dot{\gamma}} = \eta'(\omega)\left[1+\left(\frac{\eta''}{\eta'}\right)^2\right]^{0.5}\Bigg|_{\omega=\dot{\gamma}} \tag{2.23}$$

where η^* is the complex viscosity, η' and η'' correspond to the in- and out-of-phase part of the complex viscosity, ω and $\dot{\gamma}$ are the frequency and the shear rate, respectively.

Bousmina and Muller (1993) measured the storage and loss moduli of PMMA copolymerized with 4% ethyl acetate with a parallel-plate geometry from 0.01 to 100 rad/s over a temperature range of 151.1°C to 288.8°C. Using Cox-Merz rule they estimated η_0 at a reference temperature of 200°C. In a subsequent study (1996) they found that the viscosity measurement by capillary viscometry at high shear rates agreed with the data calculated from dynamic measurements. All these experimental studies of PMMA illustrate the difficulty of obtaining directly low shear rate viscosity and first normal stress difference data with standard methods.

Hieber and Chiang (1992) found that the Cross viscosity model fitted the viscosity-shear rate data obtained at high shear rate better than the Carreau model, but not as well as the Carreau-Yasuda model for a number of polymer melts. Specifically, comparing the averaged root-mean-square deviation between the calculated viscosity from the model and the experimental data for 17 sets of PMMA viscosity measurements, the averaged deviation of the Generalized Carreau model, the Cross model, and the Carreau model were found to be 4.6%, 5.1%, and 9.5% respectively. The different models are summarized as follows:

Carreau-Yasuda model

$$\eta = \eta_0(1 + (\lambda\dot{\gamma})^a)^{\frac{n-1}{a}} \tag{2.24}$$

Cross model

$$\eta = \eta_0(1 + (\lambda\dot{\gamma})^{1-n})^{-1} \tag{2.25}$$

Carreau model

$$\eta = \eta_0(1 + (\lambda\dot{\gamma})^2)^{\frac{n-1}{2}} \tag{2.26}$$

where η is viscosity, η_0 is the zero-shear-rate viscosity, λ is a time constant, n is the power-law index, and a is a parameter. The authors attributed the difference to the high "stiffness" of the Carreau model. That is, the Carreau model generally predicted a too rapid transition from the Newtonian regime to the power-law region compared with experimental data. This problem was significantly reduced by using introducing the parameter "a" as in the Carreau-Yasuda model (Yasuda, 1979).

Nagal et al. (1992) investigated the shear rate dependence of the viscosity of PMMA by using a capillary viscometer, and the birefringence pattern between crossed-polarizers flowing through a 1 mm wide slit die. At 220°C, the zero-shear-rate viscosity was not observed for shear rates as low as about 7 s^{-1}. With the crossed polarizers, the isochromatic fringe pattern was observed and the birefringence Δn was calculated by:

$$\Delta n = \frac{\lambda N}{T} \tag{2.27}$$

where λ is the wavelength of light, N is the fringe order, and T is the optical path length.

The authors found that the birefringence Δn and the shear stress τ formed a straight line on a log-log plot independent of molecular weight and temperature. A dark band covering the entire slit was seen when the pair of polarizers was rotated so that their axes were 45° with respect to the flow direction. Concluding that the extinction angle χ was 45° for the entire domain, the researchers calculated the stress-optical coefficient C from the following equation:

$$2 \cdot C \cdot \tau = \Delta n \cdot \sin(2\chi) = \Delta n \tag{2.28}$$

The stress-optical coefficient for PMMA at 220°C calculated in this way was 1×10^{-10} Pa^{-1}. However, it should be pointed out that occurence of such a thick dark isoclinic band when the polarizer pair was rotated to 45° with respect to the flow direction did not mean the extinction angle over the slit was uniform at 45°. For an idealized one-dimensional slit flow with an infinite aspect ratio, the extinction angle should decrease monotonically from 45° at the centerline toward the walls. Wales (1976), McHugh et al. (1987) and Galante and Frattini (1991) each explained the origin of this dark band as detailed in Section 2.1.2

of this thesis. Therefore, the stress-optical coefficient calculated by assuming a uniform extinction angle profile is questionable.

Retting (1979) measured the change in birefringence and tensile stress over time for PMMA and other polymers during a tensile test at constant crosshead speeds. Birefringence was measured using a pair of crossed polarizers with an optical compensator. He found that the ratio of birefringence to stress for PMMA was not constant with increasing level of strain. He nonetheless computed stress-optical coefficients of 9.3×10^{-11} Pa^{-1} at 120°C and 1.11×10^{-10} Pa^{-1} at 140°C for a sample with $\overline{M_n} = 1.8 \times 10^5$ g/mol. For another sample with $\overline{M_n} = 5 \times 10^6$ g/mol, the stress-optical coefficient was calculated to be 1.14×10^{-10} Pa^{-1}.

2.3 Rheology of Low-Moisture Starch

There have been numerous reports on the rheology of starch solutions and cereal doughs due to the extensive use of starch in food and non-food related applications. However, the amount of rheological information on low-moisture starch or starch blends is limited. Low-moisture starch is characterized by a smaller than 50% water content. As starch is heated in the presence of limited amount of water, gelation that typically occurs at about 60°C - 80°C does not occur. Instead, the crystallites are melted, leading to a molten phase (Vergnes and Villemaire, 1987). Heating and/or mechanical shearing is needed to destroy the native granular structure of starch. The process of extrusion usually provides enough heating and mechanical treatment to destructure the starch. This review focuses on "destructurized", amorphous, and low-moisture starch melts.

Two kinds of instruments are commonly used to study the rheology of low-moisture starch: the capillary viscometer and the slit die viscometer. As explained in Section 1.2, a

capillary viscometer measures the viscosity of polymer melts by recording the force need to ram-extrude the sample through a capillary at a certain flow rate. A slit die viscometer provides a simple way of studying low-moisture and "destructurized" starch rheology because the heat and shearing during extrusion destroy the starch granules (Verges and Villemaire, 1987). Figure 2.6 shows a typical setup for such a viscometer (Senouci and Smith, 1988). It essentially consists of a long rectangular or cylindrical die with pressure transducers mounted along the length of the die connected to an extruder which melts and pumps the material. Working with the same principle as a capillary viscometer, the slit die viscometer measures the viscosity by recording the pressure drop required to extrude the melt at a certain flow rate.

Similar to a capillary viscometer, the thermo-mechanical history experienced by the starch sample is not constant at different shear rate. This is because a higher screw speed is necessary to increase the flow rate in order to achieve a higher wall shear rate. Therefore, the viscometer die also introduces a changing history to the sample.

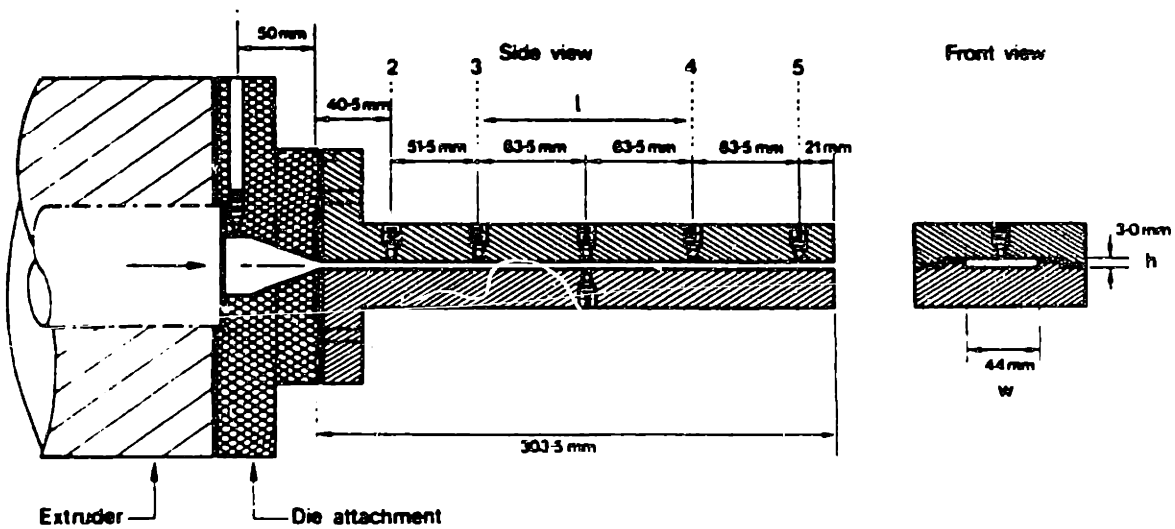

Figure 2.6: Die viscometer (Senouci and Smith, 1988)

Harper et al. in 1971 first proposed a constitutive model to fit the data on viscosity obtained by using a single-screw extruder and a cylindrical die viscometer (Harper et al., 1971). The model described the shear-thinning behavior with a power-law dependence on shear rate and an exponential dependence on temperature and moisture content (Equation 2.29). This viscosity model was found to be valid for a blend of corn and oat flour for a relatively limited shear rate range (10 - 100 s^{-1}).

$$\eta = 36.0\dot{\gamma}^{0.36-1}\exp\left(\frac{4388}{T}\right)\exp(-0.101MC) \tag{2.29}$$

where MC equals the moisture content on wet basis, η is the viscosity in Pa s, $\dot{\gamma}$ is the shear rate in s^{-1}, and T is the temperature in K.

Other viscosity data on low-moisture extrusion-cooked starch have been measured since this early study for different kinds of starch using either a slit or a cylindrical die viscometer (Cervone and Harper, 1978; Bruin et al., 1978; Fletcher et al., 1985). All of the proposed correlations follow a very similar form as the one originally put forward by Harper et al. (1971). The shear rate always follows a power-law type dependence on viscosity. Viscosity varies with temperature in an Arrhenius manner and exponentially with moisture content.

A significant advance in the characterization of low-moisture starch melt was the introduction of a rheometer by Vergnes and Villemaire (1987), which they called the "Rheoplast". This rheometer consisted of a Couette cell which gave the starch a well-characterized pre-shearing history and a plunger which forced the starch melt to go through a cylindrical tube where the viscosity was measured (Figure 2.7). The model they developed was still essentially a power-law model in shear rate, but it had a more complicated functional dependence of viscosity on temperature and moisture content. It also included an

exponential dependence of the mechanical energy input W, which was defined as the mechanical energy provided per unit volume of starch (Equation 2.30, 2.31, and 2.32).

$$\eta = m\dot{\gamma}^{n-1} \tag{2.30}$$

$$m = m_0 \exp\left[\frac{E}{R}\left(\frac{1}{T} - \frac{1}{T_0}\right) - \alpha(MC - MC_0) - \beta(W - W_0)\right] \tag{2.31}$$

$$n(T, MC) = \alpha_1 T + \alpha_2 MC + \alpha_3 (T \cdot MC) \tag{2.32}$$

where MC equals the moisture content on wet basis, T is temperature in ^{o}C, and W is the amount of mechanical energy provided in J/m^3. K_0, T_0, MC_0, W_0, α, α_1, α_2, α_3, E/R, and β are all constants.

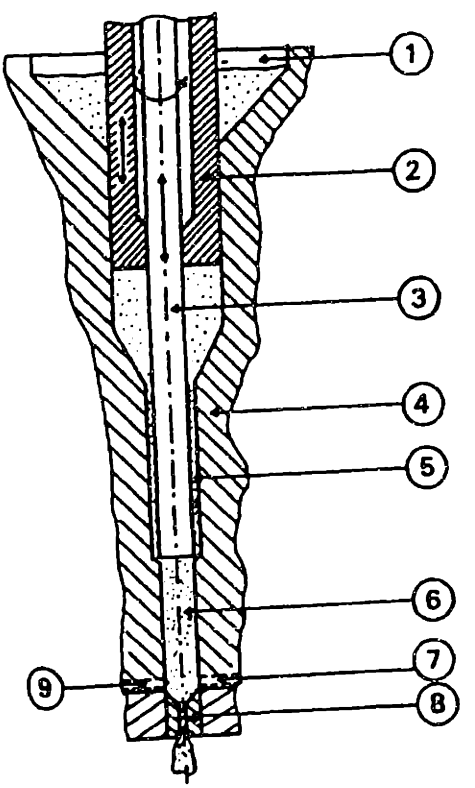

Figure 2.7: Rheoplast rheometer (Vergnes and Villemaire, 1987). The labels are defined as follows: (1) hopper, (2) annular piston, (3) inner piston, (4) thermostated barrel, (5) shearing chamber, (6) injection pot, (7) pressure transducers, (8) capillary, (9) thermocouple.

Senouci and Smith (1988) fed the starch with an independent weight feeder with a controlled rate independent of extruder speed. They used this starved-feed technique to single out the effect of screw speed on viscosity. Notice the incorporation of the screw speed (N) the viscosity expressions. They found the following two different expressions for the viscosity for corn grits and potato powder:

Corn grits

$$\eta = 215\dot{\gamma}^{0.75-1}\exp\left(\frac{2834}{T}\right)\exp(-0.032MC)N^{0.54} \tag{2.33}$$

Potato Powder

$$\eta = 9.4\times10^{4}\dot{\gamma}^{0.45-1}\exp\left(\frac{860}{T}\right)\exp(-0.083MC)N^{0.61} \tag{2.34}$$

where T is temperature in K, and N is screw speed in rpm. Similar to Vergnes and Villemaire (1987), they suggested that the specific mechanical energy (S.M.E.) was also an important process variable related with the flow rate Q_m and the screw speed N although they provided no quantitative relation between S.M.E and viscosity.

In order to obtain different shear rates, it is generally necessary to change the extrusion screw speed. Therefore, the material receives different thermo-mechanical treatment at different shear rates (Della Valle et al. 1992; Vergnes et al. 1991). Della Valle and Vergnes (1991) designed a rheometer which they called "Rheopac" with two channels to get around the problem of different thermo-mechanical history (Figure 2.8). This device was able to measure viscosity at a range of shear rates by moving two gate piston valves, but keeping the total flow rate and exit pressure constant. They found that their data were fit by

the model they previously described (Equations 2.30, 2.31, and 2.32) using the "Rheoplast" rheometer.

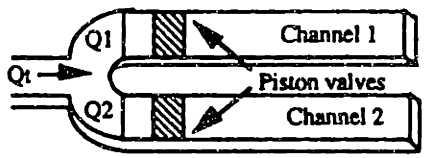

Figure 2.8: Rheopac rheometer (Della Valle et al., 1992).

Padmanabhan and Bhattacharya (1993) also pointed out that the use of screw speed, especially for a single-screw extruder, to vary the flow rate through the die could result in erroneous flow curves. They employed a side-stream valve to vary the flow rate for a given screw speed. They also argued that the extent of starch degradation increases with residence time in the extruder. With the side-stream valve, the power-law parameters m and n found by their method were not significantly different from the standard capillary viscometry, however.

Della Valle et al. (1996) studied the influence of amylose content on the viscous behavior of starch. They proposed an even more elaborate formula to describe the interaction of temperature, moisture content, and specific mechanical energy (SME) on viscosity:

$$\eta = K\dot{\gamma}^{n-1} \tag{2.35}$$

$$K = K_0 \exp\left[\frac{E}{R}\left(\frac{1}{T}-\frac{1}{T_0}\right) - \alpha(MC - MC_0) - \beta(SME - SME_0)\right] \tag{2.36}$$

$$n = n_0 + \alpha_1 T + \alpha_2 MC + \alpha_3 SME + \alpha_{12}(T \cdot MC) + \alpha_{13}(T \cdot SME) + \alpha_{23}(MC \cdot SME) \tag{2.37}$$

where n_0, α_{12}, α_{13}, and α_{23} are constants. All other labels have the same meanings as in previous equations. The quantity SME was defined as the power input to the extruder

motor drive.

The researchers still found it difficult to describe quantitatively the effect of amylose content on viscosity because of their limited number of samples and the non-monotonic trends. For instance, neither the variation of E/R nor β was monotone with respect to amylose content. It was shown that the mechanical energy input, characterized by SME, had the greatest influence on the starches without amylose but had no significant effect on the 70%-amylose starch. The difference in molecular weights was suggested to explain this trend.

Mackey and Ofoli (1990) modified the model for protein doughs (Morgan et al., 1989) to make it suitable for low-moisture starches. The new model allowed for the existence of a yield stress, the temperature-time history, and the strain history, but it contained similar shear rate, temperature, and moisture content dependence of viscosity as other models previously discussed.

$$\eta_{\dot\gamma,T,MC,\psi,\phi} = \left[\left(\frac{\sigma_0}{\dot\gamma}\right)^{n_1} + \mu_\infty \dot\gamma^{n_2-n_1}\right]\exp\left(\frac{\Delta E}{R}(T^{-1}-T_r^{-1}) + b(MC-MC_r)\right)$$

$$\times\,[1 + A(1-\exp(-k_a\psi))^a][1-\beta(1-\exp(-d\phi))] \tag{2.38}$$

$$\psi = \int_0^t T\exp\left(\frac{-\Delta E}{RT(t)}\right)dt \quad \text{for } T\geq T_d \tag{2.39}$$

$$\psi = 0 \quad \text{for } T<T_d \tag{2.40}$$

$$\phi = \int_0^t \dot\gamma(t')dt' \tag{2.41}$$

where ψ characterizes the temperature-history, ϕ characterizes the strain history, n_1, n_2, μ_∞, σ_0, k_a, d, β, ΔE/R, T_r, MC_r, and T_d are all constants. The material tested was native corn starch. The time $t' = 0$ was defined as the time when the material entered the extruder. Parameters accounting for the temperature, moisture content, shear rate dependence, and

temperature time history were evaluated with a capillary viscometer. A twin-screw extruder die viscometer assembly was used to quantify the strain history dependence on viscosity.

Novon and Novamont are two companies that have studied the rheological properties of starch polymer blends. They developed techniques that blended EVOH (polyethylene-co-vinyl-alcohol) into pure starch with plasticizers. Villar et al. (1991) measured the viscosity of the blends they compounded at Novon with a capillary viscometer. He calculated the parameters of the power-law model for blends with different starch-to-EVOH and amylose-to-amylopectin ratios. The compositions of these blends are detailed in Appendix B of this thesis. The shear rates attained ranged from 1 to 1000 s^{-1}. He found that the viscosity increased with amylose content. He attributed the increase to the more entangled structure of the linear amylose than the more branched amylopectin.

Bastioli et al. (1994) studied the rheological, morphological, and mechanical properties of starch/polymer blends made by Novamont. The blend used was Mater-Bi AF05H which contained about 60% of maize (corn) starch and additives and 40% of EVOH. Using a slit die rheometer, they found that their blends followed a Equation 2.42 with a yield stress. The yield stress reported was ~10^4 Pa. For shear rates larger then 10 s^{-1}, the viscosity curve was similar in shape and magnitude to that of LDPE:

$$\eta = m \cdot \dot{\gamma}^{n-1} \tag{2.42}$$

where $\dot{\gamma}$ is the shear rate, and m and n are the pre-exponential factor and the power-law index, respectively. In addition, the normal stress N_1 was also estimated as a function of shear rate by using the exit pressure. It was found to follow a power-law type relationship with shear rate:

$$N_1 = \alpha \cdot \dot{\gamma}^{\beta} \tag{2.43}$$

where α and β are material constants.

It is important to notice that all the viscosity results reported so far have the same form. At high shear rate ($\dot{\gamma} \geq O(1s^{-1})$), viscosity and shear rate are related by a power-law function with functional dependence of the pre-exponential factor m and the index n on temperature, moisture content, and specific mechanical energy. The power-law model, although seemingly satisfactory for predicting experimental results, is not a complete model. First of all, it lacks a zero-shear-rate viscosity. This feature is not assessable by researchers because they are not able to obtain data in the low shear rate region using a conventional viscometer die. Zero-shear-rate viscosity is an important piece of information about the polymer itself since it is a more sensitive function of the molecular structure than the high shear rate viscosity. Secondly, the power-law model also cannot describe any normal stress difference. Many important polymeric phenomena like die swell are the result of the non-zero normal stress difference and memory effects. Lastly, this model does not have any time dependence. As a result, a Deborah number cannot be defined to describe process behavior.

Chapter 3

Experimental Systems

This chapter describes the experimental details of the optical system. The way in which viscosity and first normal stress coefficient were calculated from velocity and stress measurements has been explained in Section 1.3 of this thesis. The design of the test geometry and the melt transport system are detailed in Section 3.1. Section 3.2 is devoted to a discussion of the necessary steps to maintain temperature uniformity within the test geometry. Laser Doppler velocimetry was used to measure the velocity profiles from which the shear rate profiles were calculated. The principle and implementation of LDV are detailed in Section 3.3. The stress-optic law and the difference between full-field and point-wise birefringence measurements have been discussed in Sections 2.2 and 2.3 already. A phase-modulated birefringence system was used in this study, and its working principle and implementation are explained in Section 3.4. The two conventional methods of rheological measurement, the parallel-plate rheometry and capillary viscometry, are described in Sections 3.5 and 3.6.

3.1 Test Geometry and Melt Transfer System

The ideal two-dimensional flow can be approximated by a three-dimensional rectangular slit channel flow with a large width-to-gap ratio. Wales (1976) showed that a slit die with a width-to-gap ratio of 10:1 gave the same $\langle n_{11}-n_{33} \rangle$ data as the one with a ratio of 30:1 over two decades of shear rates. Thus it has been inferred that a depth-to-width ratio of 10:1 is enough to minimize the edge effects because no further reduction of edge effects was observed with a higher aspect ratio. The current flow channel also has a depth-to-

width ratio of 10:1. The length, depth, and width of the channel are 230 mm, 40mm, and 4 mm respectively. Figure 3.1 shows a diagram of the die, with the x-axis aligns with the flow direction, the y-axis with the velocity gradient direction, and the z- axis with the neutral direction. Thus the two-dimensional picture in which the shear rate, viscosity, and first normal stress coefficients change from the centerline to the walls (Figure 1.6) can be observed from the x-y plane midway between the top and the bottom surfaces.

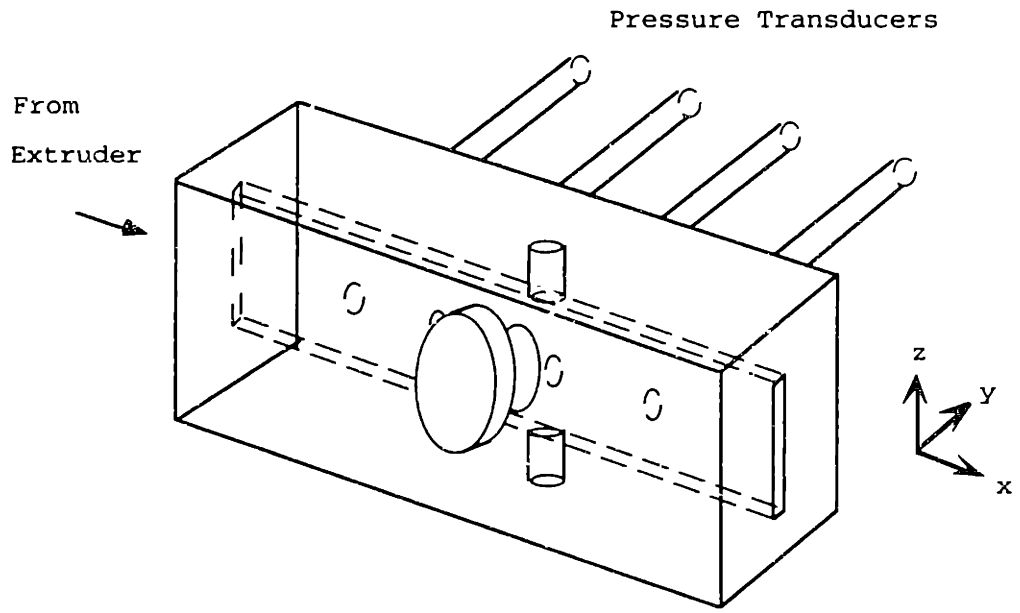

Figure 3.1: Slit die design.

The die was made of stainless steel with holes machined for mounting the pressure transducer probes and the glass windows for velocity and birefringence measurements. Polymer melt pressured by the extruder was pumped into the channel from the left. Four pressure transducers (Dynisco TPT4635) of ranges 0 - 3000 psi, 0 - 3000 psi, 0 - 1500 psi, and 0 -500 psi were flush mounted to the channel along the length of the die. Two cylindrical glass windows (Schott SF-57 with MgF_2 coating) were mounted on the top and bottom

of the die for birefringence measurements. These windows were positioned such that the birefringence profiles were measured at a distance of 38 gap widths from the entrance in order to minimize the entrance effect. A mushroom-shaped window (Schott BK-7) was mounted on the side for velocity measurements.

A single-screw extruder (Randcastle RC-1250) melted and pumped the polymer into the die. The screw diameter was 1-1/4 inch, and the length-to-diameter ratio (L/D) was 24 to 1. The throughput of the extruder increases with the screw diameter, and the residence time of the material in the barrel increased with L/D. The screw was divided into three sections: the feeding zone, the compression zone, and the pumping zone. In the feeding zone solid pellets or powders were drawn from the hopper into the space between the barrel and the screw. They were heated and began fusing together as they were transported to the compressing zone. In the compressing zone melting, pumping and mixing took place. Since the root diameter of the screw in this section increased toward the exit, the melt was compressed, typically by a ratio between 2 to 5 (Luker, 1993). In the pumping zone the melt was convected to the exit hole at the highest pressure. Three heating and cooling zones controlled the temperatures of the barrel with PID controllers (Syscon REX-C400). A 7.5 horsepower motor drove the screw with a 15:1 gear box. The maximum screw speed was about 117 revolution per minute, which corresponded to an throughput of 3.4 g/s or 27 lb/h for LDPE at 160°C.

The vertical configuration of the screw provides two advantages. First, the gear box turns the screw by grabbing the last section of it, which had a much larger root diameter. In most horizontal single-screw extruders, the gear box turns the screw close to the feeding section, which has a smaller root diameter. More torque is transferred to the screw through the gear box in the vertical configuration because the stronger part of the screw is being turned. Second, material feeding from the hopper is enhanced by gravity in the vertical

configuration. Common feeding problems such as bridging (the solid power forming "bridges" in the hopper and not falling into the screw properly) is greatly reduced (Luker, 1993).

Figure 3.2 shows how the different components of the optical system were fitted together. A static mixer (Koch KMB-100) mechanically connected the extruder to the die. The extruder, mixer, and the die were mechanically decoupled from the optics which were standing on a 3' x 5' optical table (Newport XSD-35). Both the laser probe of the laser Doppler velocimeter and the optical elements of the birefringence apparatus were mounted on translation stages (Daedal 106062C-20E & 106063C-20E) which in turn were secured on the optical table. The stages controlled minute movements of the laser beams as they scanned across the channel. The accuracy of the positioning system was 0.00008 mm per mm of movement.

3.2 Temperature Controls

The temperature of the polymer melt has to be maintained constant across the channel because of two reasons. First, the rheological properties under investigation are strong functions of temperature. Failing to maintain a uniform temperature will compromise the reproducibility of the measurements. Second, the success of the optical measurements depends on the accurate positioning of the laser beams. The beams will be diverted or bent as they travel into regions of changing refractive index because of the changing local temperature.

The temperature of the melt was controlled by controlling the temperature of the die. There are three separate zones in die for temperature control. The temperature of each zone was measured by a J-type thermocouple (Omega JMQSS-062G-6) with its tip

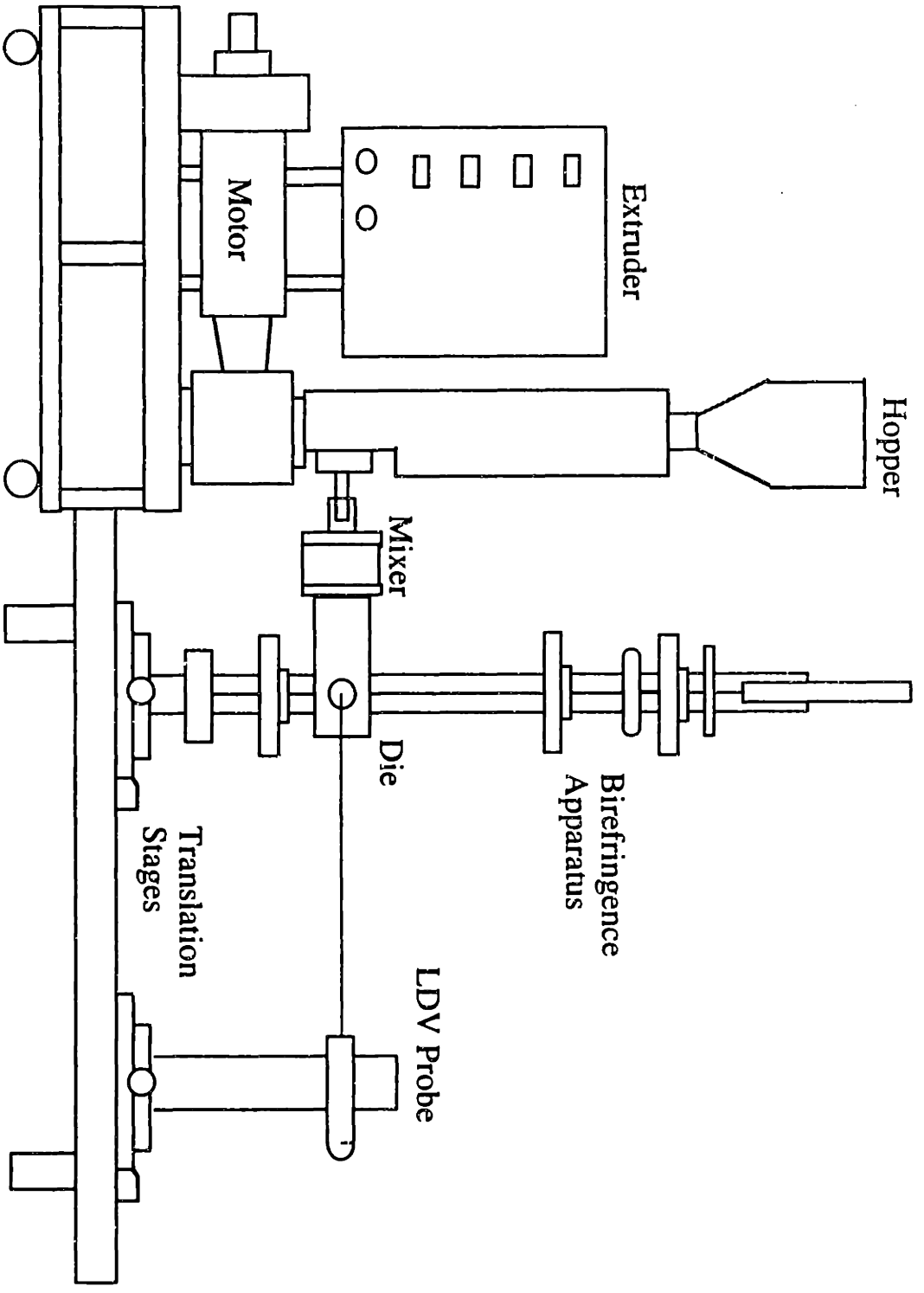

Figure 3.2: Experimental arrangement of extruder, slit die, and measurement apparatus.

located 0.125 inch from the channel wall. The measured temperature was fed to a PID temperature controller (Dynisco Model 1330) which in turn determined the frequency ofthe heating cycle of the cartridge heaters. Separate groups of cylindrical cartridge heaters (Industrial Heaters C3740D) maintained the temperature of the die in each zone. Figure 3.3 shows the location of the heaters and the different zones.

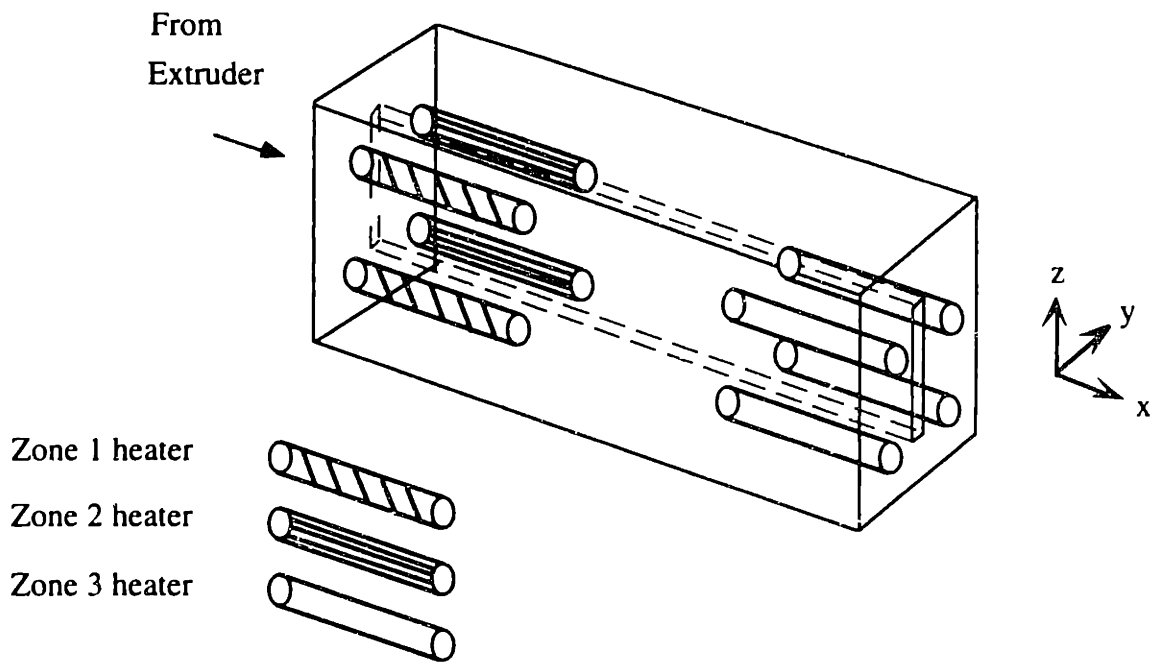

Figure 3.3: Heater distribution in the die.

It was found that without adequate insulation of the metal die, the temperature of the inner die surface or the channel walls could not be well-controlled. This was because heat was lost through the surface of the die by natural convection, the heaters had to be cycled to turn on at a very high frequency (about 50% time on). Whenever the heaters were turned on there was a local temperature gradient established across the thickness of the die wall (Figure 3.4). The temperature decreased significantly from the surface of the car-

tridge heaters (the heat source, at least 40°C higher than the setpoint of the controller), to the outer surface of the die wall (at equilibrium with the local ambient temperature). As a result, the temperature of the channel wall at the inner die surface at was not well controlled.

Ts = Temp at die surface

Th = Temp at heater surface

Tc = Temp at channel wall

Tt = Temp at thermocouple tip (set-point)

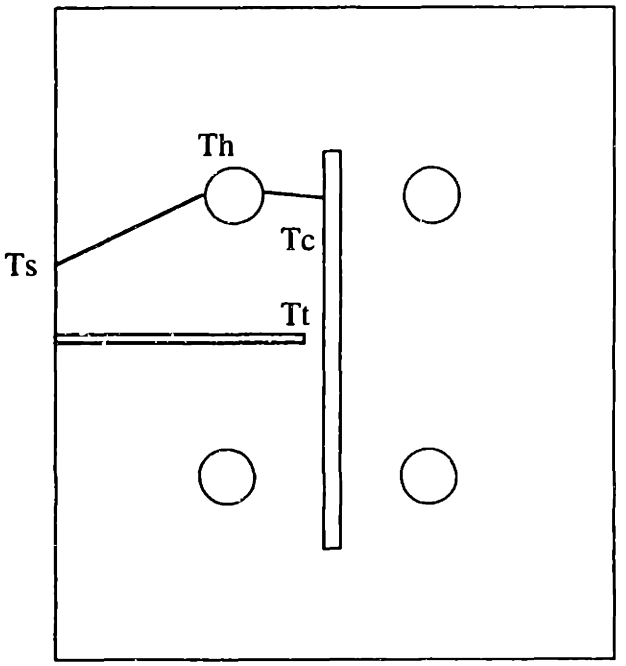

Figure 3.4: Temperature profile across die thickness when the heaters are turned on.

Insulation was provided by wrapping the die with fiber glass wool (McMaster Carr No. 9356K11). This material has a thermal conductivity of 0.40 W/(m K). The low thermal conductivity lowered the rate of heat loss by conduction. With the insulation, the cartridge heaters were turned on a lot less frequently (less than 5% time on). The ideal case was to keep the local heat source - the heaters - from turning on at all, but it could not be realized since no insulation is perfect. With about one inch thickness of insulation the temperature of the whole metal die was very close to the set-point.

Even with the fiber glass wool wrapped around the die, it was found that the temperature of melt at the exit of the extruder (T_m) was higher than that at the exit of the die (T_{exit}). When T_m was 160°C, T_{exit} was about 154°C. The temperature drop indicated a heat loss from the melt as it traveled into and along the die. Putting more insulating material around the die did not seem to reduce the temperature drop. Upon closer examination of the heating mechanism along and at the exit of the extruder, it was proposed that the temperature of the melt coming out of the extruder exit might not be uniform. Direct contact temperature measurement of the melt with a hand-held thermocouple confirmed this hypothesis. The melt temperature fluctuated over time and position because of two reasons. First, it has been shown that depending on the shape and size of the extruder screw, the temperature profile of the melt varies differently in the radial direction (Figure 3.5). Therefore, there is a non-uniform local temperature profile at the hole where the melt exits the extruder barrel. Second, the extruder exit hole was located a few inches before the end of the screw. The last section of the screw after the hole has reverse flights to transport the melt which passes the hole back to the exit. This zone was found to be unheated and uninsulated (Figure 3.6). As a result, cooled polymer was blended into the hot polymer as it was brought back to the hole by the reverse flights.

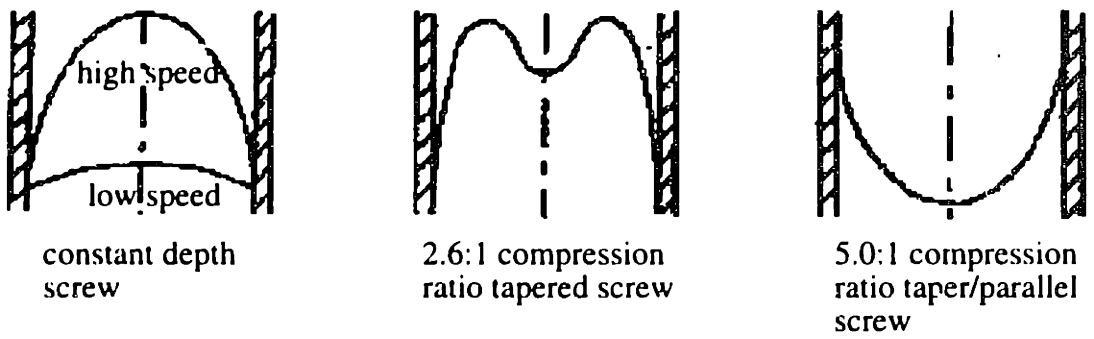

Figure 3.5: Radial temperature profiles at the end of an extrusion screw for several different screw designs and operating conditions (Stevens, 1985).

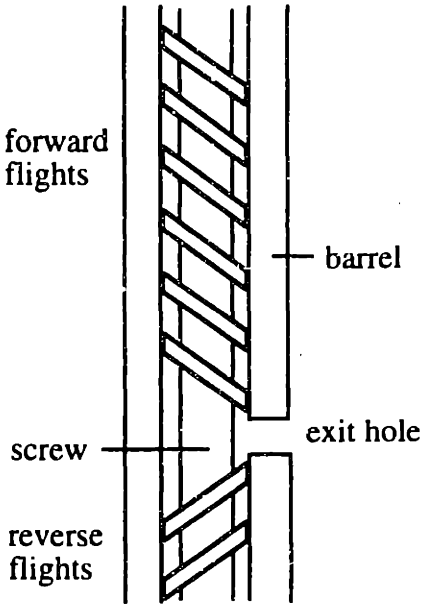

Figure 3.6: Last section of the extruder screw and the exit hole

To solve the problem of non-uniform temperature, the first step was to control the temperature of the last section of the barrel lower than the exit hole. In addition, a static mixer was installed between the extruder and the die. A static mixer is typically composed of cylindrical elements filled with stainless steel intertwining bars which divide and recombine polymer melt regions with different temperatures in order to facilitate heat transfer. Out of the many different types of mixing elements, the Koch SMX^{TM} static mixing elements were selected because of the high numbers of subdivisions they generate at the expense of a relatively short element length. For example, the four elements with eight intersecting bars per element yielded 32768 subdivisions of the melt stream (Koch Blender Catalog, 1986). Four one-inch-length elements were connected to the extruder and the die by a mixer housing.

A 1/8" diameter thermocouple (Omega JMQSS-125G-6) was mounted at the short converging section between the mixer and the die to measure directly the temperature of

the polymer melt going into the die. This temperature dictated how the temperatures of the extruder zones and the mixer should be set. After adding extra insulation, controlling the temperature of the last barrel section, installing the static mixer, and carefully tuning the extruder and mixer temperatures, the melt temperature at the entrance of the die channel finally matched with that at the exit of the channel to $\pm 0.5°C$.

3.3 Laser Doppler Velocimetry

3.3.1 Basic Principles

The advantages of using laser Doppler velocimetry to measure fluid velocity are two-fold. It is a non-evasive technique because the flow being studied is not disturbed in any way. Also, the small size of the measuring volume enables one to measure the velocity at many different locations in order to map out the velocity profile.

The principle of LDV is explained in great detail and clarity in Drain (1980). The following derivation of the basic equations is adapted from the discussion in Drain for the heterodyne system used in this study. Doppler shift refers to the change in frequency of wave motion due to the relative motion of the source and receiver (Drain, 1980). The increase in frequency apparent to a observer moving at speed v at an angle θ with respect to a stationary source is:

$$\Delta\nu = \frac{\nu\cos\theta}{\lambda} \tag{3.1}$$

where $\Delta\nu$ is the change in the observed frequency, $\nu\cos\theta$ is the component of the observer velocity in the direction of the stationary source, λ is the wavelength.

When the source of the wave is moving at a velocity v at an angle θ with respect to the observer, the frequency detected by the stationary observer is changed by $\Delta\nu$,

$$\Delta\nu = \nu\left(\frac{v}{c}\cos\theta + \frac{v^2}{c^2}\cos^2\theta + \ldots\right) \tag{3.2}$$

where ν is the unshifted frequency, $\nu \cos\theta$ is the component of the source velocity in the direction of the stationary observer, and c is the velocity of the wave. Equations 3.1 and 3.2 are different because in the moving observer case, the observed wave speed is changed while the wavelength remains the same; whereas in the moving source case, the wave travels at the same speed but the observed wavelength is changed.

In the case of laser Doppler velocimetry, the main concern is the frequency shift of light scattered from a moving object, with the source and the observer being relatively stationary with respect to each other. This case can be considered as a double Doppler shift, from the stationary source to the moving scattering object, and then from the moving object to the stationary observer. The system used in this study measures the beating frequency between two signals, one from the double Doppler shift of the first laser beam due to the moving particle, and another one from the double Doppler shift of the second laser beam due to the same moving particle. Figure 3.7 shows that the two incident laser beams are separated by an angle α. The scattering particle is moving at a velocity $\underline{v}$, making an angle β with respect to the line normal to the bisector line for the beams. The angle between the velocity and the first laser beam is defined as θ_1, and the angle between the velocity and the second laser beam is defined as θ'_1. The detector is located at an arbitrary angle θ_2 with respect to the velocity.

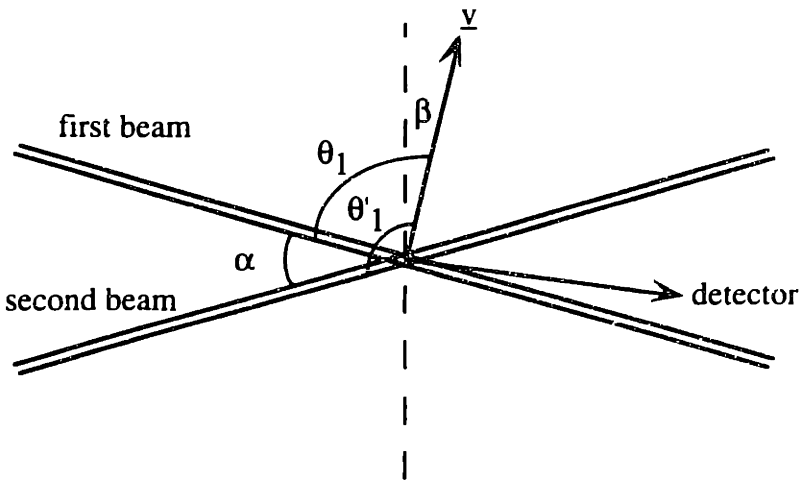

Figure 3.7: Configuration of the laser beams and the detector in a heterodyne LDV system

Using the relativistic equations, the Doppler shifts in frequency observed by the detector from the light scattered from the first and second laser beams are respectively:

$$\Delta\nu = \frac{\nu v}{c}(\cos\theta_1 + \cos\theta_2) \tag{3.3}$$

$$\Delta\nu' = \frac{\nu v}{c}(\cos\theta'_1 + \cos\theta_2) \tag{3.4}$$

The beat frequency, f, observed by the detector as a result of the beating between these two Doppler shifted frequencies is:

$$f = (\nu + \Delta\nu) - (\nu + \Delta\nu') = \Delta\nu - \Delta\nu' = \frac{\nu v}{c}(\cos\theta_1 - \cos\theta'_1) \tag{3.5}$$

$$f = \frac{v}{\lambda}\sin\left(\frac{\alpha}{2}\right)\cos\beta \tag{3.6}$$

where $\alpha = (\theta'\text{-}\theta_1)$ and $\beta = 0.5(\theta_1+\theta_1'\text{-}\pi)$. It is important to note that the beat frequency picked up by the detector is independent of the reception direction (no θ_2 dependence).

The quantity v cosβ is proportional to the measured frequency f through known constants α and λ. The fringe model is commonly used to illustrate the principle of LDV. However, the fringe model is valid only at situations of low particle density and when the size of the particles is small compared to the fringe spacing (Drain, 1980). The above derivation is valid for most cases regardless of particle density and size, except when the fluid speed v is close to the speed of light.

3.3.2 Spectrum fitting technique

The LDV system used in this study consists of a laser (Ion Laser Technology 5500A-00, 300mW Argon ion), a beam splitter with a Bragg cell, a probe with focusing lens (focal length 80 mm), a photomultiplier, and a spectrum analyzer (Dantec Burst Spectrum Analyzer Model 57N 10). A schematic diagram of the system is shown in Figure 3.8. The laser light is filtered and splitted into two beams. One of them passes through the Bragg cell and its frequency is shifted by a known amount. The shifting of one beam is a common scheme used to resolve the direction of the scattering particles. That way a certain velocity in one direction will produce a scattering frequency different from that produced by the velocity with equal magnitude but opposite direction (McKinley, 1991).

A fiber optic cable carries the two beams to the probe. This flexible cable simplifies the optical alignment between the laser beams and the flow system because only the probe has to be mounted and oriented precisely with respect to the flow system. However, the alignment between the laser and the beam splitter still has to be done with great precision. The two light beams are then focused onto the position of interest by the focusing lens on the probe. Scattered light is detected by the same probe which transfers the scattered light by the same fiber optic cable to the photomultiplier. This configuration is called a back-scattering system which means that scattered light is detected from the same direction as the

incident light. Figure 3.9 shows that the beams actually cross inside the flow channel at an angle different from the original angle a due to the difference of refractive index between air and polymer.

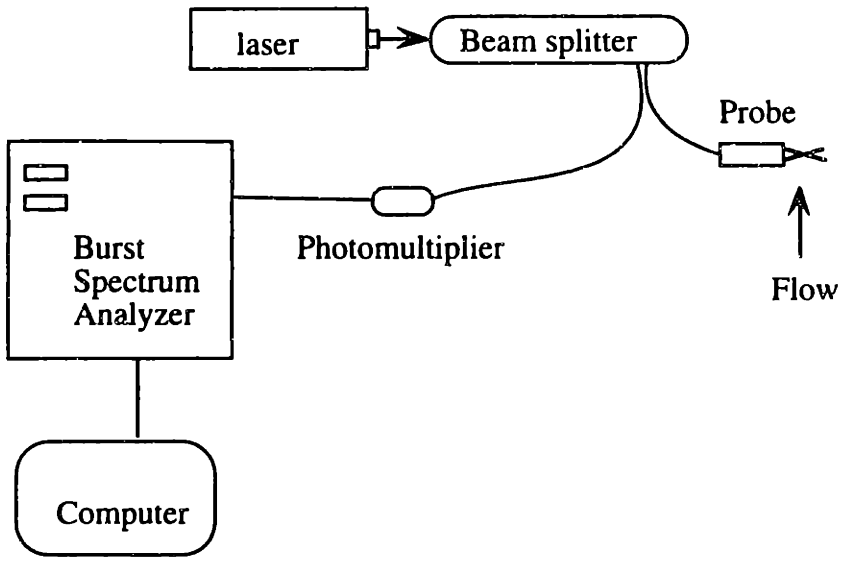

Figure 3.8: Schematic diagram of laser Doppler velocimeter

The velocity is given by rearranging Equation 3.6:

$$v\cos\beta = \frac{f \cdot \lambda_P}{\sin\left(\frac{\alpha_P}{2}\right)} \tag{3.7}$$

where λ_P and α_P are the wavelength and the beam separation angle of the light in the polymer. The separation angle in polymer is related to that in air and glass by Snell's law:

$$n_A \sin\theta_A = n_G \sin\theta_G = n_P \sin\theta_P \tag{3.8}$$

where n_A, n_G, and n_P are the refractive indices of the air, glass, and the polymer respec-

tively, and θ_A, θ_G, and θ_P are the angles the beam makes with the interface in air, glass, and polymer respectively. From Figure 3.9 $\vartheta_A = \alpha_A/2$, so $\sin\alpha_P/2 = (n_A/n_P)\sin\alpha_A/2$. It is also necessary to take into account the effect of refractive index on the wavelength. The wavelength λ_A in air is reduced by a factor n_P in the polymer to $\lambda_P=\lambda_A/n_P$, assuming $n_A = 1$. As a result, Equation 3.7 can be rewritten as:

$$v\cos\beta = \frac{f\cdot\lambda_P}{\sin\left(\frac{\alpha_P}{2}\right)} = \frac{f\cdot\frac{\lambda_A}{n_P}}{\frac{1}{n_P}\cdot\sin\left(\frac{\alpha_A}{2}\right)} = \frac{f\cdot\lambda_A}{\sin\left(\frac{\alpha_A}{2}\right)} \tag{3.9}$$

The effect of the different refractive indices in air and in the polymer is seen to cancel out.

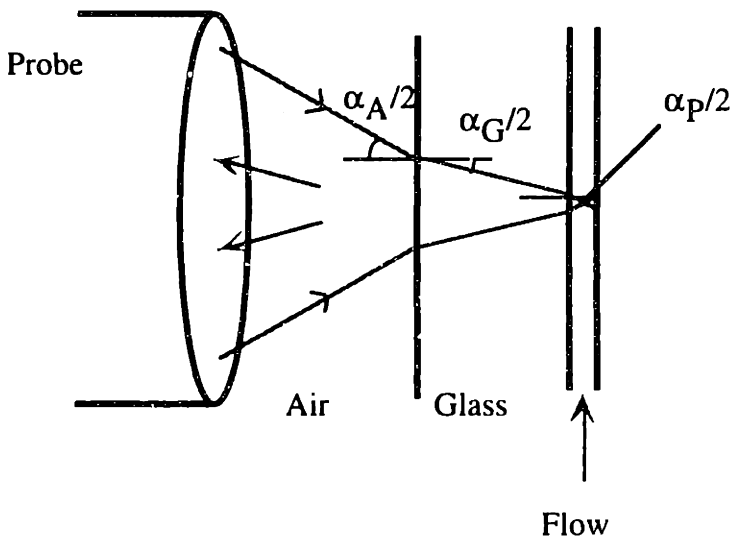

Figure 3.9: Top view of slit channel with laser Doppler velocity measurement

The photomultiplier is a vacuum tube in which electrons are released as a result of light falling on a special photo-emissive surface (Drain, 1980). Amplification is achieved by secondary emissions of photocurrent at successive electrodes arranged inside the photomultiplier tube with successively higher voltages with respect to the cathode. The high

voltage between the cathode and the anode can be set by the user for the system used in this study. The value of this "high voltage" correlates with the amplitude of the Doppler signal and signal-to-noise ratio. It should be set at a value which gives a signal with high enough amplitude to be analyzed but not too strong to incorporate an excessive amount of noise.

The burst spectrum analyzer modifies and analyzes the signal it receives from the photomultiplier with a particular algorithm in order to calculate the velocity. The rapid execution of this algorithm enables a lot of data to be analyzed very efficiently, which gives this particular spectrum analyzer an advantage over other LDV signal processing systems. This algorithm is highlighted below. For a complete description of this algorithm, interested readers are referred to the Dantec Burst Spectrum Analyzer User's Guide.

The electrical signal generated by the photomultiplier is called a Doppler signal or Doppler burst. In this study, each velocity value was averaged from the velocity calculated from 1000 such Doppler bursts. The top diagram in Figure 3.10 shows the shape of an ideal Doppler signal. How does the spectrum analyzer know that it has collected data from 1000 burst? It recognizes the beginning and the end of a burst by analyzing the pedestal or the envelope of that burst. The pedestal is a low-frequency component of a Doppler signal. It can be isolated by first clamping the baseline of the original signal to zero, and then filtering out the high frequency components (Figure 3.10). The envelop is the outline of a band-passed Doppler signal. It is obtained by rectifying and low-passing the band-passed signal (Figure 3.10). In this study the envelop is used to identify the passing of a burst because sometimes a distorted Doppler burst gives a high-quality pedestal but a wrong Doppler frequency.

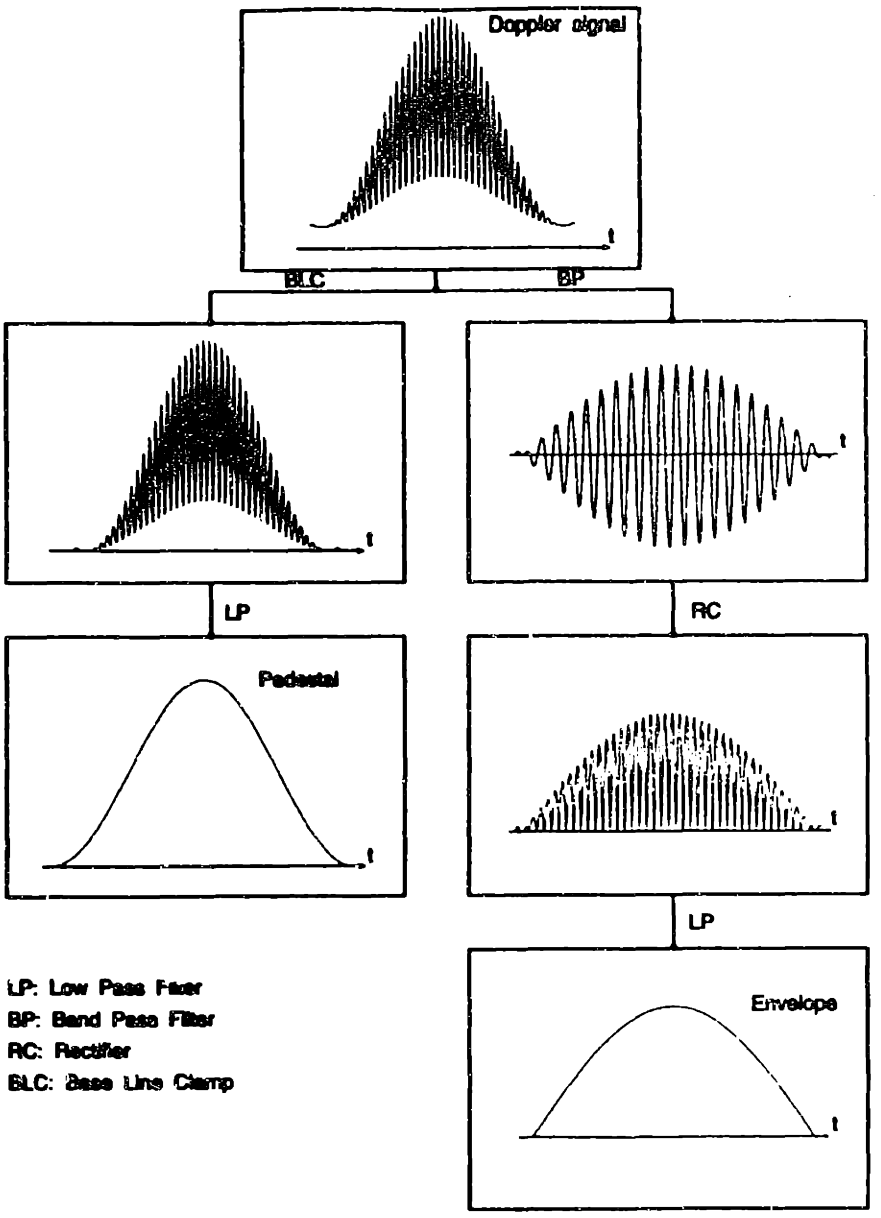

Figure 3.10: Generating process for the envelope and the pedestal (Dantec Burst Spectrum Analyzer User's Guide)

The burst analyzer calculates the spectrum of the incoming signal by using the discrete Fourier transform:

$$f_k = \sum_{n=0}^{N-1} x_n e^{-j2\pi n \frac{k}{N}} \tag{3.10}$$

where x_n is the n^{th} sample in the time series incoming signal, N is the total number of samples, k enumerates the samples, i.e. f_k is the k^{th} sample, and n is the summation variable. During the experiments the analog signal x(t) is sampled at regular intervals of period T_s, so that $x_n = x(nT_s)$. The resolution of the system can be characterized by a quantity $1/f_n$, where f_n is defined as the sampling frequency f_s divided by the total number of samples N.

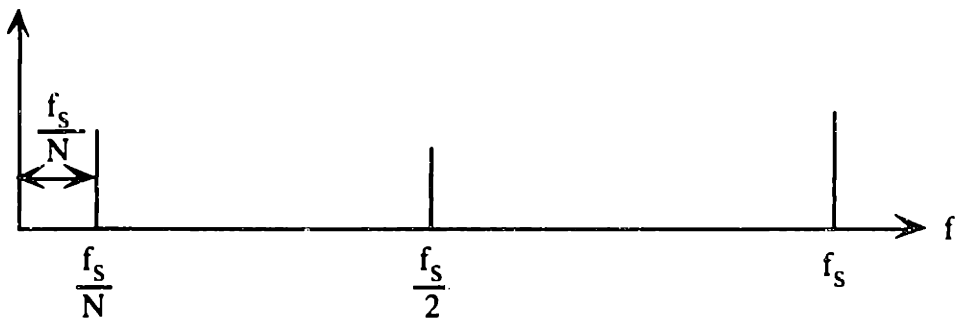

Figure 3.11: Frequency domain

$$f_n = \frac{f_s}{N} = \frac{1}{NT_s} \tag{3.11}$$

From this equation it can be seen that the resolution of the spectrum can be increased by increasing the sample number N, but increasing the sampling frequency will actually decrease the resolution.

The spectrum analyzer requires the user to enter a center frequency f_0 and a bandwidth BW for the calculations. Figure 3.12 shows that the highest frequency being investigated will be $f_0 + 0.5$ BW. Because of spectral aliasing, the sampling frequency has to be at least twice as big as the highest frequency of interest in order to avoid distortion (Nyquist criterion). Therefore, the sample frequency has to be as high as 2 times ($f_0 + 0.5$ BW). At such

high sampling frequency, the resolution will be compromised. The spectrum analyzer uses a zooming technique to increase the resolution. This technique shifts the entire spectrum to the negative side by a frequency f_0. Figure 3.12 shows that the highest frequency becomes the bandwidth divided by two. Following the Nyquist criterion, the sampling frequency is now 2 times BW/2, or BW. The analyzer samples the signal at a set frequency of 1.5 BW, which is usually much lower than the $2(f_0 + 0.5\ BW)$ without the zooming technique.

Figure 3.12: Frequency spectrum of a signal with center frequency f_0(Dantec Burst Spectrum Analyzer User's Guide)

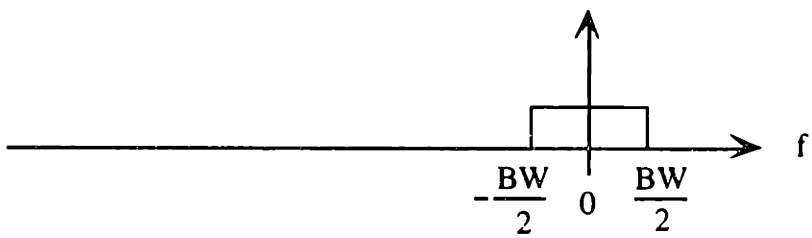

Figure 3.13: Frequency spectrum of the signal downshifted by f_0(Dantec Burst Spectrum Analyzer User's Guide)

Suppose the signal is idealized to be a single-frequency cosine function $\cos(2\pi ft)$. The zooming technique requires multiplying this signal by $e^{-j2\pi f_0 t}$. The resulting signal after filtering $e^{j2\pi(f-f_0)t}$ has a single frequency at $f\text{-}f_0$. Sampling this signal for a duration of NT_s is equivalent to multiplying a rectangular window function (Figure 3.13) with the shifted cosine signal. In frequency space, the filtered signal can be represented by a delta

function $\delta(f-f_0)$, and the rectangular window function becomes $\frac{\sin \pi f N T_s}{\pi f N T_s}$. Multiplying these two functions in the time space is equal to convoluting them in the frequency space. As a result, the sampled signal becomes $\frac{\sin[\pi(f-f_0)NT_s]}{\pi(f-f_0)NT_s}$, where $1/NT_S$ is the distance between two frequency samples, or the resolution.

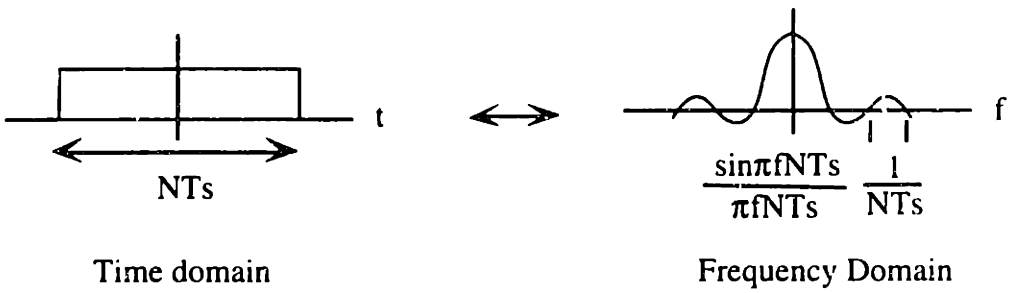

Figure 3.14: The rectangular window function and its Fourier transform (Dantec Burst Spectrum Analyzer User's Guide)

The most important job of the spectrum analyzer is to calculate the velocity from the maximum frequency in the processed spectrum. This frequency is identified by fitting the $\frac{\sin[\pi(f-f_0)NT_s]}{\pi(f-f_0)NT_s}$ function centered at $f-f_0$ to the spectrum. To enhance fitting , the spectrum analyzer uses a zero-filling technique that adds N zeroes to the N signal samples. The discrete Fourier spectrum is then calculated for these 2N samples. Figure 3.14 compares the discrete spectrum of a cosine function before and after zero-filling.

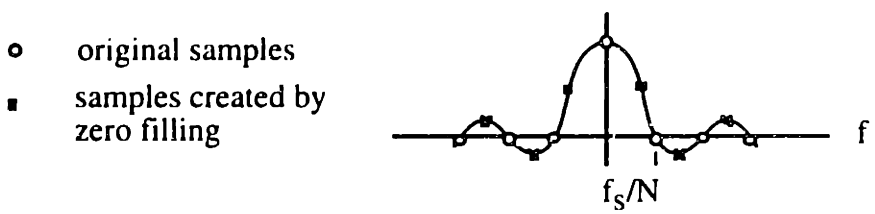

Figure 3.15: Effect of zero-filling on the spectrum of a cosine function (Dantec Burst Spectrum Analyzer User's Guide)

The last step by the spectrum analyzer is validation. The two highest local maxima are compared. If the ratio between them is larger than 4, then the spectrum is of good quality, and thus the burst is validated. This factor 4 is chosen empirically. Too high a factor will lower the data rate significantly, yet too low a factor will pass on too many low-quality bursts which do not have a well-defined maximum.

In running an LDV experiment, the high voltage between the two electrodes in the photomultiplier, the gain in the spectrum analyzer circuit, the center frequency, the bandwidth, and the number of samples per analysis N all have an impact on the data rate and the validation rate. It is desirable to have a high input rate of high-quality burst, but more often than not a high data rate corresponds to a low validation rate and vice versa. If the experiment is steady over time, and there is an infinite amount of time to run the experiment, then the goal should be to get the highest validation rate possible, at the expense of the long time that the experiment may take.

3.4 Birefringence Apparatus

The principles behind using birefringence to measure the stress field hav been discussed in Section 2.2 and 2.3. This section focuses on the implementation of the phase-modulated birefringence system used in this study.

Phase-modulation is a technique used to facilitate measurements of more than one variable in real time. The two variables of interest are birefringence and extinction angle. The phase-modulation technique provides an artificial time dependence to the intensity of the detected light. The intensity can generally be expressed in a series:

$$I(t) = I_{dc} + I_{\omega}(\delta, \chi)\sin(\omega t) + I_{2\omega}(\delta, \chi)\sin 2\omega t + \ldots \tag{3.12}$$

Except I_{dc} which is time-independent, each term in the series is a unique function of the birefringence δ and the extinction angle χ. Independently measuring each term provides more than one equation to solve for the two unknowns.

Two common methods are used to modulate the light intensity. One method is to insert a rotating optical element with a constant retardance in the optical training immediately before the sample. An example of such an optical element is a quarter or a half wave-plate. The other method is to place an optical element with a time-dependence retardance in the optical train immediately before the sample. A photo-elastic modulator is such an element. In this study an octagonal fused silica plate subjected to time-harmonic strain by a piezo-active crystal is used as the photo-elastic modulation unit.

Figure 3.15 shows the components of the birefringence apparatus used in this study. All elements on the optical train except the sample were mounted onto a vertical rail (Newport X95). This rail of elements was mounted on two translation stages (Daedal 106062C-20E) for precise movement of the beam in the flow field. A 10 mW HeNe laser (Uniphase 1135P) produced a single wavelength (632.8 nm) light source to be focused onto the sample by a 400 mm focal length plano-convex lens. The light then passed through the polarizer (Karl Lambrecht MGT3E8) whose orientation defined the coordinates of the optical axis system. The polarizer was mounted on a precision stage (Eifle) to facilitate optical alignment. The light then passed through the optic head of the photo-elastic modulator (Hinds PEM-90) to acquire a time dependence in its polarization state. After the light passed through the sample, its polarization state was changed by the birefringence and the extinction angle of the sample. However, the light intensity did not contain information about the sample's birefringence and extinction a[illegible]he analyzer (Karl Lambrecht MGT3E8) served to change the polarization state of light again so that the intensity depended on the birefringence and extinction angle of the sample. The light

intensity was recorded by a photodetector (Eifle). The photodetector was made of a photodiode with an order 1 ns response time. It had a low-pass filter circuit to isolate the time-independent component.

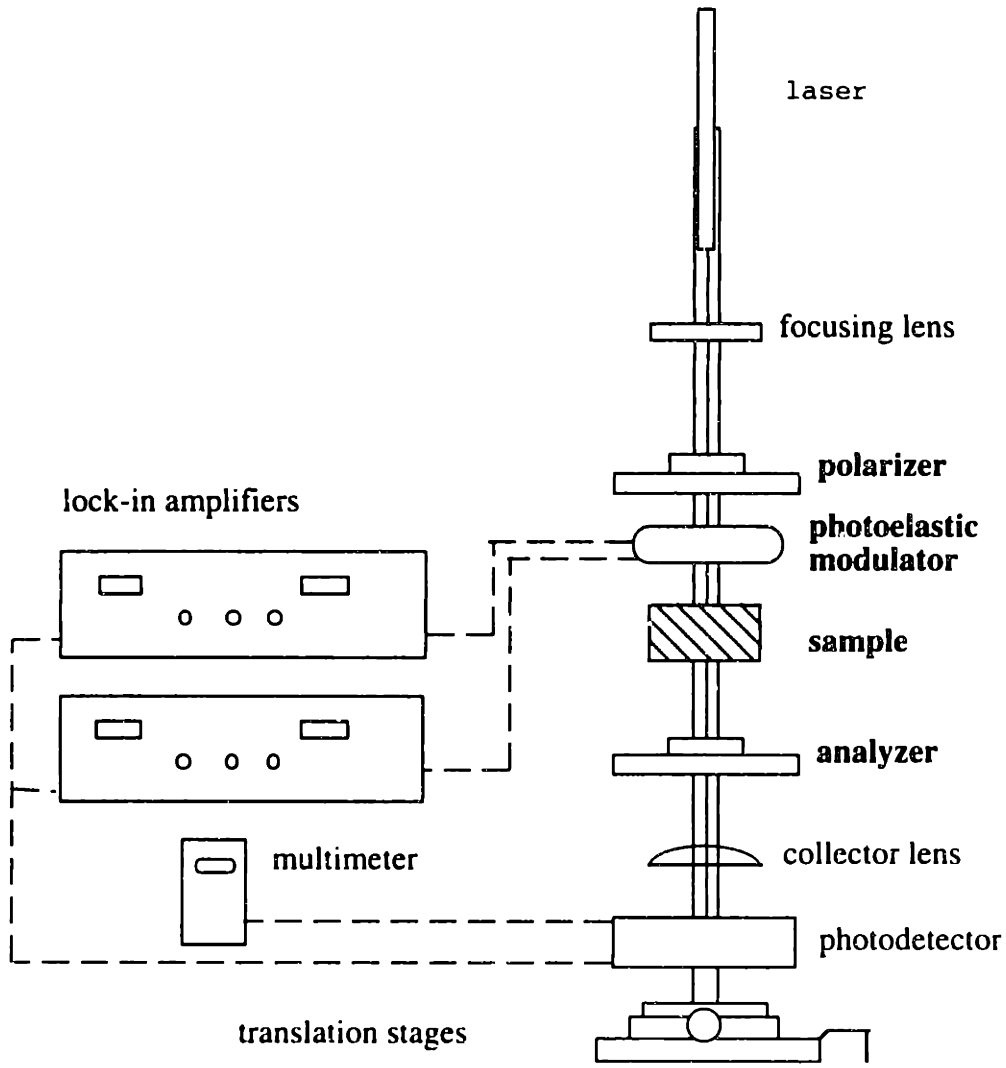

Figure 3.16: Birefringence apparatus

The intensity of the light signal was analyzed as a voltage by two lock-in amplifiers (EG&G 5110) and a digital multimeter (GoldStar DM 9183). The two lock-in amplifiers multiplied the incoming light intensity signal with the reference signals (42 kHz & 84

kHz) generated by the photo-elastic modulator control module. The coefficients for the first and second harmonics of the intensity $I_\omega(\delta,\chi)$ and $I_{2\omega}(\delta,\chi)$ were measured as a result. The multimeter showed the time-independent part of the intensity signal I_0. The three numbers I_0, $I_\omega(\delta,\chi)$, and $I_{2\omega}(\delta,\chi)$ were stored and analyzed by a computer (Macintosh Quadra 800 with LabVIEW^{TM}).

Out of the many components that the light passed through, only four of those changed the polarization state of light. They were the polarizer, photo-elastic modulator, the sample, and the analyzer, all shown in bold in Figure 3.15. Mueller calculus is a rigorous way to calculate the how the intensity depends on the parameters of the system (Azzam, 1977). This calculation is outlined as follows.

The polarization state of light can be represented by either a Jones vector or a Stokes vector. The two components of a Jones vector represent the two orthogonal components of the electric vector in the plane normal to the beam propagation direction. The intensity of light is obtained by summing the squares of each component of the Jones vector. Although simpler to understand, the Jones vector cannot represent partially polarized light. A Stokes vector contains four components. The first component indicates the intensity and the remaining three describe the polarization state. A stokes vector is used here to describe the light propagation, because the intensity can be calculated more easily using this representation.

After light of a certain polarization state $\underline{S}_0$ passes through a medium **M**, its new polarization state $\underline{S}_1$ can be calculated by multiplying the Stokes vector of the incident light by a Mueller matrix which describes the optical properties of that medium.

$$\underline{S_1} = \boldsymbol{M} \cdot \underline{S_0} \tag{3.13}$$

A Mueller matrix is a 4 x 4 matrix with components depending on both the retardance or orientation of that medium. To calculate the Stokes vector of the light passing through a series of optical elements, one simply multiplies the Stokes vector of the incident light by a series of Mueller matrices in the order that the light encounters the elements.

$$\underline{S}_n = \boldsymbol{M}_n \ldots \boldsymbol{M}_2 \boldsymbol{M}_1 \underline{S}_0 \tag{3.14}$$

where $\mathbf{M}_1 \ldots \mathbf{M}_n$ are the Mueller matrices of the optical elements, and $\underline{S}_n$ is the resultant Stokes vector that represents the polarization state of light after passing through the *n* elements.

In the birefringence system used in this study, the laser light with intensity I_0 passes through the optical elements in the following order and orientation: a polarizer oriented at 90°, the photo-elastic modulator oriented at 45° the sample with unknown retardance δ and unknown extinction angle χ, and the analyzer oriented at -45°. The intensity of the light detected by the photodiode I(t) can be calculated by:

$$\begin{bmatrix} I(t) \\ \cdot \\ \cdot \\ \cdot \end{bmatrix} = \left[\boldsymbol{M}_A(-45°)\right] \cdot \left[\boldsymbol{M}_S(\delta, \chi)\right] \cdot \left[\boldsymbol{M}_{PEM}(A\sin(\omega t), 45°)\right] \cdot \left[\boldsymbol{M}_P(90°)\right] \cdot \begin{bmatrix} I_0 \\ 0 \\ 0 \\ 0 \end{bmatrix} \tag{3.15}$$

where $\mathbf{M}_P$, $\mathbf{M}_{PEM}$, $\mathbf{M}_S$, and $\mathbf{M}_A$ are the Mueller matrices of the polarizer, photo-elastic modulator, the sample, and the analyzer, respectively. The retardance of the photo-elastic modulator is a sine function with amplitude A and frequency ω.

The Mueller matrix of a polarizer oriented at an angle θ is (Frattini and Fuller, 1984):

$$\frac{1}{2}\cdot\begin{bmatrix} 1 & \cos 2\theta & \sin 2\theta & 0 \\ \cos 2\theta & (\cos 2\theta)^2 & \sin 2\theta\cos 2\theta & 0 \\ \sin 2\theta & \sin 2\theta\cos 2\theta & (\sin 2\theta)^2 & 0 \\ 0 & 0 & 0 & 0 \end{bmatrix} \tag{3.16}$$

The Mueller matrix of the sample with retardance δ oriented at an angle χ is (Frattini and Fuller, 1984):

$$\begin{bmatrix} 1 & 0 & 0 & 0 \\ 0 & \cos^2(2\chi)+\sin^2(2\chi)\cos\delta & \cos 2\chi\sin 2\chi(1-\cos\delta) & -\sin 2\chi\sin\delta \\ 0 & \cos 2\chi\sin 2\chi(1-\cos\delta) & \cos^2(2\chi)+\sin^2(2\chi)\cos\delta & \cos 2\chi\sin\delta \\ 0 & \sin 2\chi\sin\delta & -\cos 2\chi\sin\delta & \cos\delta \end{bmatrix} \tag{3.17}$$

Upon multiplying the incident light Stokes vector by all the element Mueller matrices as shown in Equation 3.15, the intensity of light can be expressed as:

$$I(t) = \frac{I_0}{4} + \frac{I_0}{2}J_1(A_c)[\sin\delta\cos 2\chi]\sin\omega t + \frac{I_0}{2}J_2(A_c)[(1-\cos\delta)\sin 2\chi\cos 2\chi]\cos 2\omega t + .. \tag{3.18}$$

where I_{dc}, I_ω and $I_{2\omega}$ are the three quantities measured. $J_1(A_c)$ and $J_2(A_c)$ are the first and second order Bessel functions of the first kind evaluated at A_c. The amplitude of frequency modulation, A, is chosen to be equal to 2.407. This is because the time independent term in the intensity expression is $\frac{1}{4}I_0(1 + J_0(A)\sin 2\alpha\sin\delta)$ and $J_0(Ac=2.407) = 0$. This way the first term in Equations 3.18 do not depend on δ or χ and subsequent calculations is simplified.

Since both $J_1(A_c)$ and $J_2(A_c)$ are known constants (equal to 0.51907 and 0.43170, respectively), there are only three unknowns in Equation 3.18: I_0, δ, and χ. The three equations to solve for them are found by equating Equations 3.12 and 3.18:

$$I_{dc} = \frac{I_0}{2} \tag{3.19}$$

$$I_{\omega} = J_1(A) I_0[\sin\delta\cos 2\chi] \tag{3.20}$$

$$I_{2\omega} = J_2(A) I_0[(1 - \cos\delta)\sin 2\chi\cos 2\chi] \tag{3.21}$$

Since the absolute value of I_0 is not of any practical interest, we first eliminate it by considering the following two ratios: Rω and R2ω, which are defined as follows:

$$R\omega = \frac{I_{\omega}(\delta, \chi)}{2I_{dc}J_1(A)} = \sin\delta\cos 2\chi \tag{3.22}$$

$$R2\omega = \frac{I_{2\omega}(\delta, \chi)}{2I_{dc}J_2(A)} = (1 - \cos\delta)\sin 2\chi\delta\cos 2\chi \tag{3.23}$$

The values of δ and χ are then obtained from the following equations:

$$\cos\delta = \frac{-R2\omega^2 \pm R\omega^2\sqrt{(1 - R\omega^2 - R2\omega^2)}}{R\omega^2 + R2\omega^2} \tag{3.24}$$

$$\cos(2\chi) = \frac{R\omega}{\sin\delta} \tag{3.25}$$

By scanning the laser beam across the width of the slit channel gap, the profiles of δ and χ were obtained. The details of how these data were interpreted and the limits of the system are discussed in Chapter 4 of this thesis.

3.5 Parallel Plate Rheometry

The viscosity and first normal stress difference at low shear rates were measured in the parallel plate mode of the Rheometrics Mechanical Spectrometer (RMS 800). The princi-

ple and the specifics of the measurement are described in this section. Bird et al. (1987) details the derivation of the equations listed below.

Consider a polymer melt being confined in the space between two parallel plates. The radius of the plates is R, and they are separated by a distance H. When the bottom plate is rotated at a fixed angular velocity W, the shear rate $\dot{\gamma}$ inside the melt changes along the radial direction:

$$\dot{\gamma} = \frac{rW}{H} = \frac{\dot{\gamma}_R r}{R} \tag{3.26}$$

where $\dot{\gamma}_R$ is the shear rate at the edge of the plate. The viscosity can be calculated by measuring the shear rate and the torque T required to achieve this motion.

$$\eta(\dot{\gamma}_R) = \frac{(T/2\pi R^3)}{\dot{\gamma}_R}\left[3 + \frac{d\ln(T/2\pi R^3)}{d\ln\dot{\gamma}_R}\right] \tag{3.27}$$

The first normal stress coefficient cannot be calculated directly. The difference between the first and second normal stress coefficients can be expressed by:

$$\Psi_1 - \Psi_2 = \frac{1}{\dot{\gamma}_R}\left(\frac{F}{\pi R^2}\right)\left[2 + \frac{d\ln(F/(\pi R^2))}{d\ln\dot{\gamma}_R}\right] \tag{3.28}$$

where F is the total force required to maintain the plates at a separation H. Very often Ψ_2 is assumed to be small and negligible compared to Ψ_1. Therefore, Equation 3.28 is used directly to calculate Ψ_1.

During the measurement conducted in this thesis, two plates of 25 mm radius were separated at a distance of about 2 mm. It was discovered that the viscosity of LPDE melt increased by a decade over 24 hours due to oxidation inside the oven with circulating air

as the medium of forced heat convection. Therefore, all the experiments were done under a nitrogen blanket such that the change of viscosity and first normal stress coefficient due to oxidation was insignificant during the time of measurement.

3.6 Capillary Viscometry

Capillary viscometry was used to measure the viscosity of LPDE at high shear rates (>1 s^{-1}). The principle and implementation of this method is described below. Polymer pellets were ram extruded by a plunger through a heated barrel into a capillary. Steady state pressure-driven shear flow of melt is achieved inside this capillary after a certain amount of time. The viscosity is calculated from taking the ratio of the wall shear stress to the wall shear rate. The wall shear stress is related to the pressure drop over the length of the capillary ($\Delta P/L$) by:

$$\tau_w = \frac{\Delta P}{L} \cdot \frac{R}{2} \tag{3.29}$$

where R is the radius of the capillary. The wall shear rate can be calculated from:

$$\dot{\gamma}_w = \frac{4Q}{\pi R^3}\left(\frac{3n+1}{4n}\right) \tag{3.30}$$

where $n = \frac{d\log\tau_w}{d\log\dot{\gamma}_{app}}$ with $\dot{\gamma}_{app} = \frac{4Q}{\pi R^3}$, Q is the volumetric flow rate of the polymer coming out of the capillary. The quantity $\frac{4Q}{\pi R^3}$ is called the apparent shear rate because it is equal to the real wall shear rate for a Newtonian fluid, i.e. n = 1. The factor of $\frac{3n+1}{4n}$ is called the Rabinowitsch factor. The Bagley correction is not used in this study. The capillary viscometer (Instron Model 4505) used contains a one inch long capillary with L/D = 24.

As discussed in Section 1.3, a viscometer die is commonly used for measuring polymer melt viscosity. In this study, the rectangular slit die designed for optical measurement was also used for this purpose. For a rectangular slit die, the wall shear rate is given by:

$$\dot{\gamma}_w(\tau_w) = \frac{1}{\tau_w} \cdot \frac{d}{d\tau_w}\left(\frac{Q\tau_w^2}{2WB^2}\right) \tag{3.31}$$

where Q is the volumetric flow rate, τ_w is the wall shear stress, W is the depth of the channel, and B is the half width. The wall shear stress is given by $\tau_w=(\Delta P/L)(B)$. Many researchers have assumed and indeed found that the high shear rate viscosity is well-described by a power-law model:

$$\tau = m\dot{\gamma}^n \tag{3.32}$$

In this case, the wall shear rate can be more simply calculated by:

$$\dot{\gamma}_w = \frac{3Q}{2WB^2}\left[\frac{2n+1}{3n}\right] \tag{3.33}$$

where n can be obtained from the slope of the log-log plot between τ_w and $\frac{3Q}{2WB^2}$ because

$$\log(\tau_w) = n\log\frac{3Q}{2WB^2} + n\log\frac{2n+1}{3n} + \log(m) \tag{3.34}$$

Chapter 4

Results and Discussion

The optical method developed for studying PMMA was t ed using low density polyethylene (LDPE) to quantify its accuracy. LDPE was chosen as the test material because it was easy to process and was clear enough for optical measurements. In addition, the rheology of LDPE could be measured by standard rheometers for a large range of shear rates because it contained no volatile components. This chapter is divided into four sections. Section 4.1 discusses the results obtained from standard mechanical rheometers on LDPE. Key data include the viscosity and first normal stress coefficients as functions of shear rate and temperature. In Section 4.2, the viscosity of LDPE obtained from pressure and velocity measurements are discussed and compared to that obtained by using the standard mechanical rheometers. Section 4.3 details the retardance and extinction angle profiles measured from the point-wise birefringence apparatus. The effects of the end walls and the finite beam cross-sectional area on the data are explained. The first normal stress coefficient of LDPE measured with the optical method is compared to that measured by the parallel-plate mode of a Rheometrics RMS-800. Finally, an application of the optical method using PMMA is demonstrated in Section 4.4.

4.1 LDPE Rheology from Mechanical Methods

4.1.1 Results from standard rheometers

The density of the LDPE used (Federal Plastics FPC 42) is 0.92 g/cm^3 at room temperature (Federal Plastics Inc., 1993). At processing temperature, 160°C, the density of this particular type of LDPE was measured to be 0.78 $\pm$ 0.03 g/cm^3, less than 1% different

from the value reported in the literature (Bird et al., 1987). The density of the melt was measured by extruding a known amount of material at the set temperature using a capillary viscometer. The volume of the material being extruded at molten state was calculated from the cross-sectional area of the barrel and the displacement of the plunger. Dividing the weight of the solid extrudate by the calculated volume yielded the density at the set temperature.

The parallel-plate mode of the rheometer was used to measure the rheological properties at low shear rates (< 3 s^{-1}). The pellets were first molded into a cylindrical rod in a heated chamber with a plunger, which was part of a fiber-spinning machine. The rod was then cut into discs of 2 to 3 mm thickness to be melted and tested in the rheometer. As pointed out in Section 3.5, nitrogen was purged through the oven during the melting and testing in order to minimize oxidation. Capillary viscometry was used to measure viscosity at high shear rates (> 3 s^{-1}).

Figure 4.1 shows how viscosity depended on shear rate and temperature. Like all polymer melts, the viscosity decreased with increasing temperature. The polymer started shear thinning at about 0.07 s^{-1} at 160°C, and shear thinning began at lower shear rates as temperature was decreased. In the shear-thinning region the viscosity decreased with a continuously decreasing slope. The rate of decrease in slope tapered toward higher shear rates. The change in density was insignificant over the temperature range investigated in this study (130°C - 190°C).

Ignoring the density dependence on the shift factor a_T, it can be expressed by:

$$a_T = \frac{\eta_0(T)T_0}{\eta_0(T_0)T} \tag{4.1}$$

Table 4.1 shows the shift factors for the different temperatures. A master curve of reduced

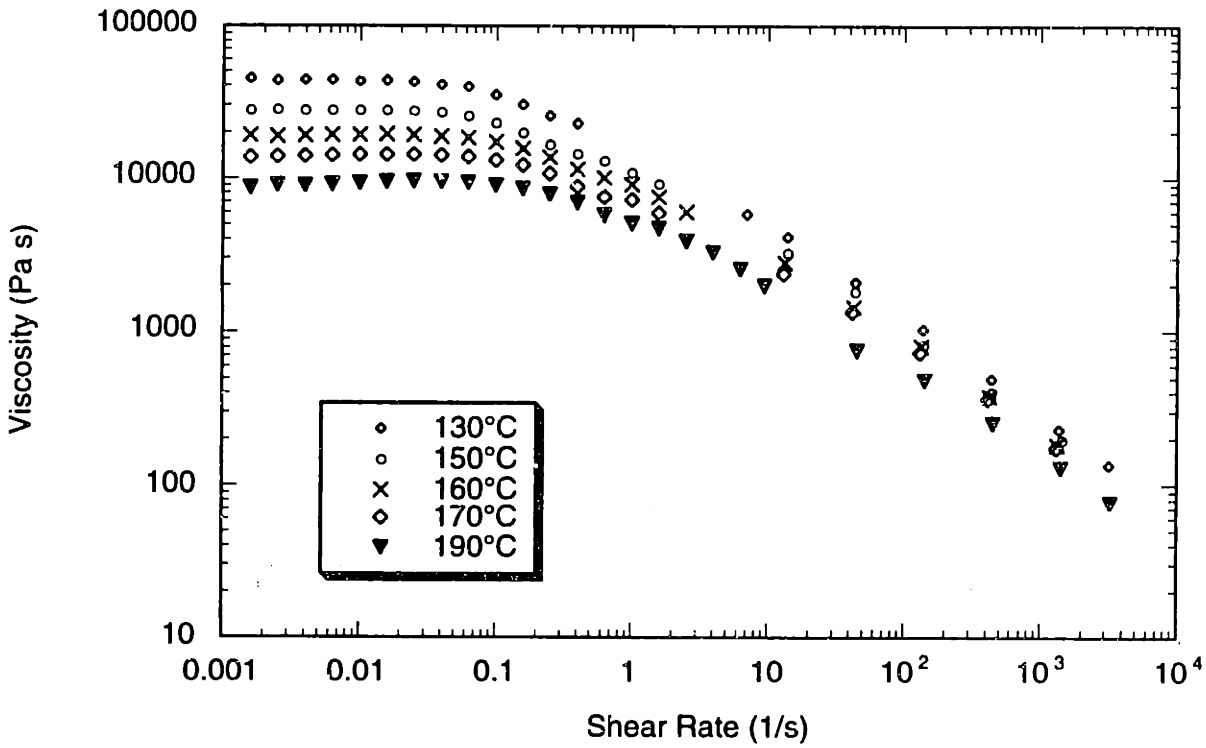

Figure 4.1: Viscosity of LDPE as function of shear rate and temperature. Gaps in data represents regions not accessible by parallel-plate rheometer or capillary viscometer.

viscosity versus reduced shear rate was plotted with reference temperature at 160°C (Figure 4.2). The zero-shear-rate viscosity at this temperature was 1.94 x 10^4 Pa s. The Carreau model (Equation 4.2) was used to describe the shear rate dependence of viscosity for use in the computer simulation. The model predicted the viscosity to within 3% for shear rates smaller than 10 s^{-1} (Figure 4.3).

Temperature (°C)	Shift factor a_T
130	2.459
150	1.418
160	1
170	0.723
190	0.452

Table 4.1: Shift factor a_T at the temperatures investigated

$$\eta = 1.94 \cdot 10^4 (1 + (6.7\dot{\gamma})^2)^{\frac{0.565-1}{2}} \; [Pa \cdot s] \tag{4.2}$$

The first normal stress coefficient Ψ_1 was also measured by parallel-plate rheometry. Figure 4.4 shows how it changes with shear rate and temperature. Within the shear rate range investigated, Ψ_1 decreases with shear rate except at the lowest shear rates. Figure 4.5 shows the master curve of Ψ_1. The zero-shear-rate value $\Psi_{1,0}$ estimated from the master curve at 160°C was 2.2 x $10^5 \pm 0.1$ x 10^5 Pa s^2.

The accuracy of the rheometer was estimated from both the calibration results of the force and torque transducers and from the viscosity measurements of a Newtonian fluid with a certified viscosity (Brookfield Standard η = 0.965 Pa s). Recall that viscosity is

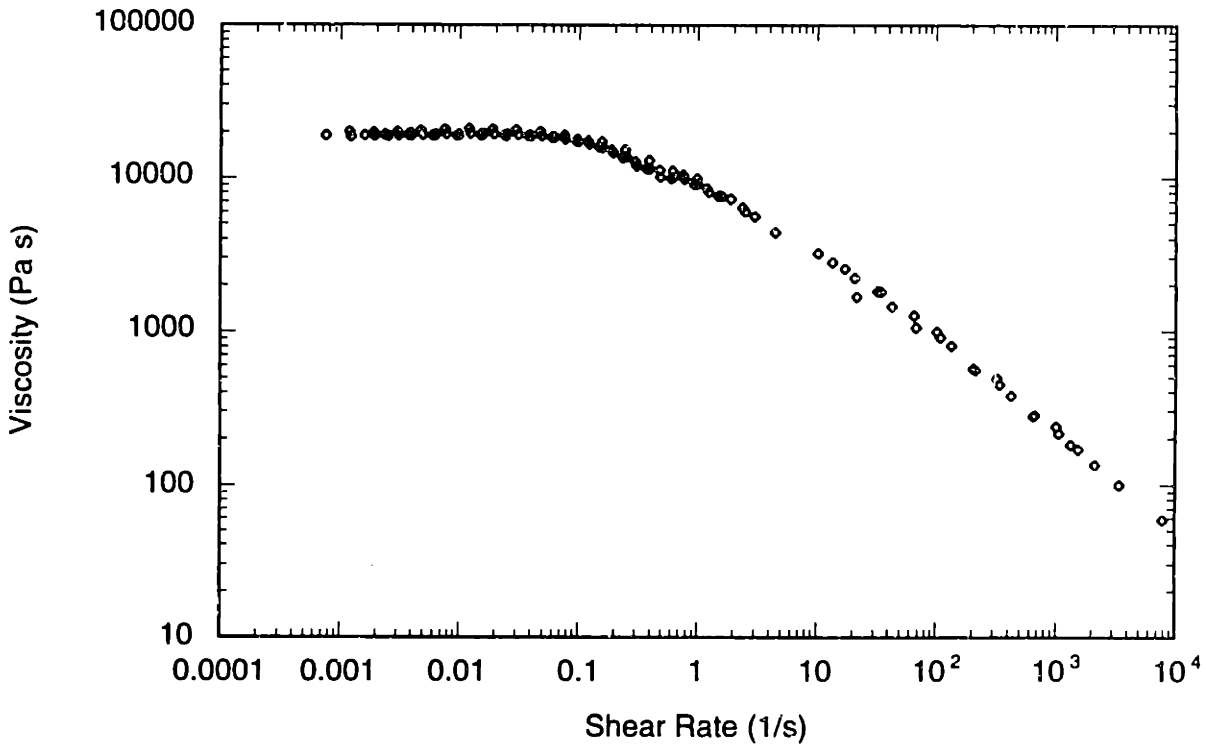

Figure 4.2: Master viscosity curve of LDPE obtained from data taken at 130°C - 190°C. Reference temperature is taken to be 160°C.

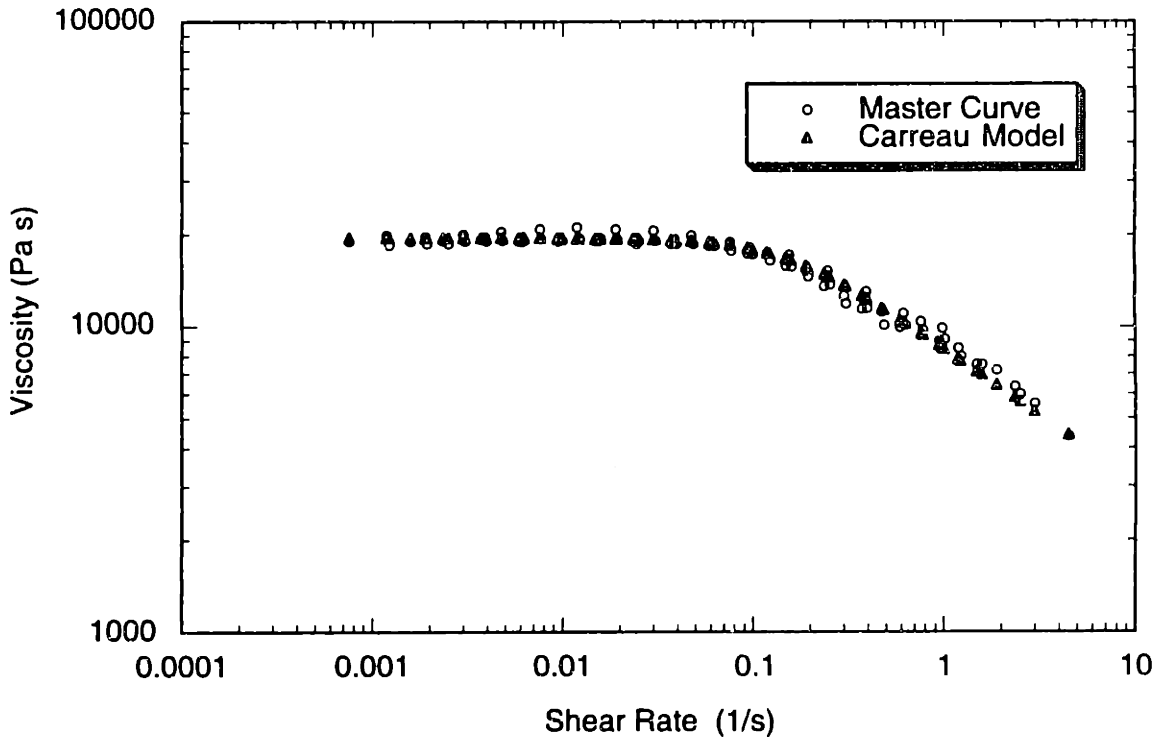

Figure 4.3: Master Curve compares with a fit using Carreau model. The parameters of the fit is shown in Equation 5.2.

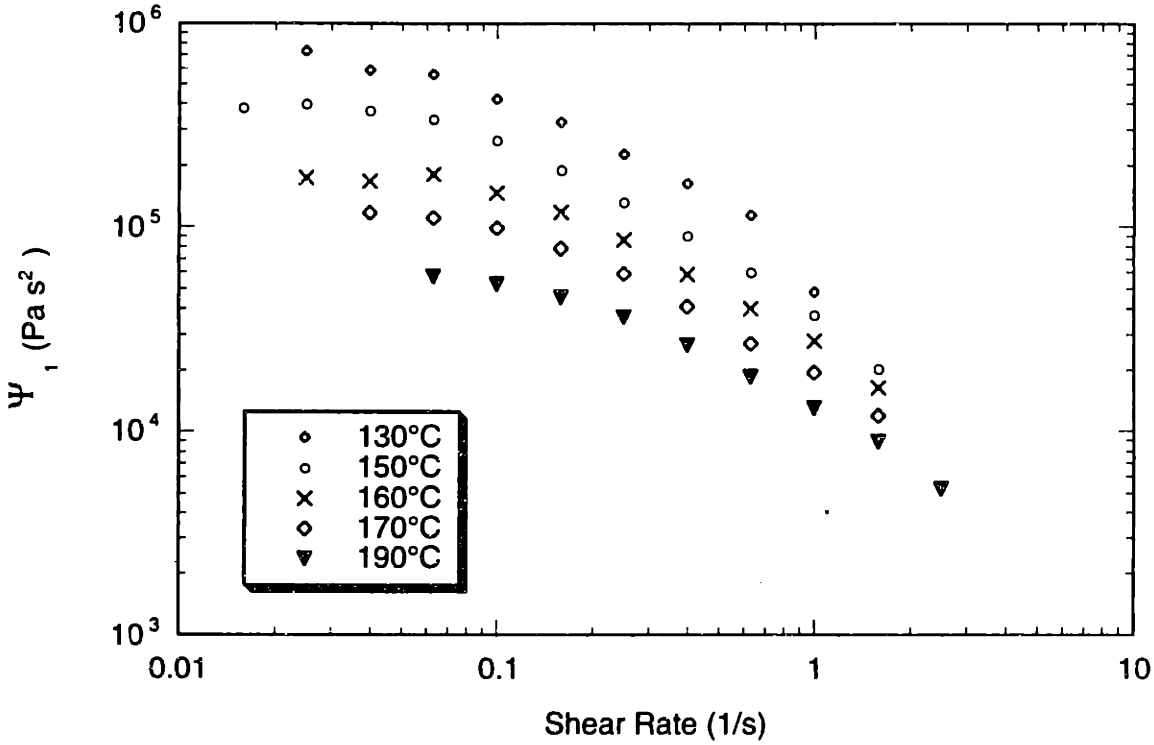

Figure 4.4: First normal stress coefficient of LDPE as a function of temperature and shear rate. All data were taken in the parallel-plate mode with a Rheometrics RMS-800.

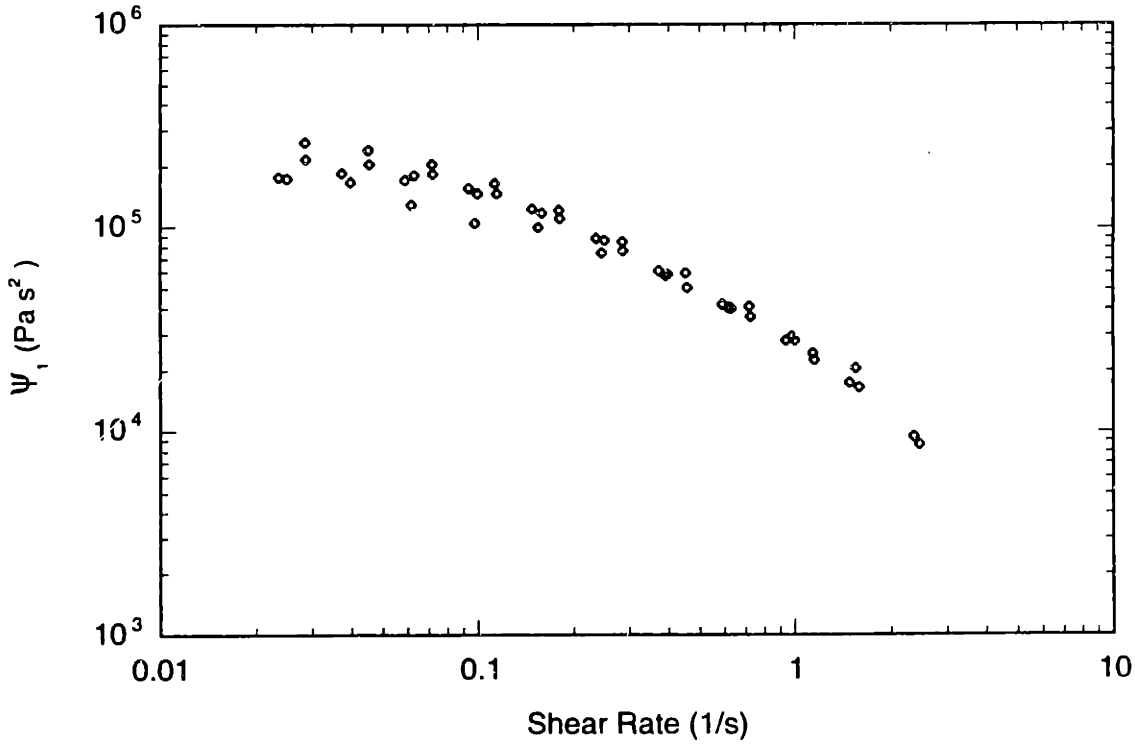

Figure 4.5: Master curve of LDPE first normal stress coefficient. Reference temperature is 160°C.

calculated from the measured torque, and the first normal stress coefficient is calculated from the normal force. Figure 4.6 shows a plot of the percentage error of both transducers measured with standard calibration weights. Using the relationship between the torque and normal force obtained during viscosity and first normal stress coefficient measurement of from LDPE at 160°C, the axes of Figure 4.6 can be changed to the corresponding shear rates, as in Figure 4.7. This figure shows that the percentage error dropped below 5% for a typical measurement of viscosity and first normal stress coefficient at shear rates of over 0.03 s^{-1} on LDPE at 160°C. Results from the Newtonian viscosity standard show an averaged 7.5% deviation from the specified viscosity over the torque range which corresponds to a shear rate range from 0.001 s^{-1} to 0.15 s^{-1}. Note that the 7.5% deviation is higher than the percentage error determined solely based on calibration weights. Therefore, the other sources of error such as uncertainties in gap size measurement or uncertainties in shear rate determination are not negligible. Moreover, although the resolution of the distance gauge (1 μm in 2 to 3 mm) and the stepper motor (5 x 10^{-4} radians per step) are both very high, their accuracy cannot be independently determined very easily.

Equipment manufacturers usually cite the percentage resolution at full scale as a measure of the accuracy. For example, the manufacturer of the rheometer Rheometrics™ claimed that the resolution of the force transducer was 0.1% of full range or 2 g out of 2000 g. It is thus incorrect to assume the accuracy of the transducer is 0.1% throughout the whole range of detection. Measuring the viscosity and first normal stress coefficients of certified calibration standard fluids remains the best way to estimate the accuracy of a rheometer.

Linear viscoelastic properties of this LDPE were examined by measuring its storage and loss moduli as functions of frequency and temperature. The master curves for the moduli are shown in Figure 4.8 with the curve of $\eta_0 \cdot \omega$, where η_0 is the zero-shear-rate

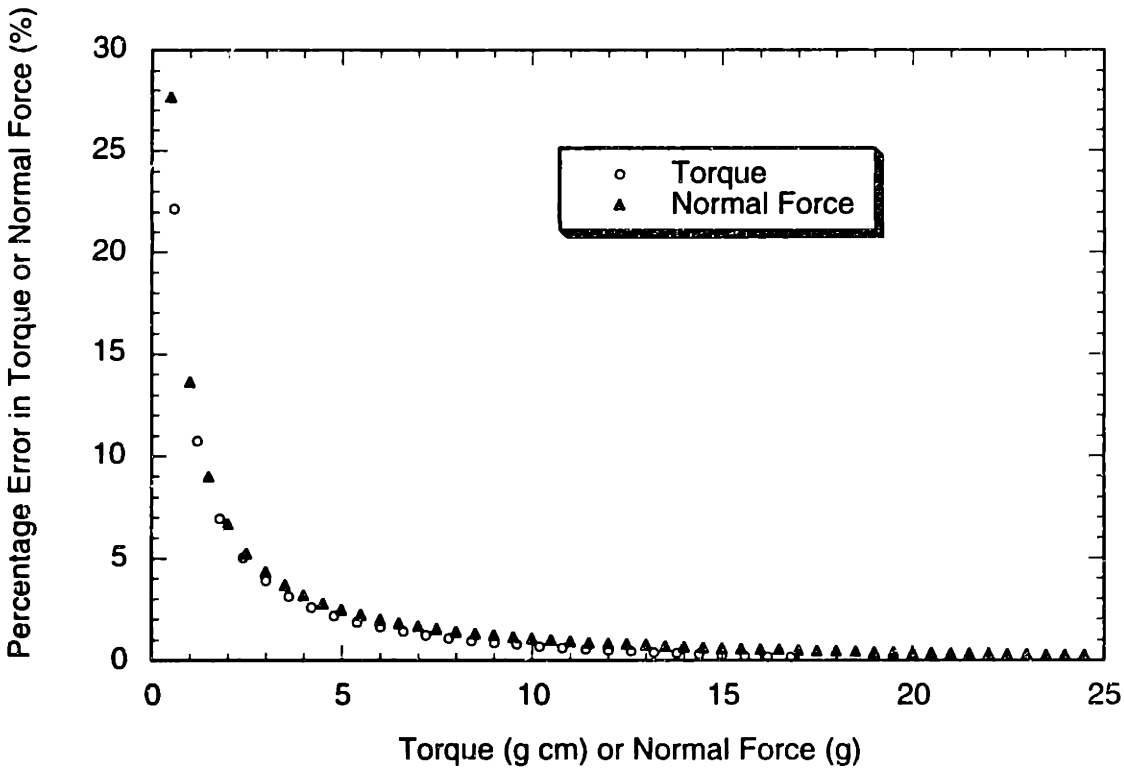

Figure 4.6: Errors in the torque and normal force measurements of the rheometer RMS 800 obtained by using calibrating weights (calculated based on data obtained by Geneiser, 1996).

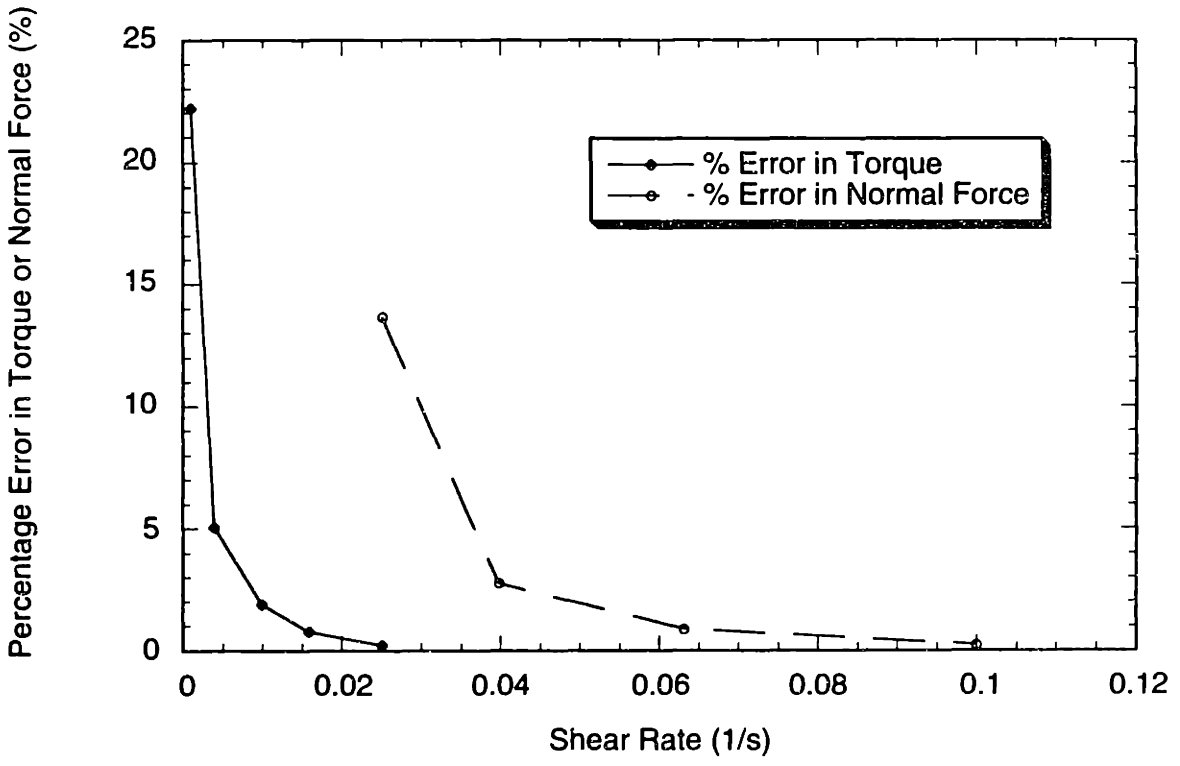

Figure 4.7: Errors in the torque and normal force measurements of the rheometer RMS 800 obtained by using calibrating weights (calculated based on data obtained by Geneiser, 1996).

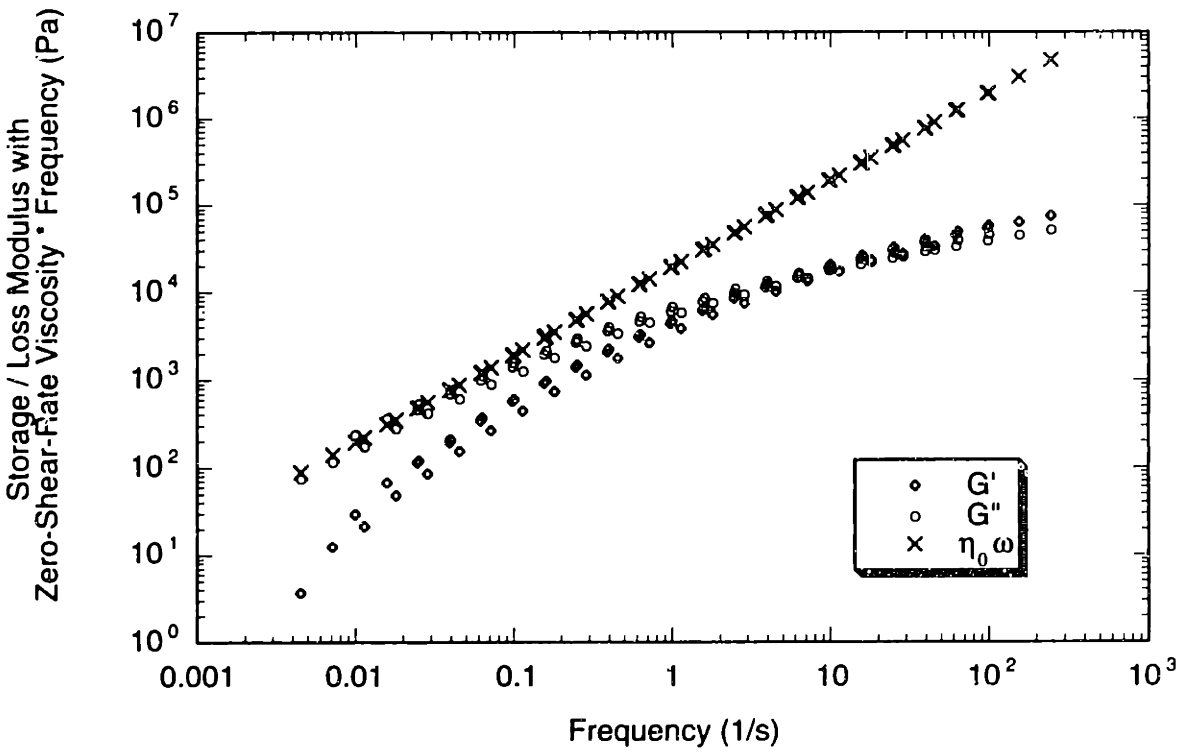

Figure 4.8: Master curves of LDPE storage and loss moduli as functions of frequency ω. Reference temperature is 160°C. The loss modulus G' is compared to $\eta_0\,\omega$ at low frequencies.

viscosity, and ω is the frequency of oscillation. The merging of this curve and the G' curve toward $\omega=0$ shows that as the frequency goes to zero, the value $G''/\omega=\eta'$ approaches that of the zero-shear-rate viscosity η_0, because only the viscous response is dominant at very low frequencies in the linear viscoelastic region. The storage and loss moduli were fit with a 6-mode Maxwell model (Equations 4.3 and 4.4) by minimizing the difference between the measured and predicted moduli (Bird et al., 1987). This spectrum was obtained by first assuming a set of relaxation times λ_k. Then the η_k values were calculated by least square minimization of the difference between the experimental G' and G'' curves and the values predicted by Equations 4.3 and 4.4. The relaxation spectrum obtained this way is tabulated in Table 4.2. Figure 4.9 shows the storage and loss moduli of LDPE compared to the six-mode Maxwell model fit. The relaxation spectrum was used to construct the $\eta^-(t)$ curve (Figure 4.10) which characterizes the viscous stress relaxation after cessation of steady shear flow. Equation 4.5 relates $\eta^-(t)$ and the relaxation spectrum (η_k's and λ_k's).

$$G'(\omega_j) = \sum_{k=1}^{N} \frac{\eta_k \lambda_k \omega_j^2}{1 + (\lambda_k \omega_j)} \tag{4.3}$$

$$G''(\omega_j) = \sum_{k=1}^{N} \frac{\eta_k \omega_j}{1 + (\lambda_k \omega_j)^2} \tag{4.4}$$

$$\frac{\eta^-}{\eta_0} = \frac{\sum_k \eta_k e^{-t/\lambda_k}}{\sum_k \eta_k} \tag{4.5}$$

The quantity $2\eta''/\omega$ approximates Ψ_1 at low shear rates. Figure 4.11 shows that this approximation is not as close as the approximation of G''/ω to η_0 as shown in Figure 4.9.

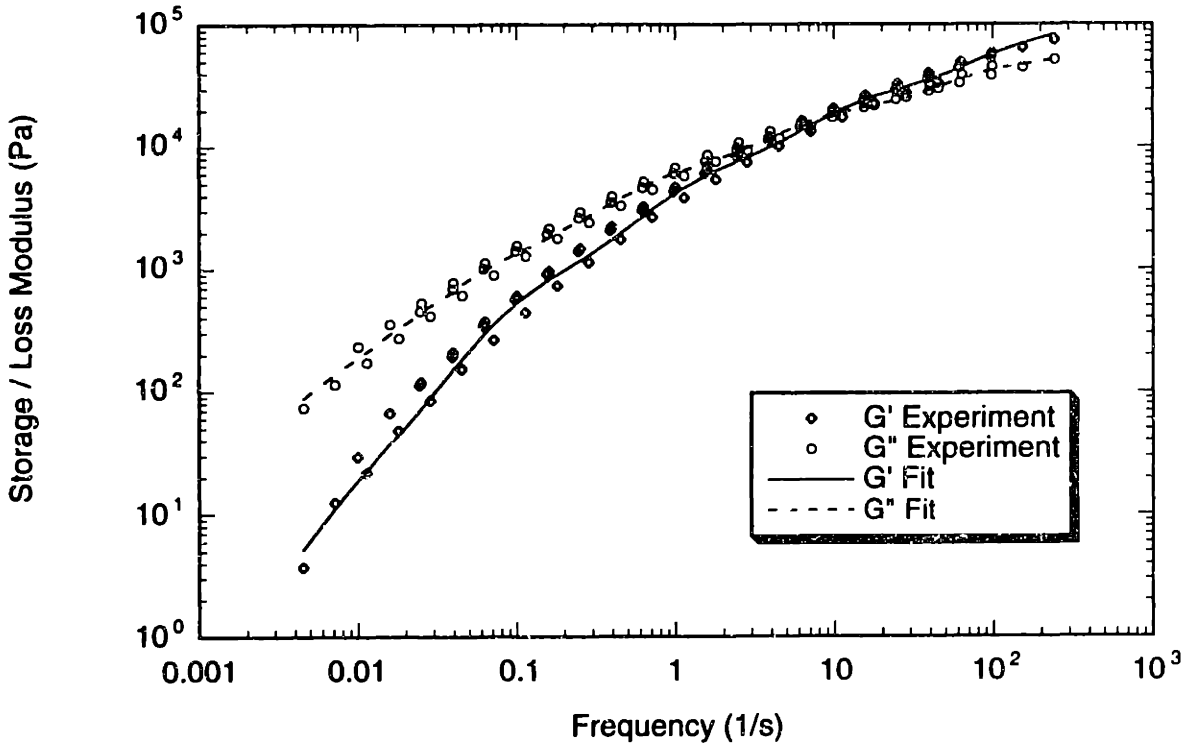

Figure 4.9: Storage and loss moduli of LDPE compared to a six-mode Maxwell model fit with the constants shown in Table 4.2.

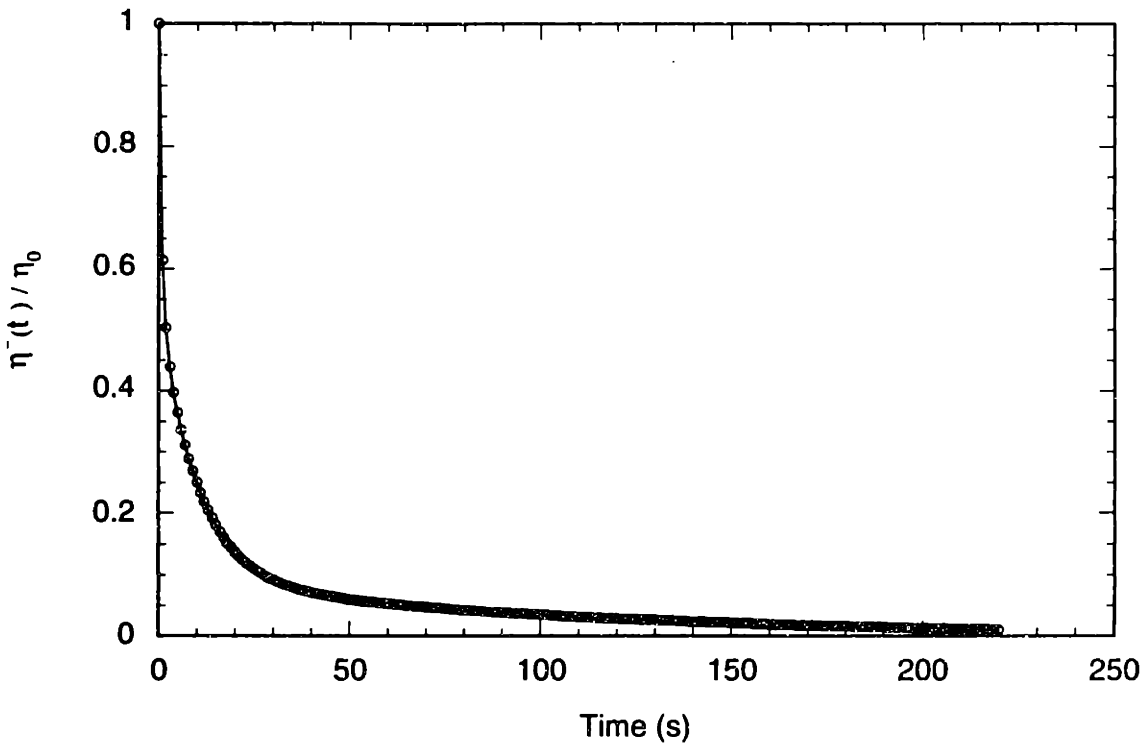

Figure 4.10: Stress relaxation material function $\eta^-(t)$ scaled by η_0 as a function of time after cessation of steady shear flow. This function was computed by Equation 4.5.

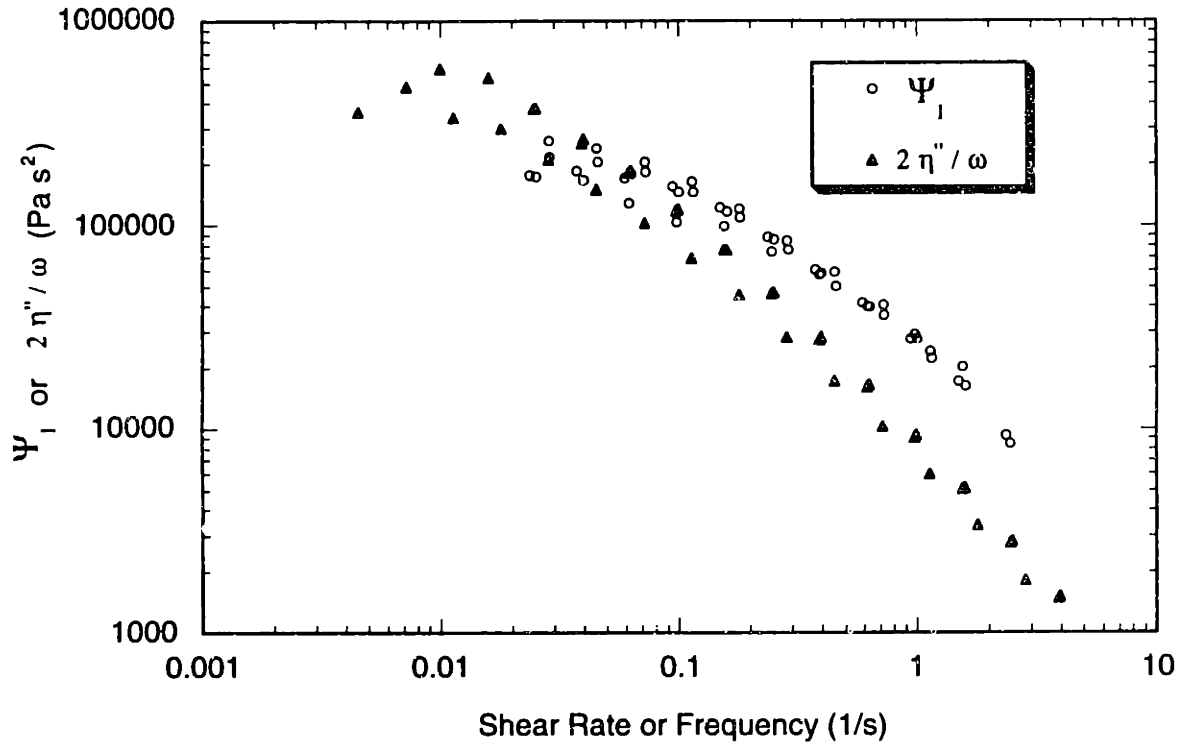

Figure 4.11: Master curve of LDPE first normal stress coefficient with $2\eta''/\omega$. Reference temperature is 160°C.

k	λ_k	η_k
1	100	1845
2	10	8971
3	1	6130
4	0.1	2228
5	0.01	528
6	0.001	142

Table 4.2: Relaxation spectrum of LDPE at 160°C.

4.1.2 LDPE Results from slit die viscometer

As explained in Chapter 1 of this thesis, a slit die viscometer measures viscosity by using the same principle as a capillary viscometer. The shear stress at the wall is proportional to the pressure gradient along the length of the channel. Figures 4.12 and 4.13 show that the pressure gradient increased with increasing screw speed or decreasing temperature. This is because a larger driving force was necessary to extrude the polymer at a higher flow rate or to extrude a polymer with a higher viscosity. The straight pressure profiles indicated that the driving force was constant throughout the channel and that the flow was fully-developed.

The mass flow rate increased proportionally with the extruder screw speed (Figure 4.14). The wall shear stress or driving force increased with the mass flow rate, but the rate of increase decreased with increasing flow rate (Figure 4.15). The latter observation is a characteristic of non-Newtonian fluid flows.

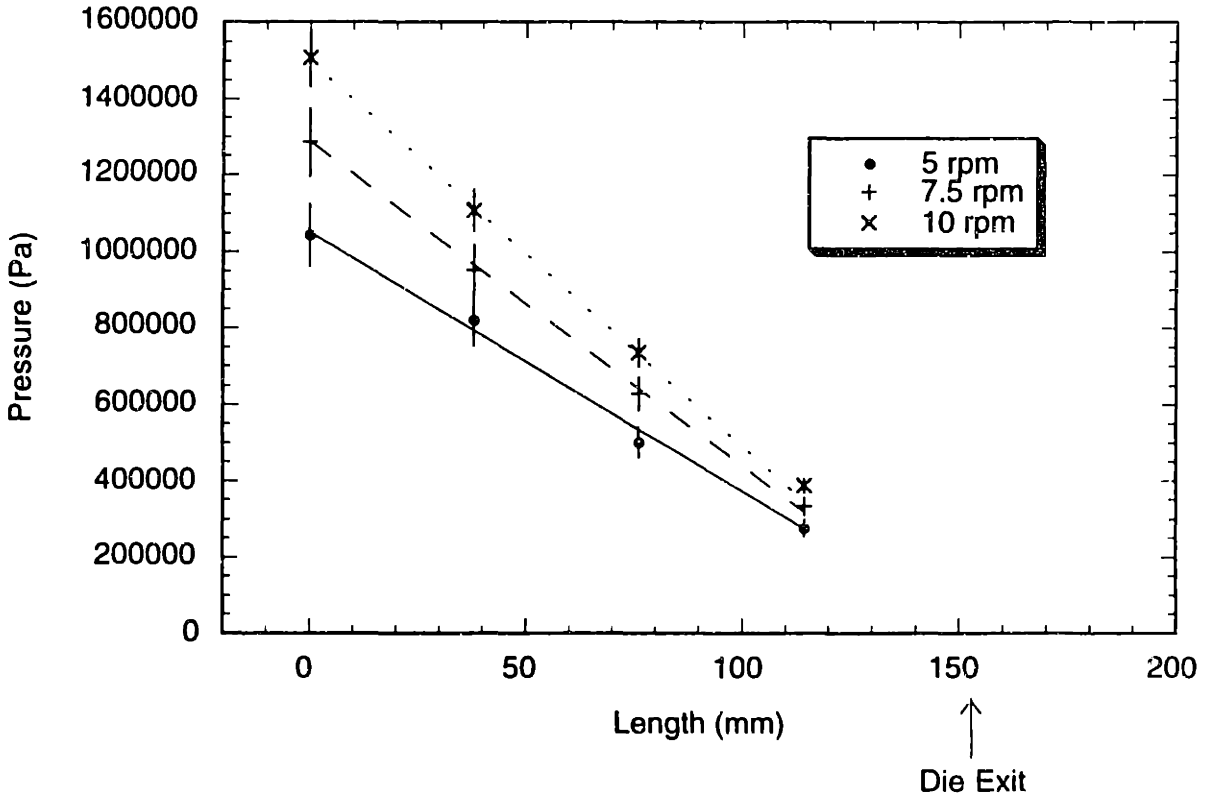

Figure 4.12: Pressure profiles along the length of slit channel at different screw speeds. The error bars show the resolution of the pressure transducers.

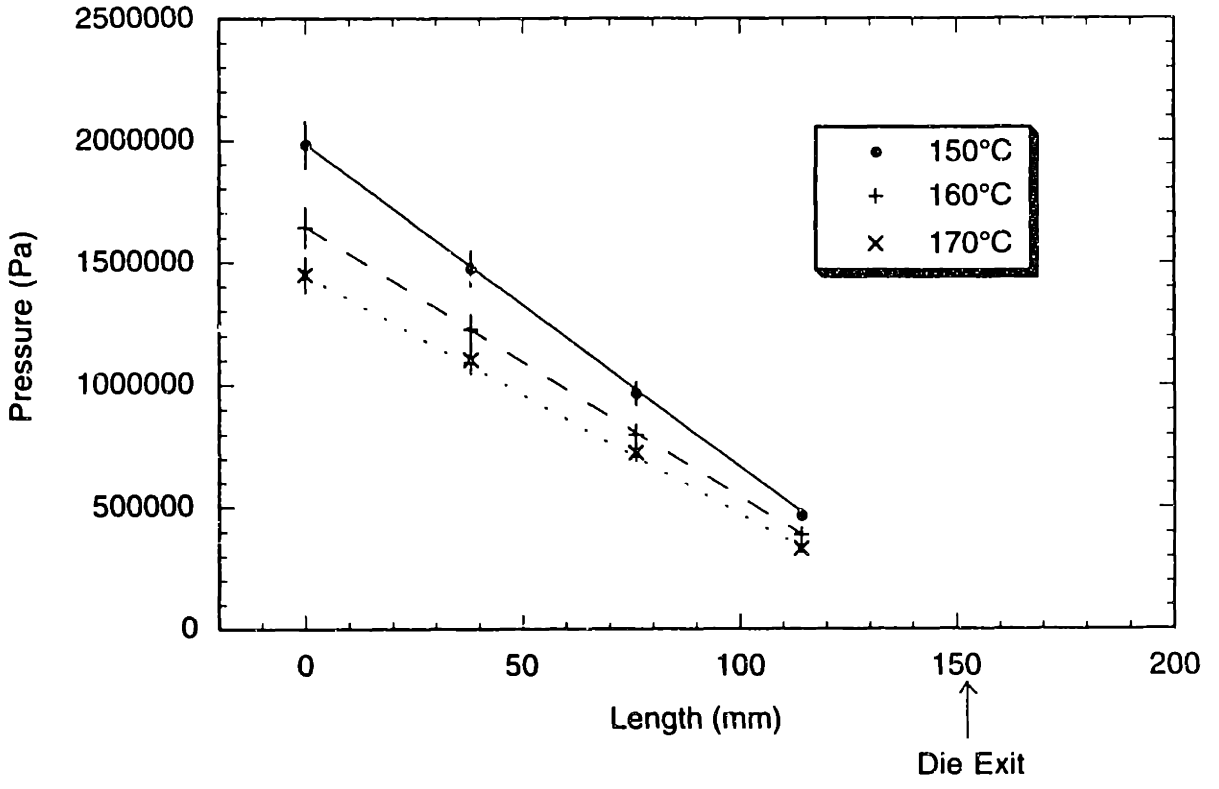

Figure 4.13: Pressure profiles as a function of distance along the length of the slit channel for several different, isothermal conditions. Error bars show the resolution of the pressure transducers.

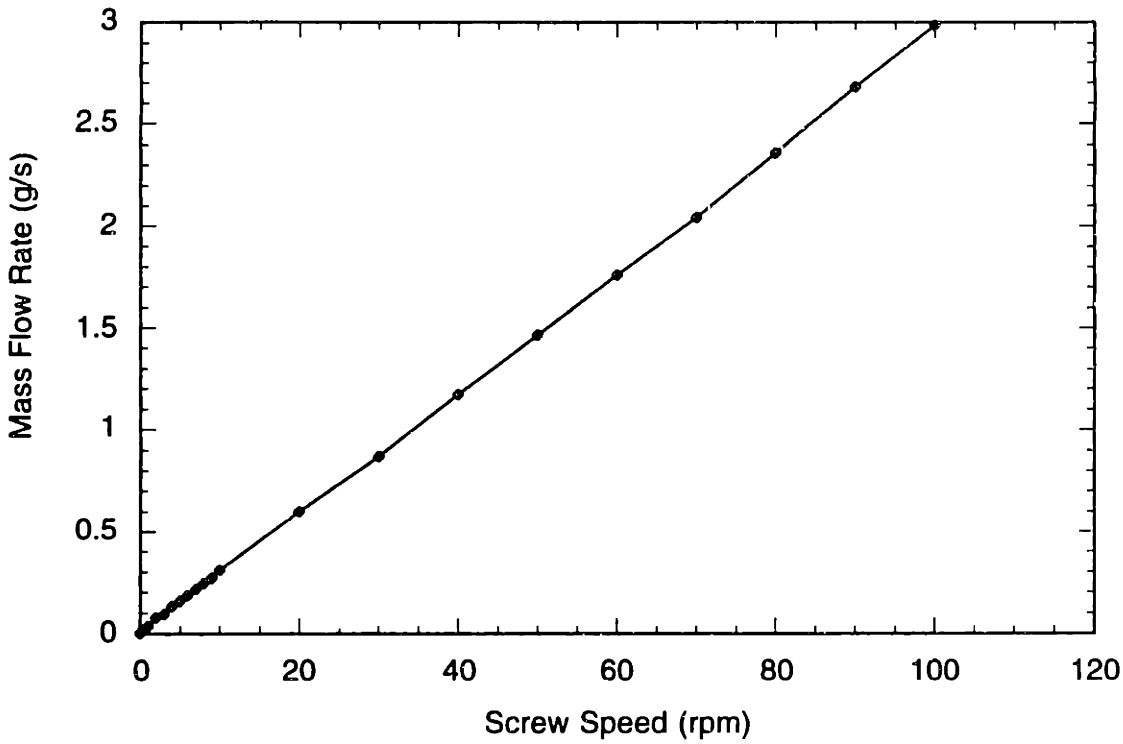

Figure 4.14: Mass flow rate of the 1-1/4 inch screw diameter single screw extruder based on LDPE at 160°C.

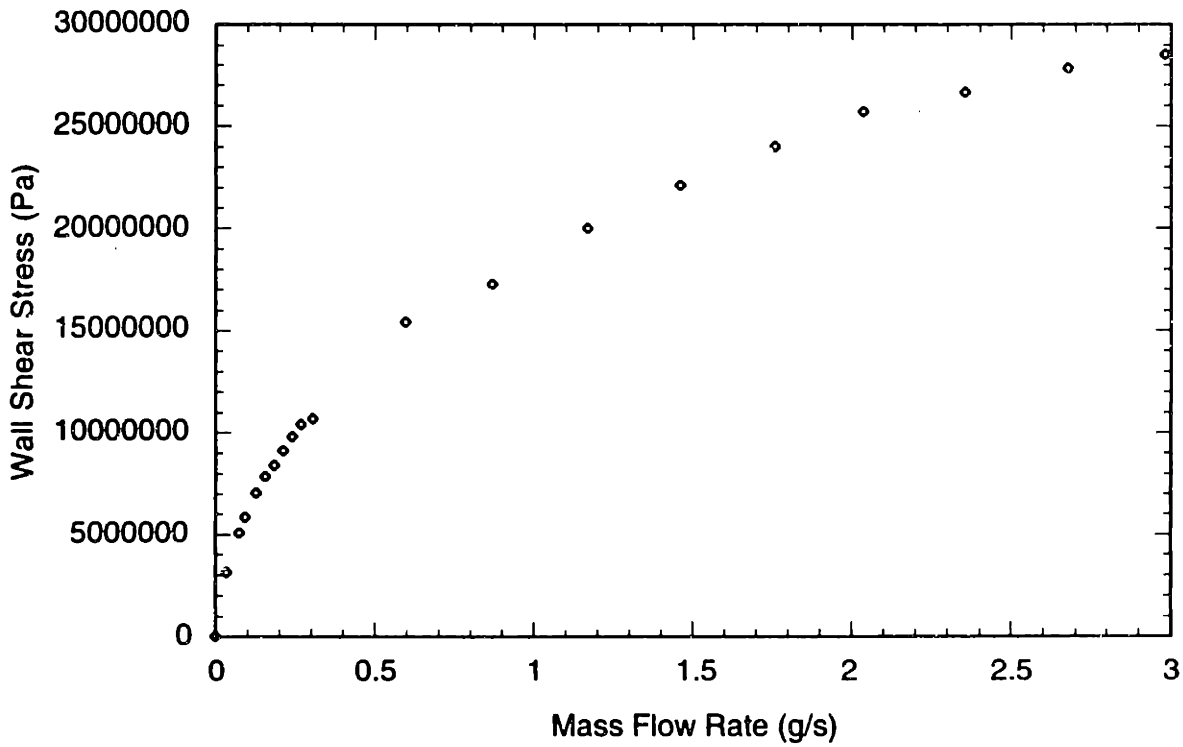

Figure 4.15: The shear stress at the wall of the slit channel as a function of mass flow rate through the channel at 160°C. The changing slope indicates non-Newtonian, shear thinning behavior.

As explained in Section 3.6, viscosity can be calculated from measuring the wall shear stress τ_w and the flow rate Q obtained for different throughput. The wall shear rate was calculated as follows:

$$\dot{\gamma}_w(\tau_w) = \frac{1}{\tau_w} \cdot \frac{d}{d\tau_w}\left(\frac{Q\tau_w^2}{2WB^2}\right) \tag{4.6}$$

where W and B are the depth and half-width of the channel, respectively. Viscosity calculated from this method was compared to that obtained from parallel plate rheometry and capillary viscometry in Figure 4.16. Results obtained from the different methods agreed to within 25%.

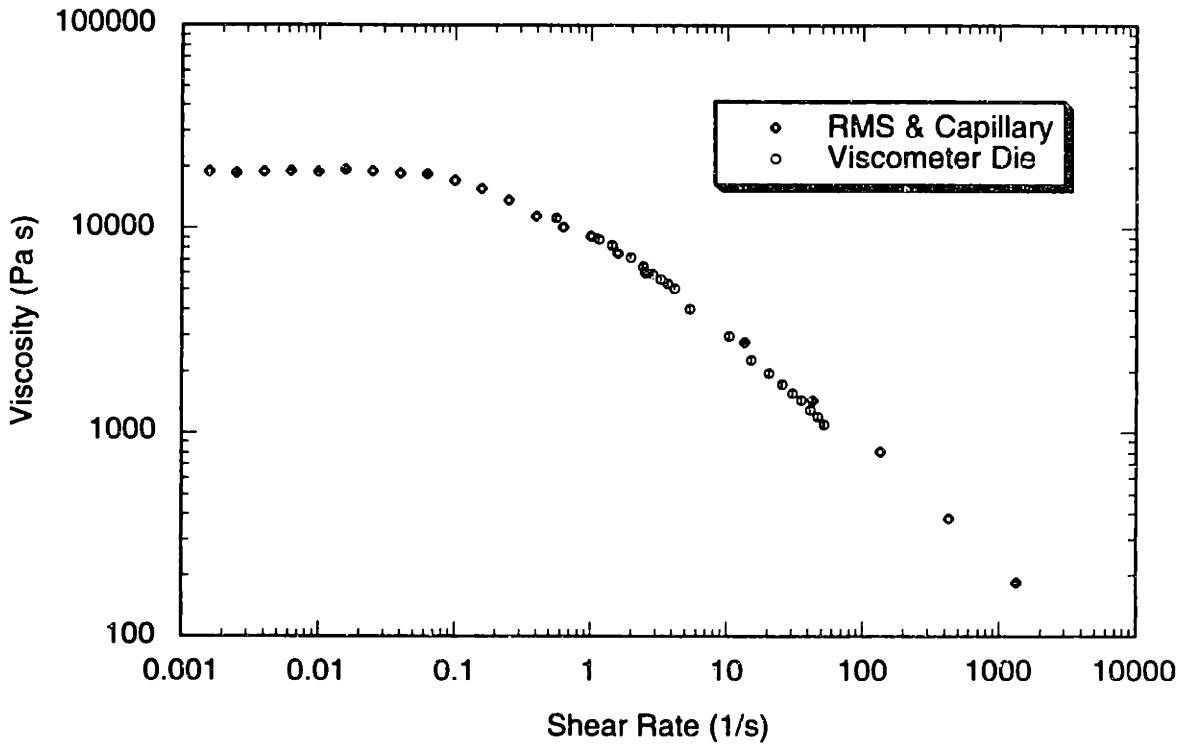

Figure 4.16: Viscosity measured by the slit viscometer die compared to that measured by parallel-plate rheometry and capillary viscometry.

4.2 Results From Laser Doppler Velocimetry

This section summaries the results obtained by using laser Doppler velocimetry. Because the eventual goal of this section is to quantify the viscosity measured by the optical method, the uncertainty level in velocity measurement by using LDV also needs to be quantified. Therefore, a discussion of LDV calibration is also included in this section. Each point on the velocity profiles presented below was averaged from the velocity calculated from 1000 Doppler bursts. As explained in Section 3.3, the LDV parameters had to be set correctly in the burst analyzer such that high quality bursts came in at the highest possible rate. Figure 4.17 shows a high-quality burst obtained during an LDV run as a scattering particle went through the measuring volume. If too many low-quality bursts were recorded to calculate the velocity average, the velocity distribution would be flattened due to the high number of outlying points. As a result the mean velocity would be changed, and the velocity profile would become skewed with big standard deviation (Figure 4.18). In contrast, the velocity profile composed of averages obtained from a narrow velocity distribution because of correctly-tuned parameters is much smoother (Figure 4.19).

The accuracy of the laser Doppler velocimeter was investigated by using it to measure the velocity on the surface of a rotating cylinder. The angular velocity of the cylinder was measured by a chopper-wheel timer with LabVIEW^{TM}. The resolution of the time register on the board was smaller than 16 ms in 12000 ms or 0.13%. Figure 4.20 compares the velocity measured by both LDV and the timer in the velocity range of interest. The deviation was 3%.

The velocity profile was measured across the smallest dimension of the channel (4 mm) midway between the top and the bottom walls. Figure 4.21 shows the profiles

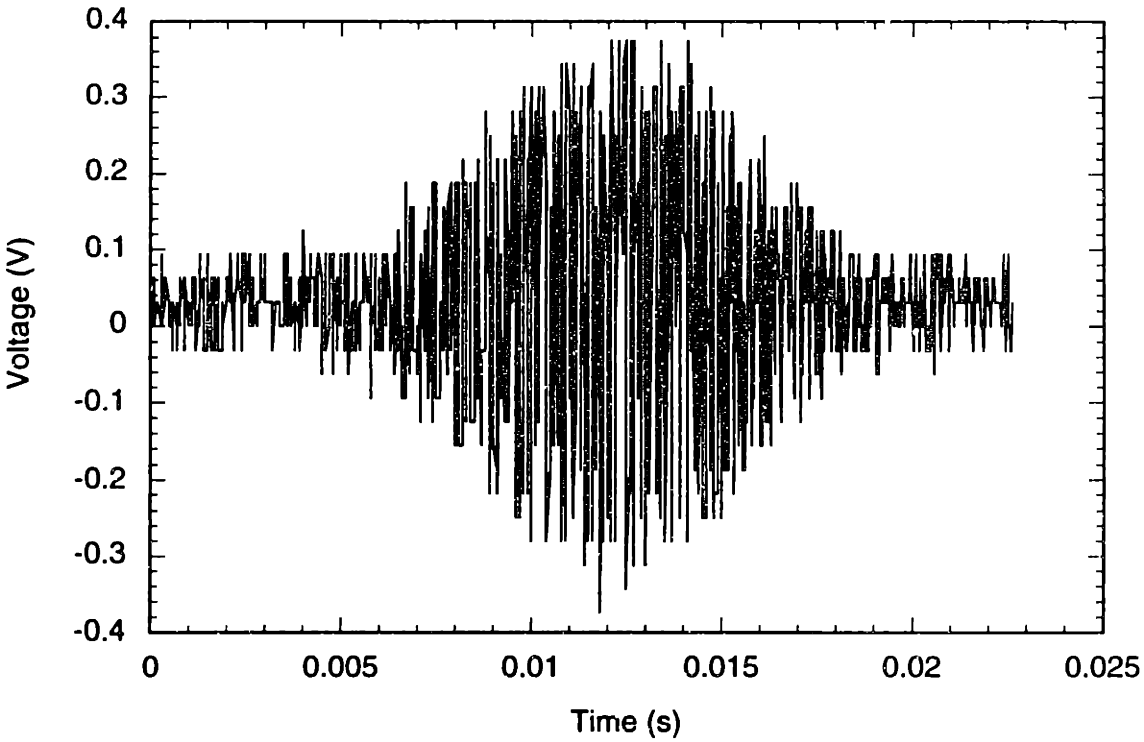

Figure 4.17: The voltage signal from the photomultiplier after based-line clamping and low-pass filtering (Section 3.3) as a function of time. This ball-shaped signal is called a Doppler burst.

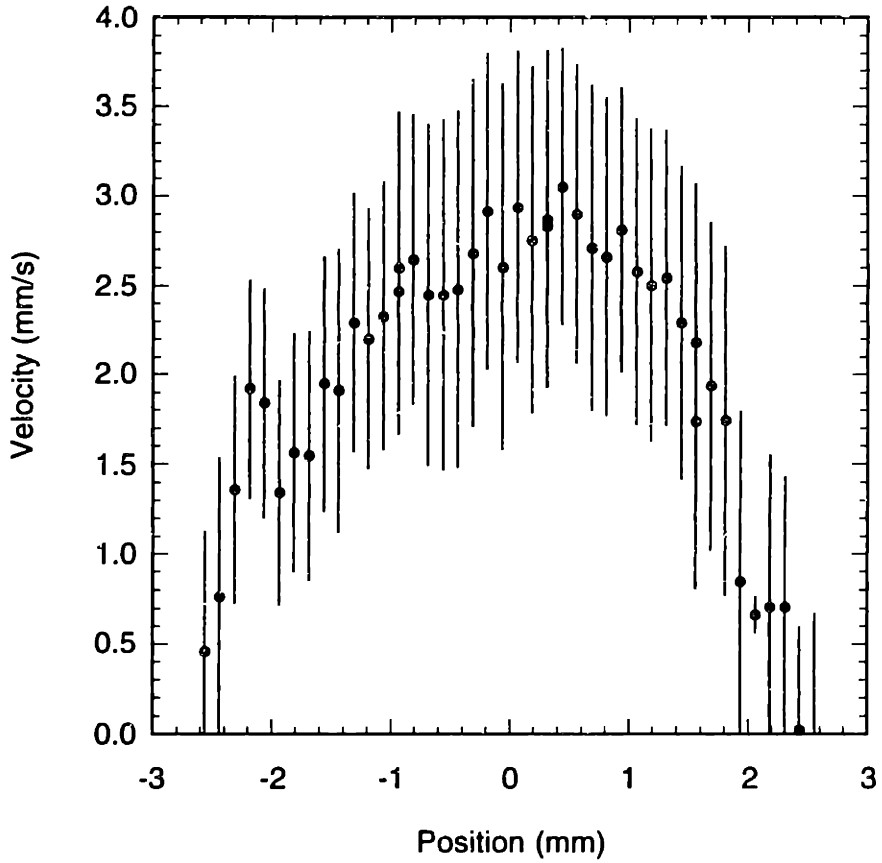

Figure 4.18: Velocity profile of LDPE at 10 rpm with suboptimal parameters on the burst analyzer. The error bars represent one standard deviation of the velocity distribution out of 1000 bursts.The position is shown in relative steps of the stepper motor which controls the LDV probe. The boundary walls of the gap are at x = $\pm$2 mm.

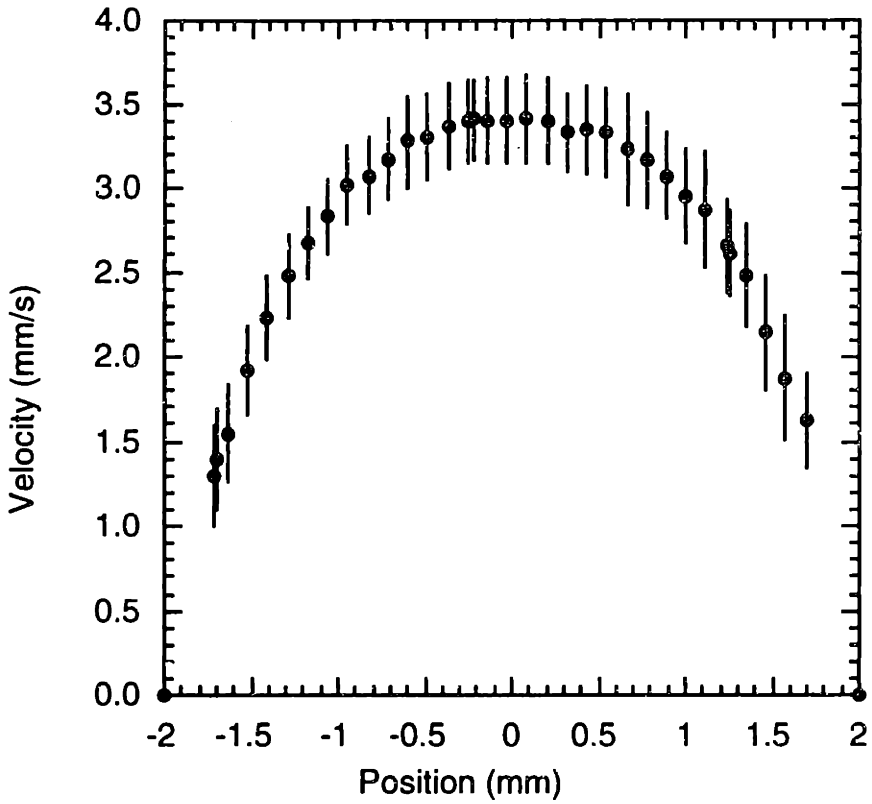

Figure 4.19: Velocity profile of LDPE at 10 rpm with optimal parameters on the burst analyzer. The error bars represent one standard deviation of the velocity distribution out of 1000 bursts. The boundary walls of the gap are at x = ±2 mm.

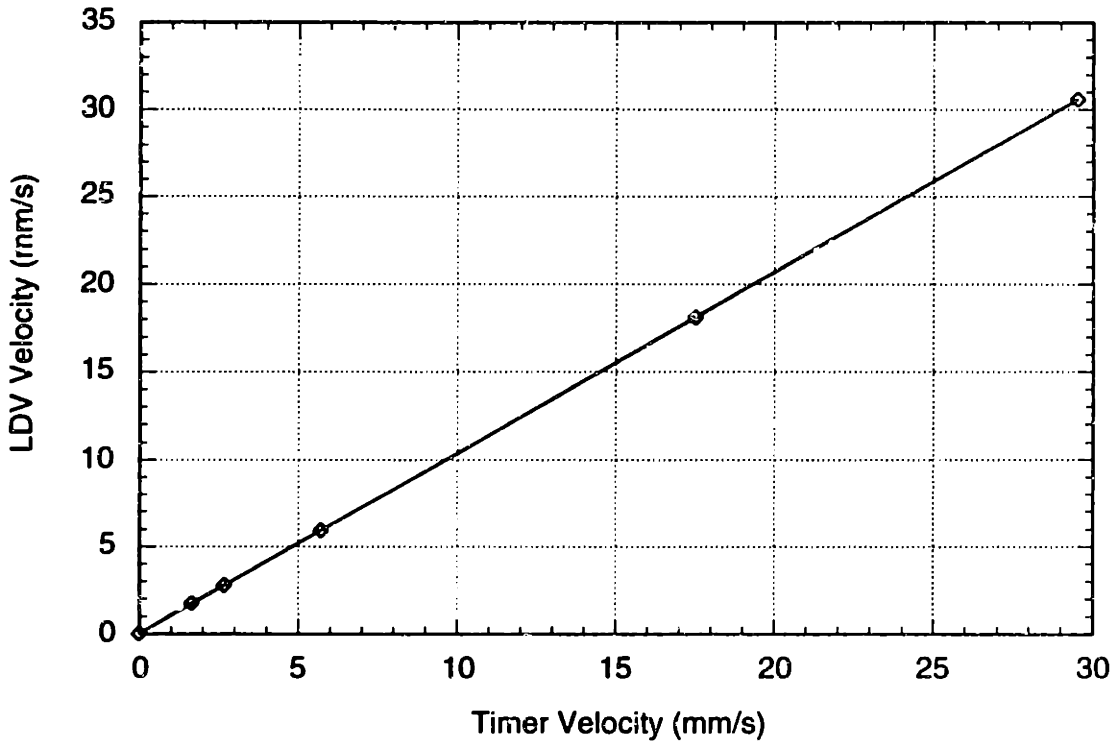

Figure 4.20: The velocity of the surface of a rotating cylinder whose speed was recorded by a LabVIEW™ timer. The straight line (y =1.0348 x) fits the data with R=1.00000.

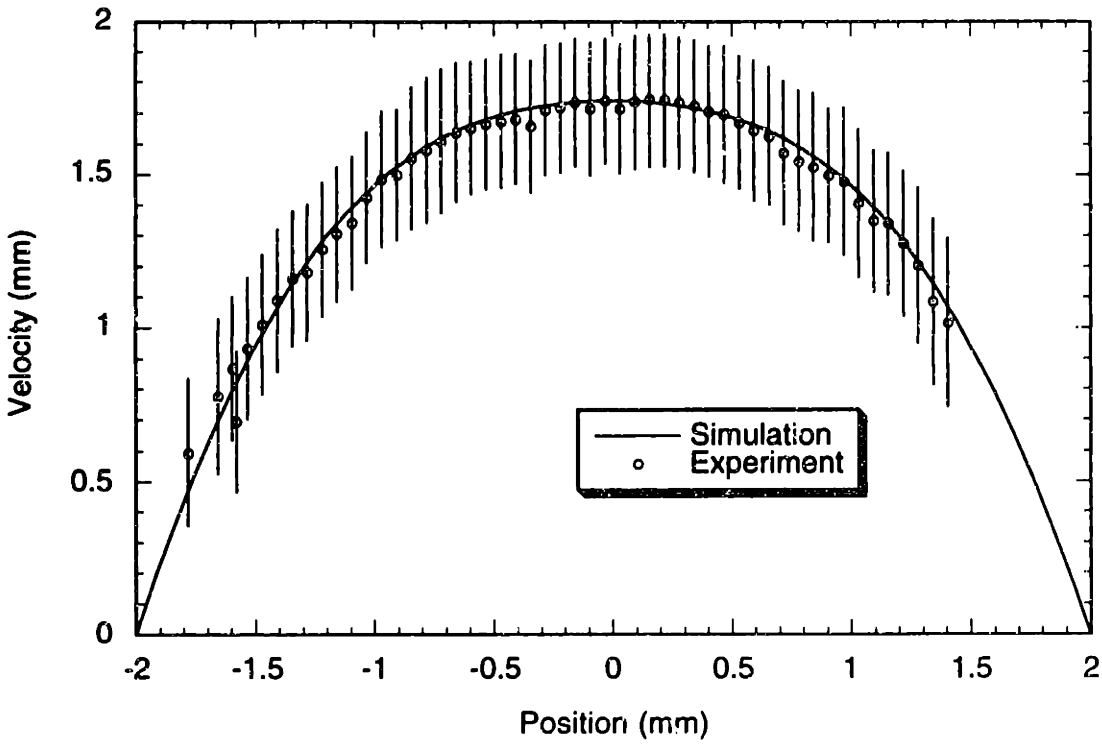

Figure 4.21: Experimental and simulated velocity profiles at 5 rpm and 160°C. The error bars represent one standard deviation of the velocity distribution obtained from 1000 bursts.

obtained from an experiment with the extruder running at 5 rpm at 160°C and from the FIDAP^{TM} simulation. The error bars show one standard deviation of the experimental data out of 1000 bursts. The two profiles agreed within the accuracy of the experimental data. There was a lack of reliable data close to the two walls due to a number of reasons. First, the velocity near the wall was close to zero. The signal-to-noise ratio decreased rapidly as the noise and the signal became comparable in size. Five rpm was the lowest extruder speed for which LDV could still measure a relatively smooth velocity profile. Second, the metal wall strongly reflected the two light beams and contaminated the signal. (Coating the inner metal wall with a dark material was not feasible at this point because of the unevenness of the surface after use.) Therefore, there was a larger region of unreliable data (discarded) on the side of the metal wall (+2 mm) than the glass wall (-2 mm). The maximum shear rate at a typical run in which the velocity was measured was about 3 s^{-1}.

The velocity profiles measured at 7.5 rpm and 10 rpm are shown in Figures 4.22 and 4.23. These profiles agreed with the simulated ones within the accuracy of the experimental data in general except in the region close to the glass wall at 10 rpm. As the flow rate increased, the amount scatter in the data decreased because of the lower signal-to-noise ratio. The larger discrepancy between the experimental and simulated profiles was probably not due to the error in the viscosity model because the fit was uniformly good up to the maximum shear rate of 5 s^{-1} in this experiment. Instead, the discrepancy might be due to an slight increase in flow rate after the extruder was warmed-up.

Only the left half of the velocity profile was used to determine the shear rate profile. This is because the velocity profiles were symmetric, and there were more reliable data on the side closer to the glass wall. The shear rate increase monotonically from the centerline to the walls. In order to capture the slopes of the velocity profile faithfully without introducing significant noise in the calculation, the shear rate was estimated from the slopes of

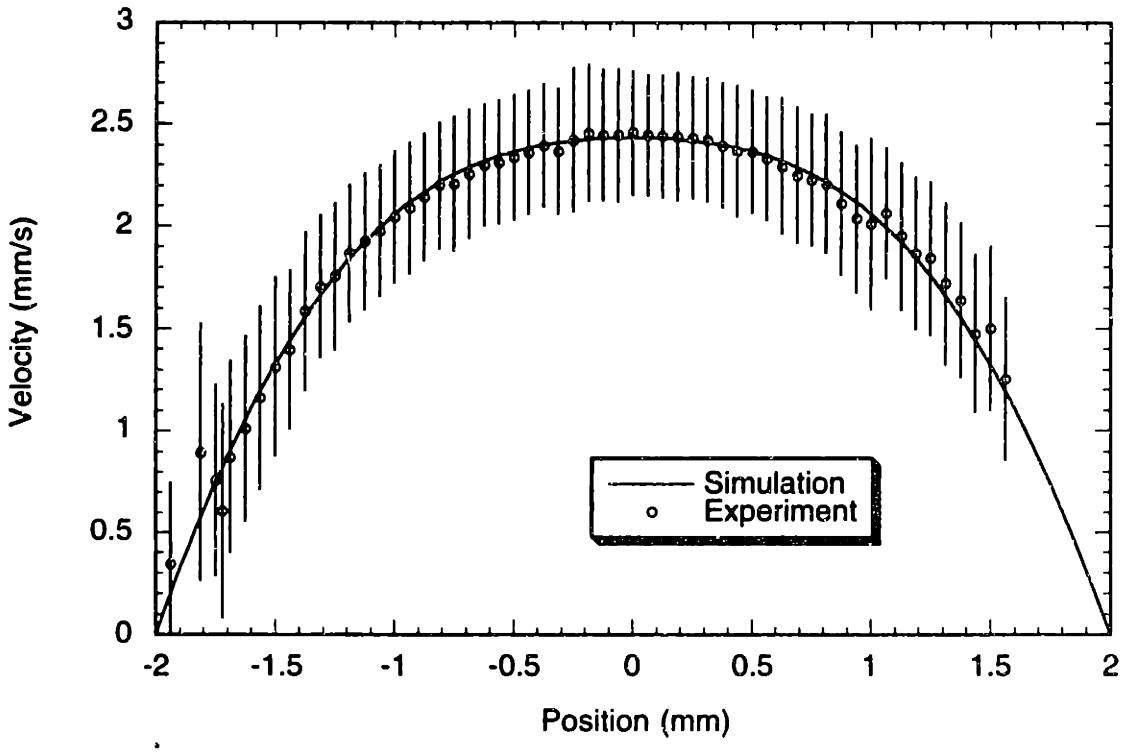

Figure 4.22: Experimental and simulated velocity profiles at 7.5 rpm and 160°C. The error bars represent one standard deviation of the velocity distribution obtained from 1000 bursts.

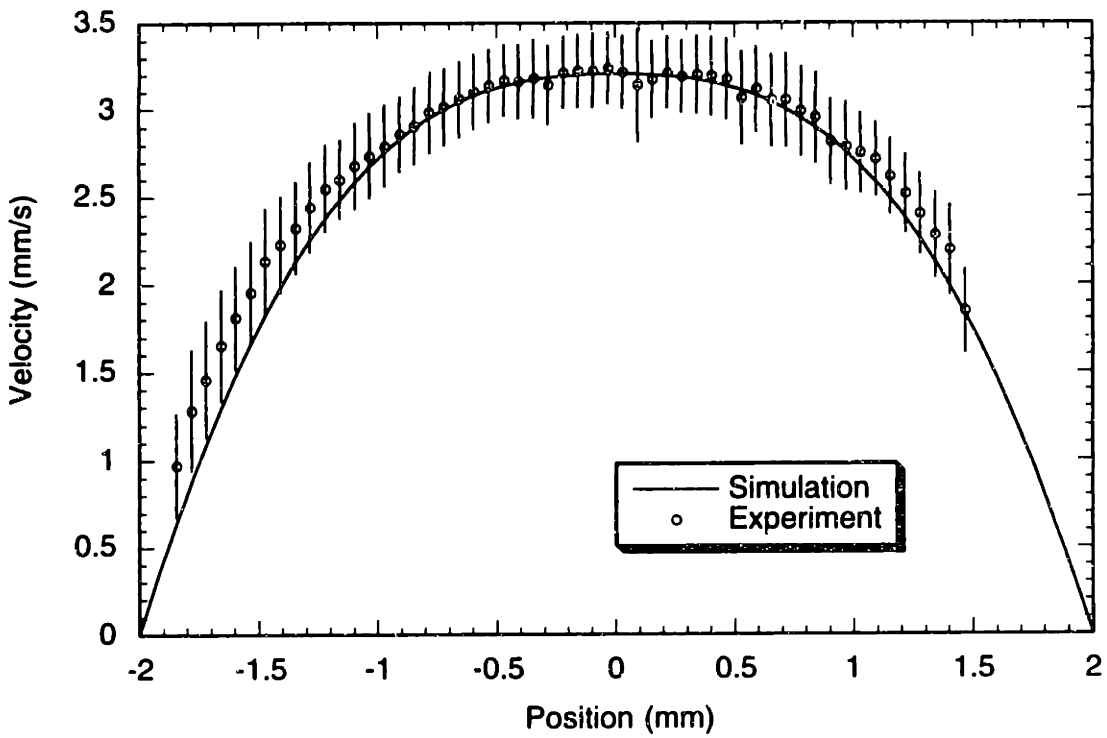

Figure 4.23: Experimental and simulated velocity profiles at 10 rpm and 160°C. The error bars represent one standard deviation of the velocity distribution obtained from 1000 bursts.

quadratic curves fit to every 11 consecutive velocity data points. The shear rates calculated this way are shown in Figure 4.24 for the case of 5 rpm at 160°C. The error bars were estimated from one standard deviation of the velocity distribution obtained from 1000 bursts. In reality the shear rate should change very smoothly from the centerline to the wall. This idea was expressed by the fit of a smooth function through the data points. In fitting the data, the curve also had to go through zero at the centerline since the centerline shear rate was zero at all times. The function used was a sum of an exponential function and a constant. The use of a fit was more important close to the centerline because at that region, the local shear rate was very small and was decreasing very rapidly. The noise in the velocity profile might translate into a shear rate uncertainty many times larger than the actual shear rate itself. With the current experimental setup and die design, the fit represented the best estimate of the shear rate profile based on experimental data.

The shear rate profiles calculated from velocity data obtained at 7.5 and 10 rpm are shown in Figures 4.25 and 4.26. The scattering in the case of 7.5 rpm was very large compared to the other cases because of the relatively large amount of scattering in the few velocity data points close to the wall (Figure 4.22). In all the cases, the wall shear rates were used as a guideline for the fitting.

The viscosity calculated by dividing the local shear stress by the local shear rate is shown in Figure 4.27 for the cases of 5 rpm to 10 rpm at 160°C. The shear rate used in calculating the viscosity is the one obtained from the exponential fit. Data from three flow rates give the onset of shear thinning at about the same shear rate as indicated in the data obtained by parallel plate rheometry. The viscosity measurement was more accurate at high shear rates than low shear rates. For shear rate higher than 0.3 s^{-1}, viscosity calculated by the optical method agreed with that obtained from parallel-plate or capillary within 10%. The viscosity difference between the slit die limits the resolution of the

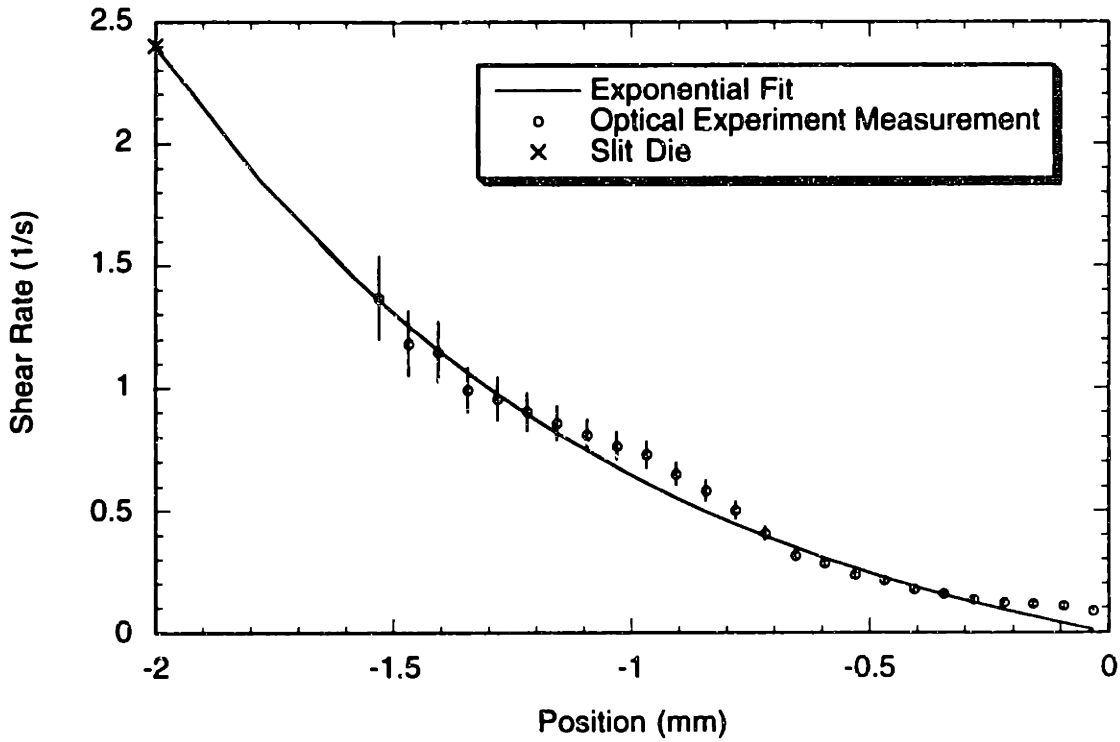

Figure 4.24: Shear rate profile from centerline to the glass wall at 5 rpm and 160°C. The error bars represent two times one standard deviation of the velocity distribution. The wall shear rate was obtained at the same flow rate and temperature but during a separate experiment.

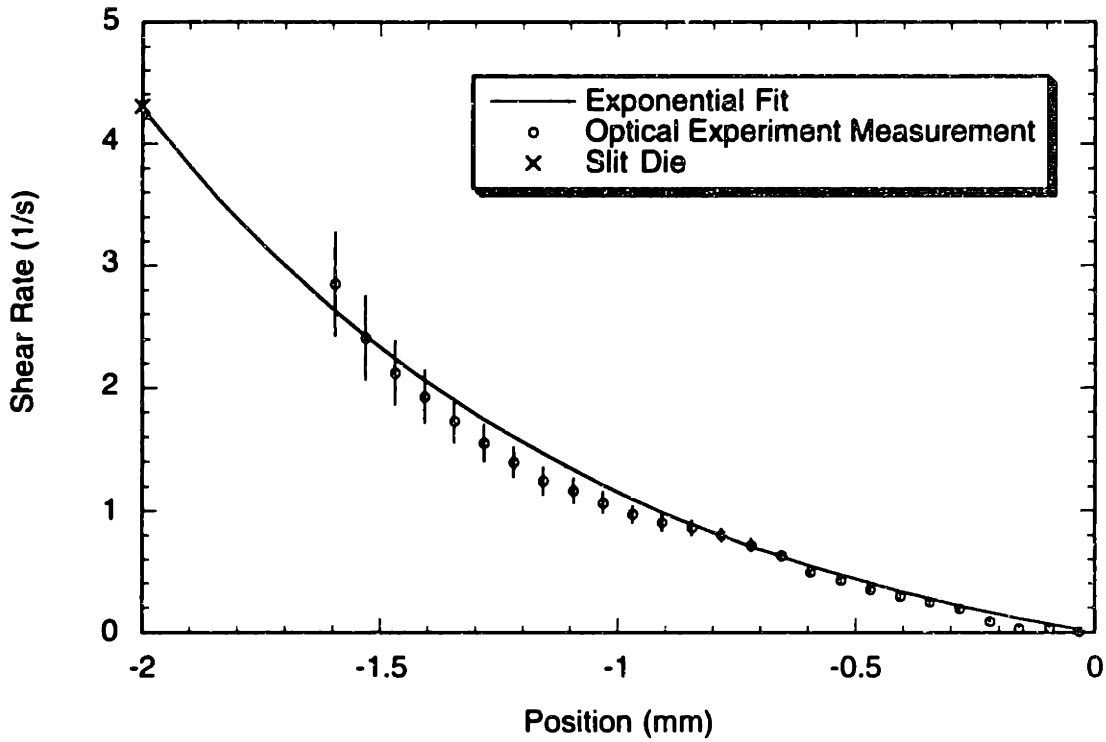

Figure 4.26: Shear rate profile from centerline to the glass wall at 10 rpm and 160°C. The error bars represent two times one standard deviation of the velocity distribution. The wall shear rate was obtained at the same flow rate and temperature but during a separate experiment.

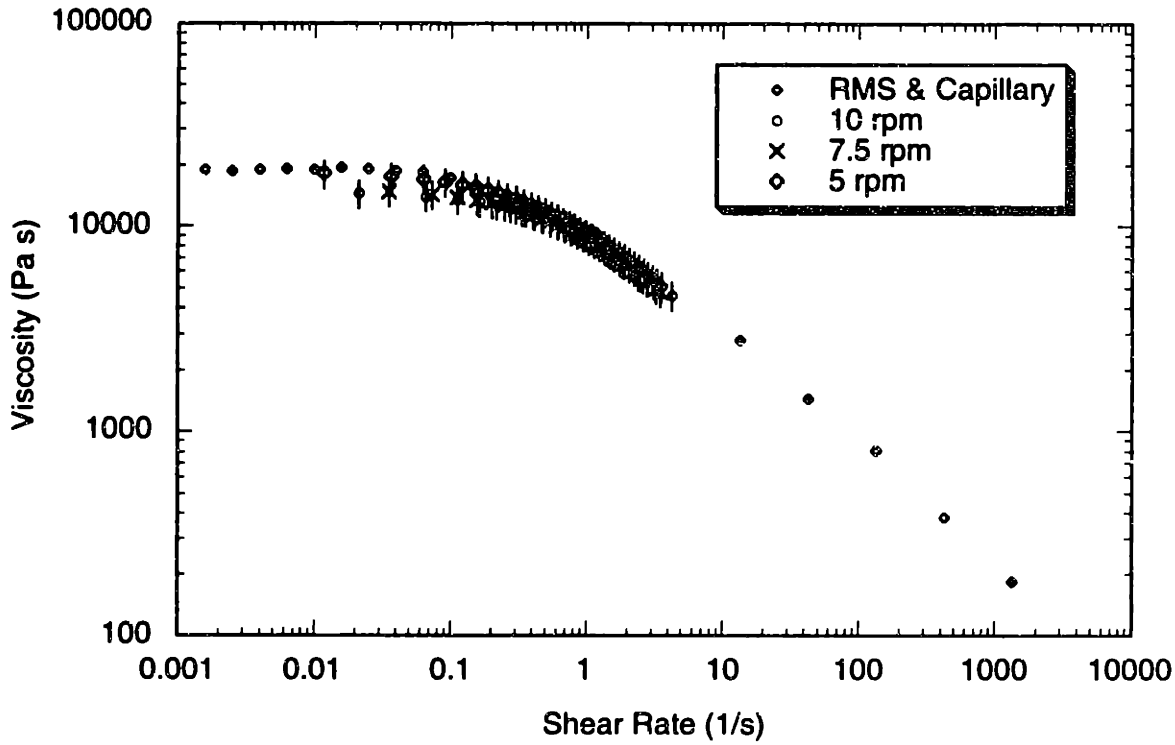

Figure 4.27: Viscosity calculated from the optical method at 160°C from different flow rates compared to the data obtained by parallel-plate rheometry and capillary viscometry.

velocity profile at the low shear rates. This resolution of LDV would have been increased if the dimensions of the channel gap were to increase while keeping the width-to-gap ratio constant. Another way to increase the accuracy of this technique is to increase the magnitude of the centerline velocity. This is because the signal-to-noise ratio of the velocity measurement from LDV increases with velocity, so the resolution around the centerline should be higher at higher flow rates.

The viscosity measurement at other temperatures are shown in figures 4.28 and 4.29. One can see at 170°C the predictions at low shear rates (< 10%) were more accurate than the ones at high shear rates (< 25%). At 150°C the difference was less than 18% throughout. Considering the data at these two temperatures, the overall percentage difference between the optical and the standard mechanical methods should be about 25%. One should note that the parallel plate geometry data have an accuracy of 7.5% at the shear rates ranging from 0.001 s^{-1} to 0.15 s^{-1}, and an unknown accuracy beyond that shear rate. Therefore, one can only establish the accuracy of this optical system relatively to another system with a 7.5% accuracy at low shear rates.

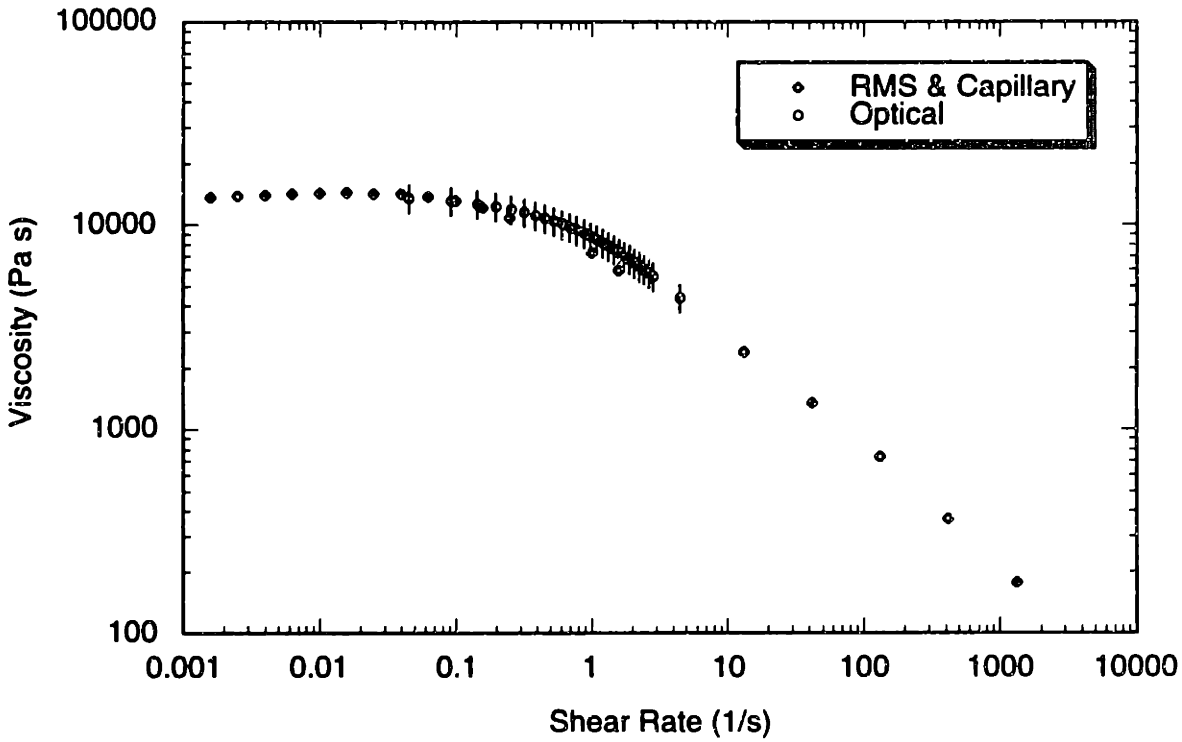

Figure 4.28: Viscosity calculated from the optical method at 170°C and 10p rpm compared to the data obtained by parallel-plate rheometry and capillary viscometry.

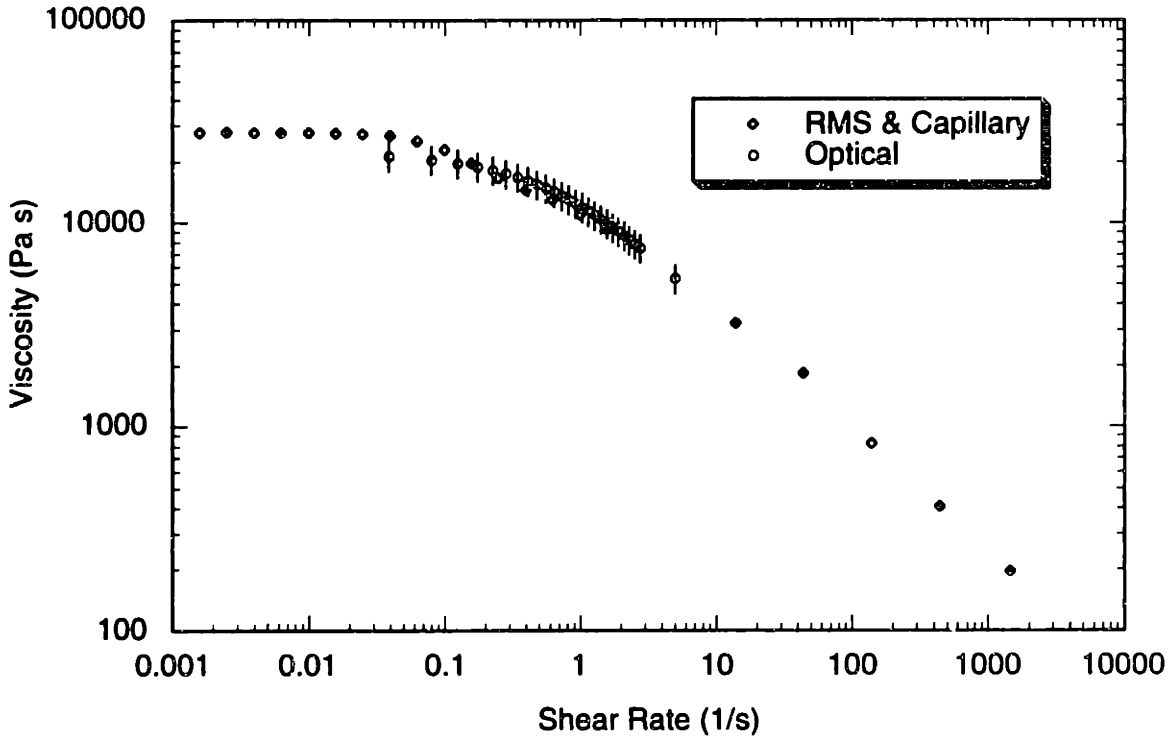

Figure 4.29: Viscosity calculated from the optical method at 150°C and 10 rpm compared to the data obtained by parallel-plate rheometry and capillary viscometry.

4.3 Birefringence and Extinction Angle Measurements of LDPE

The literature review in Chapter 2 shows how full-field and point-wise birefringence methods have been used in studying the stress fields of polymer melts and solutions. This section discusses the results of a point-wise birefringence study on LDPE melt flowing inside a slit channel and how the data are interpreted. Specifically, an algorithm developed to account for the finite beam size is described. In Section 4.3.1 the accuracy of the system is quantified with standard wave-plates and fluids of known properties. Section 4.3.2 summaries the results obtained by using a crossed-polarizer configuration without beam modulation. The results obtained using a modulated beam follow in Section 4.3.3. The effects of the top and bottom observing windows on the optical data are described in Section 4.3.4. As mentioned before, the finite diameter of the beam distorted the results. Section 4.3.5 details an algorithm to recover the data. The stress-optical coefficient of LDPE at 160°C is determined in Section 4.3.6. Finally, the first normal stress coefficients predicted by the optical method are compared to those obtained from parallel plate rheometry in Section 4.3.7.

4.3.1 Calibration

The point-wise, phase-modulated birefringence system used in this study was calibrated with air and two wave-plates of known retardation. These two wave-plate retarded red (λ = 632.8 nm) and green (λ = 514.5 nm) light by 90 degrees, respectively.

To calibrate the system with air as the sample, the optical elements were oriented a little differently than the normal configuration. Specifically, the polarizer and the analyzer were oriented 90 degrees from each other. The resultant light intensity I(t) can be calculated from the following Mueller matrices:

$$\begin{bmatrix} I(t) \\ \cdot \\ \cdot \\ \cdot \end{bmatrix} = \left[M_A(0°)\right] \cdot \left[M_{PEM}(A\sin(\omega t), 45°)\right] \cdot \left[M_P(90°)\right] \cdot \begin{bmatrix} I_0 \\ 0 \\ 0 \\ 0 \end{bmatrix} \tag{4.7}$$

$$I(t) = I_{dc} + I_{2\omega}\cos 2\omega t + \ldots \tag{4.8}$$

$$I(t) = \frac{I_0}{4}[1 - J_0(A)] + \frac{J_2}{2}(A) I_0 \cos 2\omega t + \ldots \tag{4.9}$$

The Bessel function $J_2(A)$ was measured and compared with the theoretical value. When A = 2.4058, $J_0(A) = 0$ and $J_2(A) = 0.43170$ in theory. In practice, an experimental $J_2(A)$ is determined by measuring this quantity:

$$\frac{I_{2\omega}}{2 \cdot I_{dc}} \tag{4.10}$$

The deviation of this quantity from the theoretical $J_2(A)$ served to indicate how well the system was aligned optically and calibrated electronically. This experimental quantity was measured before each experiment and was consistently found to be about 2% lower than the theoretical value of 0.43170. A similar procedure using an extra quarter wave-plate for red light was carried out before every experiment to determine the deviation of another constant $J_1(A)$ from the theoretical value. This experimentally obtained $J_1(A)$ was consistently larger than the theoretical value of 0.51907 by less than 1.5%. Some researchers (Galante, 1991; Frattini and Fuller, 1984) have used these experimentally determined $J_1(A)$ and $J_2(A)$ in the equations to calculate the ratios Rω and R2ω instead of using the theoretical values. In this study the theoretical values were always used because they were not sufficiently different from the theoretical ones.

The system was then calibrated by measuring the retardance and the extinction angle of two quarter wave-plates at different orientations. This time the first and second polarizers were 45° with respect to each other. This was the normal configuration for optical measurement as described in detail in Section 3.4. Because the red quarter wave-plate retarded the red light by 90 degrees and a red laser light was used in this system, the measured retardance should always be 90 degrees. The measured extinction angle should correspond to the angle between the axes of the wave-plate and that of the incident polarizer.

Figure 4.30 shows a comparison of the ideal retardance and extinction angle values with those measured by the system. On average, the system measured a retardance of 88.93° ± 4.83°. The measured extinction angles deviated from the ideal value by ± 0.52°, which was equal to one standard deviation of the differences between the ideal and the observed extinction angles at different orientations of the wave-plate. The measured retardance was between 160° and 170° for orientation angles of 45°, 135°, 225°, and 315°. All these angles corresponded to an extinction angle of 45°. This phenomenon was caused by the high sensitivity to noise in the equations used to calculate the retardance and the extinction angle. Recall from Section 3.4 that the retardance δ and extinction angle χ are related to the experimentally observable $R\omega$ and $R2\omega$ through these equations:

$$R\omega = \frac{I_\omega(\delta, \chi)}{I_{dc} J_1(A)} = \sin\delta\cos 2\chi \tag{4.11}$$

$$R2\omega = \frac{I_{2\omega}(\delta, \chi)}{I_{dc} J_2(A)} = (1 - \cos\delta)\sin 2\chi\delta\cos 2\chi \tag{4.12}$$

$$\cos\delta = \frac{-R2\omega^2 \pm R\omega^2\sqrt{(1 - R\omega^2 - R2\omega^2)}}{R\omega^2 + R2\omega^2} \tag{4.13}$$

$$\cos(2\chi) = \frac{R\omega}{\sin\delta} \tag{4.14}$$

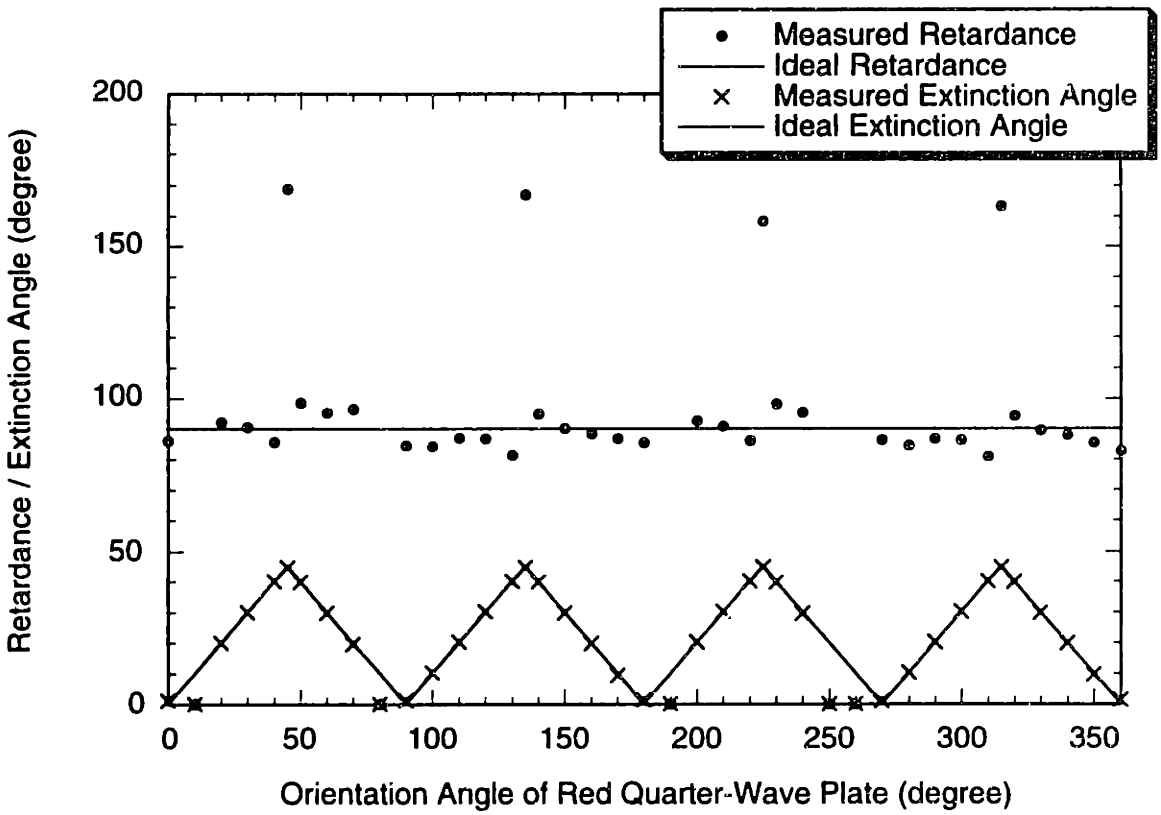

Figure 4.30: Retardance and extinction angle of a red quarter wave plate measured by the phase-modulated birefringence system. The retardance for a perfect red quarter wave plate is 90°. The axis of retardance of the wave plate is rotated from 0° to 360°. The measured extinction angle is the reduced angle ($|\chi| \leq 45°$) between the optical axis of the apparatus and the retardance axis of the wave plate.

When the extinction angle $\chi = 45°$, both Rω and R2ω became zero. As a result, cos δ in Equation 4.14 approached 0/0, and the retardance became indeterminate at this special angle. Similar problems with large uncertainties in data when Rω and R2ω are small have been reported by other researchers (Zhang et al., 1994; Larson et al., 1988). At this point the only solution is either to repeat the measurement with the entire optical train rotated by a known angle (Zhang et al., 1994), or to use different wavelengths of light (Hongladarom et al., 1993).

Noise in the signal transfer and data acquisition routine also presented a problem for the data analysis. One example is shown on the same figure at orientation angles of 10°, 80°, 190°, and 260°. These four wave-plate positions corresponded to two specific orientation angles of the wave-plate axis: 10° and 80°. The origin of this problem was that the noise in the system was large enough to make the experimentally measured value of $(R\omega^2+R2\omega^2)$ bigger than unity even though this quantity should theoretically be exactly unity. Under this condition the square root term in Equation 4.13 $\sqrt{1 - R_{\omega}^2 - R_{2\omega}^2}$ became imaginary, and the equations were unsolvable. The remedy for this situation was to install filters to reduce the noise or to run the experiment with the entire optical system rotated by a known angle. This problem will be prominent only if the retardance is exactly equal to 90°, because only under this condition will $(R\omega^2+R2\omega^2)$ be close to 1 and $\sqrt{1 - R_{\omega}^2 - R_{2\omega}^2}$ be close to being imaginary (Equations 4.11 - 4.13). To prove this assertion a green quarter wave-plate was used to calibrate the system.

The retardance of a green quarter wave-plate was 90° for green light, but 64.9° for red light (Recall $\lambda_{red}/\lambda_{green}$ = 632.8 nm/ 514.5 nm = 90°/64.9°). Figure 4.31 compares the ideal and observed retardance and extinction angle. As seen with the red quarter wave-plate, the retardance was about 160° when the extinction angle is 45°. This phenomenon was again due to the high sensitivity of Rω and R2ω when they are close to zero. The

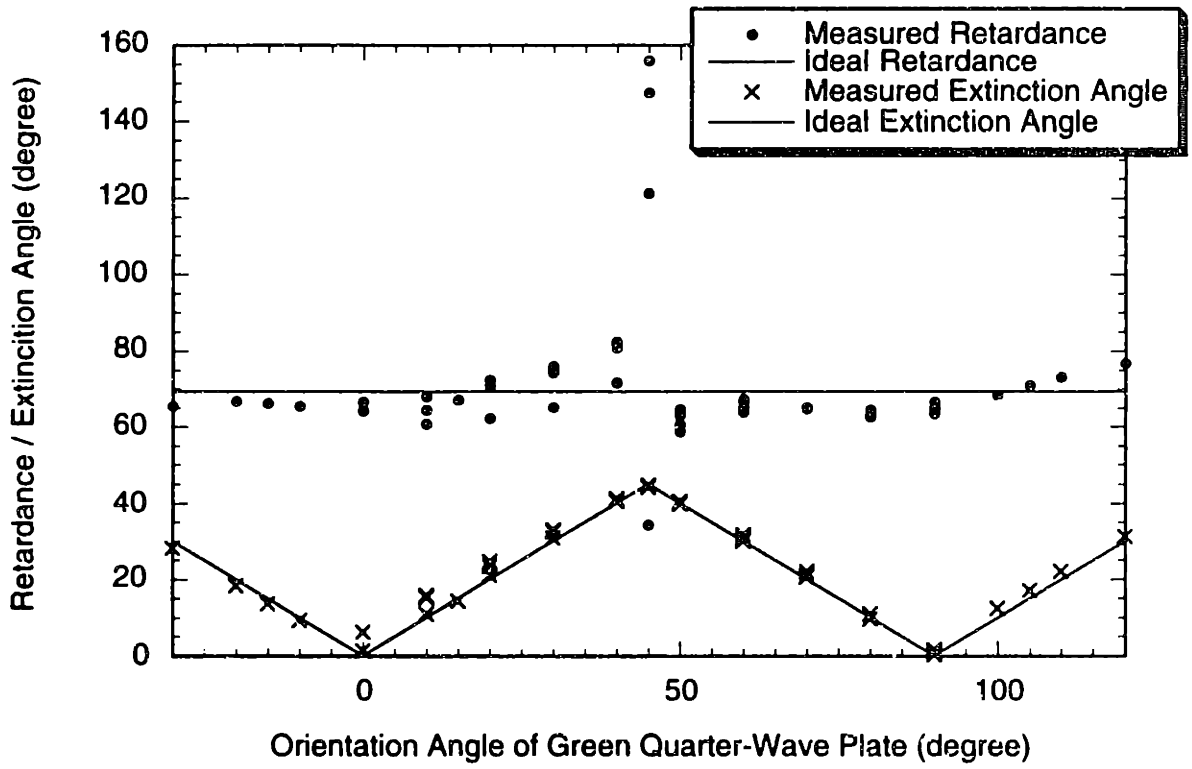

Figure 4.31: Retardance and extinction angle of a green quarter wave plate measured by the phase-modulated birefringence system. The retardance for a perfect green quarter wave plate is 69.4°. The axis of retardance of the wave plate is rotated from 0° to 360°. The measured extinction angle is the reduced angle ($|\chi| \leq 45°$) between the optical axis of the apparatus and the retardance axis of the wave plate.

problem of $R\omega^2+R2\omega^2$ being too close to unity is no longer observed. The measured retardance was 67.82° ± 5.70° on average. The measured extinction angle differed from the ideal case by ± 1.21°. Combining with the previous results, the error in the retardance measurement is about ± 6° and that in the extinction angle measurement is ± 1.2°.

The birefringence apparatus was used to measure the stress-optical coefficients of highly elastic poly(isobutylene) PIB and almost Newtonian poly(butene) PB with a Couette flow cell. The reason for carrying out this experiment was to compare the stress-optical coefficients of PIB and PB measured using this system to those measured using another system, namely a two-color non-modulated system. The details of this two-color birefringence system can be found in Quinzani's thesis (Quinzani, 1991). The procedure to measure the stress optical coefficients is outlined as follows. A 0.30wt% solution of PIB ($\overline{M_w}$ = 2 x 10^6 g/mol) in PB ($\overline{M_n}$ = 1.3 x 10^3 g/mol) was made and carefully poured into a Couette flow cell. The detailed description of how to make this solution can be found in Genieser's thesis (Genieser, 1997). The viscometric properties of this solution, namely the viscosity and the first normal stress coefficient, were previously characterized as functions of shear rate and temperature. This Couette flow cell consisted of two concentric cylinders. The inner one was connected to a motor while the outer one was fixed in position. The radius of the inner cylinder was 16 cm and the axial length was 8 cm. The flow cell gap width was 1.9% of the inner cylinder radius, so that the flow kinematics could be approximated by that of a planar shear flow. The design of the flow cell is detailed by Quinzani (Quinzani, 1991). By rotating the inner cylinder of the Couette cell at a fixed rate, the solution was sheared at a uniform shear rate throughout the gap given by $\dot{\gamma} = \frac{\Omega R_1}{(R_2 - R_1)}$, where Ω is the angular velocity of the rotating cylinder, R_1 and R_2 are the radii of the inner and outer cylinder respectively. A shear stress was exerted by both of the components in the solution, and a normal stress was only exerted by the non-Newtonian

component PIB. According to Fuller (1995), the stress of a mixture of two components is equal to the sum of stresses resulted from each individual component. Assuming that the stress-optical coefficients of the individual components do not change after blending, the stress-optical laws for this solution can be written as:

$$\Delta n \cos(2\chi) = C_{PIB} \cdot N_{1PIB} \tag{4.15}$$

$$0.5\Delta n \sin(2\chi) = C_{PB} \cdot \tau_{PB} + C_{PIB} \cdot \tau_{PIB} \tag{4.16}$$

where C_{PB} and C_{PIB} are the stress-optical coefficients of PB and PIB respectively. C_{PIB} was first computed by using Equation 4.15. $N_{1\ PIB}$ was the first normal stress difference of PIB defined by product of $\Psi_{1\ PIB}$ and the square of the shear rate $\dot{\gamma}$. At each rotation speed the shear rate, first normal stress difference, the birefringence, and the extinction angle were recorded. Figure 4.32 shows a plot of $\Delta n \cos(2\chi)$ versus $N_{1\ PIB}$. The slope of the straight line fit equaled C_{PIB} and was found to be $1.43 \times 10^{-9} \pm 10^{-9}$ Pa^{-1}. This number is 3.2% lower than that measured by the two-color birefringence system, which measured $C_{PIB} = 1.48 \times 10^{-9} \pm 0.18 \times 10^{-9}$ Pa^{-1} (Genieser, 1997).

The stress-optical coefficient of PB, C_{PB}, was calculated by using Equation 1.16. The shear stresses on the right-side of this equation were computed from the shear rate and viscosity data previously determined. Plotting $\{0.5\ \Delta n \sin(2\chi) - C_{PIB}\ \tau_{PIB}\}$ versus τ_{PB} shows a zero-intercept straight line with slope equal to $1.07 \times 10^{-9} \pm 10^{-9}$ Pa^{-1} (Figure 4.33). This value is 9% higher than that measured by the two-color birefringence device, which yielded $C_{PB} = 0.98 \times 10^{-9} \pm 0.07 \times 10^{-9}$ Pa^{-1}. There are no other data that the author is aware of for direct comparison of C_{PB} and C_{PIB} in the literature.

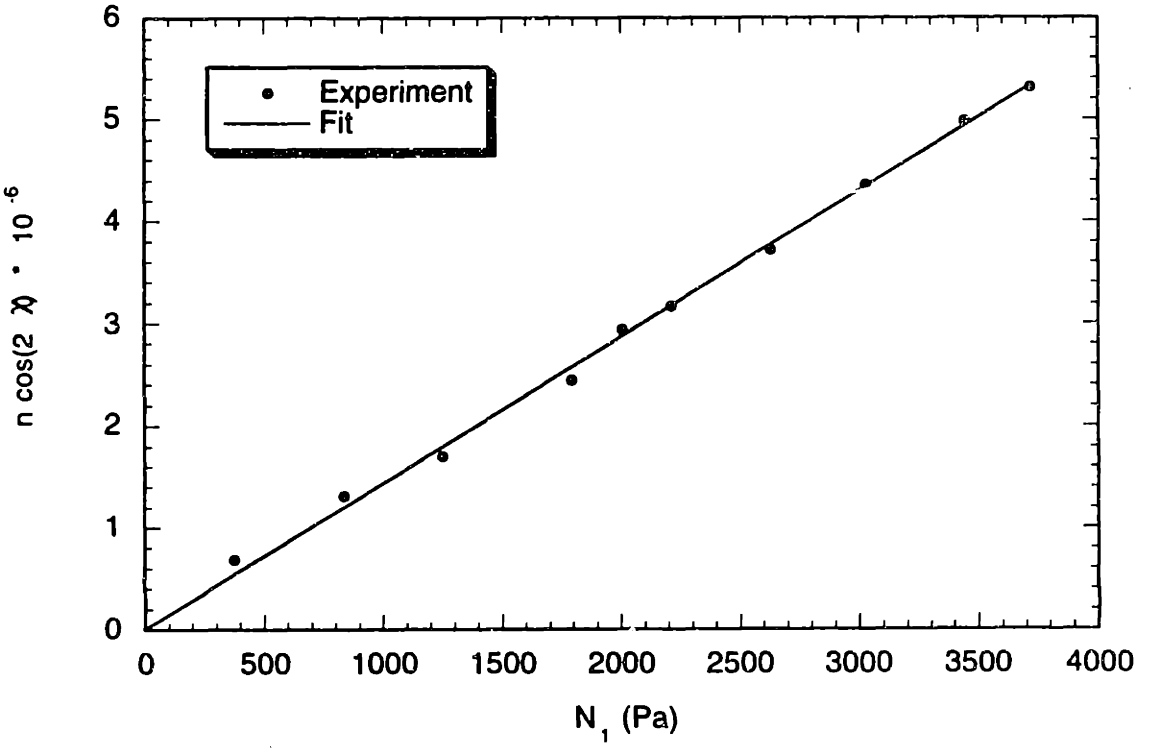

Figure 4.32: The slope of this graph represents the stress-optical coefficient of polyisobutylene PB. The straight line fit with zero intercept yields $C_{PIB} = 1.43 \times 10^{-9} \pm 10^{-9}$ Pa^{-1} ($R^2 = 0.99692$).

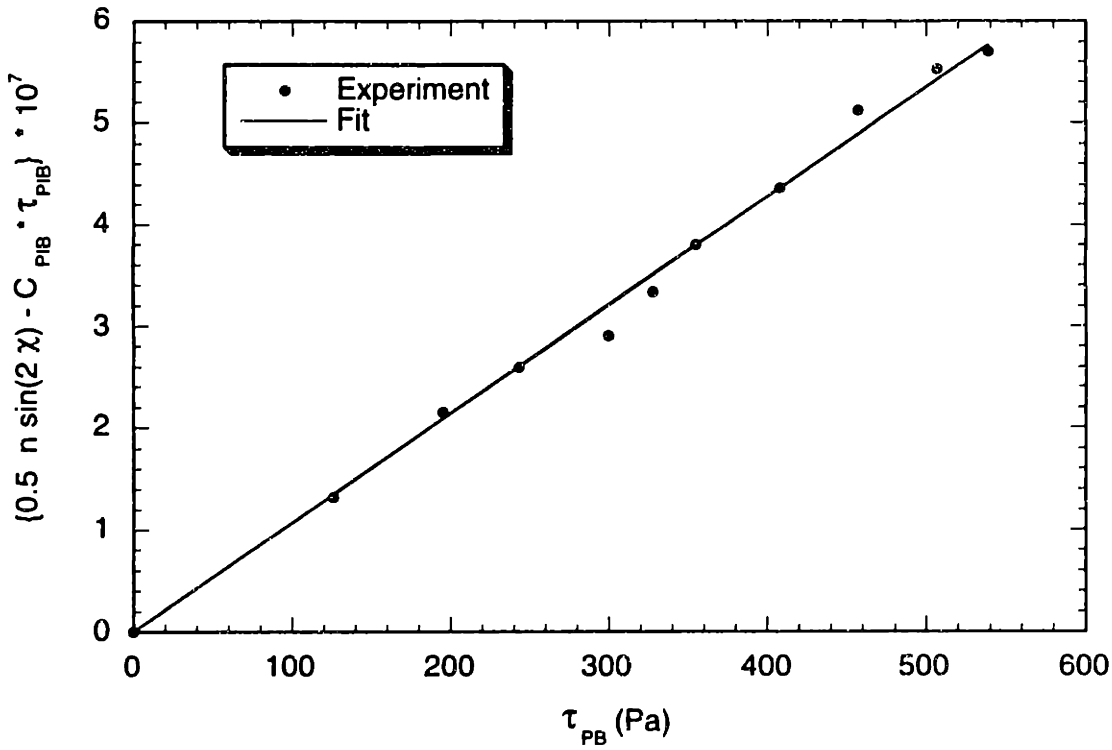

Figure 4.33: The slope of this graph represents the stress-optical coefficient of polybutene PB. The straight line fit with zero intercept yields $C_{PB} = 1.07 \times 10^{-9} \pm 10^{-9}$ Pa^{-1} (R^2 = 0.99407).

4.3.2 Results with Crossed Polarizers

Placement of a flow cell between crossed polarizers is a popular optical configuration for birefringence studies. In fact, all the full-field birefringence studies were done with this configuration. In the ideal case, isochromatics identify contours of constant retardance, and isoclinics show contours of constant extinction angle. The light intensity depends on the local retardance and extinction angle:

$$I = \frac{I_0}{4}\sin^2\left(\frac{\delta}{2}\right)\sin^2(2(\chi-\alpha)) \tag{4.17}$$

where I_0 and I are the light intensity before and after passing the optical elements, δ is the retardance, χ is the extinction angle with respect to the flow, and α is the orientation angle of the optical system with respect to the flow direction.

Researchers (Wales, 1976; McHugh et al., 1987) have reported that while the isochromatics were clearly observed in a full-field cross-polarizers configuration in a slit channel, the isoclinics were difficult to locate. This is because the isoclinic was observed as a thick dark band which could cover as much as half the flow field as the polarizer-analyzer pair were rotated together, instead of a fine dark line. Thus the precise location of the dark band could not be assigned easily. McHugh et al. (1987) explained that the finite width of the isoclinics came from the variation of τ_{yx} along the optical path. From their results of finite element simulations they noted that "there was a range of x_2 values (along the velocity gradient direction) over which a given stress level and associated ellipsoid orientation would occur" (McHugh et al., 1987). They further suggested that the inside edge of the isoclinic band should be used to locate the position of the constant extinction angle contour because their simulation showed that the inside edge of the band corresponded to a

stress level reached by over 80% of the flow field. The 20% of the optical path close to the observing windows were responsible for almost all of the outward spread in the band. However, Galante and Frattini (1991) showed that for an idealized one-dimensional slit flow with the upper-convected Maxwell model, the extinction angle profile changed only by 7 degrees from midway between the centerline and the wall to the wall for We > 3.0. Therefore, a broad isoclinic band should be expected. We is the Weissenberg number defined by $We = \tau \cdot \left\{ \frac{B}{\eta} \left(-\frac{dP}{dx_1} \right) \right\}$, where B is the channel half-width.

In this study, instead of illuminating the entire flow field at once, the laser beam scanned across the gap in order to identify more quantitatively the locations of the fringes. From Equation 4.17, the intensity minimum corresponds either to δ being equal to 0°, 360°, 720°,... or χ being equal to α. In slit flow the orientation angles of the molecules seldom reach zero but decrease from 45° along the centerline to a non-zero angle at the walls. Therefore, the local minima along the gap width can be attributed to the occurrence of δ = 0°, 360°, 720°,.... The top diagram in Figure 4.34 shows the intensity pattern across the gap. The positions of the relative high and low intensity precisely locate the bright and dark fringes. These fringes correspond to the isochromatics. The pattern became difficult to interpret when the isoclinics were sought by rotating the polarizer-analyzer pair. The lower diagram of Figure 4.34 shows the light intensity profile when the optical system was rotated. The reduced intensity on the left side of the channel corresponded to the dark isoclinic band observed by the other researchers. Even though the isochromatics were still observed, their positions were shifted. The rules developed by McHugh et al. are not applicable in this case. The bottom figure shows an intensity maximum at the centerline, which is incorrect because the retardance at the centerline should be zero. Therefore, one should locate the isochromatics from the intensity pattern when the optical axis is aligned with the flow.

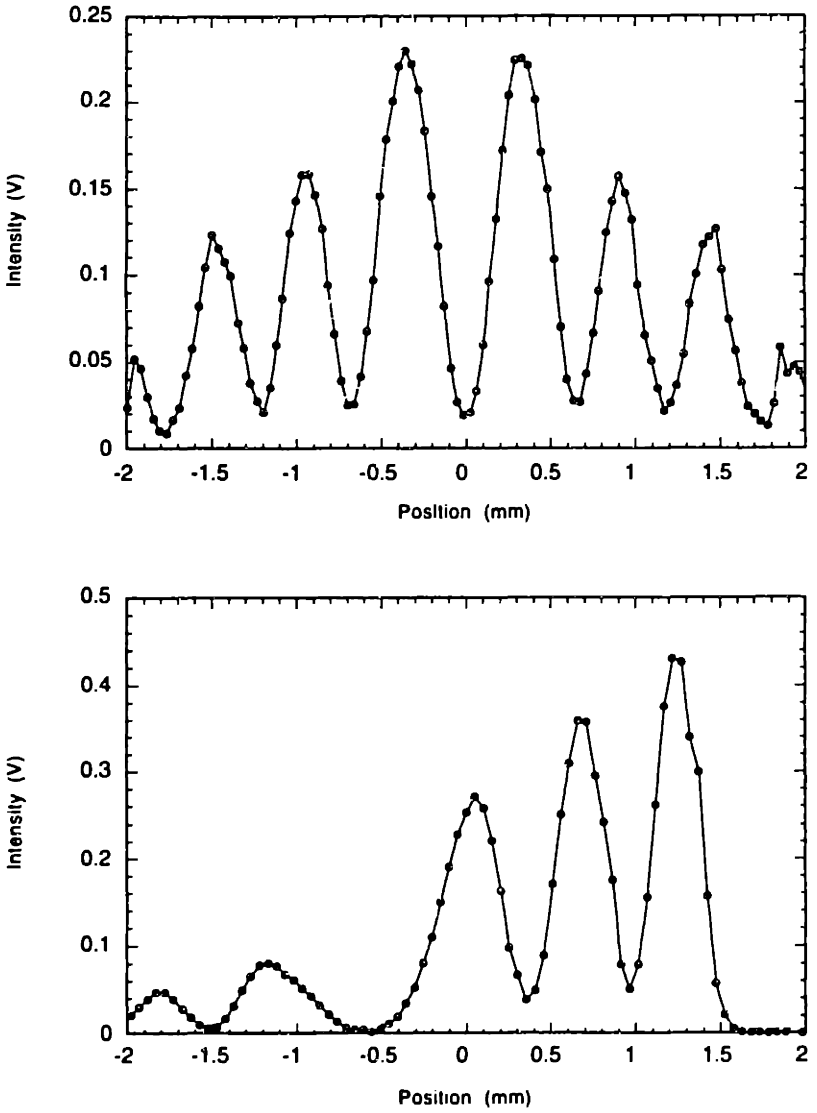

Figure 4.34: Top diagram: optical system aligned with respect to the flow direction. Bottom diagram: optical system oriented at 30° with respect to the flow direction.

The intensity profiles across the gap were measured at different screw speeds, ranging from 0.5 rpm to 20 rpm (Figures 4.35 and 4.36). These screw speeds corresponded to a flow rate range from 0.020 g/s to 0.57 g/s. Each local minimum indicated an isochromatic line. The number of fringes increased with increasing screw speed. Starting from 2 rpm, the intensity at the minima were no longer zero. Instead, the baseline intensity shifted upwards as flow rate increased. This was not because the retardance never reached a multiple of 360° anywhere, but because the intensity within the area covered by the beam cross-section varied locally. The effect of the finite beam size on point-wise birefringence measurement will be discussed in detail in Section 4.3.5 of this chapter.

One also notices the tapering of intensity from the centerline to the walls. This trend can be explained by the decreasing extinction angle profile from the centerline to the walls. The intensity patterns were symmetric about the centerline because both the retardance and extinction angle profiles were symmetric. This symmetric pattern was observed at all the speeds except 20 rpm. At this speed, the slight asymmetry might be due to the fluctuation of incident laser power over time and the insufficient number of data points to fully resolve the pattern.

Each of the local minimum was assigned a retardance value (0° for centerline, 360° for the first pair from centerline, etc.). The retardance profiles obtained from all these cases are shown on Figure 4.37. The maximum retardance achieved at the wall increased with increasing flow rate, but the rate of increase seemed to decrease with increasing flow rate. This is because retardance is proportional to birefringence, which is proportional to the difference in the principal values of the stress tensor according to the stress-optical law. However, as shown in Figure 1.15 in this thesis, the wall shear stress increased with flow rate but the rate of increase tapered off at higher flow rates as expected for a shear-thinning

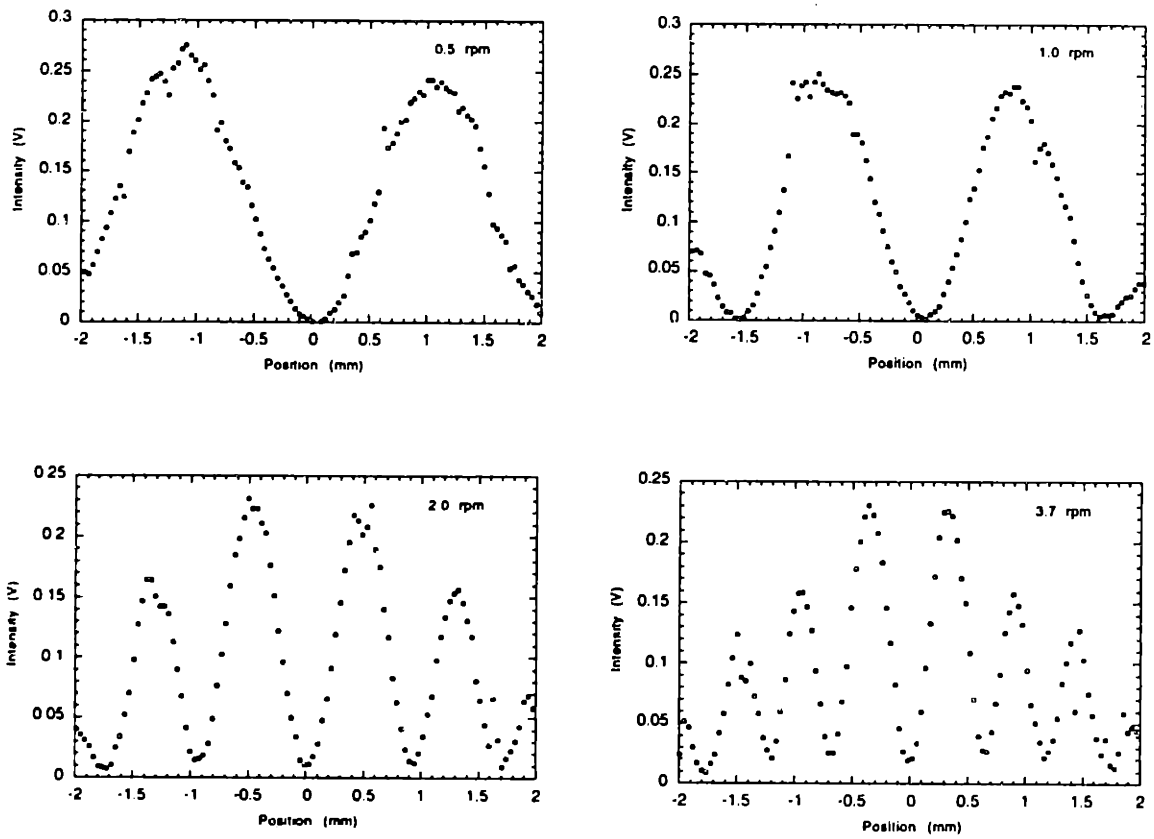

Figure 4.35: Intensity profiles across the channel width at 0.5 rpm to 3.7 rpm between two crossed polarizers. The error bars are within the symbols.

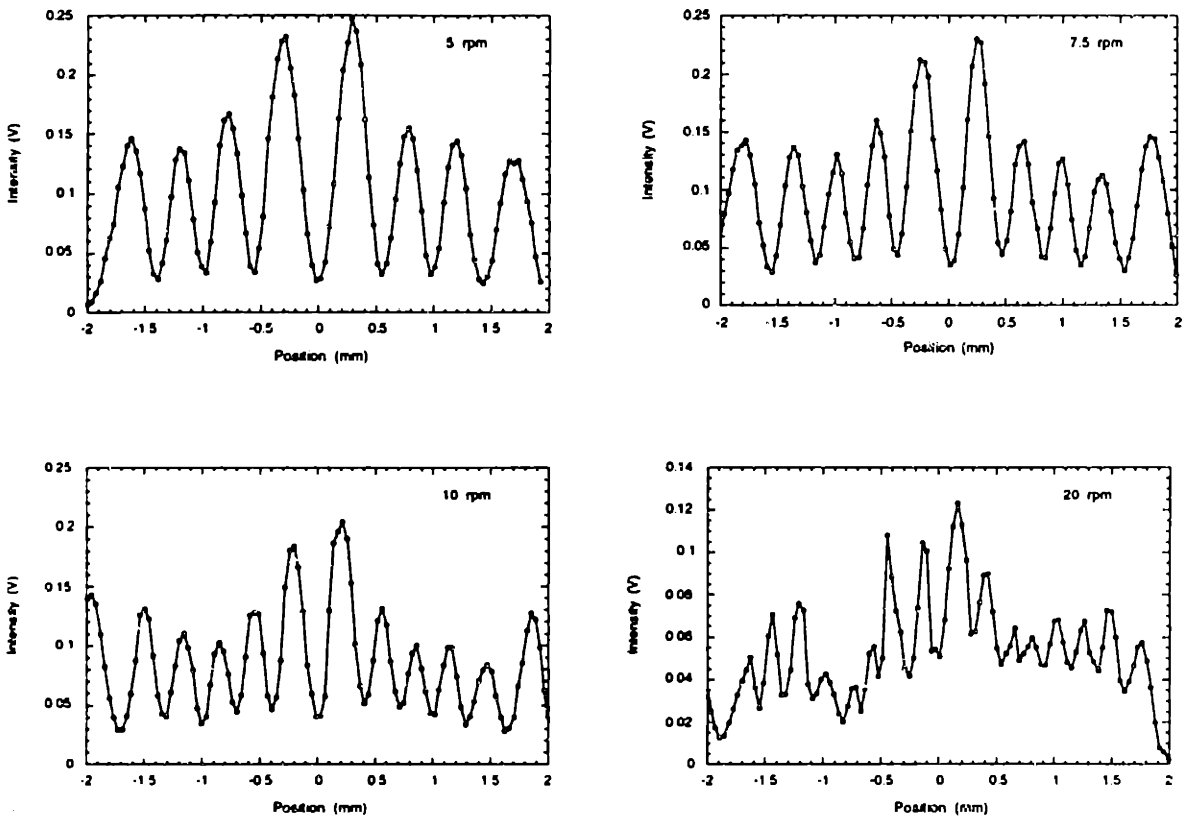

Figure 4.36: Intensity profiles across the channel width at 5 rpm to 20 rpm between two crossed polarizers. The error bars are within the symbols.

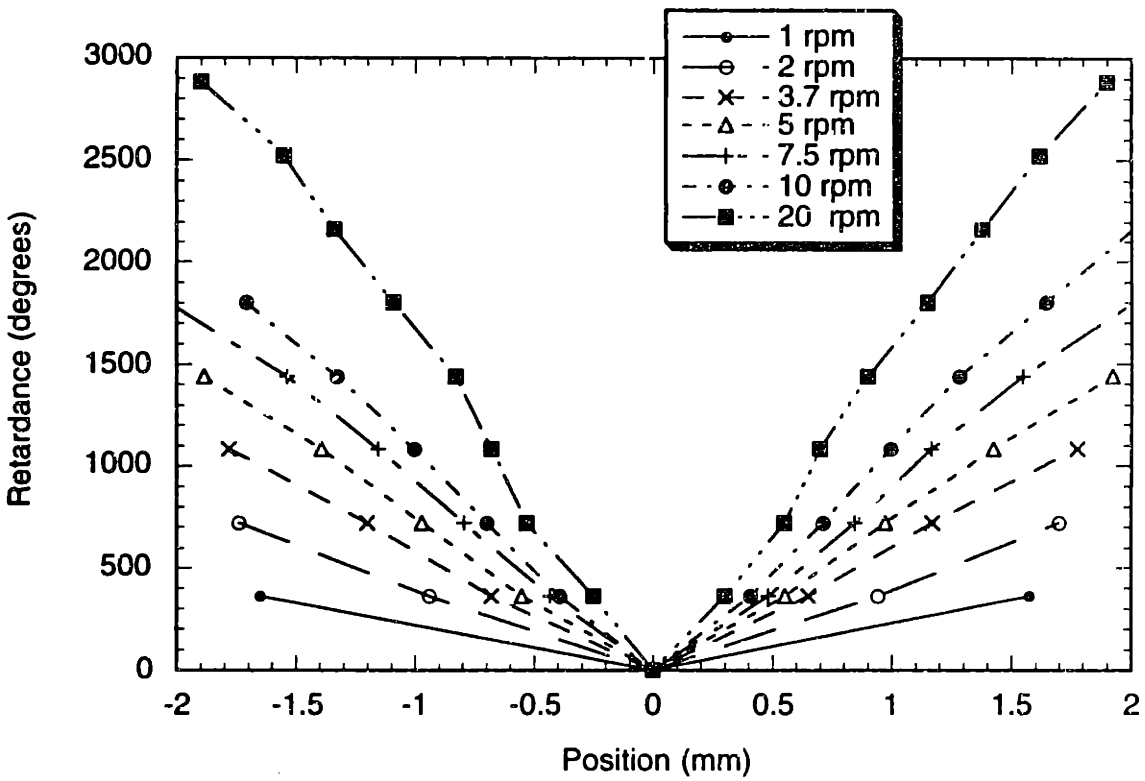

Figure 4.37: Retardance profiles across the channel width. Data points are computed from the local minima on each intensity profile (Figures 4.35 & 4.36). The straight line segments connect the data points.

fluid. Therefore, rate of increase in the stress and the retardance both tapered off as the flow rate was increased.

4.3.3 Results with Modulated Light Beam

As explained in Chapter 2 of this thesis, the disadvantage of using an non-modulated light source is that two unknowns, the retardance and the extinction angle, have to be calculated from one number, the light intensity. Rotating the polarizer-analyzer pair provides a means to measure the extinction angle contour in theory. In practice, the thick isoclinic band makes the data difficult to interpret. Moreover, a non-modulated system in general does not allow real time measurement of two variables, unless more than one color is used at the same time, such as the two-color birefringence system developed by Chow and Fuller (1980). The concept of frequency modulation has been popular in solving problems in the field of electrical engineering for decades. By modulating the light at a known frequency, more than one unknown can be calculated from the Fourier transform of the signal, provided that the variables of interest do not change faster than the modulation frequency.

The retardance profiles measured by the phase-modulated birefringence system at increasing screw speeds are shown in Figures 4.38 and 4.39. This point-wise measurement technique does not require scanning the entire profile to calculate the retardance at each point. On each graph the retardance profile is compared with that obtained from the cross-polarizer experiment at the corresponding screw speed except for the case of 0.5 rpm. In that case the highest retardance was smaller than 360°. For all the plots except the one at 20 rpm, the retardance measured by both methods were in good agreement. One may note that the error bars of 6° retardance became increasingly insignificant as the retardance level increased with screw speed. At 20 rpm the retardance profiles obtained by the two

method did not match perfectly. This was probably due to the resolution limit of the system in resolving large changes within the finite size of the beam cross-sectional area.

It is interesting to observe that the gaps in the retardance profiles all occur at retardance levels of 360° or its multiples. Moreover, the data in the vicinity of these gaps seem to be "out of line" with the rest of the data. The data provided by the non-modulated crossed polarizer method compliment the current profiles by filling in the gaps at retardance levels of 360° and its multiples. Why are there gaps in the data? As discussed in the literature review chapter of this thesis, researchers have reported gaps in the retardance measured by a phase-modulated system and attributed the gaps to the unreliable data resulting from the high sensitivity to noise at those retardance levels. Recall that for most phase-modulated systems the retardance is calculated from an expressions with $R\omega^2+R2\omega^2$ in the denominator. As the retardance approaches multiples of 360°, both $R\omega$ and $R2\omega$ approach zero.

The extinction angle ideally should decrease monotonically from 45° at the centerline to a number smaller than 45° at the wall. This is because the molecular alignment with respect to the flow direction increases as the shear rate increases toward the walls. Figures 4.40 and 4.41 show the extinction angle profiles from 0.5 rpm to 20 rpm. The plot at 0.5 rpm shows the shape of an expected profile because the extinction angle drops monotonically from the centerline to the walls. Extinction angles were negative on the left side of the channel because the angle between the molecular orientation and the optical axis became negative as the beam traversed across the centerline. The measured extinction angles did not attain the ideal value of 45° because as the beam cross-sectional area straddled both the left and right-hand side of the channel, the effective extinction angle averaged to become zero. Therefore, in all the profiles, the experimentally measured value of the extinction angle was zero at the centerline.

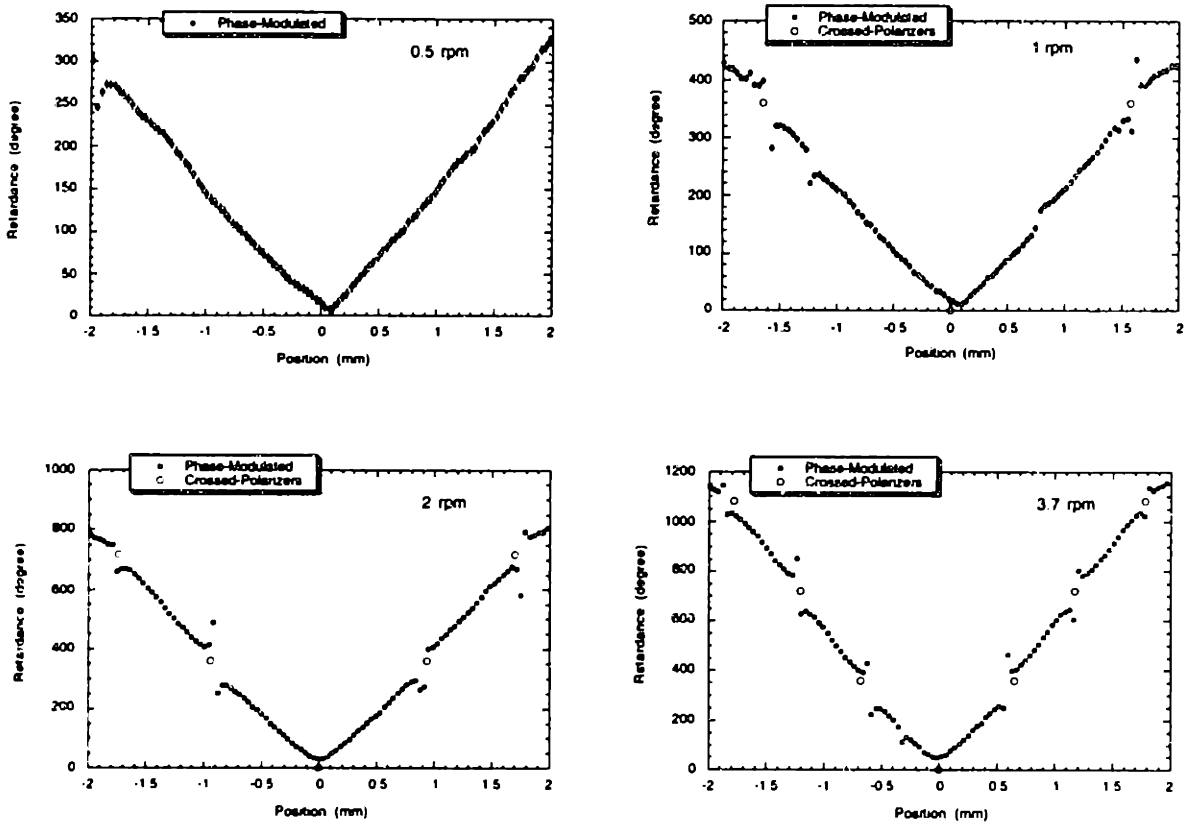

Figure 4.38: Retardance profiles across the width of the channel at screw speeds of 0.5 rpm to 3.7 rpm. The retardance results computed from crossed polarizers and the phase-modulated systems are compared on the same graph. The error bars are $\pm$ 6°.

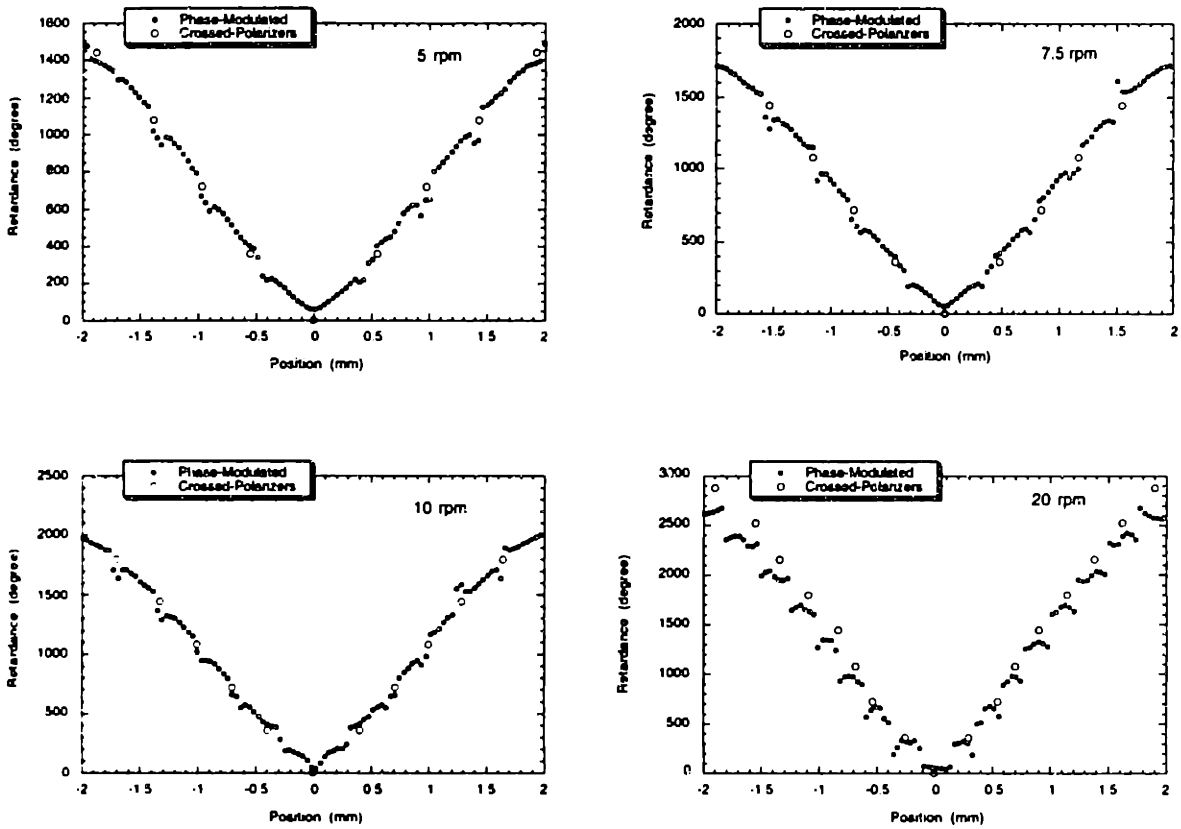

Figure 4.39: Retardance profiles across the width of the channel at screw speeds of 5 rpm to 20 rpm. The retardance results computed from crossed polarizers and the phase-modulated systems are compared on the same graph. The error bars are $\pm$ 6°.

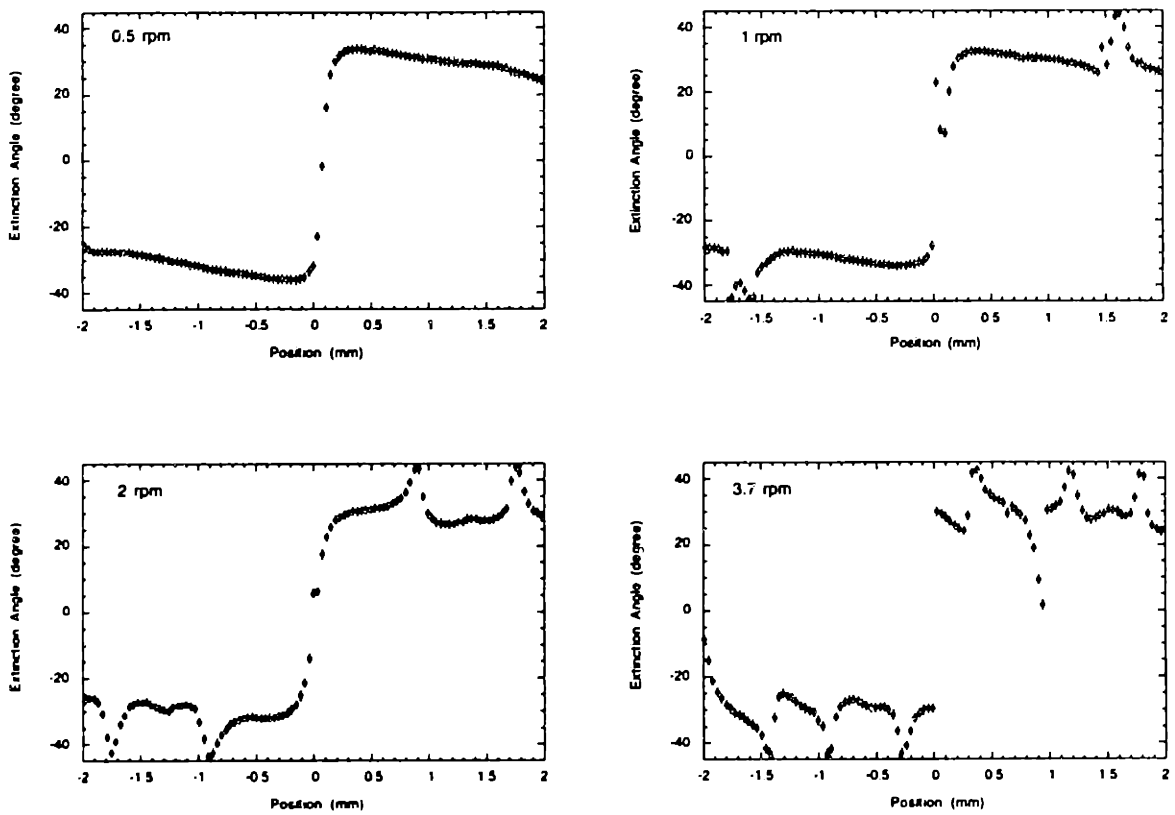

Figure 4.40: Extinction angle profiles across the channel width at screw speeds of 0.5 rpm to 3.7 rpm. The $\pm$ 1.2° error bars are insignificant compared to the size of the spikes.

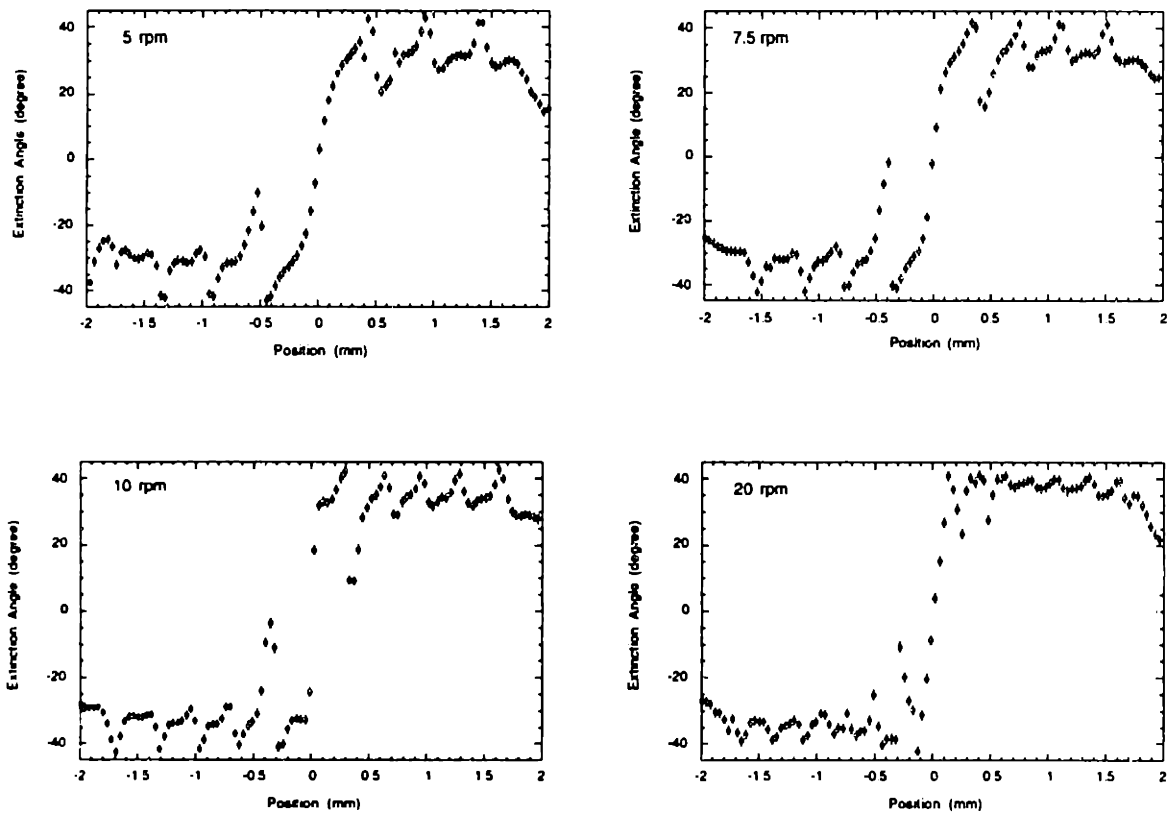

Figure 4.41: Extinction angle profiles across the channel width at screw speeds of 5 rpm to 20 rpm. The $\pm$ 1.2° error bars are insignificant compared to the size of the spikes.

The extinction angle profiles contain a number of unexpected features which cannot be explained satisfactorily by the error bars of $\pm$ 1.2°. One of them is the presence of various spikes observed at the same locations as the gaps in the retardance profile. The spikes increased in number toward higher flow rates. In addition to the presence of the spikes, the measured extinction angle at other positions did not tend to decrease toward the wall at extruder screw speeds higher than 1 rpm. These observations are inconsistent with the monotonically decreasing behavior one would expect. Both of these features can be explained by considering the effects of the observing windows on the flow field and the effects of the finite beam cross-sectional area on the raw data $R\omega$ and $R2\omega$. These two effects are explained in the following sections.

4.3.4 The Effects of the Observing Windows

In this study a two-dimensional pressure-driven flow between two infinitely large parallel walls is approximated by the slit channel with 10:1 aspect ratio. This ratio was chosen based on Wales' experiment (1976). He found that the birefringence in the 1-3 (flow-neutral) direction $\langle n_{11}-n_{33}\rangle$ did not change with the width-to-gap ratio of the channel when this ratio was larger than 10:1. Researchers since then have followed this guideline when designing slit channels and have mostly ignored the effects caused by the two end walls normal to the neutral direction (Baaijens, 1994; Quinzani, 1991; Davidson et al., 1994).

Azzam (1978) described a method to calculate the polarization state of light through an inhomogeneous medium. The effect of a medium on the polarization state of a light beam which passes through that medium can be calculated by the following equation. The Stokes vector S(z) that represents the new state of polarization at position z is equal to $\mathbf{M}_z$ times the initial Stokes vector S(0) at z=0:

$$S(z) = M_z \cdot S(0) \tag{4.18}$$

The Mueller matrix $\mathbf{M}_z$ describes the influence of a medium of thickness z on the polarization state of light. The Mueller matrix for a medium with constant retardance δ and extinction angle χ over the entire thickness is:

$$\begin{bmatrix} 1 & 0 & 0 & 0 \\ 0 & \cos^2(2\chi) + \sin^2(2\chi)\cos\delta & \cos 2\chi \sin 2\chi(1-\cos\delta) & -\sin 2\chi \sin\delta \\ 0 & \cos 2\chi \sin 2\chi(1-\cos\delta) & \cos^2(2\chi) + \sin^2(2\chi)\cos\delta & \cos 2\chi \sin\delta \\ 0 & \sin 2\chi \sin\delta & -\cos 2\chi \sin\delta & \cos\delta \end{bmatrix} \tag{4.19}$$

where the retardance δ is depends on z by $\delta=2\pi(\Delta n)z/\lambda$. For a medium of changing optical properties, the Mueller matrix $\mathbf{M}_z$ can be approximated by a product of n Mueller matrices, each of constant optical properties over its thickness z/n:

$$M_z = M_n \ldots M_2 M_1 \tag{4.20}$$

The components of these matrices $\mathbf{M}_1$.. $\mathbf{M}_n$ can be calculated by assuming that over a thin slice of thickness z/n, the optical properties and the stresses are constant along the depth. For such a medium, one can write:

$$(n_{11} - n_{22}) \cdot \sin(2\chi) = 2 \cdot C \cdot \tau_{yx} \tag{4.21}$$

$$(n_{11} - n_{22}) \cdot \cos(2\chi) = C \cdot (\tau_{xx} - \tau_{yy}) \tag{4.22}$$

where n_{11}-n_{22} is the birefringence, χ is the extinction angle, C is the stress-optical coefficient, τ_{yx}, τ_{xx}, and τ_{yy} are the components of the stress tensor.

It is important to note the resultant retardance and extinction angle calculated using the equations listed above will only be affected by some of the stress components τ_{yx}, τ_{xx}, and

τ_{yy}. This point was also noted by Frocht (1950) who stated that the polarization state of light is only directly affected by the stresses on the plane normal to the beam propagation direction. The shear stress in the xz-plane τ_{xz}, however, changes the second invariant of the rate-of-strain tensor $\dot{\gamma} = \sqrt{\frac{1}{2}\dot{\boldsymbol{\gamma}}:\dot{\boldsymbol{\gamma}}} = \sqrt{\left(\frac{dv_x}{dy}\right)^2 + \left(\frac{dv_x}{dz}\right)^2}$ and influences the magnitude of τ_{xy} and τ_{xx}-τ_{yy} through viscosity and the first normal stress coefficient.

The influence of end effects on birefringence measurements in a three dimensional pressure-driven flow in a rectangular channel was first analyzed by Galante and Frattini (1991). By integrating the differential Mueller matrix for an infinitesimal slab along the optical path with an upper-convected Maxwell fluid model, they were able to quantify the deviation of the retardation and extinction angle from the values calculated for the idealized two-dimensional case. They described their results in terms of two parameters, the characteristic retardation $\delta_0 = \frac{-4\pi CW}{\lambda}\left\{B \cdot \left(-\frac{dP}{dx_1}\right)\right\}$ and the Weissenberg number $We = \tau \cdot \left\{\frac{B}{\eta}\left(\frac{-dP}{dx_1}\right)\right\}$ where C is the stress-optical coefficient, W is the length of the optical path, B is the channel half-width, $-dp/dx_1$ is the pressure gradient, τ is the characteristic relaxation time for the fluid, and η is the viscosity. For $\delta_0 = 1.0$ and We = 10.0, the retardance profile is about 7% lower than the corresponding two-dimensional case whereas the extinction angle profile is identical to that of the 2-D case, except at the position where a change-order ($\delta = 360°$ or its multiple) occurs. For $\delta_0 = 10.0$ and We = 1.0, the retardance profile is again about 7% lower. However, the extinction angle profile shows large scale variations at about the positions where the change-order occurs. In this experimental study, the characteristic retardation changed from 5 (0.5 rpm) to 32 (10 rpm) and the Weissenberg number changed from 1 (0.5 rpm) to 6 (10 rpm). To further understand the edge effect for a shear-thinning fluid at the flow rates used in this study, the retardance and extinction angle profiles were calculated for two cases: 0.5 rpm and 5 rpm. The procedure is outlined as follows.

Note: This integration procedure used in their study, which was developed by Azzam and Bashara (1965), was not the same as the Wertheim's law (Theocaris and Gdoutos, 1979) $\delta = \left(\frac{2\pi}{\lambda}\right)\{\int_0^L \Delta n dx_3\}$. Wertheim's law is only valid when the extinction angle is constant throughout the optical path.

Using finite element method with the software FIDAP^{TM}, the velocity profile of LDPE $v_x(y,z)$ at 160°C was calculated as a function of the velocity gradient y and neutral z directions for at different flow rates. The details of this exercise is described in Appendix B of this thesis. The shear rates $\frac{dv_x}{dy}$ and $\frac{dv_x}{dz}$ were calculated by differentiating the velocity over a small distance in the y and z directions, respectively. The second invariant of the rate-of-strain tensor was then computed as $\dot{\gamma} = \sqrt{\frac{1}{2}\dot{\boldsymbol{\gamma}}:\dot{\boldsymbol{\gamma}}} = \sqrt{\left(\frac{dv_x}{dy}\right)^2 + \left(\frac{dv_x}{dz}\right)^2}$. The shear stress in the xz-plane τ_{xz} increases from zero at the bulk to some positive value at the end walls. The shear stress in the xy-plane τ_{yx}, however, decreases from the maximum value midway between the two end walls to zero at the walls. Figure 4.42 compares the change in shear stress τ_{yx} at different positions across the gap between the two-dimensional and three-dimensional cases at 5 rpm and 160°C. Recall the centerline is located at y = 0 mm and the walls are at y = ± 2 mm. The graph shows τ_{yx} for four cases: close to centerline (y = 0.04 mm), a quarter of the distance from the centerline (y = 0.52 mm) to the wall, midway between centerline and the wall (y = 1 mm), and close to the wall (y = 1.96 mm). At any positions across the gap, the effect of the end walls on the shear stress τ_{xy} is not negligible.

Figure 4.43 compares the retardance profiles calculated between a two-dimensional and a three-dimensional case at 0.5 rpm and 5 rpm. At both screw speeds the retardance was lower when the variation in the beam propagation direction were taken into account. At a fixed position across the gap, the ratio of retardance of the 2-D case to that of the 3-D

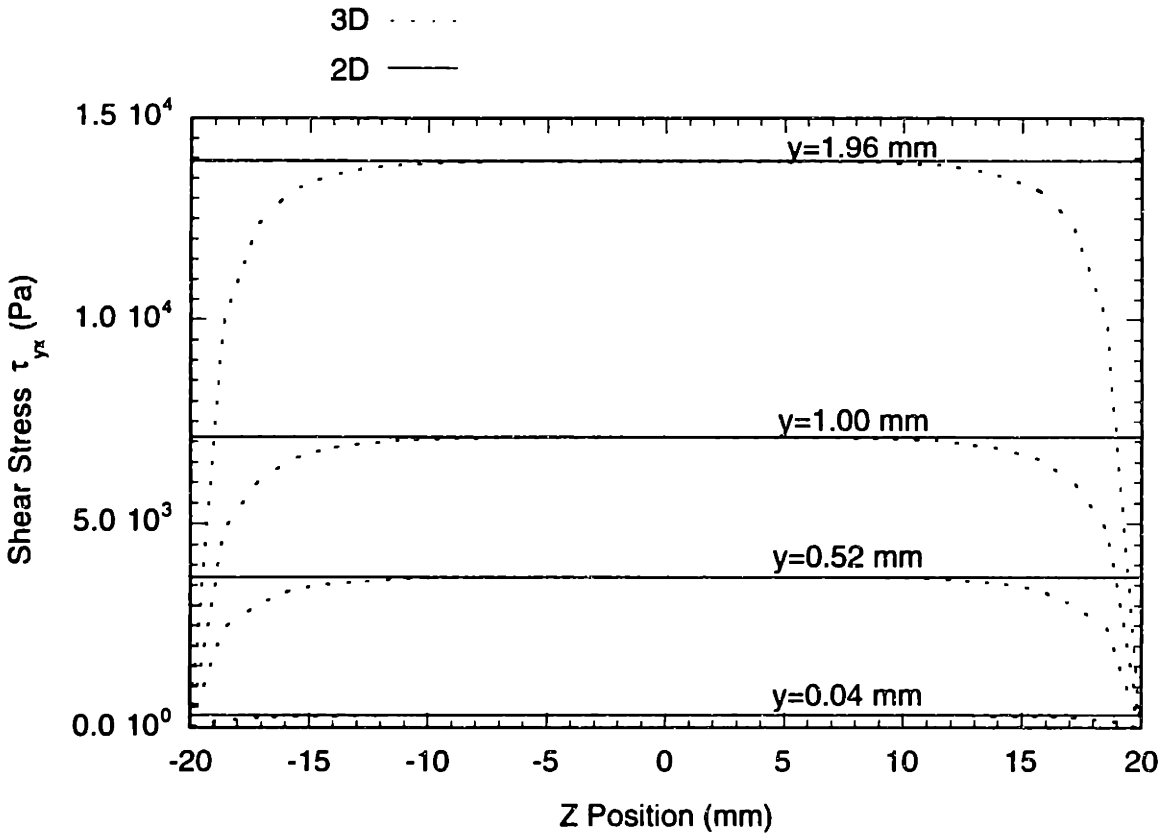

Figure 4.42: Shear stress τ_{xy} profiles along the beam propagation direction at different positions on across the gap. The centerline and the walls are located at y = 0 and y = $\pm$2 mm respectively. The 1D profiles are calculated from the equation $\tau_{yx} = (-dp/dx)(y)$. The 2D profiles are calculated based on the shear rate results obtained from a FIDAP^{TM} finite element calculations.

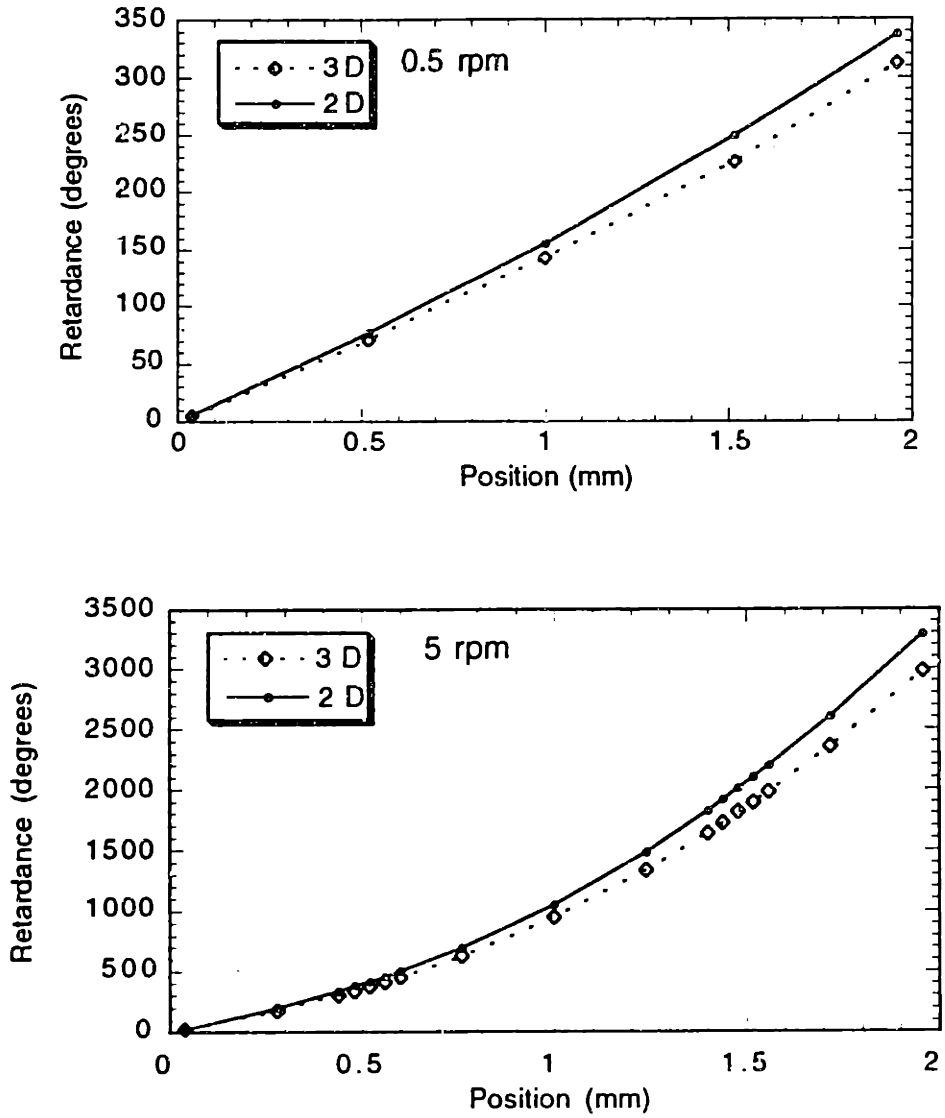

Figure 4.43: Retardance profiles simulated by using FIDAP^{TM} for difference screw speeds assuming C=2.0x10^{-9} Pa^{-1}. The edge effects are examined by comparing the 3D and 2D curves.

case is 1.1 for both screw speeds. Galante and Frattini (1991) also found that the retardance across the gap was reduced by a constant amount (7%) when the edge effect was considered. The extinction angle profiles for 0.5 rpm and 5 rpm are compared in Figure 4.44. At 0.5 rpm the extinction angle was almost identical with between the 2-D and 3-D cases, except at y=1.96 mm (δ=312.5°) the extinction angle in the 3-D case is noticeably lower than that in the 2-D case. At 5 rpm, large spikes are observed at two locations. These locations corresponds to regions where the retardance is close to 360° and 2160°. The extinction angle profiles observed in this exercise is similar in nature to those observed by Galante and Frattini (1991) with an upper-convected Maxwell fluid model. The profiles calculated in both studies under high flow rates have the same two features: a general decreasing behavior toward the walls and the presence of spikes at certain locations at positions where a change-order occurs (the retardance is close to 360° or its multiples). One noticeable difference is that Galante and Frattini observed spikes at all change-order positions, whereas in this study the spikes were only observed at some of the change-order positions.

In summary, this analysis shows that the presence of the observing windows reduced the measured retardance by a factor of 1.1 and caused large variations in the extinction angle profiles at high flow rates. However, not all the features of our experimentally measured extinction angle profiles can be explained by the presence of the end walls alone. First, the experimental extinction angle profiles did not show a decreasing trend at high flow rates (screw speeds at and higher than 2 rpm). Second, the spikes in the experimental profiles occurred at all change-order positions. In the next section, these features are explained by analyzing the effect of the finite cross-sectional area of the laser beam.

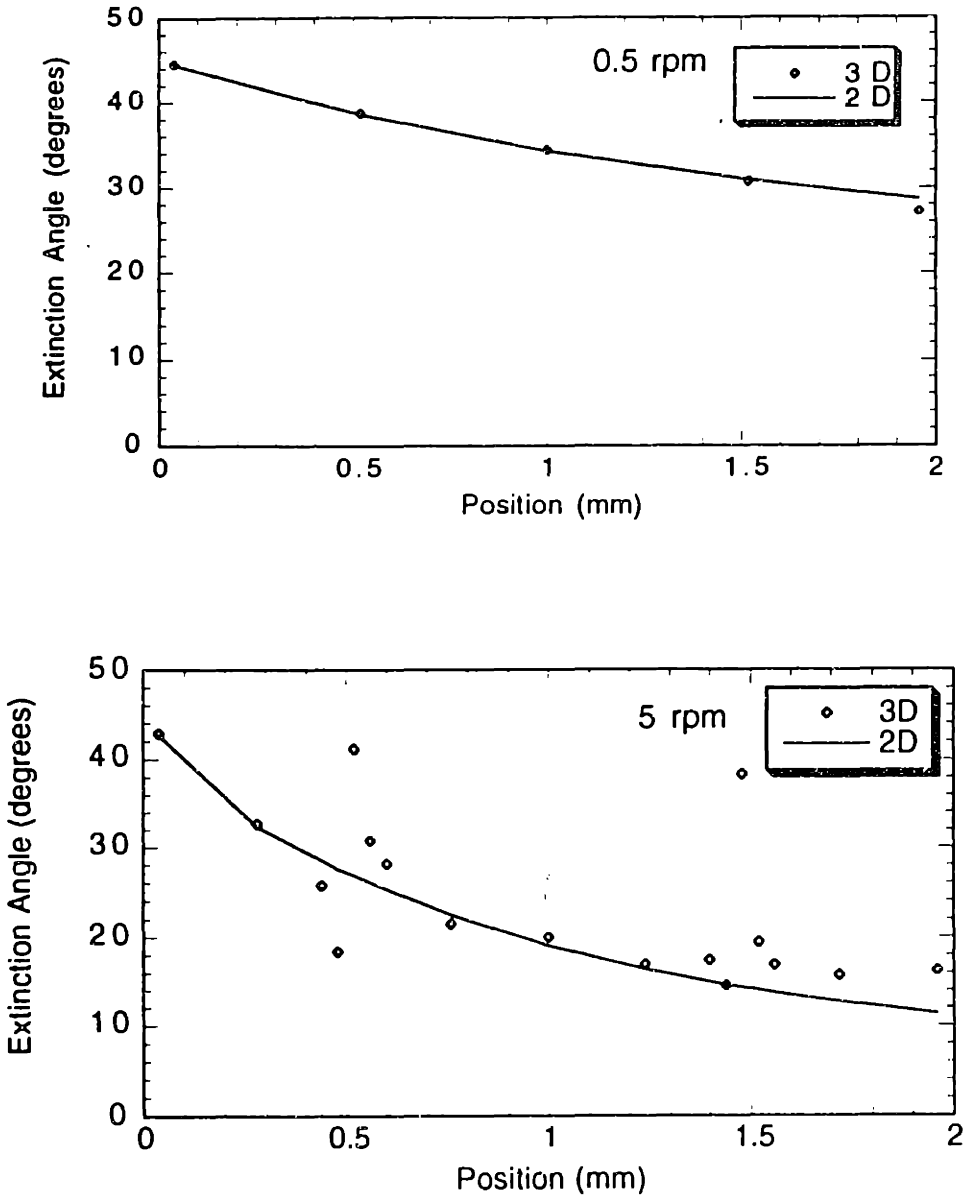

Figure 4.44: Extinction angle profiles simulated by using FIDAP^{TM} for difference screw speeds assuming C=2.0x10^{-9} Pa^{-1}. The edge effects are examined by comparing the 3D and 2D curves.

4.3.5 Effect of Finite Beam Size

In order to study how the finite cross-sectional area of the laser beam affects the raw data and the calculated profiles, it is necessary to measure the beam size and its intensity profile in the plane normal to the propagation direction. Galante (1991) described a simple but accurate method to measure the intensity profile. This procedure starts with measuring the power of a light beam which is partially occluded by a knife edge or a razor blade. The power measured by the photodetector P(y) is the integral of the intensity profile from $-\infty$ to the blade position y. Since the intensity profile of commonly used lasers follows a Gaussian function, the power detected as the blade moves to different positions can be described by an error function. The radius of a light beam is defined as the distance between the center and the position at which the intensity of the light drops to $1/e^2$ of its maximum value. The best fit for the intensity or the power profile yields the beam radius.

Figure 4.45 shows a plot of the ratio of the power detected from a partially occluded beam to the non-occluded beam as a function of blade position. Also shown on the figure is the best fit with an error function:

$$P(y) = \frac{P_{Total}}{2}\left(1 - \mathrm{erf}\left(\frac{\sqrt{2}y}{w(z)}\right)\right) \tag{4.23}$$

where P_{Total} is the power detected from the non-occluded beam, and w(z) is the radius of the beam that corresponds to a particular power profile P(y). The intensity profile of a Gaussian beam at a distance z from the point where the waist w(z) is formed is given by (Galante, 1991):

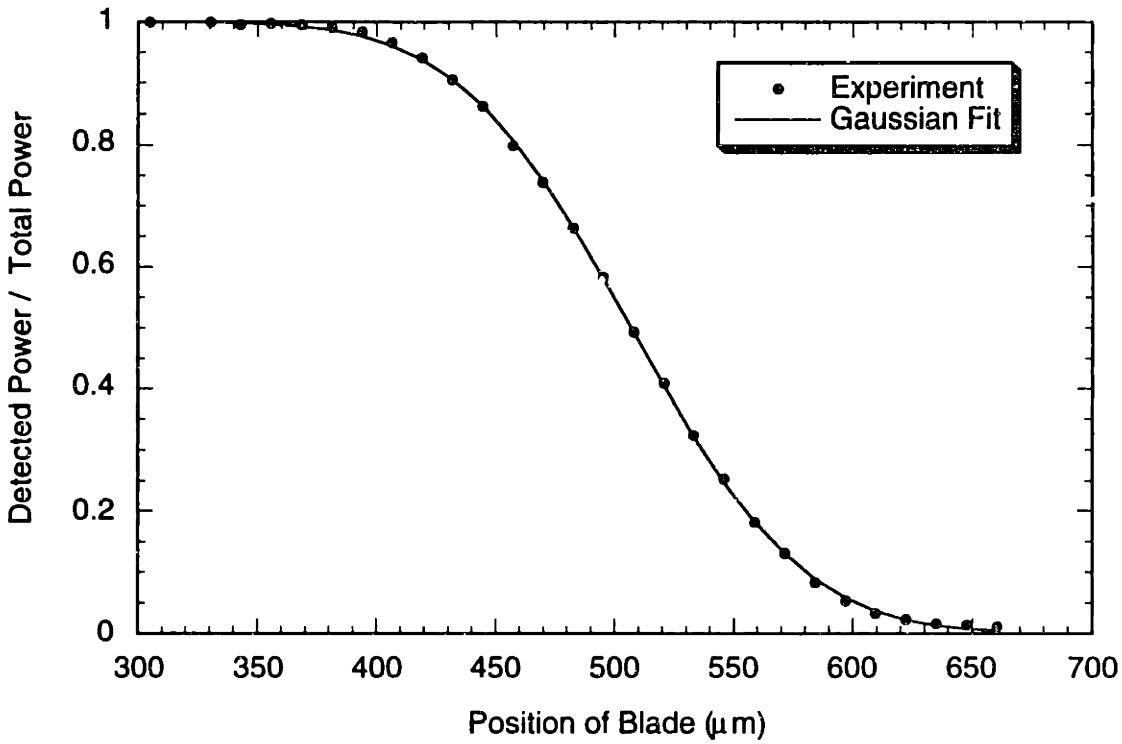

Figure 4.45: Plot of the ratio of the detected power to the total power as the beam is partially blocked by a razor blade. The error bars (2%) are within the size of the symbol.The error in the detected power was estimated from the resolution of the multimeter which translated the detected power into a voltage and from the resolution of the micro-stepping motor which positioned the blade. The Gaussian fit is a curve of the error cofunction with a beam diameter of 230 μm, determined by a least square fit between the between the measured power profile and the one calculated from Equation 4.23.

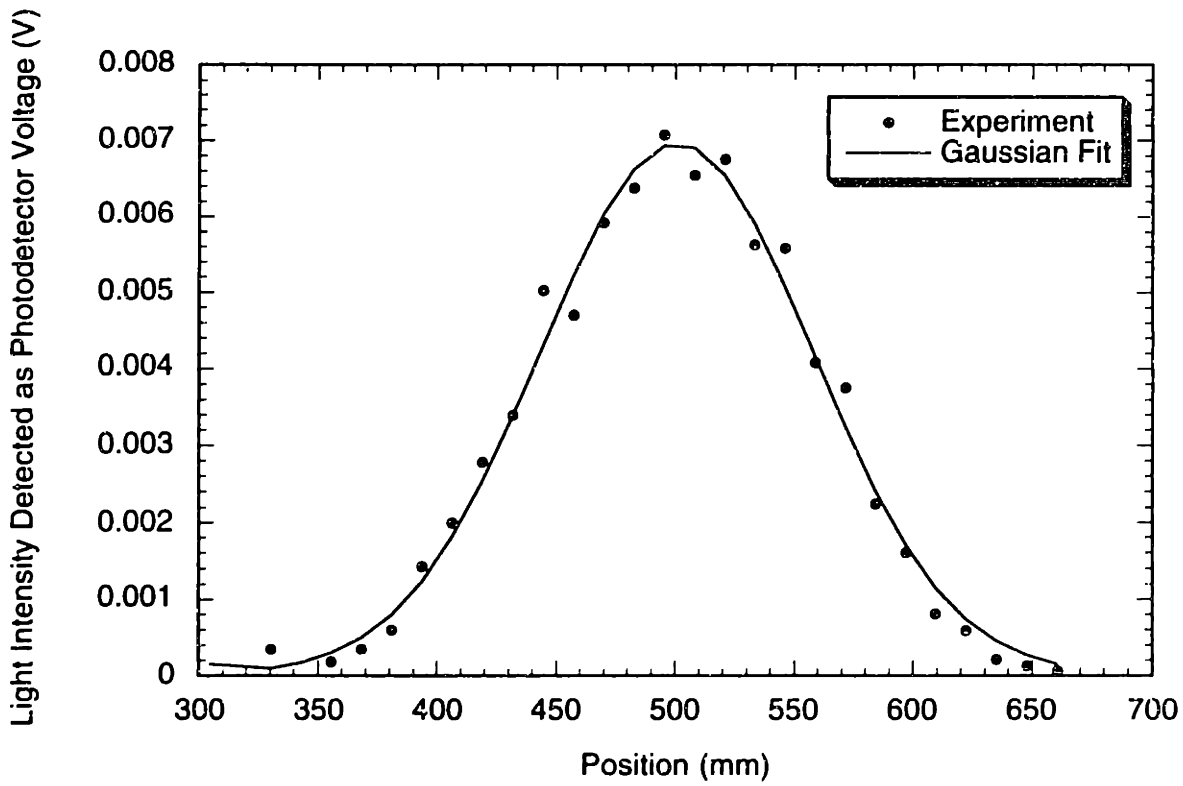

Figure 4.46: Intensity profile of the beam measured by differentiating the power profile (Figure 4.45). The Gaussian fit is a Gaussian function with a beam diameter of 230 μm.

$$I(x, y) = \frac{2P_{Total}}{\pi w^2(z)} \exp\left(-\frac{2}{w^2(z)}(x^2 + y^2)\right) \tag{4.24}$$

where x and y are the coordinates in the plane normal to the propagation direction.

The beam diameter was measured at three positions along the beam path: the interface between the top window and the fluid, the interface between the bottom window and the fluid, and mid-way between the first two positions. Recall that the channel was 40 mm thick in the beam path direction, so these positions were 20 mm apart. In this study a 400 mm plano-convex lens was used to focus the beam. As the diameter increased over distance from the source due to divergence, focusing was necessary to minimize the beam diameter at the region of interest. The position of the beam waist (the smallest beam radius) and the radius of the beam at any distance from the lens were calculated using the ABCD law developed by Kogelnik and Li (1966). Unlike geometrical optics, this law takes into account of the finite cross-sectional area of the light beam. The key equations which relate the positions of the light source, the lens, and the focus are:

$$f_0 = \frac{\pi w_1 w_2}{\lambda} \tag{4.25}$$

$$d_1 = f \pm \frac{w_1}{w_2}\sqrt{f^2 - f_0^2} \tag{4.26}$$

$$d_2 = f \pm \frac{w_2}{w_1}\sqrt{f^2 - f_0^2} \tag{4.27}$$

where f_0 is a characteristic focal length determined by the beam radii and the wavelength, f is the focal length of the lens, d_1 is the distance between the light source and the focusing lens, d_2 is the distance between the focusing lens and the focus, w_1 and w_2 are the beam waist radii at the source and at the focus, and λ is the wavelength of light. Because of

space limitation, the center of the slit channel cannot be placed exactly at the position of the focus. The radius of the beam in any axial position can be related to that at the focus by:

$$w^2(z) = w_0\left[1 + \left(\frac{\lambda z}{\pi w_2^2}\right)^2\right] \tag{4.28}$$

where w_z is the radius at position z measured from the focus along the propagation axis.

The radii calculated from theory and the experimental results are shown in Figure 4.47. The center of the channel was 2143 mm from the light source. The calculated beam waist diameter at the center of the channel was 210 μm, as supposed to 228 μm measured by the razor blade method. The discrepancy between the measured and calculated diameters was partly due to the uncertainty in the distance and power measurements. The uncertainty in distance and power measurement were estimated to be ± 10 mm and 5% respectively. Also, the laser beam intensity profile might not be perfectly Gaussian. From this point onwards a nominal beam diameter of 230 μm will be used as the beam diameter for subsequent calculations because the measured beam diameter ranged from 228.2 μm to 230.6 μm.

The effects of the finite beam size in point-wise optical measurement with a Gaussian beam has been considered theoretically by Galante (1991). Using the ideas of the geometrical theory of diffraction set forth by Keller (1962, 1971), he concluded that the apparent Mueller matrix $\langle[M(x, y)]\rangle$ was actually a weighted average of the matrices within the area illuminated by the beam:

$$\langle[M(x, y)]\rangle = \frac{\int\int_{Area} I(x, y)[M(x, y)]dxdy}{\int\int_{Area} I(x, y)(dx)dy} \tag{4.29}$$

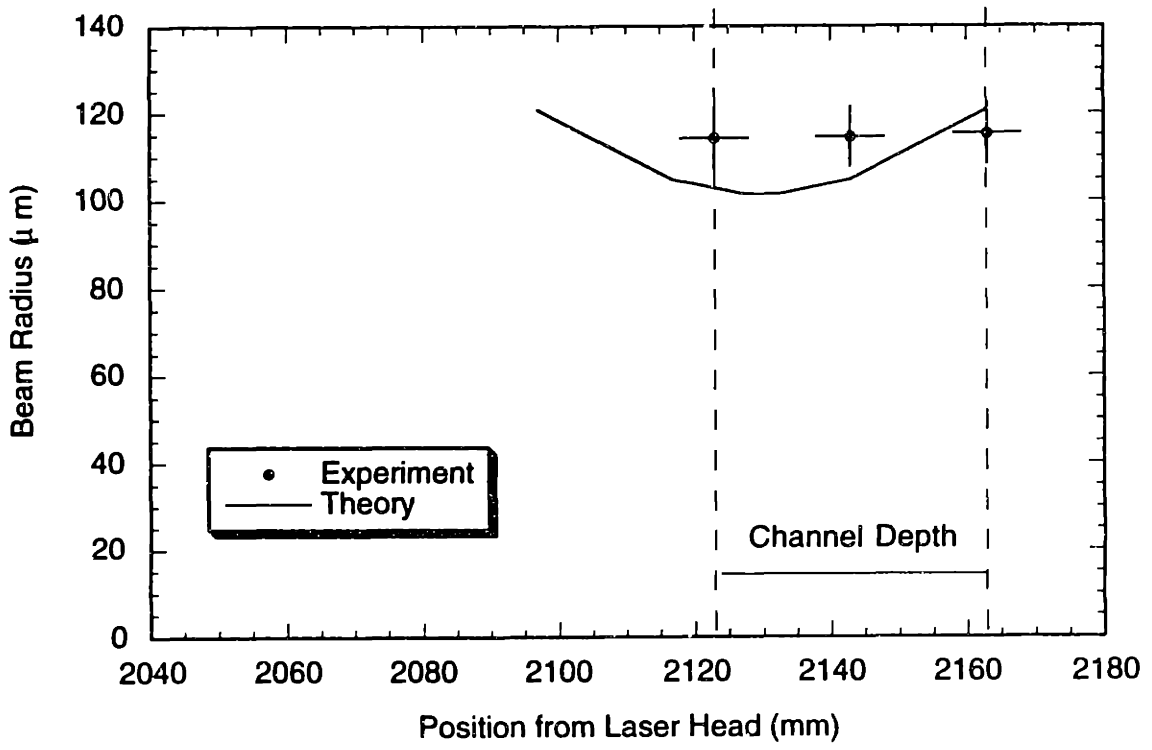

Figure 4.47: Beam radius as a function of position along the propagation direction. The error bars of 5 mm are estimated for long distance measurements with a tape measure. The theoretical radii are calculated from formulas outlined by Kogelnik and Li (1966).

where I(x,y) is the intensity at position (x,y). "Area" is the cross-sectional area of the beam.

The Mueller matrix for the sample with retardance δ and extinction angle χ can be written as:

$$\begin{bmatrix} 1 & 0 & 0 & 0 \\ 0 & \cos^2(2\chi)+\sin^2(2\chi)\cos\delta & \cos 2\chi \sin 2\chi(1-\cos\delta) & -\sin 2\chi \sin\delta \\ 0 & \cos 2\chi \sin 2\chi(1-\cos\delta) & \cos^2(2\chi)+\sin^2(2\chi)\cos\delta & \cos 2\chi \sin\delta \\ 0 & \sin 2\chi \sin\delta & -\cos 2\chi \sin\delta & \cos\delta \end{bmatrix} \tag{4.30}$$

The birefringence apparatus measures two specific elements in this matrix, namely $M_{34} = R\omega$ and $M_{24} = R2\omega$. One can rewrite this matrix as:

$$\begin{bmatrix} 1 & 0 & 0 & 0 \\ 0 & \sqrt{1-R\omega^2-R2\omega^2} & R2\omega & -\sin 2\chi \sin\delta \\ 0 & R2\omega & \sqrt{1-R\omega^2-R2\omega^2} & R\omega \\ 0 & \sin 2\chi \sin\delta & -R\omega & \cos\delta \end{bmatrix} \tag{4.31}$$

Focusing on the two elements $M_{34} = R\omega$ and $M_{24} = R2\omega$, we see that the measured $R\omega$ and $R2\omega$ are therefore average values weighted by the intensity distribution over the beam cross-sectional area.

$$\langle R\omega \rangle = \frac{\int\int_{Area} I(x,y) R\omega \, dxdy}{\int\int_{Area} I(x,y) \, dxdy} \tag{4.32}$$

$$\langle R2\omega \rangle = \frac{\int\int_{Area} I(x,y) R2\omega dxdy}{\int\int_{Area} I(x,y) dxdy} \tag{4.33}$$

To rewrite this integral in a more useful form, the following simplifications were made. First, since the intensity was axisymmetric, it only depended on one variable r, the radius measured from the center of the beam. Second, for a gap width of 4000 μm, one could fit approximately 17 beam diameters from one wall to the other across the gap. The birefringence data points were 150 micro-steps apart, which amounts to a 38.1 μm separation between every two data points. Therefore, the beam area covered six measurement positions. The intensity variation along r was then modeled by a piece-wise constant function shown in Table 4.3:

I/I_{max}	r/R
1	0<r/R<1/3
0.773	1/3<r/R<2/3
0.338	2/3<r/R<1

Table 4.3: Intensity distribution used in calculations

where I_{max} is the maximum intensity at the center of the beam and R is the radius of the beam. The I/I_{max} values were calculated from a Gaussian curve fit with a 230 μm diameter.

As shown in Figure 4.48, the beam area covered seven measurement positions. Since the raw data Rω and R2ω did not vary along the flow direction (x direction), they were weighted averages only in the y direction:

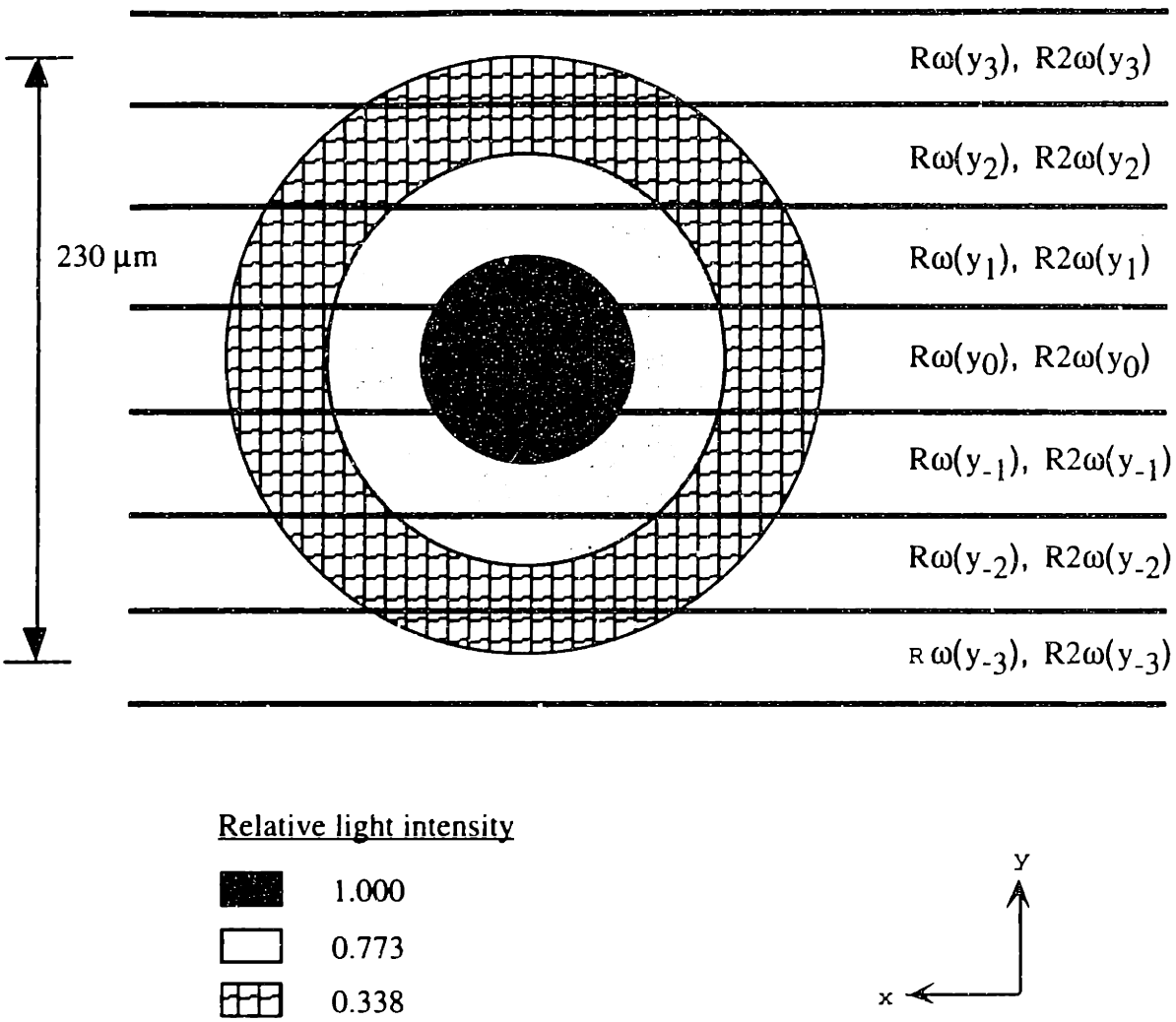

Figure 4.48: Cross-sectional intensity profile of the laser beam as modeled by a Gaussian function. The raw data Rω and R2ω are averages of the local values weighted by the intensity profile within each stripe. "x" is the flow direction and "y" is the velocity gradient direction.

$$R\omega_{averaged}(y_0) = w_1 R\omega(y_{-3}) + w_2 R\omega(y_{-2}) + w_3 R\omega(y_{-1}) + w_4 R\omega(y_0) + \quad (4.34)$$
$$w_3 R\omega(y_1) + w_2 R\omega(y_2) + w_1 R\omega(y_3)$$

$$R2\omega_{averaged}(y_0) = w_1 R2\omega(y_{-3}) + w_2 R2\omega(y_{-2}) + w_3 R2\omega(y_{-1}) + w_4 R2\omega(y_0) + \quad (4.35)$$
$$w_3 R2\omega(y_1) + w_2 R2\omega(y_2) + w_1 R2\omega(y_3)$$

The normalized weights w_1... w_4 were calculated by first summing up the intensity contributions from each sector within a stripe. The intensities of the first four stripes were then normalized to yield the relative weights. Only four stripes were considered since the intensity profile was symmetric in y. Table 4.4 lists the relative weights.

Normalized relative weights	Value
w_1	0.0242
w_2	0.1196
w_3	0.2236
w_4	0.2653
$w_1+w_2+w_3+w_4+w_3+w_2+w_1$	1

Table 4.4: Relative weights calculated from measured beam diameter

With the relative weights listed in Table 4.4, Equations 4.34 and 4.35 were used to calculate the effect of changing intensity within the beam cross-sectional area on a set of simulated data. Figure 4.49 compares the Rω and R2ω profiles with and without the beam size averaging effect. The ideal profiles were calculated based on the shear rate profile obtained using the finite element calculations discussed in Appendix B of this thesis and the rheological data of LDPE obtained from parallel-plate rheometry. The local maxima and minima of the averaged profiles had smaller magnitudes than the correct local values (the ideal values directly obtained from simulation). Using these averaged Rω and R2ω

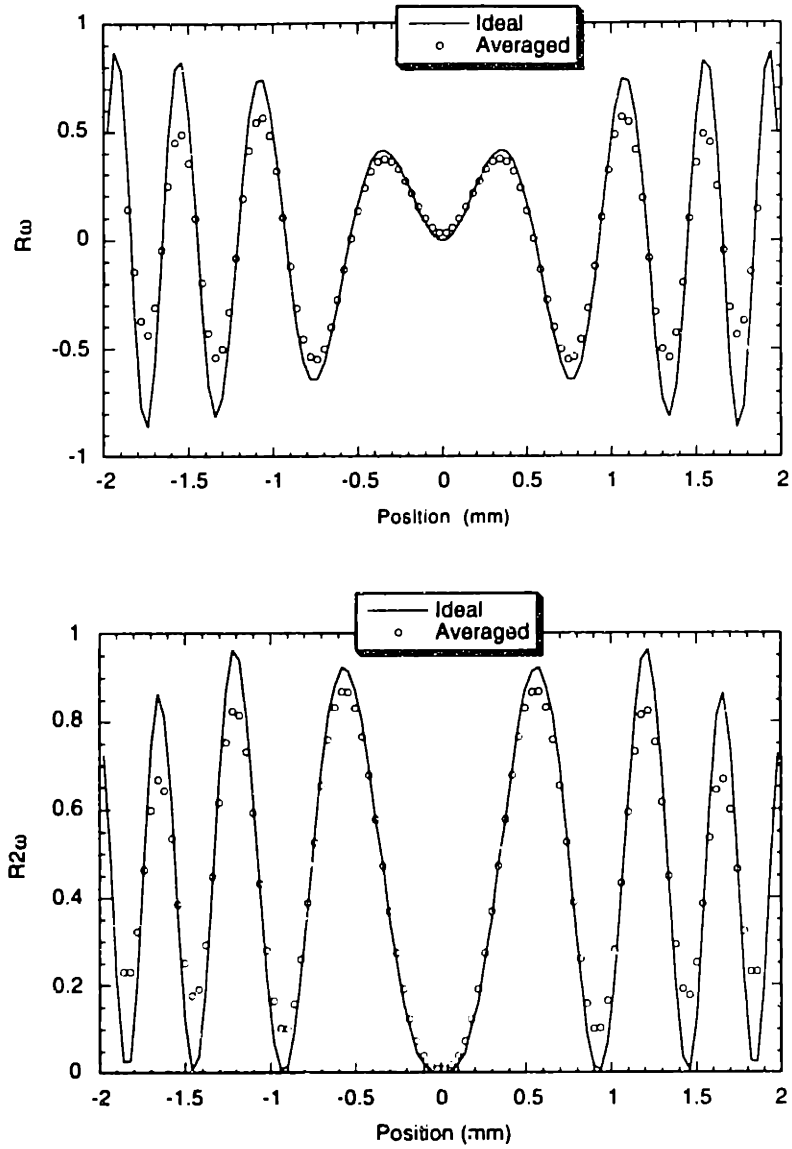

Figure 4.49: .Rω and R2ω profiles averaged with the relative weights shown in Table 6.2 (Averaged) along with the original profiles (Ideal). The original profiles are calculated from an ideal one dimensional pressure-driven flow between two parallel walls assuming the stress-optical coefficient = 1.0 x 10^{-9} Pa^{-1} at 3.7 rpm.

profiles, one could calculate the retardance and extinction angle profiles (Figures 4.50 and 4.51). The retardance profile clearly shows the gaps found in the experimental data. These gaps are recognized by their occurrence at retardance level of 360° and its multiples. The simulated extinction angle profile also reproduced the features observed from the experimental data. There were spikes approaching 45° at the same y positions where the retardance was at 360° or its multiples. Moreover, the "averaged" profile showed an increase toward the walls. Therefore, the observed increase in extinction angle from the experimental profile was also an artifact of the beam size averaging effect.

The eight experimental Rω profiles are shown in Figures 4.52 and 4.53, and the R2ω profiles at the corresponding screw speeds are shown in Figures 4.54 and 4.55. All these experimental Rω and R2ω profiles had maxima and minima smaller than those in the ideal simulated profiles. The reduction in the peak values can be explained by the averaging effect over the finite beam cross-sectional area.

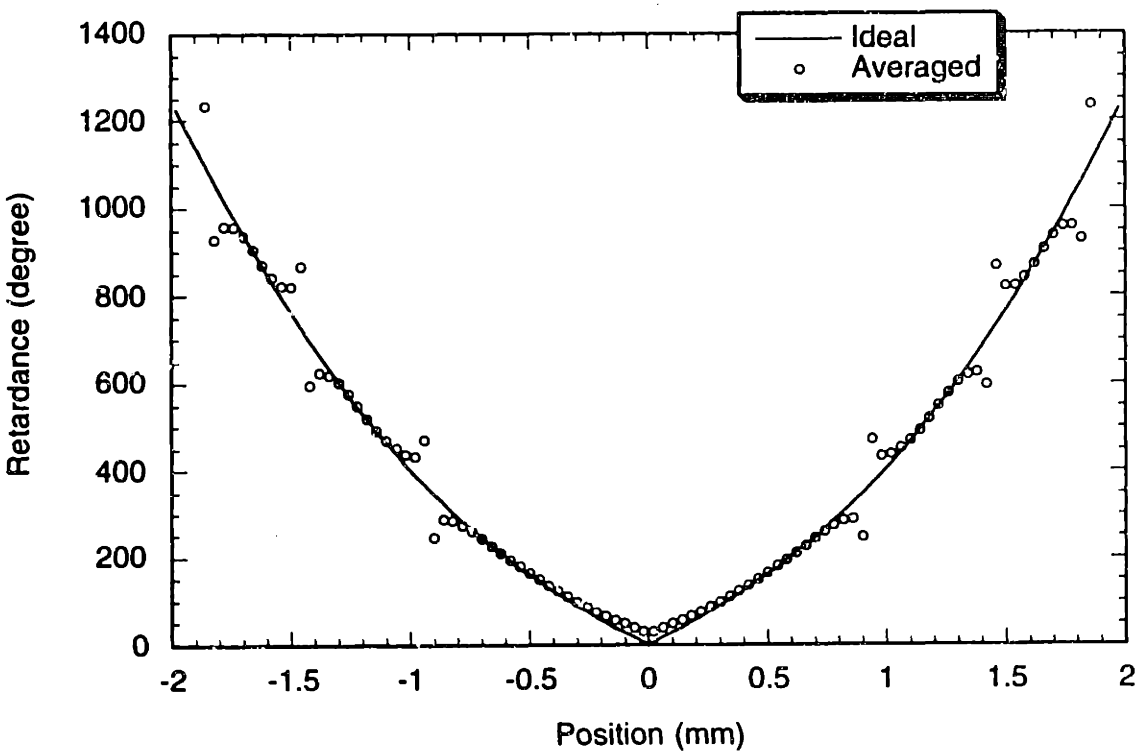

Figure 4.50: The effect of finite beam cross-sectional area on the measured retardance profiles. The "averaged" results are calculated from the weighted averages of the "ideal" Rω and R2ω profiles.

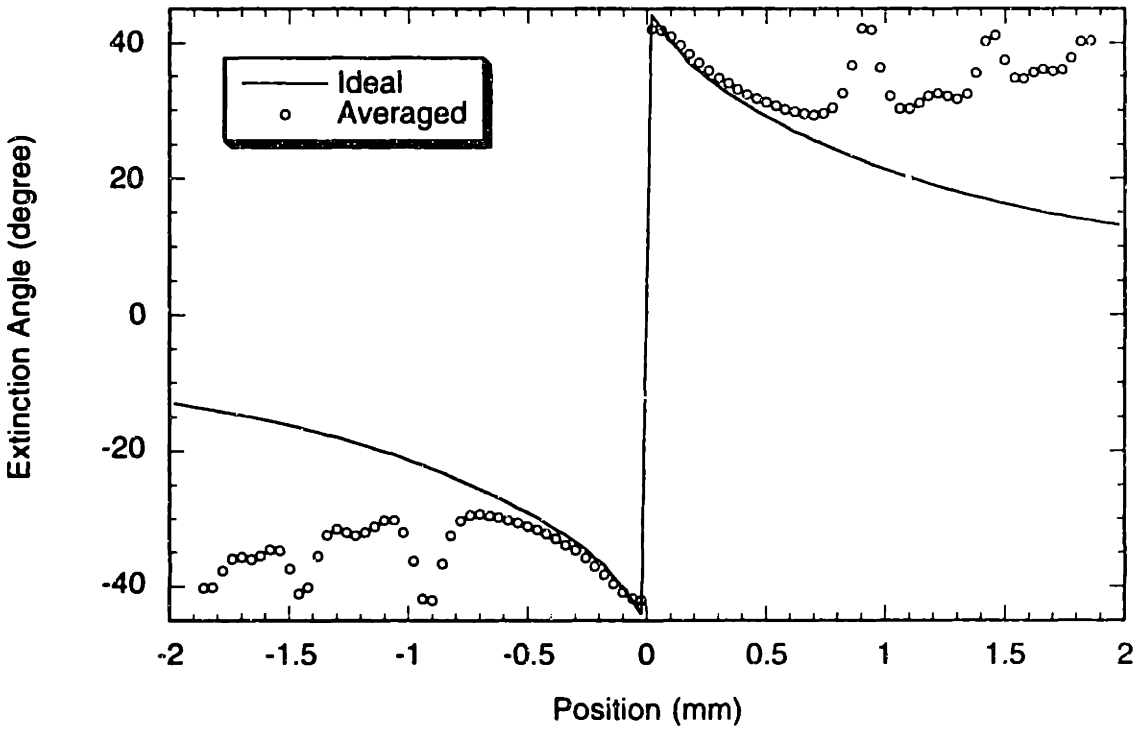

Figure 4.51: The effect of finite beam cross-sectional area on the measured extinction angle profiles. The "averaged" results are calculated from the weighted averages of the "ideal" Rω and R2ω profiles.

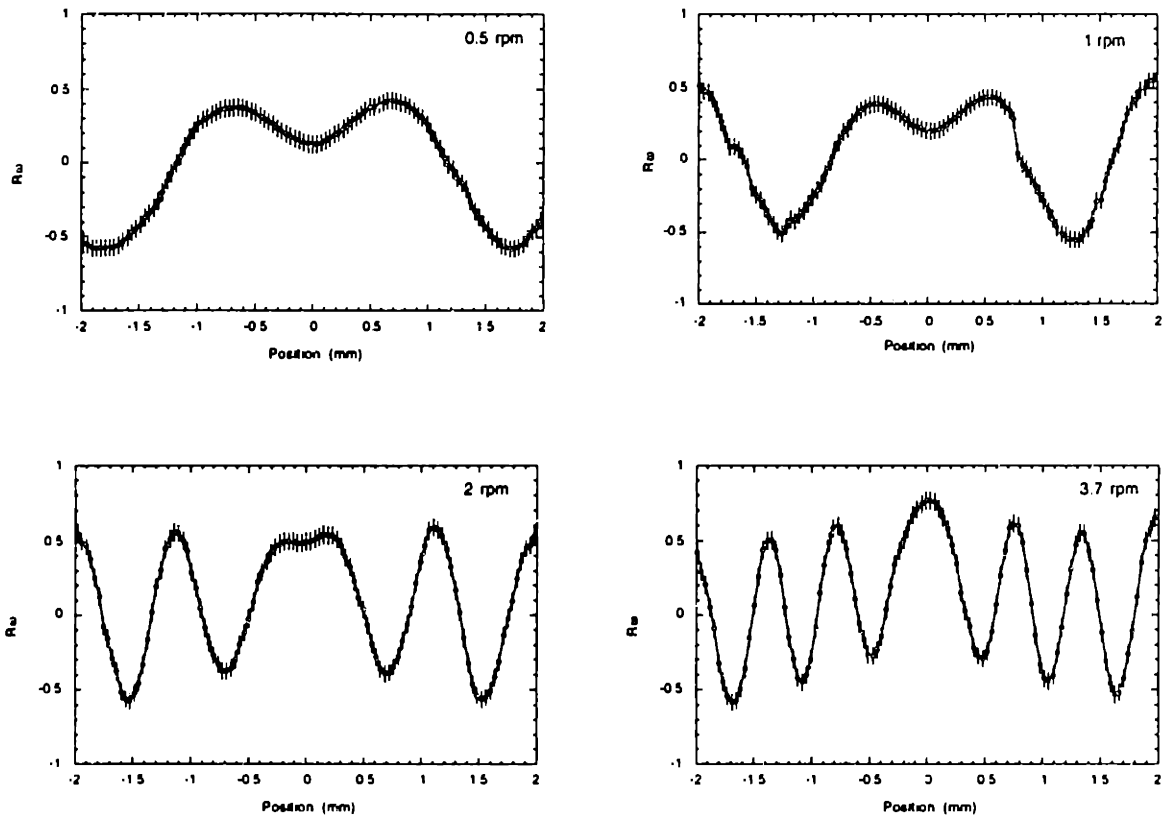

Figure 4.52: Rω profiles across the channel width at screw speeds of 0.5 rpm to 3.7 rpm. Each data point is an averaged value of 200 raw data points without filtering at one particular run. The error bars represent one standard deviation about the mean values.

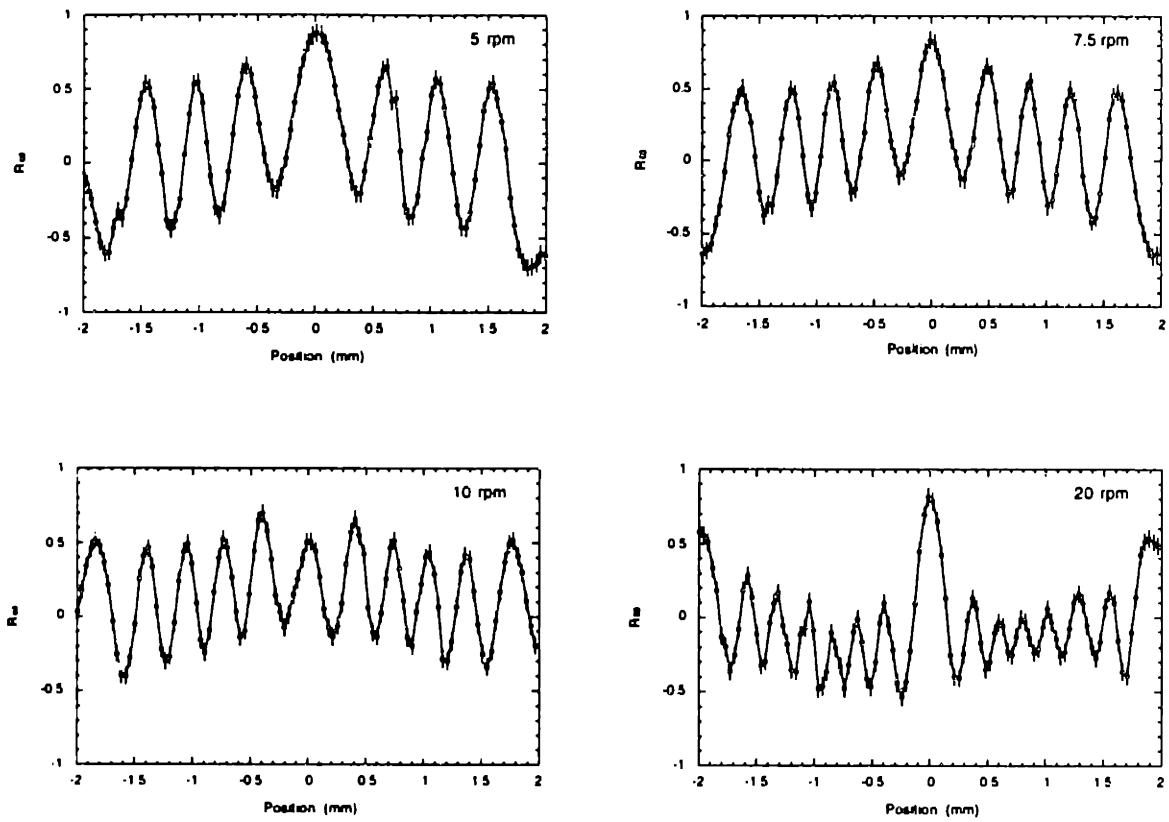

Figure 4.53: Rω profiles across the channel width at screw speeds of 5 rpm to 20 rpm. Each data point is an averaged value of 200 raw data points without filtering at one particular run. The error bars represent one standard deviation about the mean values.

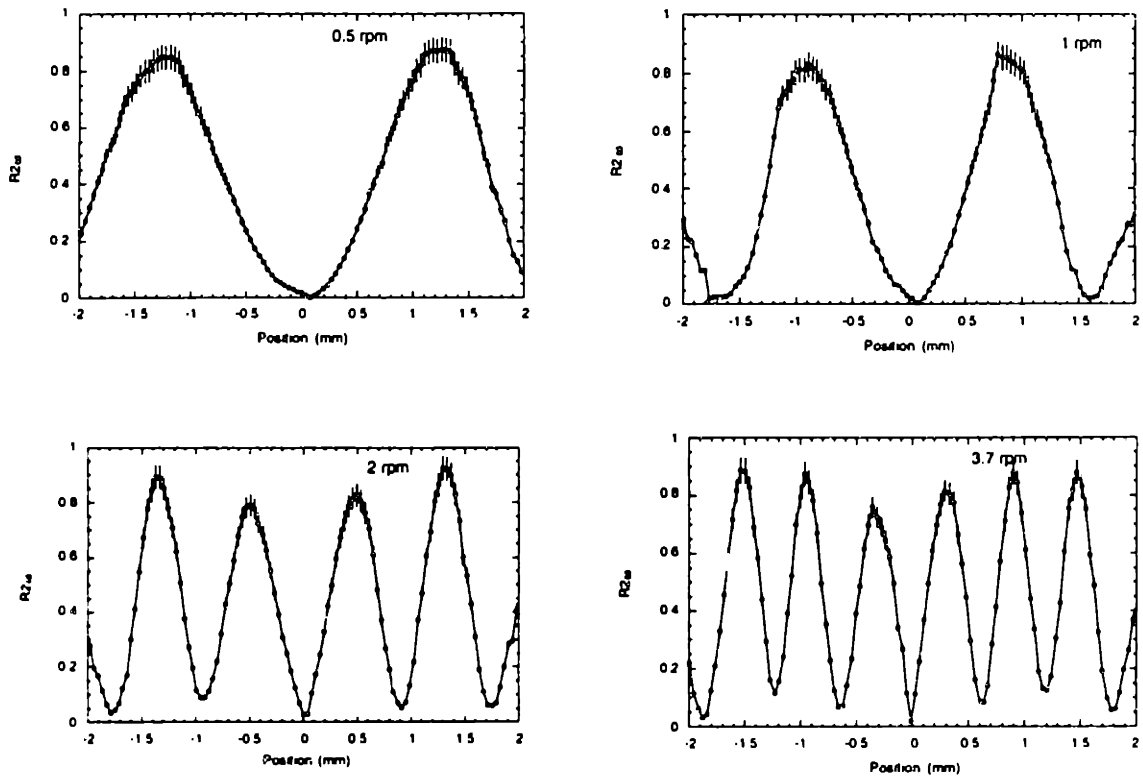

Figure 4.54: R2ω profiles across the channel width at screw speeds of 0.5 rpm to 3.7 rpm. Each data point is an averaged value of 200 raw data points without filtering at one particular run. The error bars represent one standard deviation about the mean values.

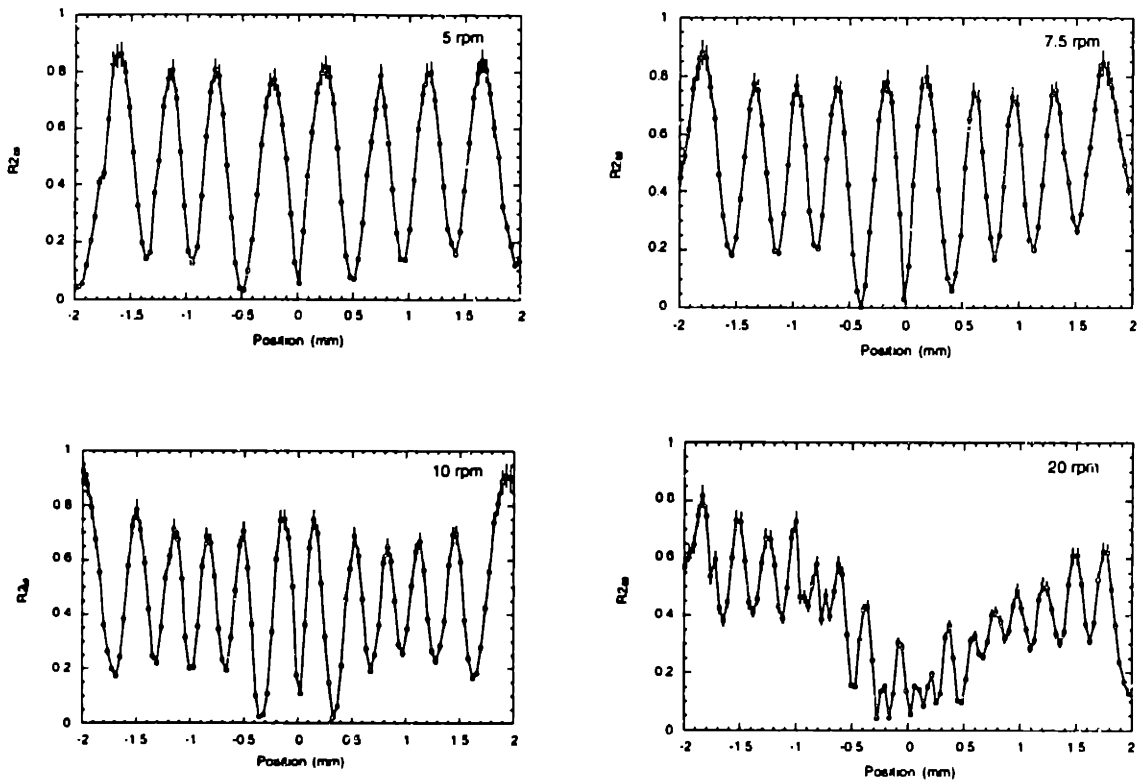

Figure 4.55: R2ω profiles across the channel width at screw speeds of 5 rpm to 20 rpm. Each data point is an averaged value of 200 raw data points without filtering at one particular run. The error bars represent one standard deviation about the mean values.

Given the measured relative weights $w_1 \ldots w_4$, one can theoretically recover the correct local values $R\omega_{correct}(y)$ and $R2\omega_{correct}(y)$ from the measured, averaged values. To reverse the averaging one needs to solve the following matrix equations for $R\omega_{average}(y_4) \ldots R\omega_{average}(y_{n-3})$ and $R2\omega_{average}(y_4) \ldots R2\omega_{average}(y_{n-3})$:

$$\begin{bmatrix} w_1 & w_2 & w_3 & w_4 & w_3 & w_2 & w_1 & . & . & . & . \\ . & w_1 & w_2 & w_3 & w_4 & w_3 & w_2 & w_1 & . & . & . \\ . & . & . & . & . & . & . & . & . & . & . \\ . & . & . & . & . & . & . & . & . & . & . \\ . & . & . & . & w_1 & w_2 & w_3 & w_4 & w_3 & w_2 & w_1 \end{bmatrix} \cdot \begin{bmatrix} R\omega_{correct}(y_1) \\ R\omega_{correct}(y_2) \\ R\omega_{correct}(y_3) \\ R\omega_{correct}(y_4) \\ . \\ . \\ . \\ R\omega_{correct}(y_{n-3}) \\ R\omega_{cosrrect}(y_{n-2}) \\ R\omega_{correct}(y_{n-1}) \\ R\omega_{correct}(y_n) \end{bmatrix} = \begin{bmatrix} R\omega_{average}(y_4) \\ R\omega_{average}(y_5) \\ . \\ . \\ R\omega_{average}(y_{n-3}) \end{bmatrix} \quad (4.36)$$

$$\begin{bmatrix} w_1 & w_2 & w_3 & w_4 & w_3 & w_2 & w_1 & . & . & . & . \\ . & w_1 & w_2 & w_3 & w_4 & w_3 & w_2 & w_1 & . & . & . \\ . & . & . & . & . & . & . & . & . & . & . \\ . & . & . & . & . & . & . & . & . & . & . \\ . & . & . & . & w_1 & w_2 & w_3 & w_4 & w_3 & w_2 & w_1 \end{bmatrix} \cdot \begin{bmatrix} R2\omega_{correct}(y_1) \\ R2\omega_{correct}(y_2) \\ R2\omega_{correct}(y_3) \\ R2\omega_{correct}(y_4) \\ . \\ . \\ . \\ R2\omega_{correct}(y_{n-3}) \\ R2\omega_{cosrrect}(y_{n-2}) \\ R2\omega_{correct}(y_{n-1}) \\ R2\omega_{correct}(y_n) \end{bmatrix} = \begin{bmatrix} R2\omega_{average}(y_4) \\ R2\omega_{average}(y_5) \\ . \\ . \\ R2\omega_{average}(y_{n-3}) \end{bmatrix} \quad (4.37)$$

Using "error" free, theoretical profiles of $R\omega_{average}$ and $R2\omega_{average}$, the "correct" profiles $R\omega_{correct}$ and $R2\omega_{correct}$ could be recovered perfectly by inverting Equations 4.36 and 4.37 using the numerical program MATLAB™. However, when experimental $R\omega_{average}$ and $R2\omega_{average}$ data were used in the program, some of the resultant $R\omega_{correct}$ and

$R2\omega_{correct}$ values went beyond ± 1. This was because the experimentally obtained profiles contained too much noise. Therefore, straight-forward inverting of the experimental averaged data did not recover the local correct values.

It was known that the retardance and extinction angle should be smooth functions of positions because the stress field changed smoothly across the channel. Moreover, the retardance at the centerline has to be zero, and the extinction angle at that point should be 45°. From the analysis of the edge effect in the previous section, the measured retardance was reduced by a factor of 1.1 due to the presence of the observing windows. Using all the information listed here, the retardance profile was approximated as by a continuous curve which best fits the phase-modulated data. To model the ideal extinction angle profile, a sum of monotonic decreasing functions was used as a first approximation:

$$\chi(y) = \sum_{i=1}^{m} a_i e^{-b_i y} \tag{4.38}$$

where a_i's are the unknown coefficients and b_i's are preset constants. One constraint was that the sum of a_i's had to be equal to 45° because the extinction angle at the centerline was 45°. With this expression for the extinction angle profile and the fit for the retardance data, it was possible to calculate the raw data profiles $R\omega(y)$ and $R2\omega(y)$ using Equations 3.21 and 3.22, which relate the measured quantities $R\omega(y)$ and $R2\omega(y)$ with the retardance δ and extinction angle χ. These profiles of δ and χ were then averaged with the relative weights $w_1 \ldots w_4$ measured by the beam size experiment described in this section. In this study the sum in Equation 4.38 was limited to 5 terms. These averaged profiles still contained the unknown parameters a_i's, which were chosen to fit the averaged $R\omega$ and $R2\omega$ profiles to the experimental ones. The optimal a_i's were defined as the ones which minimized the sum of the square difference between the experimental and fitting $R\omega(y)$ and

$R2\omega(y)$.

The extinction angle profiles calculated using this fitting method are compared in Figure 4.56. As expected, the extinction angle decreased as the screw speed went up. Within the range of screw speed used in this study, the minimum extinction angle decreased from 16.7° at 0.5 rpm to 12.4° at 10 rpm. Surprisingly, the fitted extinction angle profile for the 20 rpm run decreased from 45° at the centerline to about 16.6° at the wall. This profile is not consistent with the trend established by all other lower speeds. Recall that the retardance profiles obtained using the crossed polarizers configuration at this speed did not match well with that obtained from the phase-modulated beam (Figure 1.39). Therefore, the phase-modulated retardance profile at 20 rpm is not as reliable as those obtained at lower speeds. As a result, the limit of this technique lies between the conditions in the 10 rpm and the 20 rpm cases. The maximum shear stresses for those cases were 2.02×10^4 Pa and 2.92×10^4 Pa, respectively.

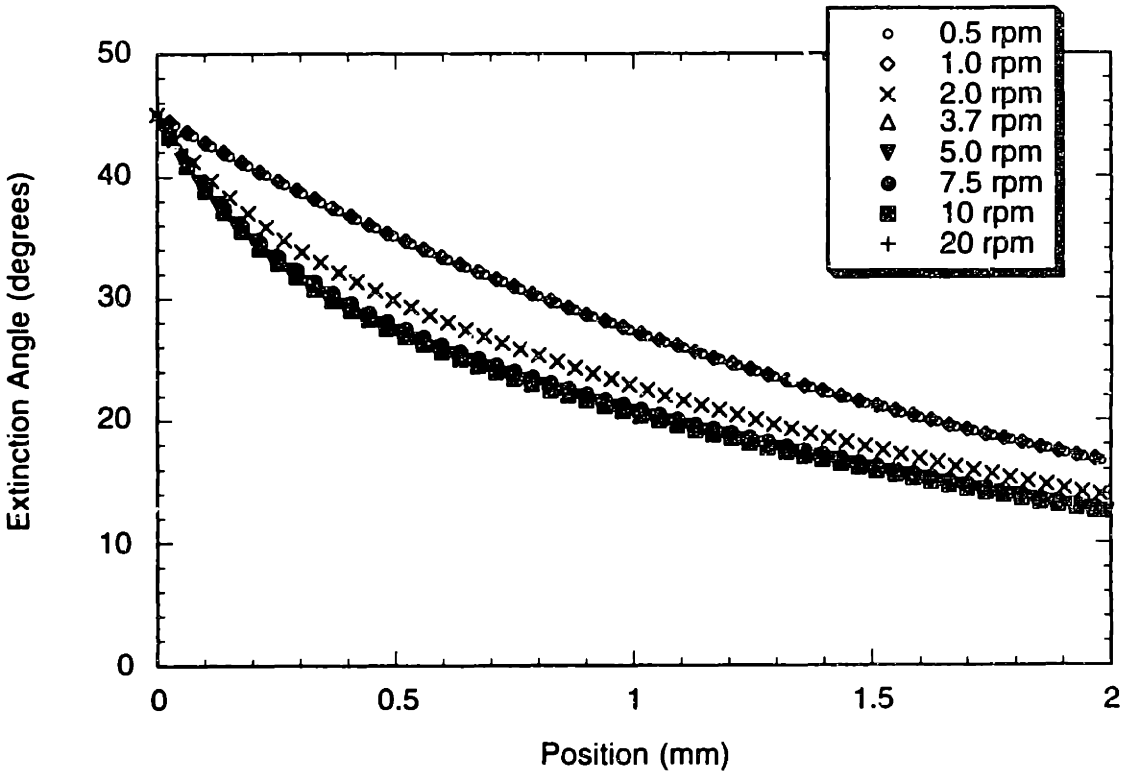

Figure 4.56: Extinction angle profiles calculated from data regression scheme.

4.3.6 Stress-Optical Coefficient and First Normal Stress Coefficient Measurement

The stress-optical coefficient is equal to the ratio of $\Delta n \sin(2\chi)$ to $2\tau_{yx}$. These plots are shown in Figure 4.57 for the different screw speeds investigated in this study. The shear stresses were calculated from the pressure gradients in the flow direction. The retardance and extinction angles were obtained by using the fitting procedure explained in the previous section. The curves in Figure 4.57 did not have a constant slope throughout the channel gap for any of the screw speeds investigated in this study. Specifically, all the slopes of these curves decreased as the shear stress was increased. The change in slope might be caused by the invalidity of the stress-optical rule beyond a certain stress level, and/or by the edge effect due to the presence of the two observing end windows. These two effects are discussed as follows.

The success of the stress-optical rule is based on the fact that under small stresses, the second moment tensor $\langle \underline{R}\underline{R} \rangle$ is proportional to both the refractive index tensor and the stress tensor. Here $\underline{R}$ is the end-to-end vector of a polymer chain. When the stress is large enough, either one or both of these proportionalities become invalid, and the stress-optical rule fails as a result. For polymer melts in shear flow, the stress-optical rule has been proven valid up to a shear stress of 10^4 Pa. Specifically, Wales (1976) showed that the ratio $\frac{\Delta n \cdot \sin 2\chi}{2\tau_{12}}$ was constant for HDPE and LDPE up to a shear stress of 10^4 Pa using his cone-and-plate device (Section 2.2). No data beyond that stress level were supplied to show whether or not the stress-optical rule would still hold beyond that amount of stress.

The curves of $\Delta n \sin 2\chi$ versus $2\tau_{yx}$ all have the same shape with a changing slope whose smallest values are at regions of large shear stresses near the walls. The similarity of the shape of these curves seems to suggest that all these curves are manifestation of the same physical phenomenon, but only at different flow rates. If the stress-optical rule is

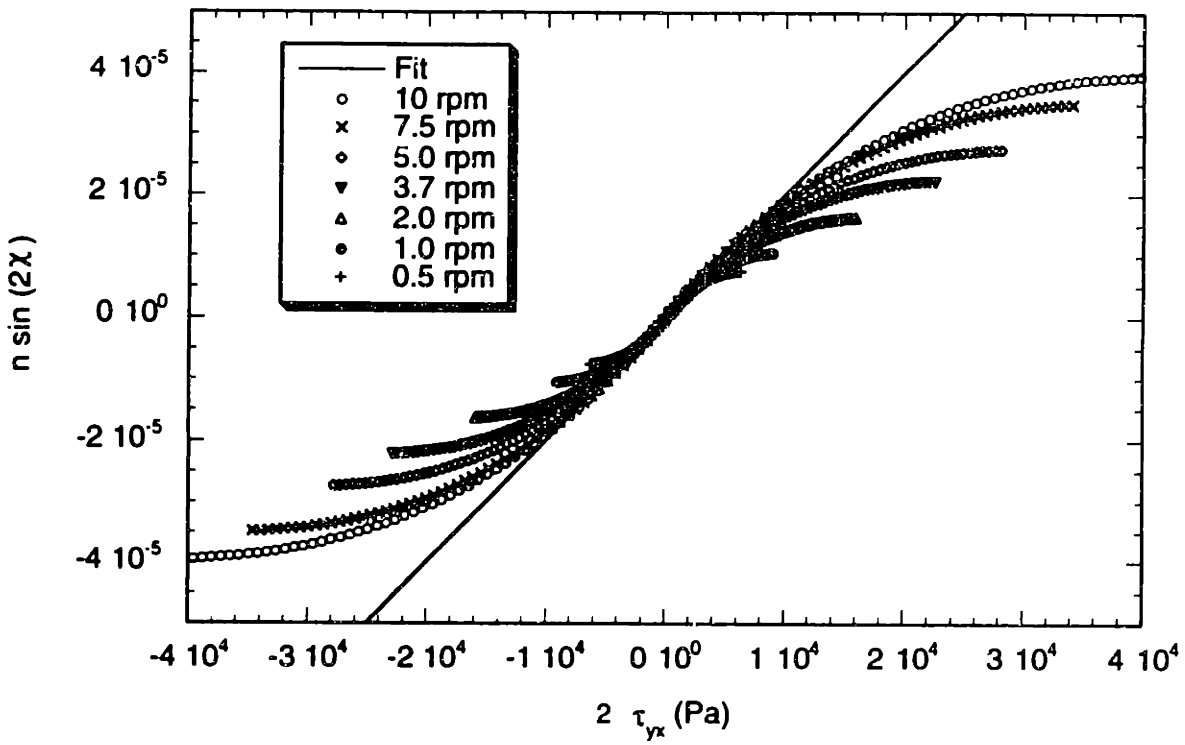

Figure 4.57: Plots of $\Delta n \sin 2\chi$ versus $2\,\tau_{yx}$ at different screw speeds. The birefringence Δn and extinction angle χ were determined from the data regression scheme described in the previous section. The shear stress τ_{yx} was measured by the pressure transducers. The slope of these plots for a purely two dimensional flow should be equal to the stress-optical coefficient of the material. The slope of the fitting line is $2 \times 10^{-9} \pm 0.2 \times 10^{-9}$ Pa^{-1}.

strictly valid for shear stresses smaller than 10^4 Pa, then for the idealized one dimensional pressure driven flow between two parallel walls, all the plots within $2\tau_{yx} = 2 \times 10^4$ Pa should be straight. The fact that they are not straight in that region suggests that there are other effects changing the ratio $\frac{\Delta n \cdot \sin 2\chi}{2\tau_{yx}}$.

To investigate whether the stress optical coefficient changed because of the "incorrect" the extinction angle profiles calculated from the regression scheme, the theoretical extinction angle profiles were calculated for each flow rate from the stress-optical rule:

$$\tan 2\chi = \frac{2 \cdot \tau_{yx}}{N_1} \tag{4.39}$$

The shear and normal stresses were calculated from the velocity and shear rate profiles obtained by using FIDAP^{TM} numerical simulation program, and the measured viscosity and first normal stress coefficients at the temperature of the experiments. Extinction angles calculated this way were substituted into $\Delta n \sin 2\chi$ and plotted against $2\tau_{yx}$ in Figure 4.58. Comparing Figures 4.57 and 4.58 one can see that both plots show the same slope at the vicinity of the centerline region. Moreover, the curves obtained by using the simulated extinction angles still show the same general shape as those obtained from the fitting method. Therefore, the changing stress-optical coefficient was not mainly caused by using extinction angle profiles.

Figures 4.59 and 4.60 show the retardance profiles computed from 0.2 rpm and 10 rpm without the edge effects. They were calculated by assuming a purely two dimensional channel without the end walls. A stress-optical coefficient of 2.0×10^{-9} Pa^{-1} was assumed in these calculations. The shear stress, the first normal stress difference profiles were computed by assuming the velocity profile obtained by FIDAP^{TM} simulation was correct. On the same plots the experimentally measured birefringence profiles were also shown. Note

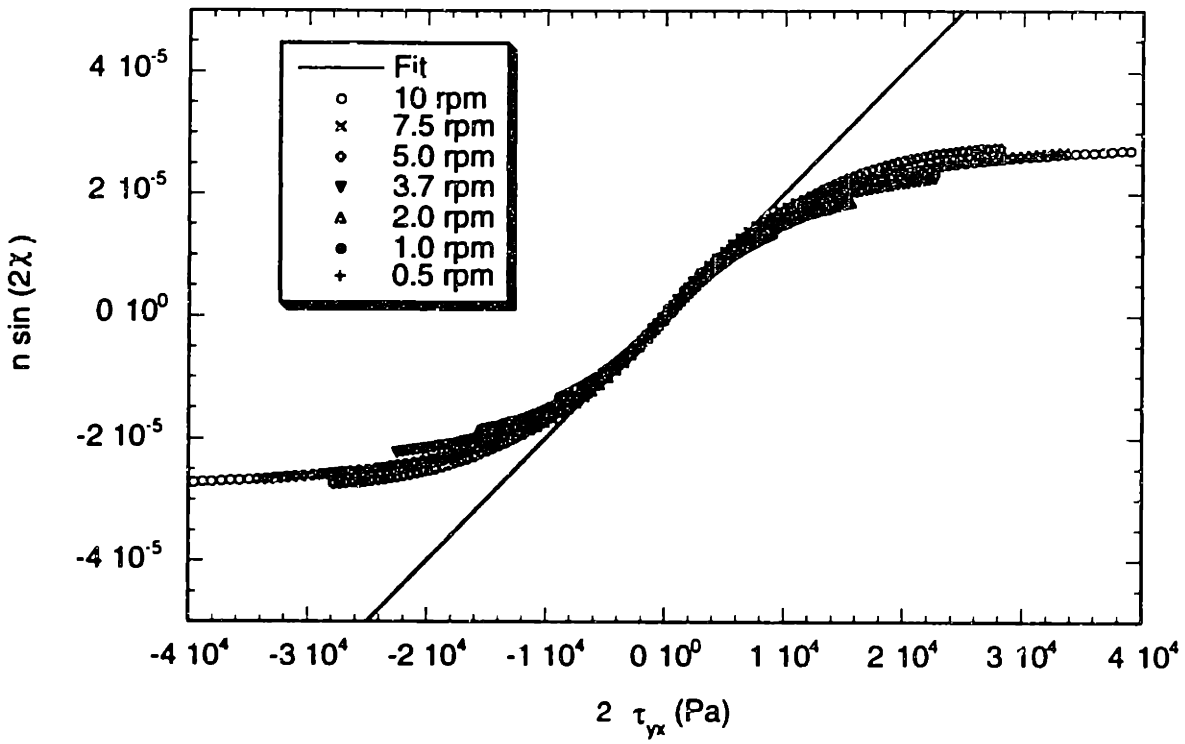

Figure 4.58: Plots of $\Delta n \sin 2\chi$ versus $2\,\tau_{yx}$ at different screw speeds. All the variables were obtained in the same way as in Figure 4.57 except that now the extinction angle was calculated by Equation 4.39. The slope of the fitting line is $2 \times 10^{-9} \pm 0.2 \times 10^{-9}$ Pa^{-1}.

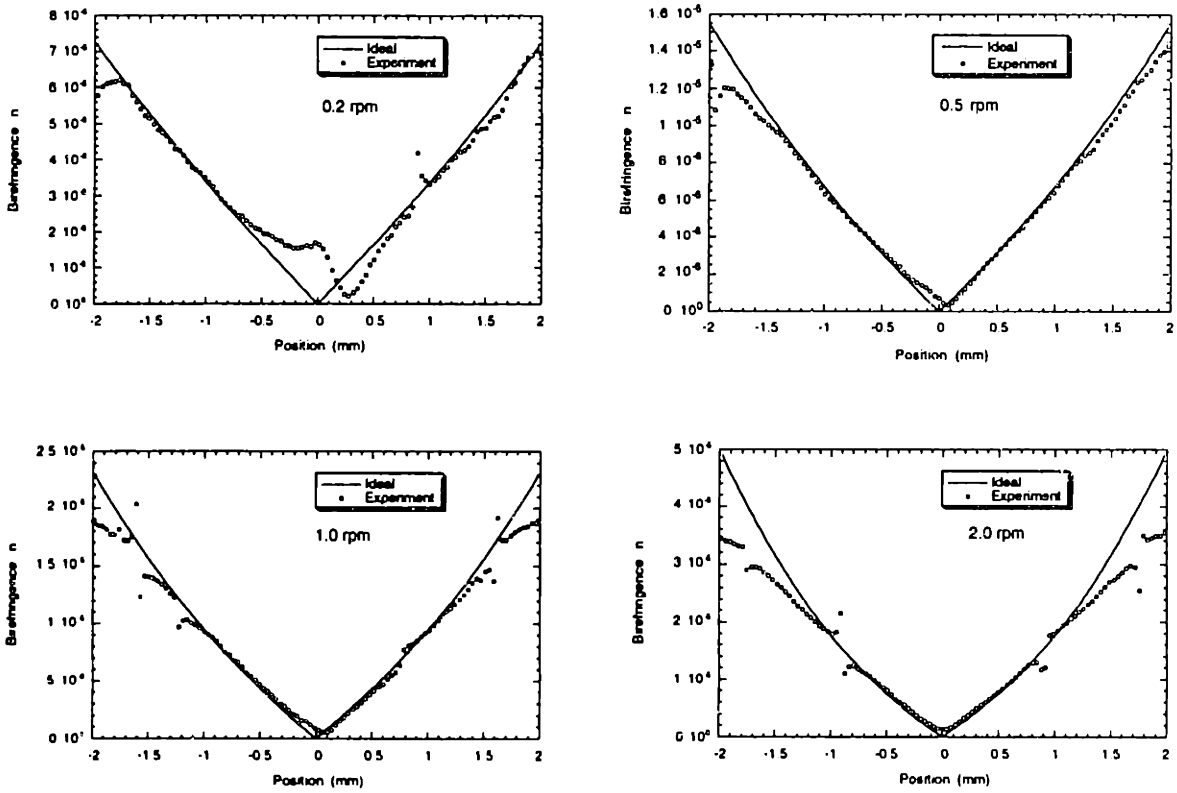

Figure 4.59: Simulated birefringence profiles compared with experimentally measured ones at different screw speeds, ranging from 0.2 rpm to 2.0 rpm.

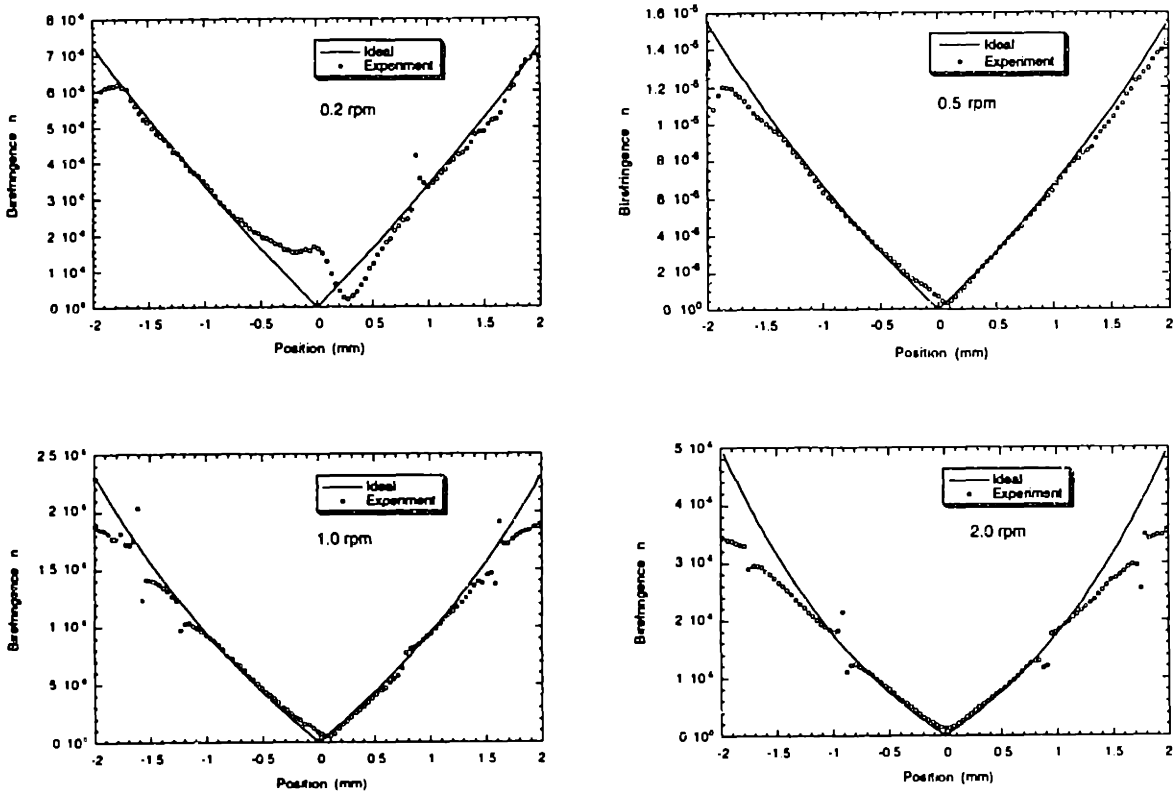

Figure 4.59: Simulated birefringence profiles compared with experimentally measured ones at different screw speeds, ranging from 0.2 rpm to 2.0 rpm.

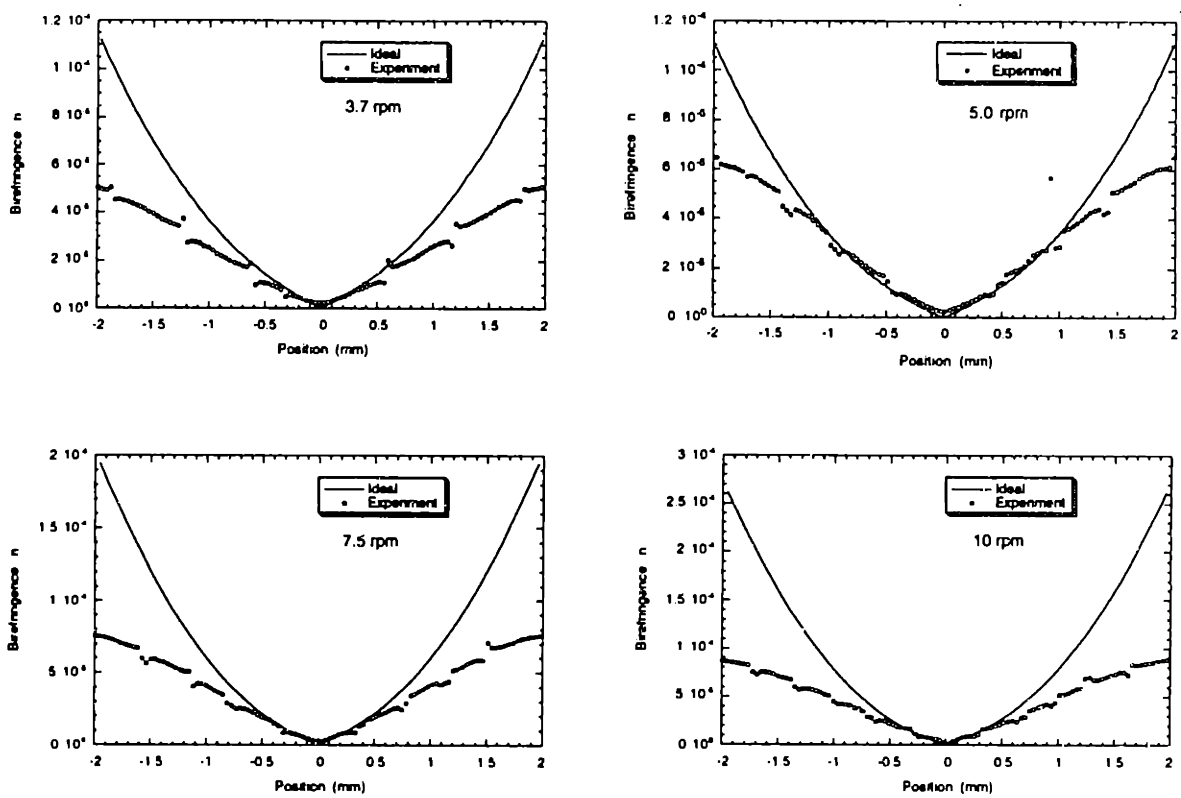

Figure 4.60: Simulated birefringence profiles compared with experimentally measured ones at different screw speeds, ranging from 3.7 rpm to 10 rpm.

that the birefringence measured experimentally does not increase as rapidly as the computed values toward the walls from zero value at the centerline. Only at birefringence level of 0.00002 or below, the ideal profile agrees with the measured one. When these two profiles agree, they are linear functions of position across the gap. This non-linear feature was not observed in any of the experimental birefringence profiles that the author is aware of. Both full-field and phase modulated birefringence experiments have shown that the birefringence or retardance measured across a slit channel can be well approximated by a linear relationship with the distance from the centerline. In fact, many full-field retardance profiles or the fringe patterns obtained with polymer flowing in a slit channel also show such a linearity with position across the gap (Han and Drexler, 1973; McHugh et al., 1985). One can easily tell the such linearity by noticing that the isochromatic fringes are separated by approximately the same distance. This distinctive linear retardance profile observed in a slit channel is most likely to be caused by the presence of the end walls. This is because the stress-optical rule has been shown to hold at such small stress levels (~4000 - 4500 Pa). If the retardance profiles were non-linear in position, such as the simulated profiles shown in Figures 4.59 and 4.60, the plot of $\Delta n \sin 2\chi$ against $2\,\tau_{yx}$ probably would not level off toward the walls.

Despite the difficulty in measuring the retardance toward the walls for an idealized two-dimensional channel flow, the measured retardance close to the center is not affected as much by the presence of the end walls. Therefore, a constant slope is observed for different flow rate when $\Delta n \sin 2\chi$ is plotted against $2\,\tau_{yx}$.The stress optical coefficient of LDPE at 160°C was estimated from the slope close to the centerline. The value was $2.0 \times 10^{-9} \pm 0.2 \times 10^{-9}$ Pa^{-1}. With the stress optical coefficient, the first normal stress difference $\tau_{xx} - \tau_{yy}$ can be calculated from the equation:

$$(n_{11} - n_{22}) \cdot \cos(2\chi) = C \cdot (\tau_{xx} - \tau_{yy}) \tag{4.40}$$

However, as discussed previously in connection with the end effects analysis, the observed birefringence near the walls will be lower than the birefringence that would have been observed if the flow were purely two dimensional in nature. If Equation 4.40 were applied directly using the observed birefringence, then the calculated first normal stress difference would be smaller than the actual value in the two dimensional flow. To avoid such reduction in birefringence for N_1 and subsequent Ψ_1 calculations, the birefringence can be calculated from the data in the centerline region. In that region, the stress optical coefficient was found to be a constant from the slope of the plot $\Delta n \sin 2\chi$ versus $2\,\tau_{yx}$. Rearranging $\Delta n \sin 2\chi = 2\,C\,\tau_{yx}$, the birefringence can be expressed as:

$$\Delta n = \frac{2 \cdot C \cdot \tau_{yx}}{\sin 2\chi} \tag{4.41}$$

After the birefringence profile was calculated at different screw speeds, the first normal stress difference N_1 was calculated by rearranging the stress optic rule:

$$N_1 = \frac{\Delta n \cdot \cos 2\chi}{C} \tag{4.42}$$

The first normal stress difference profiles calculated for the idealized one dimensional flow is shown in Figure 4.61 for different screw speeds. Only half of the channel is shown since N_1 is symmetric about the centerline. As expected, N_1 increases from zero at the centerline to a maximum at the wall and also increases with flow rate at any fixed position.

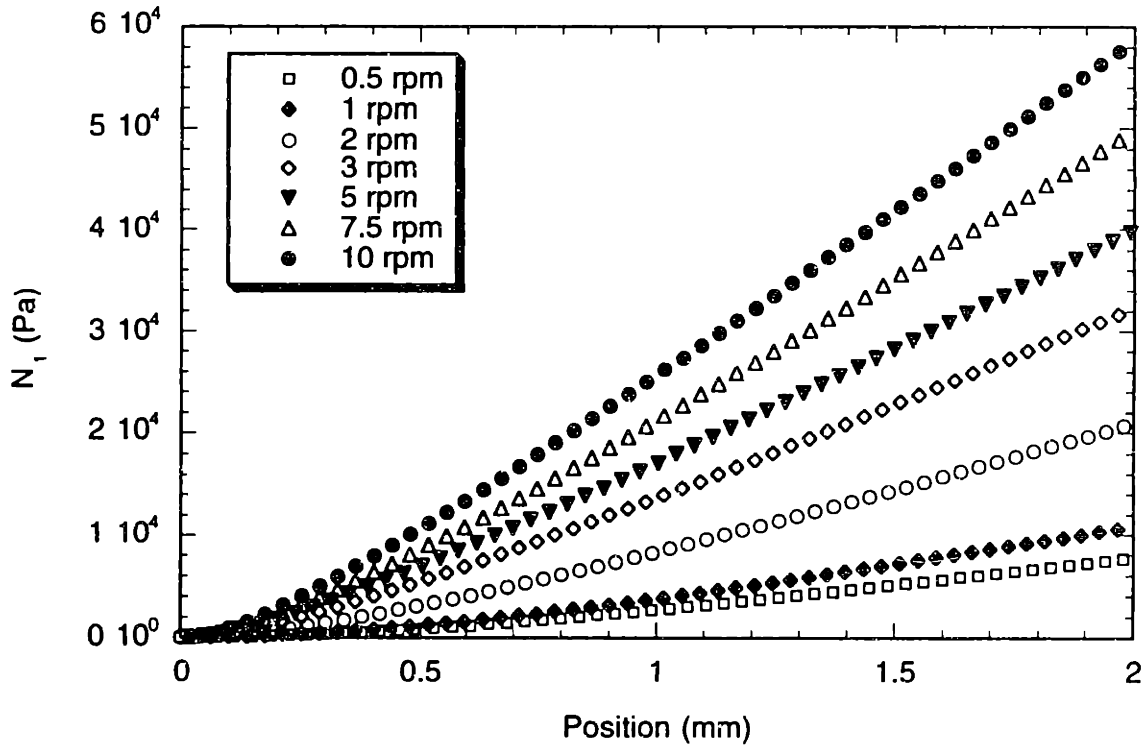

Figure 4.61: First normal stress difference profiles at different screw speeds (rpm). The results obtained from the 20 rpm case are rejected because of the unreliable retardance profile.

The first normal stress coefficient is defined as:

$$\Psi_1 = \frac{N_1}{\dot{\gamma}^2} \tag{4.43}$$

where $N_1 \equiv -(\tau_{xx} - \tau_{yy})$. At each position across the gap, the shear rate has been calculated by differentiating the velocity profile (Section 5.3). Combined with the N_1 data calculated for the two-dimensional case, the first normal stress coefficient Ψ_1 is calculated and shown as a function of shear rate in Figure 4.62. The data obtained using the parallel-plate mode of the mechanical spectrometer (RMS-800) are compared to data obtained by the optical method on the same plot. The agreement between the two methods seems to be best at higher shear rates, and the results from the five rpm run agree with the mechanical data better than the other higher speeds. The larger discrepancy in the low shear rate region is probably due to the high sensitivity of shear rate uncertainty in that region. For shear rates lower than 0.06 s^{-1}, Ψ_1 predicted by the two methods differ by 33%. For shear rates higher than 0.06 s^{-1}, the difference decreases from 20% at 0.06 s^{-1} to 7% at 1.6 s^{-1}. Recall that the uncertainty of the RMS-800 parallel plate rheometer for Ψ_1 is less than 1.5% for shear rate less than 0.06 s^{-1} and about 0.2% for $\dot{\gamma}$ larger than 0.1 s^{-1}. Clearly parallel plate rheometry offers much higher accuracy than the optical method. However, the optical method provides on-line measurement of Ψ_1 whereas the parallel plate measurement has to be done off-line. The only other methods for measuring the first normal stress difference on-line are the hole pressure method (Lodge, 1973) and the exit pressure method (Han, 1970). The hole pressure method requires very accurate measurement of the pressure difference between the bottom of the hole and along the tube at the same axial position. The normal stress predictions usually fall within the ±10% scatter band in the experimental data (Lodge, 1988). The exit pressure method seems to correlate with the first normal stress dif-

ference for polymer melts. However, the uncertainty in the velocity profile close to the exit undermines the validity of the equations which relate the first normal stress difference to the pressure at the exit.

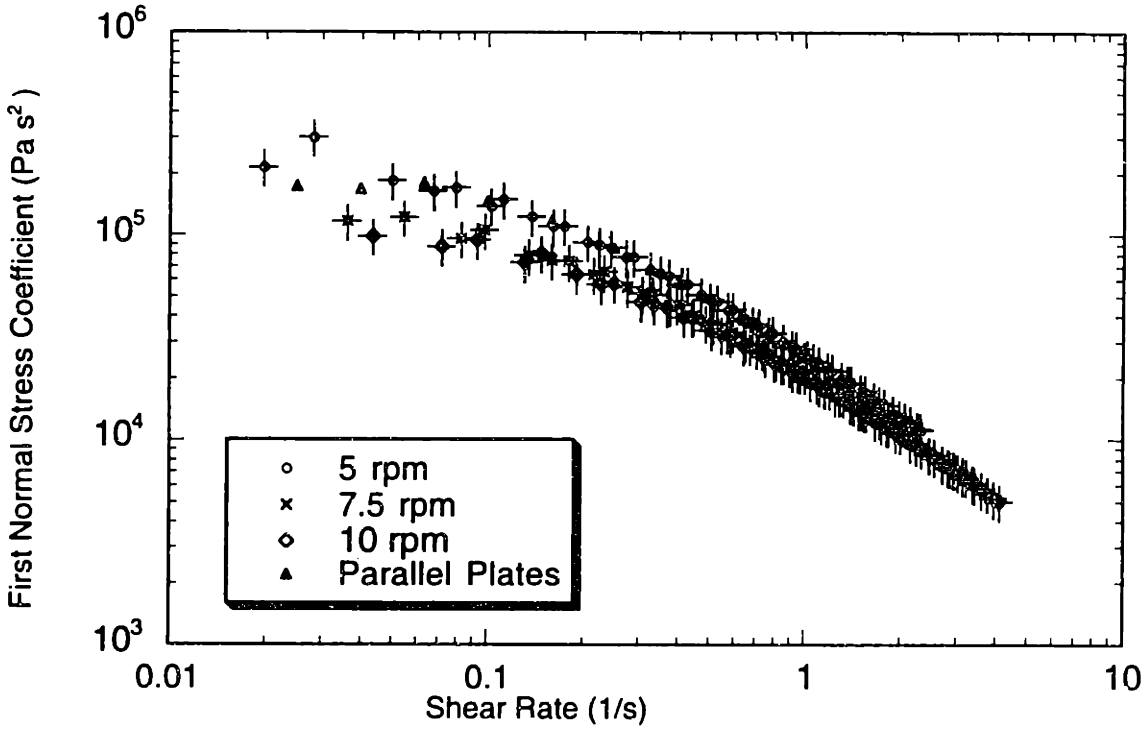

Figure 4.62: First normal stress coefficient of LDPE at 160°C as a function of shear rate. Only 3 flow rates are shown because no reliable shear rate data were obtained from other, lower screw-speed cases. Data labeled "Parallel Plates" were obtained by the parallel plate mode of a mechanical spectrometer (RMS-800).

4.4 Results from Poly(methyl methacrylate)

After establishing the accuracy of the optical methods in Sections 4.2 and 4.3, this section describes the application of this method to poly(methyl methacrylate) (PMMA). PMMA is observed to foam at processing temperatures in the range of 180°C to 260°C at atmospheric pressure. Because of foaming, conventional methods such as parallel plate rheometry fail to measure the rheological properties of this material at low shear rates. The optical method developed in this study suppresses foaming by containing the material being tested at high pressure during measurement. Hence, this method is suitable for studying the rheology of PMMA. The phenomenon of bubbling in PMMA and many other polymers is caused by unzipping (depropagation) of the polymer with monomer release (Rempp and Merrill, 1991). The kinetics of the propagation and depropagation equilibrium is discussed in Chapter 1 of this thesis. This section details the results of viscosity and first normal stress difference measurements of two types of PMMA by the optical method.

Two brands of PMMA were used in this study. The first type (Lucite 47G, ICI) came in the form of beads with size ranging from 90 μm to 250 μm. It was copolymerized with 5 mol% of ethyl acetate to reduce unzipping. The number average molecular weight ranges from 108,000 to 110,000. The intrinsic viscosity was measured to be 25.5 ml/g with acetone as the solvent at 25°C. At atmospheric pressure, the molten polymer foamed at 183°C. This value was determined by recording the temperature at which the extrudate started bubbling at the exit of the die. The second type of PMMA (Federal Plastics, C882) started foaming below 175°C. It came in pellets of length of about 3 mm. Its intrinsic viscosity in acetone was found to be 21.4 ml/g. The molecular weight was estimated from the intrinsic viscosity measurement using the Mark-Houwink coefficients determined by three

other PMMA samples with known number-averaged molecular weights (540,000, 395,000, and 75,000 g/mol). The Mark-Houwink relation states:

$$[\eta] = K \cdot (\overline{M}_v)^a \tag{4.44}$$

where $[\eta]$ is the intrinsic viscosity, K and a are the Mark-Houwink coefficients, and $\overline{M}_v$ is the viscosity-averaged molecular weight. Experimentally $\overline{M}_v$ is found to be between the number-averaged and the weight-averaged molecular weight ($\overline{M}_n$ and $\overline{M}_w$) but being closer to $\overline{M}_w$ (Young and Lovell, 1991). By using a size O Ubbelohde capillary viscometer (Cannon size "O"), the Mark-Houwink coefficients K and a at 25°C were found to be 4.1 x 10^{-3} and 0.90 respectively. Based on these coefficients, the viscosity-averaged molecular weight of the PMMA Federal Plastics C882 was found to be 160,000 g/mol.

4.4.1 Results from Lucite 47G

Because of foaming at temperatures above 183°C, conventional rotary rheometry could not be used to measure rheological properties at processing temperatures and low shear rates. At high shear rates ($\dot{\gamma} > \sim 3s^{-1}$), capillary viscometry can be used to measure the viscosity. However, at shear rates close to 3 s^{-1}, the uncertainty in the amount of friction between the plunger and the barrel became significant compared to the force required to push the polymer melt through the capillary. Hence capillary viscometry was not reliable for low shear rate measurements. In this study, the low shear rate viscosity was measured by the optical method and the high shear rate viscosity was measured by capillary viscometry. To obtain the first normal stress coefficient, rotational rheometry is not suitable because of the foaming that takes place at high temperature at atmospheric pressure. Optical method was used because foaming was suppressed during measurement.

As explained in Chapter 1 of this thesis, the shear stress and shear rate profiles of a polymer melt flowing through a slit die can be calculated from the pressure gradient along the length of the die and the measured velocity profile across the gap, respectively. At 215°C and an extrusion speed of 6.5 rpm, the Lucite 47G PMMA was extruded at an average flow rate of 0.283 g/s. The velocity profile is shown in Figure 4.63. Compared with a typical velocity profile obtained using LDPE (Figure 1.21 to 1.23), the shape of this profile is more pointed and thus better resembles a parabolic profile which is characteristic of a Newtonian fluid.

The shear rate profile was calculated by first fitting quadratic curves through every five consecutive velocity data points, and then finding the slope of each curve at the middle of the five points. The shear rate calculated this way is shown in Figure 4.64 as a function of position. The shear rate data were fitted with an exponential curve, which is also shown in the same figure.

The viscosity at each location across the gap was calculated based on the shear stress and the fitted shear rate profiles. It is expressed as a function of shear rate and compared with the viscosity measured from the capillary viscometer in Figure 4.65. The viscosity range covered by each method is complementary. It is important to note that in the high shear rate region for this material, since a log-log plot between the wall shear stress versus the volumetric flow rate did not form a straight line, one should not use a single value for the power-law index n over the decades of shear rate covered. The equation for shear rate at the wall $\dot{\gamma}_R = \frac{4Q}{\pi R^3} \cdot \left(\frac{3n+1}{4}\right)$ used by the Instron™ capillary viscometer software is true only when n is constant throughout the shear rate range of interest. Instead, one needs to calculate the wall shear rate $\dot{\gamma}_R$ from the volumetric flow rate Q and the wall shear stress τ_R by using the Rabinowitsch equation (Bird et al., 1987):

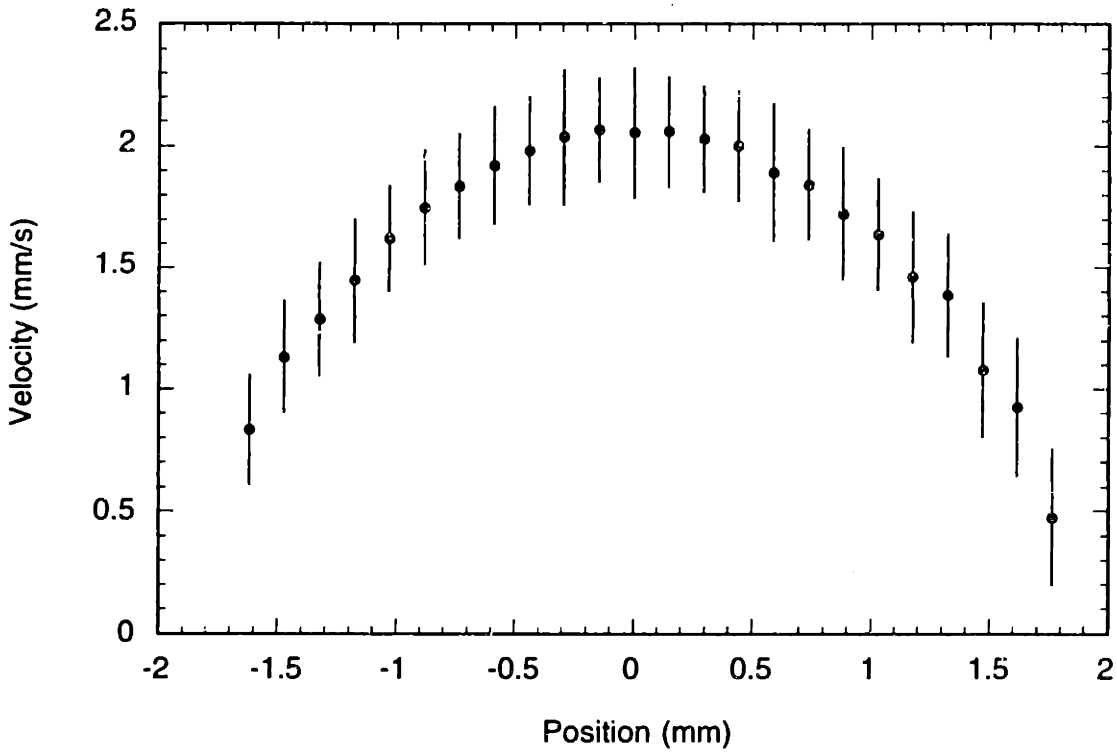

Figure 4.63: Velocity profile of Lucite 47G at 215°C and 6.5 rpm. The error bars represent one standard deviation of the velocity distribution obtained from 1000 bursts.

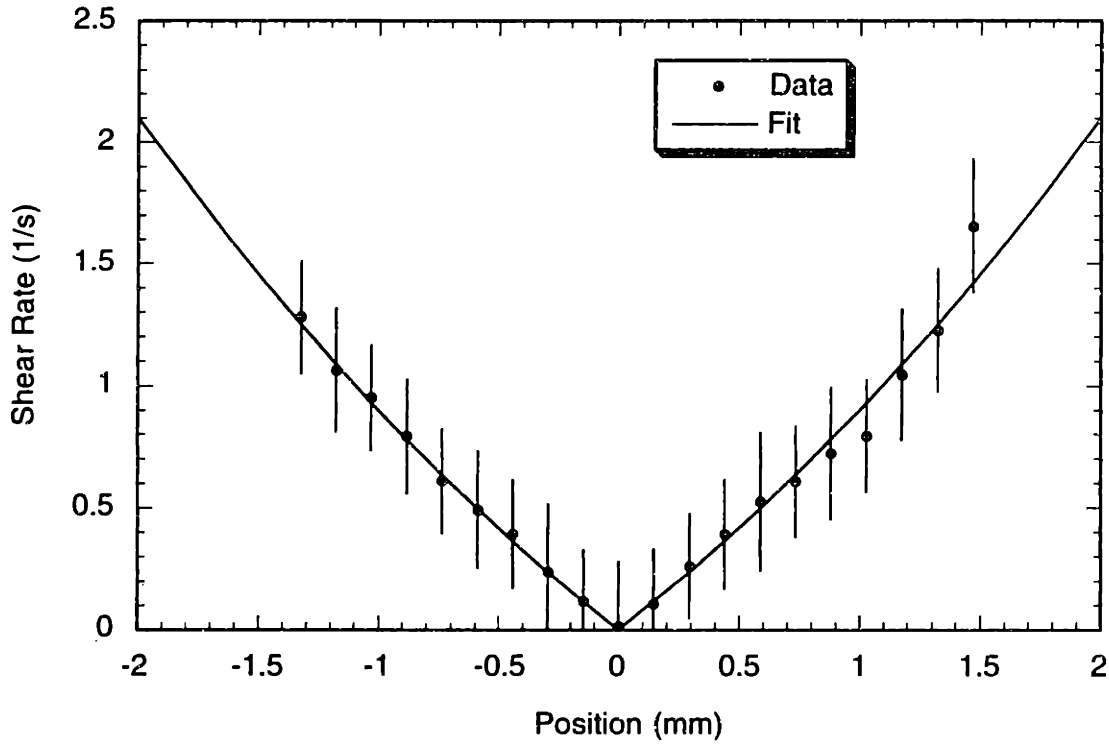

Figure 4.64: Shear rate profile of Lucite 47G at 215°C and 6.5 rpm. The error bars represent one standard deviation of the velocity distribution.

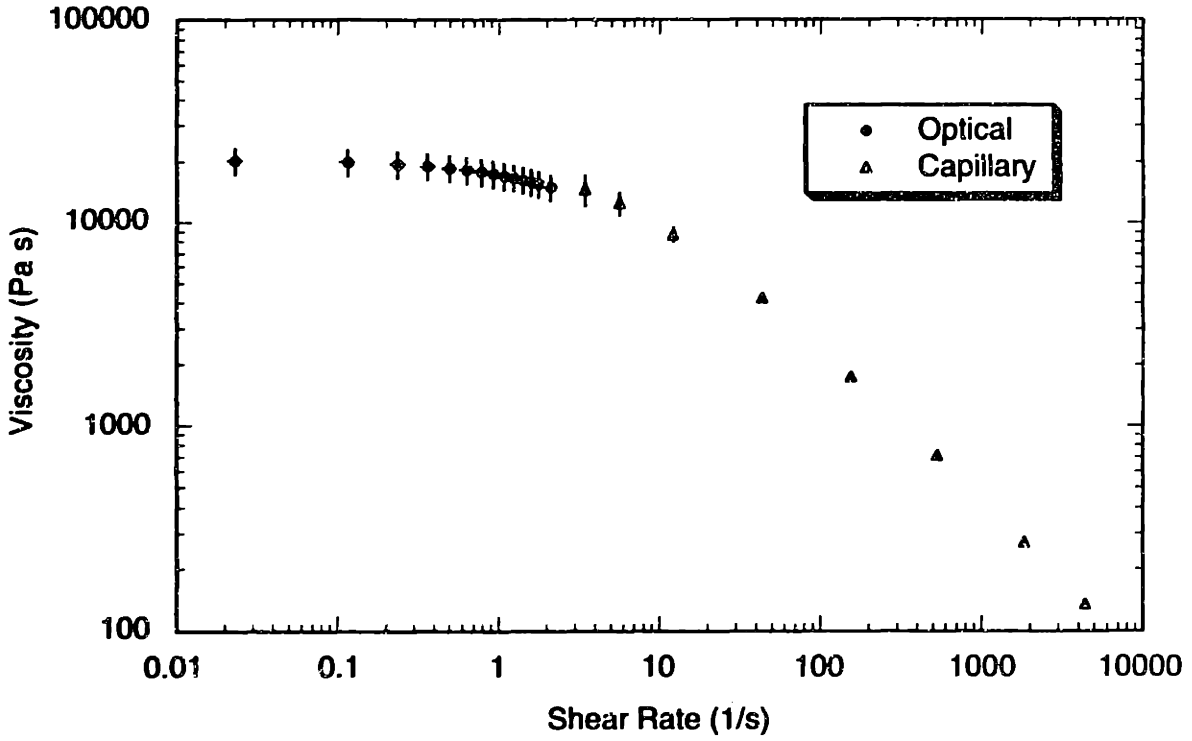

Figure 4.65: Viscosity determined by the optical method at 215°C and 6.5 rpm compared to the data obtained by capillary viscometry.

$$\dot{\gamma}_R = \frac{1}{\tau_R^2}\frac{d}{d\tau_R}\left[\tau_R^3 \cdot \frac{Q}{\pi R^3}\right]. \tag{4.45}$$

To calculate the first normal stress coefficient, it is necessary first to determine the first normal stress difference profile across the gap. The stress-optic rule relates the stress tensor to the refractive index tensor by the stress-optical coefficient C. The stress-optical coefficient C for PMMA at the temperature of the experiment (215°C) was determined from the plot of $\Delta n \sin(2\chi)$ against $2\,\tau_{yx}$ (Figure 4.66). The plot was fit with a straight line through the origin, and its slope was found to be $6.3 \times 10^{-11} \pm 0.2 \times 10^{-11}$ Pa^{-1}. Retting (1979) obtained a stress-optical coefficient of 1.11×10^{-10} Pa^{-1} at 140°C. According to the theory of rubber elasticity, the magnitude of C scales as inverse absolute temperature. However, for polystyrene this temperature dependence of C was observed only for a limited temperature range (Retting, 1979).

Figures 4.67 and 4.68 show the retardance and extinction angle profiles fit by the procedures described in the Section 4.3. The maximum level of retardance achieved was less than 360°, and therefore was not measurable by the fringe-counting method with full-field birefringence. The maximum shear stress attained in this experiment was 32000 Pa. For LDPE in a case with similar shear stress (20 rpm, τ_w=29000 Pa), the maximum retardance was about 2700°. This large difference in retardance shows that it requires a lot more stress to change the optical properties of PMMA than to change those of LDPE. This is a reflection of the difference in the stress-optical coefficients. Recall that the stress-optical coefficient for LDPE was found to be in the order of 10^{-9} Pa^{-1} in this study and by other researchers (for example, Wales, 1976), whereas the stress-optical coefficient of PMMA was found to be in the order of 10^{-10} to 10^{-11} Pa^{-1}.

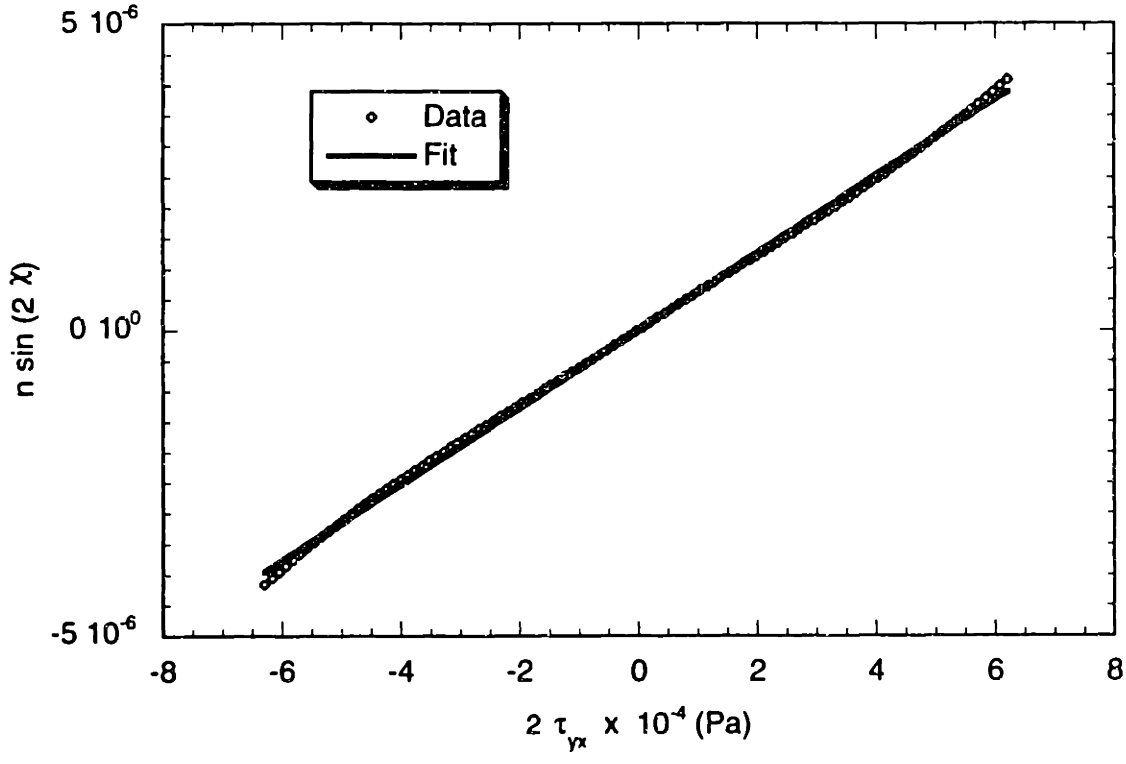

Figure 4.66: Plot of $\Delta n \sin 2\chi$ versus $2\,\tau_{yx}$ at 215°C and 6.5 rpm. The slope of this plot is equal to the stress-optical coefficient of the material at this temperature. The slope of the best fit line is $6.3 \times 10^{-11} \pm 0.2 \times 10^{-11}$ Pa^{-1}.

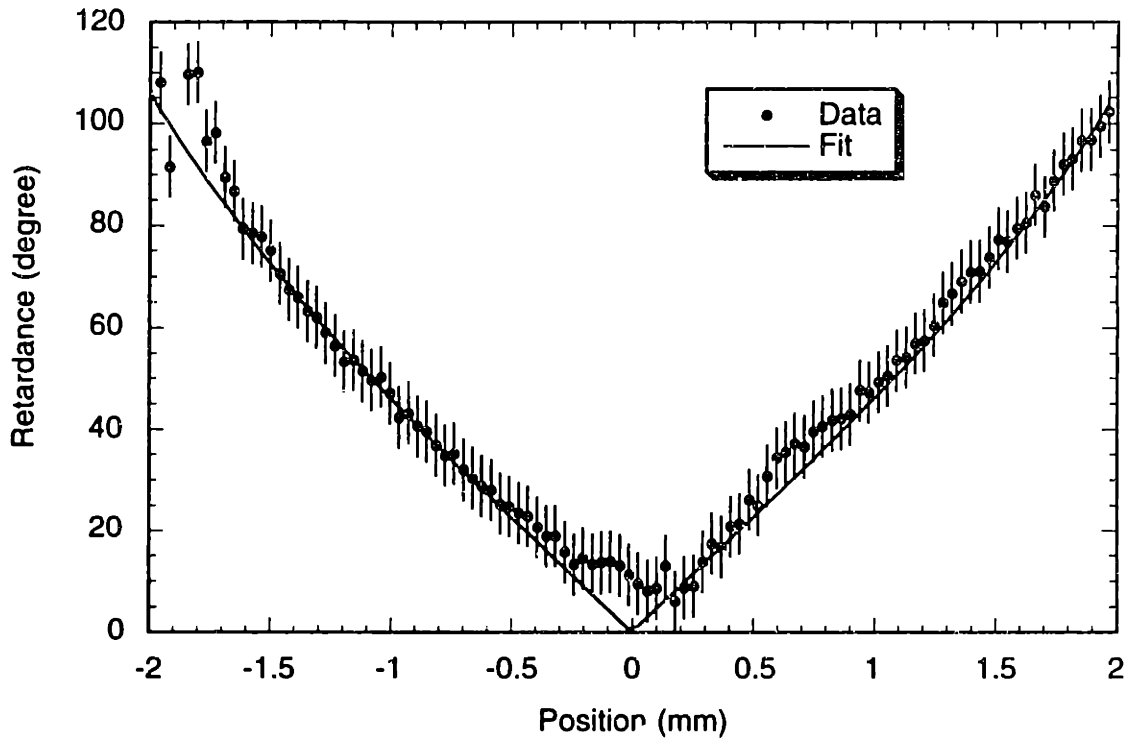

Figure 4.67: Retardance profile of Lucite 47G across the width of the channel at 215°C and 6.5 rpm. The fitting equation is of the form $y = ax^4 + bx^3 + cx^2 + dx + e$. The error bars are $\pm$ 6°.

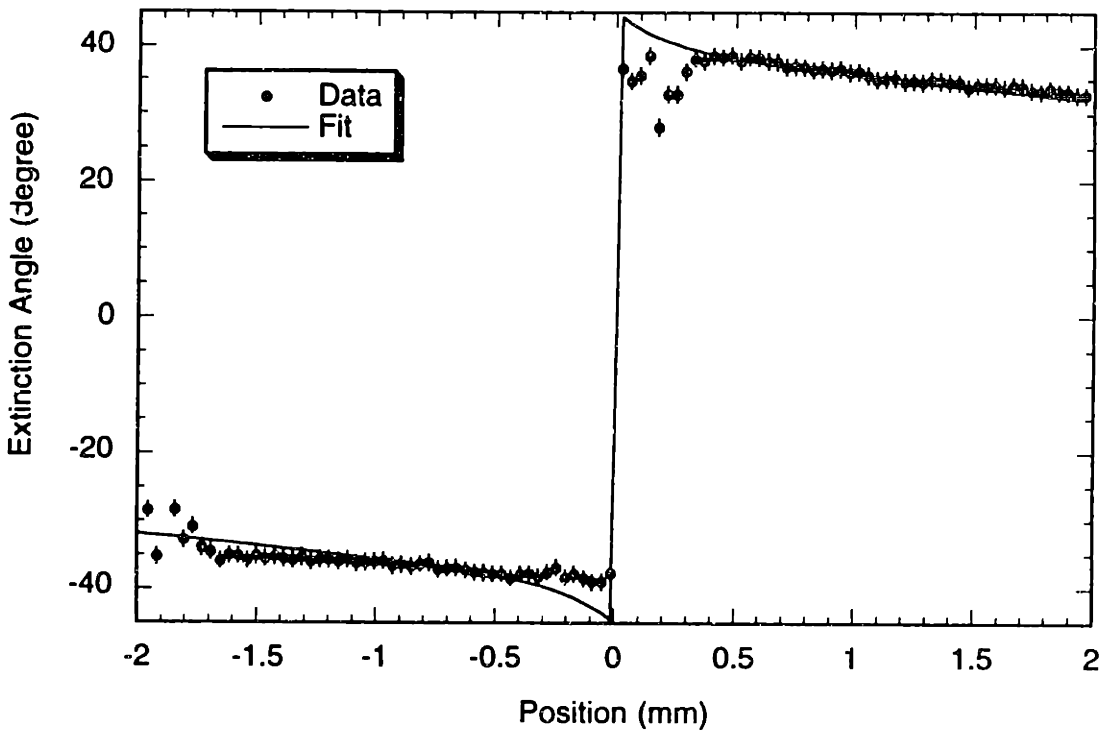

Figure 4.68: Extinction angle profile of Lucite 47G at 215°C and 6.5 rpm. The fitting equation is of the form $y = \sum_{i=1}^{5} a_i e^{b_i x}$. The error bars in the data are ± 1.2°.

Combining the first normal stress difference profile calculated from the birefringence measurements and the shear rate profile determined from LDV, the first normal stress coefficient was calculated at various shear rates (Figure 4.69). This coefficient started decreasing with shear rate at about 0.02 s^{-1}. The author is aware of no other existing data to compared with, since low shear rate data at high temperatures are not generally obtainable with mechanical methods.

4.4.2 Results from Federal Plastics C882

The viscosity of the second type of PMMA was measured by both the optical method and by capillary viscometry. This material was extruded at three different flow rates, corresponding to screw speeds of 6.5 rpm, 10.3 rpm, and 13.4 rpm. The velocity profiles measured in each case are shown in Figure 4.70. Similar to the velocity profiles of LDPE reported in Section 4.2, there was a lack of reliable data close to the metal wall farthest away from the probe due to light reflection by the metal wall. The shear rate profiles were again fit with exponential functions and are shown in Figure 4.71. The coefficients of these functions are given in Table 4.5. Notice that at the lowest speed, the shear rate profile resembles a straight line within $\pm$ 1 mm from the centerline, indicating Newtonian viscosity in that region.

Screw speed (rpm)	a	b	c
6.5	9.09	0.122	-9.09
10.3	8.49	0.193	-8.49
13.4	4.71	0.387	-4.71

Table 4.5: Coefficients of shear rate fitting equations of the form $y=a\ e^{bx} + c$

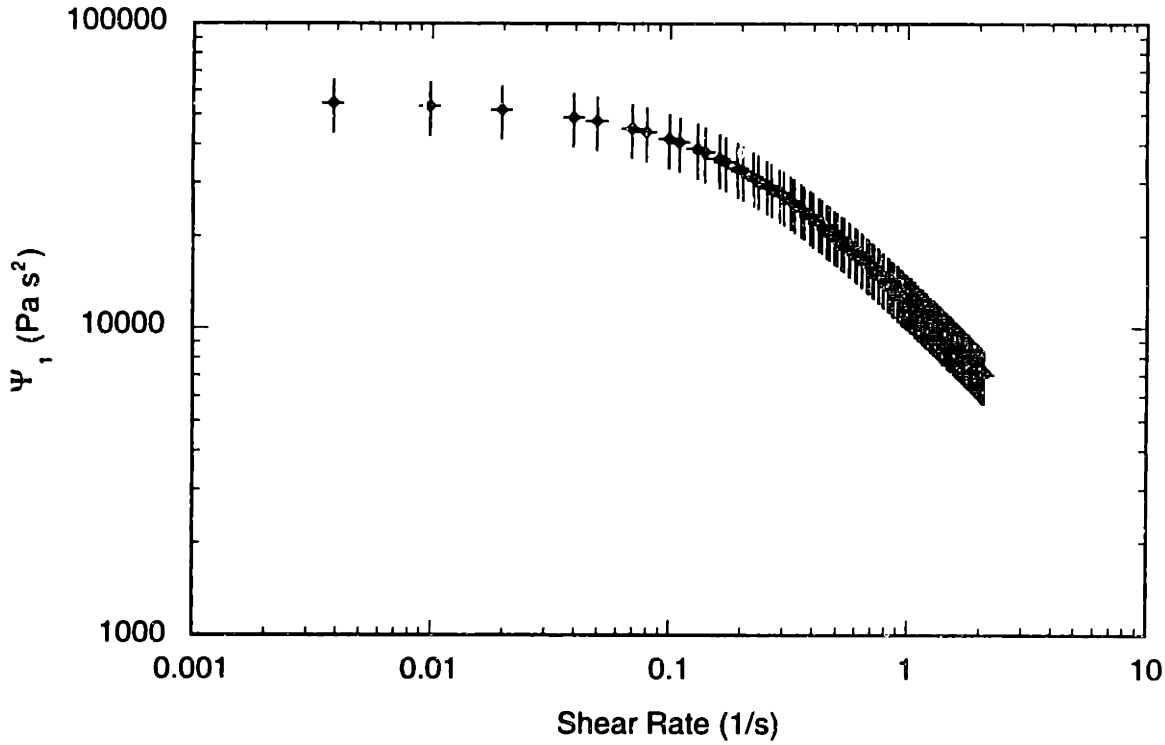

Figure 4.69: First normal stress coefficient of Lucite 47G at 215°C obtained at 6.5 rpm from the optical method.

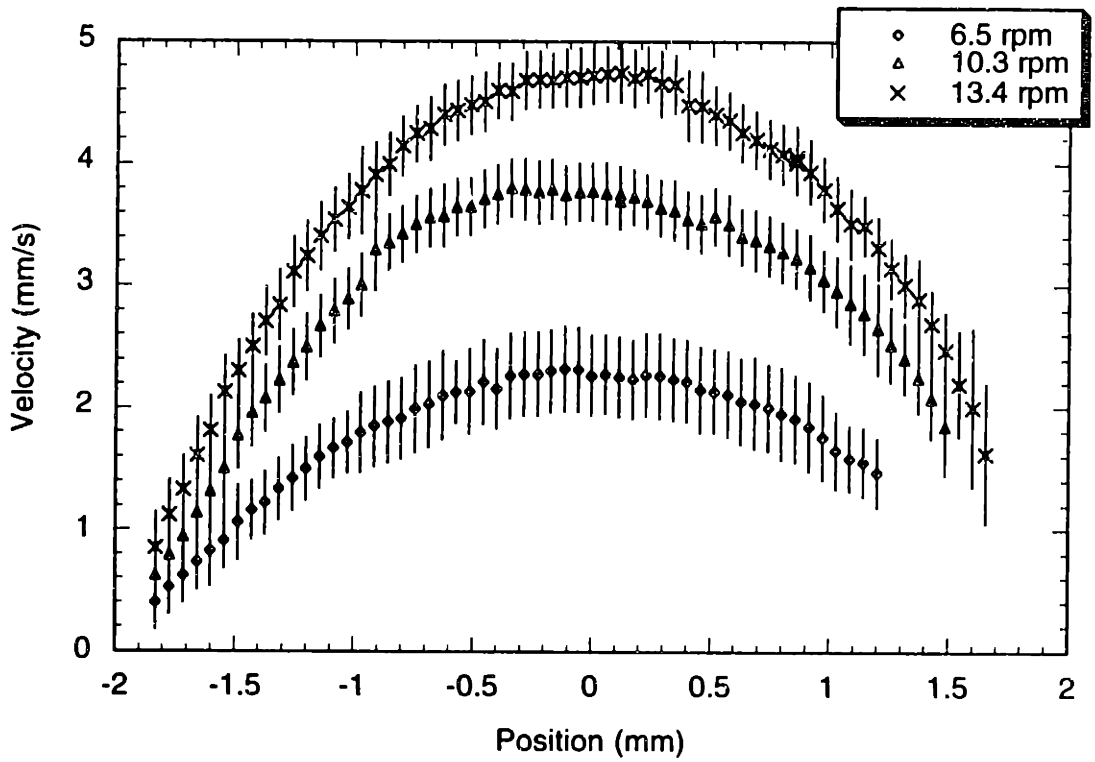

Figure 4.70: Velocity profiles of Federal Plastics C882 at 215°C and different screw speeds. The error bars represent one standard deviation of the velocity distribution obtained from 1000 bursts.

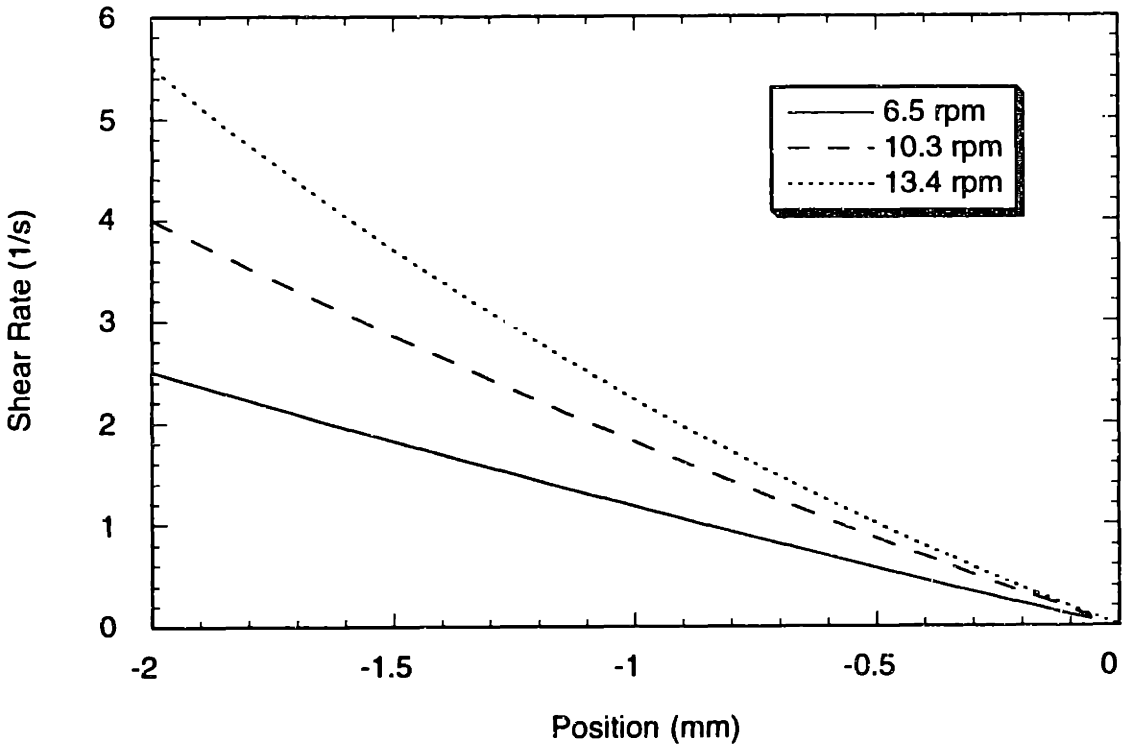

Figure 4.71: Fitted shear rate profiles of Federal Plastics C882 at 215°C and different screw speeds. The fitting equations are of the form $y = a\, e^{bx} + c$.

The viscosity profiles from these three cases are shown in Figure 4.72, along with the capillary viscometry measurements at high shear rates. The three viscosity curves calculated at the three speeds collapsed into one on this graph. The highest shear rate attained in these cases was 5.1 s^{-1}, larger than the lowest shear rate measured by the capillary viscometer. However, a much larger overlap region in shear rate was not obtainable for this material. This is because for the optical method the highest shear rate attainable was set by the extruder power, whereas for capillary viscometry the lowest shear rate was set by size of the frictional drag compared to the total force required.

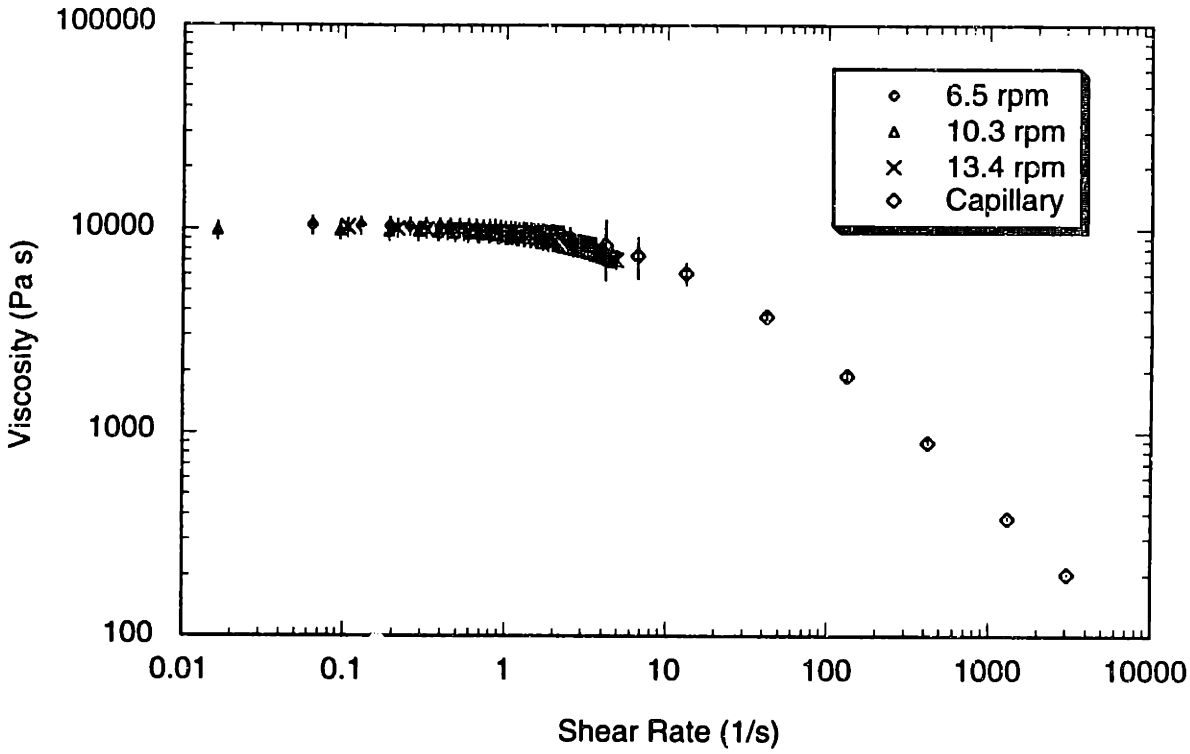

Figure 4.72: Viscosity of Federal Plastics C882 calculated from the optical method at 215°C and different screw speeds compared to the data obtained by capillary viscometry.

Chapter 5

Conclusions

This thesis describes the development and application of an optical method which measures the viscosity and first normal stress coefficient of polymer melts. This project was motivated by the need to measure the rheological properties of materials which foam at processing temperatures and one atmospheric pressure. Poly(methyl methacrylate) or PMMA and starch/poly(ethylene-co-vinyl alcohol) are examples of such materials. In developing this optical method, low density polyethylene (LDPE) was used as a test material. The shear-rate-dependent viscosity η and first normal stress coefficient Ψ_1 of LDPE were measured by both optical and mechanical methods, and the results were compared. To demonstrate an application of this optical method, η and Ψ_1 of PMMA were measured as functions of shear rate at processing temperature. Also, to correctly interpret the experimental data collected from the birefringence apparatus, the effects of the finite cross-sectional area of the laser beam and the presence of the end walls on the retardance and extinction angle profiles were analyzed. This chapter summaries the contributions of this project to experimental measurement of flow birefringence and rheological measurement techniques.

A number of researchers have studied the retardance and extinction angle profiles across the width of a slit channel produced by polymer melts flowing down a such a channel. Table 5.1 summaries their approaches to this problem. Using full-field birefringence method, Wales (1976) and McHugh et al. (1987) reported that the fine isoclinic lines, which were necessary for calculating the extinction angle profile, could not be identified.

Reference	Experiment: Full-field	Experiment: Point-wise	Theoretical
Wales (1976)	x		
McHugh et al. (1987)	x		
Galante and Frattini (1991)			x
This study		x	

Table 5.1: Summary of birefringence studies of polymer melts in a slit channel

Instead, thick dark bands were always observed whose width could increase to occupy half of the flow channel. The lack of information on the extinction angle prohibited the researchers from studying the stress field throughout the channel. Wales (1976) stated that the orientation of the molecules close to the observing windows (end walls) and the changing refractive index due to frictional heating were two probable explanations for the existence of the thick isoclinic bands. McHugh et al. (1987) concluded that relatively high shear rates ($\dot{\gamma}_{12} > 500\ s^{-1}$) were needed in order to induce temperature gradients (>10°C) sufficient to affect the velocity profile and shear rate distributions ($\dot{\gamma}_{13}$ and $\dot{\gamma}_{12}$). Therefore, friction heating should not be the primary explanation. They advocated using the inside edge of the dark band as the location of the isoclinic line based on their stress variation analysis along the beam propagation direction. However, Mackay (1985) acknowledged that this "rule" did not yield a constant stress-optical coefficient for all the polymers he tested. Galante and Frattini (1991) used differential propagation Mueller matrices to calculate the retardance and extinction angle profiles for a upper-convected Maxwell fluid model. They predicted the occurrence of periodic variations in the extinction angle profiles for high nominal retardance and Weissenberg numbers (Section 4.3). In this study, the extinction angle profiles of LDPE melt across a rectangular gap under a pressure-driven

flow were measured using point-wise birefringence method. The author is not aware of any other extinction angle profiles obtained experimentally from a channel flow to compare with. The experimental profiles did not show the expected decreasing behavior toward the walls in general and contained spikes at positions corresponding to retardance of 360° or its multiples. Moreover, the experimentally measured retardance profiles contained gaps at the same positions. In Sections 4.3.4 and 4.3.3, the effects of the finite beam cross-sectional area and the effects of the end walls were analyzed. It was found that the gaps in the retardance profiles and the shapes of the extinction angle profiles could be attributed primarily to the finite beam cross-sectional area. In addition, the simulated retardance profiles obtained by considering the effects of the end walls using differential propagation Mueller matrices did not show the linear dependence on distance across the gap as observed in most experiments (McHugh et al., 1987; Han and Drexler, 1973; this thesis). Therefore, the validity of the assumptions behind the edge effect analysis may be questionable. The main assumptions include neglecting the influence of the stress components other than τ_{yx}, τ_{xx} and τ_{yy} in the analysis of the inhomogeneity along the beam propagation direction.

A data regression scheme was devised to recover the extinction angle profiles at the limit of infinitesimal beam size based on the measured intensity distribution of the beam over its cross-sectional area. The extinction angles calculated using this method decreased with increasing flow rates at a fixed position inside the gap as expected. Moreover, the stress-optical coefficient obtained using this method is the same as that obtained the extinction angle was known a priori.

The optical method developed in this study provides an alternative way to measure the viscosity and first normal stress coefficient of polymer melts in addition to the conventional mechanical methods. Table 5.2 lists the common methods for viscosity measure-

ment. These methods are compared by their ability to measure in different shear rate ranges, and whether the measurement can be done on-line. For the purpose of comparison, shear rates below a critical shear rate of 3 s^{-1} is defined to be low shear rates, whereas shear rates of 3 s^{-1} or above is defined as high. This critical shear rate was chosen based on the author's experience with these methods during viscosity measurement of LDPE at 160°C.

Method	Low shear rates	High shear rates	On-line
Cone-and-plate or parallel-plates	x		
Capillary		x	
Die viscometer		x	x
LDV & pressure transducers	x	x	x

Table 5.2: Comparison of different methods in measuring polymer melt viscosity

From Table 5.2, one can see that the first two conventional mechanical methods, namely the cone-and-plate or parallel-plates viscometry, and the capillary viscometry are complementary in their applicable shear rates ranges. The cone-and-plate or parallel-plates method can be used indirectly to calculated viscosity at high shear rates from dynamic oscillatory measurements using Cox-Merz rule (Bird et al., 1987). This rule states that viscosity can be approximated by the magnitude of the complex viscosity at corresponding values of frequency and shear rate (Section 2.1). Neither cone-and plate nor parallel-plates method can be adapted easily to probe any changes in rheological properties in a continuously running production line. In contrast, a die viscometer can be readily adapted to measure viscosity of material flowing in a continuous production line in real time. However, this viscometer is not applicable for low shear rate measurements, which corresponds to low flow rates inside the die. This is because firstly, a steady and very low

flow rate is difficult to be maintained by a commercial extruder designed to have a high throughput, and secondly, the signal-to-noise ratio of the pressure measurements is very low at such flow rates, thus introducing large uncertainties in the measurements. The optical method developed in this study has been shown to measure viscosity over a range of shear rates (<0.01 s^{-1} to ~5 s^{-1}) to within 25% agreement with conventional methods. The upper shear rate limit for viscosity measurement is determined by the power of the extruder and the dimensions of the die channel. The extruder-die assembly used in this study allows common polymers such as LDPE to flow at a maximum shear rate of about 50 s^{-1} (Section 4.2). The system built for this study can also be adapted to probe viscosity changes in a production line in real time. The zero-shear-rate viscosity is always obtainable because measurements can be made at the zero-shear-rate region at the centerline of the die channel. The drawback of the optical method is that the material studied has to be transparent enough for the laser beams to penetrate into the flow.

Table 5.3 summaries the major existing methods to measure the first normal stress coefficient of polymer melts. Again, these methods are compared in terms of their applicable shear rate ranges, and whether the method can be adapted for on-line measurement. The first normal stress coefficient Ψ_1 is most commonly measured by the cone-and-plate or parallel-plates methods. Similar to viscosity measurements, the high shear rate Ψ_1 data are not obtainable directly from these methods. Laun's rule provides a way to estimate Ψ_1 from linear viscoelastic measurements (Bird et al., 1987):

$$\Psi_1(\dot{\gamma}) = \frac{2\eta''(\omega)}{\omega}\left[1+\left(\frac{\eta''}{\eta'}\right)^2\right]^{-0.7}\Bigg|_{\omega=\dot{\gamma}} \tag{5.1}$$

where η' and η'' are defined by $\eta'=G'/\omega$ and $\eta''=G''/\omega$, G' and G" are the storage and loss moduli, respectively, ω is the frequency of oscillation, and $\dot{\gamma}$ is the shear rate. This rule

has been shown to predict Ψ_1 accurately for a number of polymers (Laun, 1986).

Method	Low shear rates	High shear rates	On-line
Cone-and-plate or parallel plates	x		
Hole pressure		x	x
Exit pressure		x	x
LDV & birefringence	x	x	x

Table 5.3: Comparison of methods to measure first normal stress coefficient of polymer melts

The hole pressure method calculates Ψ_1 from the difference in pressures measured by a flushed-mounted and a hole-mounted pressure transducer located at the same distance from the die exit (Lodge, 1973). Because this pressure difference is very small compared to the local pressure, it is difficult to determine Ψ_1 accurately. Moreover, the result obtained from this method is sensitive to the finite area of the transducer probe (Lodge, 1988). Another on-line method to measure Ψ_1 is to study the pressure at the die exit (Han, 1973). The so-called "exit pressure" has to be linearly extrapolated from pressure readings along the length of a slit or capillary die. However, complicated flow rearrangement that happens at the die exit may undermine the ability of the equations used in the method to describe the actual pressure distribution. The optical method developed in this study has been shown to measure Ψ_1 of LDPE at 160°C. The results agree with those measured by parallel-plate rheometry to within 33%. This method can measure Ψ_1 on-line at low shear rates. However, at high shear rates higher than about 10 s^{-1}, this method ceases to give reliable results. This is because at high flow rates, the number of fringes covered by the cross-sectional area of a laser beam increases beyond the resolution of the experimental apparatus, as shown in the 20 rpm case (Section 4.3).

Appendix A

Low-Moisture Starch Blends Study

As discussed in Chapter 1, starch rheology is difficult to measure due to foaming of water during low shear rate measurements in a rotational rheometer on the one hand, and due to the changing thermo-mechanical history during high shear rate measurements in a capillary viscometer on the other. The optical method developed in this study is capable of suppressing foaming and thus would be a candidate for measuring starch rheology. Moreover, the optical method measures rheological properties at different shear rates without changing the flow rate, thus maintaining a constant thermo-mechanical history of the material. Despite these advantages, the optical method was not able to measure the rheological properties of the starch blends that were used in this study. The blends consisted of three basic components, starch, poly(ethylene-co-vinyl alcohol) (EVOH), and glycerine, along with a small amount of other plasticizers. The ratios of starch to EVOH include 100:0, 70:30, 50:50, and 30:70. Fifteen percent of the total weight of each blend is glycerol. Three starch types were included in this study, and they have different amylose-amylopectin proportions. Amylose is the non-branched glucose link while amylopectin is the branched version. Waxy maize contains over 99% amylopectin, native corn contains 70% amylopectin and 30% amylose, and Hylon VII contains about 30% amylopectin and 70% amylose. There were a total of 12 blends with different compositions. Simmons (1995) provides a detailed description of the composition of these blends.

These blends were chosen for this study because their morphology was well-characterized by Simmons (1995) by using scanning electron microscopy (SEM) and transmission electron microscopy (TEM). Moreover, Villar et al. (1994) studied the viscosity of these

blends with capillary viscometry. Rheological information about these blends would be complementary to these results in terms of understanding the effects of starch-EVOH ratio and amylose-amylopectin ratio on material structure and properties.

The optical method failed because the laser beams for neither velocity nor birefringence measurement could penetrate into the interior of the flow. The power of the LDV and the birefringence beams were 25 mW and 2.5 mW, respectively. Both of the light beams were diffused and scattered upon entering the fluid. The scattering of light probably occurred at the phase boundaries between the different components. Scanning electron microscopy and transmission electron microscopy studies on these blends in the solid state revealed the presence of starch-rich and EVOH-rich domains (Simmons, 1995). EVOH was found to be the matrix component up to 70% of starch. The starch domain size decreased as amylose content was increased. The domain size measured by SEM for the waxy maize-EVOH blends ranged from less than 0.1 μm to about 10 μm, and of the order of 1 μm or smaller for the native corn and Hylon VII blends (Simmons, 1995). The wavelengths of the lasers used for LDV and birefringence studies were 514.5 nm and 632.8 nm, respectively. It was likely that the these laser beams were scattered by domain sizes in the same order as the wavelengths.

The other factor that prohibited rheological measurement for some of the blends was the migration of EVOH. Transparent layers of EVOH were seen coating the extrudate of the high EVOH blends (starch/EVOH=30/70). At the shear rates of the optical experiments (order of 1 to 10 s^{-1}), the viscosity of EVOH is lower than that of starch (Villar et al., 1994; Sagar, 1994). Thus the low viscosity component tended to shield the more viscous one from the highest stress region along the edge by migrating to the edge. Simmons (1995) also observed EVOH coating on the outer surface in some of her spun fibers.

The higher power LDV beams also did not penetrate into the blends with no EVOH components. For these blends, the boundaries between the starch and the micro-voids of plasticizer as observed by Simmons (1995) might have contributed to the scattering. Moreover, scattering could also occur if any crystalline phase of starch was present. Although the starch components in the blends had been destructurized when the blends were compounded about six years ago, crystalline phases might have formed in the starch-rich domains due to retrogradation. Waxy maize blends are known to undergo crystallization over time (Simmons, 1995). Crystallization of amylopectin is facilitated by the presence of water in amounts greater than 14%. However, wide-angle X-ray diffraction (WAXS) measurements of the waxy maize blend with no EVOH (with ~8% moisture, preconditioned at 25°C and 65% relative humidity) by Simmons (1995) did not show a peak indicative of crystalline structure after 2 years of aging. The moisture content of the unconditioned blends were lower than 8% due to moisture uptake from the blends to the atmosphere. Therefore, the low humidity (~20 - 30% relative humidity) of the storage environment has not been favorable to crystallization. Nonetheless, WAXS measurements on the six-year-old blends would be needed to conclude more definitively whether retrogradation had occurred.

Although the optical method was found to be unsuitable for the starch blends, the viscosity of some of these blends was nonetheless measured by using the extruder-die assembly as a slit die viscometer. Before discussing the results, a number of points were noted during extrusion of these blends. First, there was only a small operating window in terms of the screw speed and extrusion temperature. This is because the high pressure needed to suppress water evaporation inside the die demanded a low operating temperature and a high screw speed. Under such condition the power input to the was very high. If the current drawn by the extruder reached the safety limit set by the circuit breaker, the extruder

would turn off automatically, and the pressure inside the die and the barrel would decrease to a level where water would evaporate. Therefore, these blends can only be extruded at a limited window of operating conditions. Second, the pressure gradient fluctuated more severely over time during starch blend extrusion than during extrusion of common thermoplastics. The pressure gradient could vary by up to 13% in about an hour whereas the variation for LDPE was typically about 5 - 7% maximum. The excessive fluctuation in pressure might be due to the formation of steam packets inside the barrel or the die whenever the extruder was shut off due to a current surge.

Blends with the most Hylon VII were the ones most difficult to extrude because a lot of current was needed for even a low throughput. Villar et al. (1994) also reported blends containing the most Hylon VII had the highest viscosity. In contrast, blends with the most EVOH were the easiest to extrude because the low viscosity EVOH shielded the more viscous starch component from the high stress regions.

The viscosity of two starch-EVOH blends were measured by the slit die viscometer and capillary viscometer at 150°C. These starch-EVOH ratios in these blends were 50:50. One of them contained native corn and the other contained Hylon VII, and these blends were not conditioned (they were stored at 20 - 30% relative humidity). The results are shown in Figures A.1 and A.2. The viscosity of the Hylon VII blend is higher than that of the native corn blend. The viscosity obtained in this study were higher than that obtained by Villar et al. (1994) at all shear rates. This is either due to the fact that the samples used in their study had been conditioned at 65% relative humidity for at least one week while no conditioning was done to the samples reported here, and/or that retrogradation might have happened to the current samples and altered their viscosity over time. Villar et al. showed that the starch blends measured without conditioning had a lower viscosity than the conditioned samples for native corn and Hylon VII samples, but a higher viscosity for

the waxy maize blends. Therefore, the difference in viscosity between these studies can be more easily explained in terms of the effects of aging.

The viscosity of the Hylon VII blend measured by the slit die viscometer was a little lower than that measured by the capillary viscometer at the same temperature of 150°C. This is probably due to the temperature rise from viscous heating inside the die. Recall that Hylon VII was the most viscous starch type (Villar et al., 1994). The viscosity was measured by capillary viscometer at 160°C to show the possible amount of temperature rise due to viscous heating. In the capillary viscometer, the polymer temperature was controlled more tightly because the capillary had a much smaller die dimension. For the native corn blend, the viscosity measured by both methods tend to agree. Viscous heating might still be a problem but it should be less severe than that of Hylon VII since the viscosity of the native corn blend was not as high. Newtonian behavior was not observed for either one of these blends.

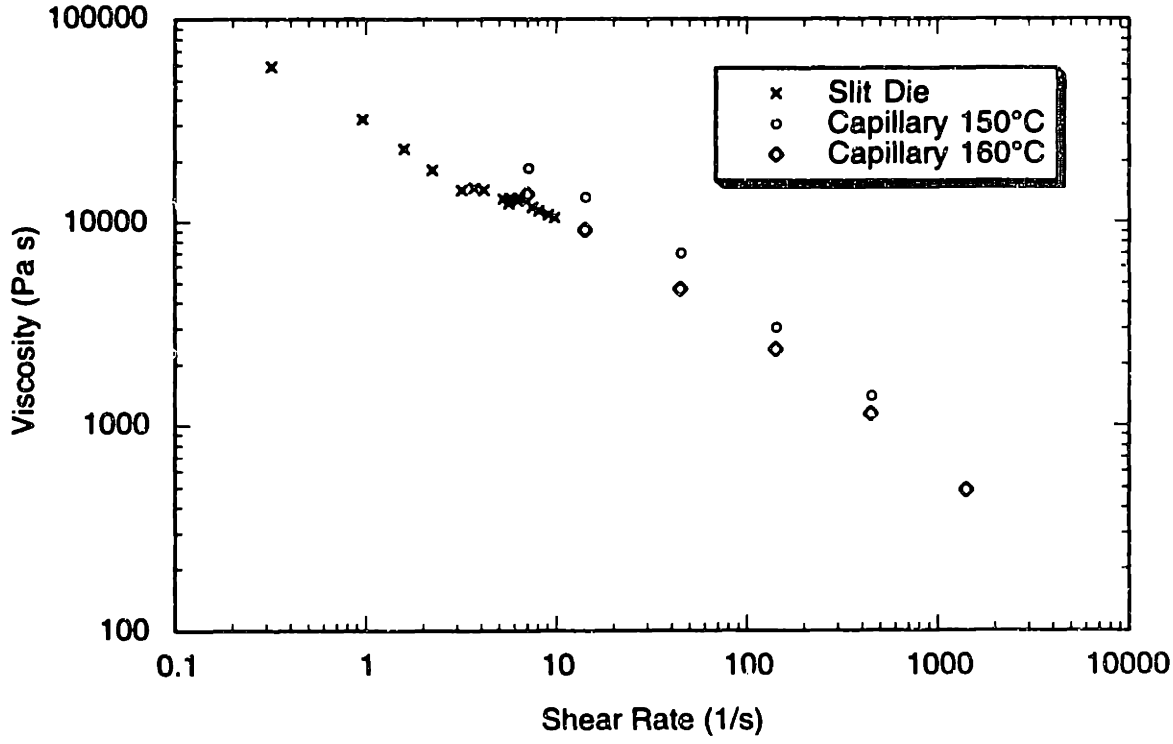

Figure A.1: Viscosity of Hylon VII-EVOH blend (50:50) as a function of shear rate at 150°C. Viscous heating lowered the viscosity in the slit die measurement.

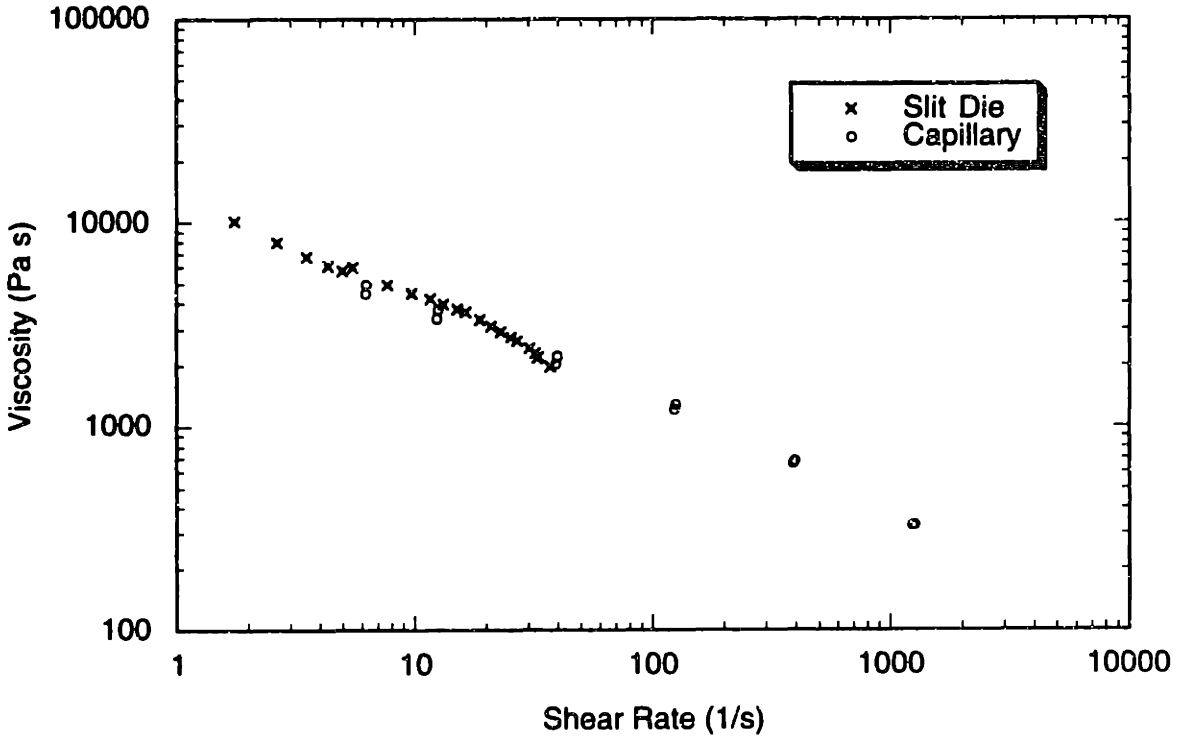

Figure A.2: Viscosity of native corn-EVOH blend (50:50) as a function of shear rate at 150°C.

Appendix B

Numerical Methods

The goal of this appendix is to explain the numerical methods used in this work to calculate the velocity profiles under the experimental conditions. The results of this simulation exercise are presented in Sections 4.2 and 4.3 of this thesis. In Section 4.2, these profiles are compared with those obtained by using LDV. In Section 4.3, the effects of the end walls on the retardance and extinction angle were studied based on these simulated profiles. Close to the end walls, it is difficult to obtain velocity data with LDV because the beams are blocked by the metal walls.

The velocity profiles of polymer melts flowing inside a slit channel die is best calculated by numerical methods. Analytical solution does not exist for the slit flow problem which includes the main features of the flow studied in this work. These features are the presence of the end walls, and a viscosity gradually decreasing with shear rate. Boussinesq (1868) gave the analytical solution of a pressure-driven flow in a slit channel with end walls, whereas Rothemeyer (1969) presented the velocity profile for a power-law fluid flowing in a square channel. The results of Rothemeyer is not used in this research because the power-law model does not describe accurately how the viscosity of the LDPE used in this study changes with shear rate. In the shear rate range achieved in the experiments (0 s^{-1} to 5 s^{-1}), there is no single power-law index that fits the viscosity data for the entire shear rate range (Figure 4.1). Moreover, the power law model does not predict a constant viscosity as the shear rate approaches zero, yet most commercial polymers show such a zero-shear-rate viscosity. Therefore, the power-law model is not suitable for the LDPE used in this study, so Rothemeyer's results cannot be used.

In contrast, the Carreau model allows a gradual change in viscosity over a particular shear rate range. It describes the change in viscosity of the LDPE employed much better than the power-law model (Figure 4.3). Therefore, the Carreau model was used in this simulation exercise. To solve such a pressure-driven flow problem in a slit channel with the Carreau model, finite element method was used. Boundary condition specification, mesh generation, and the velocity calculations were done by using a commercially available program FIDAP^{TM}. In Section B.1, the equations to the solved are discussed, followed by an analysis on the significance of viscous heating. Section B.2 explains the principle behind finite element method and some of the specifics of formulating this mathematical problem using FIDAP^{TM}.

B.1 Formulation of the continuum problem

Molten LDPE flowed down a rectangular channel at a fixed temperature inside the die because of the pressure differential between the entrance and the exit of the die. Given the pressure gradient, the channel dimensions, and the viscosity model, what is the velocity of the fluid as a function of position across the channel?

The resultant velocity profile is governed by the mass and momentum balance equations and the boundary conditions. From mass balance:

$$\nabla \cdot \boldsymbol{u} = 0 \tag{B.1}$$

assuming the fluid is incompressible, and **u** is the velocity. From momentum balance:

$$\rho \frac{D\boldsymbol{u}}{Dt} = -\nabla p - [\nabla \cdot \boldsymbol{\tau}] + \rho \boldsymbol{g} \tag{B.2}$$

where ρ is the density, $\frac{Du}{Dt}$ is the substantial derivative of velocity, ∇p is the pressure gradient, $\mathbf{g}$ is the gravitation force, and τ is the stress tensor. The Reynolds number for typical flow conditions used in this research is in the order of 10^{-6}. Therefore, the convective part can be dropped:

$$0 = -\nabla p - [\nabla \cdot \tau] + \rho g \tag{B.3}$$

The stress tensor is related to the rate-of-strain tensor by:

$$\tau = -\eta \dot{\gamma} \tag{B.4}$$

where $\dot{\gamma}$ is the rate-of-strain tensor, and η is the viscosity defined as a function of shear rate by the Carreau model:

$$\frac{\eta(\dot{\gamma}) - \eta_\infty}{\eta_0 - \eta_\infty} = [1 + (\lambda\dot{\gamma})^2]^{(n-1)/2} \tag{B.5}$$

where $\dot{\gamma} = \sqrt{\frac{1}{2}(\dot{\gamma}:\dot{\gamma})}$ is the second invariant of the rate-of-strain tensor, η_0 is the zero-rate-shear viscosity, η_∞ is the viscosity at infinite shear rate, λ is a time constant, and n is a constant that characterizes the power-law behavior of the viscosity at high shear rates.

With proper die insulation and material mixing as explained in Section 3.2, the temperature of the channel walls and the polymer coming into the channel were found to be the same and were fairly constant over time. The only way that temperature could affect the velocity profile was by viscous heating. The following scaling analysis shows that viscous heating did not change the velocity significantly in the experimental conditions of this study. The key dimensionless groups are the Peclet number ($Pe = \frac{\rho C_p \langle u_z \rangle B}{k} = \frac{\langle u_z \rangle B}{\alpha}$) and the Graetz number ($Gr = \frac{\langle v_z \rangle B^2}{\alpha z}$). The Peclet number

indicates the relative rates of heat convection to conduction, convection is the dominant mode of heat transfer if the Peclet number is large. The symbols ρ, C_p, $\langle u_z \rangle$, B, k, and α represent the density, specific heat capacity, average velocity in the flow direction, channel half-width, thermal conductivity, and thermal diffusivity, respectively. The Graetz number determines whether the position of measurement (z=0.15 m) is in the thermal entry region or in the thermally fully-developed region. Thermal entry region corresponds to a large Graetz number. The position z=0 represents the die entrance.

The Peclet numbers for all the flow rates were found to be larger than unity. This is because despite the low mean velocity and small gap size (B=0.002 m), the polymer used in this study have a low thermal diffusivity (α=1.2 x 10^{-7} m^2/s). With conduction controlling the rate of heat transfer, the amount of temperature rise due to viscous heating can be estimated by a balance between the viscous dissipation term and the conduction term in the energy balance equation. Three cases with screw speeds ranging from 5 rpm to 10 rpm are considered. These cases correspond to the flow rates at which the viscosity and first normal stress coefficients were measured by using the optical method.The results are shown in Table B.1.The Graetz numbers for all cases are slightly smaller than unity, indicating the position of measurement is barely in the thermally fully-developed region.

Screw speed (rpm)	Mean velocity (mm/s)	Peclet number	Graetz number	Temperature rise (°C)
5	1.2	20	0.27	0.06
7.5	1.8	29	0.39	0.12
10	2.3	39	0.52	0.22

Table B.1: Dimensionless groups and temperature rise due to viscous heating.

Assuming a constant viscosity μ, the energy equation is:

$$\rho C_v \frac{DT}{Dt} = k\nabla^2 T + \frac{1}{2}\mu(\dot{\gamma}:\dot{\gamma}) \tag{B.6}$$

At steady state,

$$0 = k\nabla^2 T + \frac{1}{2}\mu(\dot{\gamma}:\dot{\gamma}) \tag{B.7}$$

With the characteristic length scale as the channel half-width B, and the shear rate taken to be $\langle v_z \rangle / B$,

$$0 = k \cdot \frac{\Delta T}{B^2} + \frac{\mu}{2}\left(\frac{\langle v_z \rangle}{B}\right)^2 \tag{B.8}$$

$$\Delta T = O\left(\frac{\mu \langle v_z \rangle^2}{2k}\right) \tag{B.9}$$

The change in temperature due to viscous dissipation is thus of the order of $\frac{\mu \langle v_z \rangle^2}{2k}$. The temperature change at the maximum shear rates investigated in this study was about 0.06°C to 0.22°C. The viscosity change corresponding to a 0.22°C change in temperature is about 2% at these shear rates. Therefore, the velocity change due to viscous heating will be less than 2%.

B.2 Formulation of the Discrete Problem

The finite element method reduces the continuum problem with a discrete problem. For a boundary-value problem like the one posed in Section B.1, the method divides the domain of interest into a finite number of elements. Each element contains a fixed number of nodes. Piece-wise continuous polynomials are used to interpolate the value of the

unknowns between the nodes. Given these interpolation functions, the objective of the finite element method is to find the unknowns at the nodes which best satisfy the conservation equations to be solved. Mathematically, the method approximates the exact solution by:

$$\phi(x, y, z) = \sum_{i=1}^{m} \gamma_i \phi_i(x, y, z) \tag{B.1}$$

where $\phi(x, y, z)$ is the approximating function, γ_i is the value of ϕ at node i, and the $\phi_1 \ldots \phi_n$ are the linearly independent interpolation polynomials.

The solution from the finite element method will not be in general the exact solution, but the error (the difference between the exact and the discrete solution) will be reduced as the element size is reduced. The Galerkin form of the Method of Weighted Residuals seeks to minimize these errors by making the residuals orthogonal to the interpolation functions on each element. For the problem in Section B.1, the mass and momentum balances are the equations to be solved (Equations B.1 and B.2). The unknowns are the velocity vector **u** and the pressure p(x,y,z). The boundary condition is a zero velocity at the walls. Within each element, the velocity and pressure fields are approximated by:

$$\boldsymbol{u}(x, y, z) = \sum_{i=1}^{m} \varphi_i \boldsymbol{U}_i \tag{B.2}$$

$$p(x, y, z) = \sum_{i=1}^{m} \psi_i p_i \tag{2.3}$$

where $\varphi_1 \ldots \varphi_m$ and $\psi_1 \ldots \psi_m$ are the interpolation functions for velocity **u** and pressure p respectively, and $\mathbf{U}_1 \ldots \mathbf{U}_m$ and $p_1 \ldots p_m$ are the velocities and pressures at the nodes. The elements used were three dimensional iso-parametric bricks with 27 nodes. The velocity was

approximated by triquadratic interpolation functions, whereas the pressure was approximated by trilinear functions. The weak forms of Equations B.1 and B.2 were formed by first multiplying these equations by the approximating functions u and p. Then these products were integrated throughout the entire volume of interest. The resulting integrals are called the weak forms. Substituting these approximations into the weak forms of the field equations and boundary conditions yields the residuals $\boldsymbol{R}_1$ for momentum conservation and $\boldsymbol{R}_2$ for mass conservation:

$$\boldsymbol{R}_1 = \boldsymbol{R}_1(\varphi, \psi, \boldsymbol{U}, p) \tag{2.4}$$

$$\boldsymbol{R}_2 = \boldsymbol{R}_2(\varphi, \boldsymbol{U}) \tag{2.5}$$

The orthogonality of the Galerkin Method is expressed by:

$$\int_V \boldsymbol{R}_1 \varphi dV = 0 \tag{2.6}$$

$$\int_V \boldsymbol{R}_2 \psi dV = 0 \tag{2.7}$$

where V is the total volume of the domain being considered. Evaluating these integrals yields two matrix equations in terms of the unknowns $\mathbf{U}_1 \ldots \mathbf{U}_m$ and $p_1 \ldots p_m$:

$$\boldsymbol{K}(\boldsymbol{U})\boldsymbol{U} - \boldsymbol{C}p = \boldsymbol{F} \tag{2.8}$$

$$\boldsymbol{C}^T\boldsymbol{U} = 0 \tag{2.9}$$

where K(U) is the matrix that represents the diffusion of momentum, C and C^T are the matrices that represent the gradient of pressure and divergence of velocity respectively. The exact forms and derivations of the matrices K(U) and C are can be found in Strang and Fix (1973) or Dahlquist et al. (1974).

As noted before, the elements used for this simulation exercise was a 27-node iso-parametric brick. A triquadratic function was used for velocity interpolation, and pressure was interpolated trilinearly. The detail forms of the interpolation functions can be found in the FIDAP Theory Manual. There were 25 elements or 51 nodes along the smallest dimension, 10 elements or 21 nodes along the depth of the channel, and 2 elements or 5 nodes along the length of the flow channel. Further refinement of the mesh in any directions did not show a significant change in the velocity profile. Successive substitution was used to solve the matrix equation since it is very stable and efficient for this relatively small size problem. Iteration was terminated when both the relative velocity error and the relative residual error are less than 0.001:

$$\frac{\|\boldsymbol{U}_i - \boldsymbol{U}_{i-1}\|}{\|\boldsymbol{U}_i\|} \leq 0.001 \tag{B.10}$$

$$\left\|\frac{\boldsymbol{R}_i}{\boldsymbol{R}_0}\right\| \leq 0.001 \tag{B.11}$$

where **U** is the solution vector and $\boldsymbol{R}$ is the residual vector. The norm $\|.\|$ is the L_2 norm, which is the root mean square norm summed over all the equations.

The results of this simulation exercise are the velocity profiles $v_z(x,y)$. As noted before, they are important for comparing with the experimentally measured profiles, and for computing the change in birefringence and extinction angle along the beam path. The results are summarized in Sections 4.2 and 4.3 of this thesis.

References

Abetz, V. and G. G. Fuller 1990 Two-color rotary modulated flow birefringence *Rheol. Acta* **29** 11-15

Aldhouse, S. T. E., M. R. Mackley, and I. P. T. Moore 1986 Experimental and Linear Viscoelastic Stress Distribution Measurments of High Density Polyethylene Flowing Into and Within a Slit. *Journal of Non-Newtonian Fluid Mechanics* **21** 359-376.

Azzam, R. M. A. 1978 Propagation of partially polarized light through anisotropic media with or without depolarization: A differential 4 x 4 matrix calculus. *J. Opt. Soc. Am.* **68(12)** 1756-1767.

Baaijens, J. P. W. 1994 *Evaluation of Constitutive Equations for Polymer Melts and Solutions in Complex Flows* Doctoral Thesis, Technische Universiteit Eindhowen.

Bastioli, C., V. Bellotti, and A. Rallis. 1994 Microstructure and melt flow behavior of a starch-based polymer. *Rheol. Acta.* **33** 307-316.

Bird, R. B., R. C. Armstrong, and O. Hassager. 1987 *Dynamics of Polymeric Liquids. Volume 1: Fluid Mechanics.* Wiley, New York.

Bousmina, M. and R. Muller. 1993 Linear viscoelasticity in the melt of impart PMMA. Influence of concentration and aggregation of dispersed rubber particles. *Journal of Rheology* **37(4)** 663-679.

Bousmina, M. and R. Muller. 1996 Rheology/morphology/flow conditions relationships for polymethylmethacrylate/rubber blend. *Rheol. Acta.* **35** 369-381.

Bruin, S., D. J. Zuilichem, and W. Stolp. 1978 *J. of Food Proc. Eng.* **2** 83.

Burghardt, W. R. and G. G. Fuller 1988 End Effects in Flow Birefringence Measurements *J. Rheol.* **33(5)** 771-779.

Cervone, N. W. and J. M. Harper. 1978 *J. of Food Proc. Eng.* **2** 83.

Chow, A. W. , G. G. Fuller, D. G. Wallace, and J. A. Madri. 1985 Rheooptical Response of Rodlike Chains Subject to Transient Shear Flow. 2. Two-Color Flow Birefringence Measurements on Collagen Protein. *Macromolecules* **18(4)** 793-804.

Dahlquist, G and A. Bjorck. 1974. *Numerical Methods.* Translated by N. Anderson. Prentice-Hall 1st ed.

Dantec Burst Spectrum Analyzer User's Guide for Models 57N10/57N14/57N25.

Dealy, J. M. and K. F. Wissbrun. 1990 *Melt Rheology and Its Role in Plastic Processing.* Van Nostrand Reinhold, New York.

Della Valle, G., P. Colonna, and A. Patria. 1996 Influence of amylose content on the viscous behavior of low hydrated molten starches. *J. Rheol.* **40(3)** 347-362.

Doane, W. M., C.L. Swanson, and G. F. Fanta. 1991 Emerging Polymeric Materials Based on Starch. *Emerging Technologies for Materials and Chemicals for Biomass. ACS Symposium Series* **496** 197-230.

Drain, L.E. 1980 *The Laser Doppler Technique.* John Wiley & Sons. 1st Edition.

Drexler, L. H. and C. D. Han. Studies of Converging Flow of Viscoelastic Polymeric Melts. II. Velocity Measurements in the Entrance Region of a Sharped-Edged Slit Die. *J. of App. Poly. Sci.* **17** 2355-2368.

Fletcher, S. I., T. J. McMaster, A. C. Smith, and P. Richmond. 1985 *Chem. Eng. Commun.* **32** 239.

Fox, T. G. and P. J. Flory. 1948 Viscosity-Molecular Weight and Viscosity-Temperature Relationship for Polystyrene and Polyisobutylene. *Journal of the American Chemical Society* **70** 2384-2395.

Flory, P. J. 1940 Viscosities of Linear Polyesters. An Exact Relationship Between Viscosity And Chain Length *J. of the American Chemical Society* **62** 1057- 1070.

Frocht, M. M. 1941 *Photoelasticity* Wiley, New York, Vol. 1.

Fuller, G. G. 1995 *Optical Rheometry of Complex Fluids.* Oxford 1st Ed.

Galante, S. R. and P. L. Frattini. 1991 The influence of end effects on birefringence measurements in nominally two-dimensional channel flows. *J. Rheol.* **35(8)** 1551-1581.

Genieser, L. H. 1997 *Stress- and Velocity-Field Evolution in Viscoelastic Planar Contraction Flow.* Doctoral Thesis, MIT Department of Chemical Engineering.

George, E. R., T. M. Sullivan, and E. H. Park. 1994 Thermoplastic Starch Blends With a Poly(ethylene-co-vinyl alcohol): Processibility and Physical Properties. *Polymer Engineering and Science.* **34** No. 1

Han, C. D. and M. Charles. 1970 *Trans. Soc. Rheol.* **14** 409.

Han, C. D. and L. H. Drexler 1973 Studies of Converging Flow of Viscoelastic Polymeric Melts. I. Stress-Birefringent Measurements in the Entrance Region of a Sharp-Edged Slit Die. *J. of App. Poly. Sci.* **17** 2329-2354.

Han, C. D. and L. H. Drexler 1973 Studies of Converging Flow of Viscoelastic Polymeric Melts. III. Stress and Velocity Distributions in the Entrance Region of a Tapered Slit Die. *J. of App. Poly. Sci.* **17** 2369-2393.

Harper, J. M., T. P. Rhodes, and L. A. Wanninger Jr. 1971 *Chem. Eng. Prog. Symp. Ser.* **67** 40.

Hongladarom, K., W. R. Burghardt, S. G. Baek, S. Cementwala, and J. J. Magda. 1993 Molcular alignment of polymer liquid crystals in shear flows: 1. Spectrographic birefringence techniuqe, steady-state orientation, and normal stress behavior in poly(benzyl glutamate) solutions. *Macromolecules.* **26** 772-784.

Janeschitz-Kriegl, H. 1983. *Polymer Melt Rheology and Flow Birefringence.* Springer-Verlag 1st Ed.

Laun, H. M. 1986 *J. Rheol.* 30 459-501.

Larson, R. G., S. A. Khan, and V. R. Raju. 1988 *Relaxation of Stress and Birefringence in Polymers of High Molecular Weight* **32(2)** 145-161.

Lodge, A. S. 1973. U.S. Patent No. 3777549.

Lodge, A. S. Normal Stress Difference from Hole Pressure Measurements. 1988 Chapter 11 of *Rheological Measurement* Edited by A. A. Collyer and D. W. Clegg. Elsevier Applied Science.

Luker, Keith. 1993 Personal Communication.

Mackay, M. E. 1985 *Behaviour of polymer solutions and melts in shearing and elongational flow using streak photography and birefringence*, PhD thesis, University of Illinois, Urbana.

Mackay, M. E. and D. V. Boger. 1988 Flow Visualisation in Rheometry Chapter 14 of *Rheological Measurement* Edited by A. A. Collyer and D. W. Clegg. Elsevier Applied Science.

Mackey, K. L. and R. Y. Ofoli. Rheological Modeling of Corn Starch Doughs At Low to Intermediate Moisture 1990 *J. of Food Sci.* **55(2)** 417-423.

Mackley M. R. and I. P. T. Moore. 1986 Experimental Velocity Distribution Measurements of High Density Polyethylene Flowing Into and Within a Slit. *Journal of Non-Newtonian Fluid Mechanics.* **21** 337-358.

McHugh, A. J., M. E. Mackay, and B. Khomami. 1987 Measurement of Birefringence by the Method of Isoclinics *J. of Rheol.* **31(7)** 619-634.

Nagai, T., Y. Kimizuka, K. Nito, and J. Seto. 1992. Melt Viscosity and Flow Birefringence of Polycarbonate. *Journal of Applied Polymer Science* **44** 1171-1177.

Narayan, R. 1994 Polymeric Materials from Agricultural Feedstocks. *Polymers from Agricultural Coproducts. ACS Symposium Series* **575** 2-28.

Padmanabhan, M. and M. Bhattacharya. 1993 Effect of Extrusion Processing History on the Rheology of Corn Meal. *J. of Food Eng.* **18** 335-349.

Quinzani, L. M. 1991 *Birefringence Studies of Entry Flows of Concentrated Polymer Solutions*. Doctoral Thesis, MIT Department of Chemical Engineering.

Rempp, P and E. W. Merrill. 1991 *Polymer Synthesis.* Huthig and Wepf 2nd Ed.

Retting, W. 1979 Generation and relaxation of the molecular orientation during hot-stretching of amorphous thermoplastics. *Colloid & Polymer Science* **257** 689-710.

Scientists Are Proving That Natural Plastic Is Not an Oxymoron. *The New York Times.* Sunday October 21, 1990.

Senouci, A. and A. C. Smith. 1988 An experimental study of food melt rheology. I. Shear viscosity using a slit die viscometer and a capillary rheometer. *Rheol. Acta.* **27** 546-554.

Simmons, S. 1992 *Structure and Property Relationships in Biodegradable Starch-Based Thermoplastic Systems.* Research Proposal, MIT Department of Chemical Engineering.

Simmons, S. 1995 *Influence of Processing on the Structure and Properties of Semi-Crystalline Polymer Systems: 1) Biodegrable Starch/Poly(ethylene-vinyl alcohol) blends and 2) Polyolefinic Thermoplastics.* PhD Thesis, MIT Department of Chemical Engineering.

Strang, G. and G. Fix. 1973. *An Analysis of the Finite Element Method.* Wellesley-Cambridge Press.

Vergnes, B. and J. P. Villemaire. 1987 Rheological behaviour of low moisture molten maize starch. *Rheol. Acta* **26** 570-576.

Villar, M. A., E. L. Thomas, and R. C. Armstrong. 1995 Rheological Properties of Thermoplastic Starch and starch/poly(ethylene-co-vinyl alcohol) blends. Polymer **36** 1869-1876.

Wales, J. L. S. 1976 *The application of flow birefringence to rheological studies of polymer melts* Delft University Press.

Weigand, C. E. 1992 *Thermoplastic Processing of Starch ad Starch-Based Systems.* Masters Thesis, MIT Department of Materials Science and Engineering.

Wippler, C. 1991 Low frequency viscosities of PS/PMMA/PS-b-PMMA blends. *Polymer Bulletin.* **25** 357-363.

Theocaris, P. S. and E. E. Gdoutos. 1979 *Matrix Theory of Phototelasticity.* Springer, Berlin.

Yasuda, K. 1979 PhD Thesis. MIT Department of Chemical Engineering.

Young, R. J. and P. A. Lovell. 1991 *Introduction to Polymers.* Chapman and Hall 2nd Ed.

Zhang, H. P. Moldenaers, and J. Mewis. 1994 An improved method for the measurement of strong flow birefringence *Rheol. Acta* **33** 317-321.